Characterization of the degradation of carbon-supported tin and bismuth gas-diffusion electrodes applied in alkaline CO_2 electrolysis

Von der Fakultät Energie-, Verfahrens- und Biotechnik der Universität Stuttgart
zur Erlangung der Würde eines Doktors der
Ingenieurwissenschaften (Dr.-Ing.) genehmigte Abhandlung

Vorgelegt von

M. Eng. **Fabian Bienen**

aus Bünde, Westfalen

Hauptberichter:	Prof. Dr. rer. nat. K. Andreas Friedrich
Mitberichter:	Prof. Dr.-Ing. Elias Klemm
Prüfungsvorsitzender:	Prof. Dr.-Ing. Ulrich Nieken
Tag der mündlichen Prüfung:	27.10.2021

Institut für Gebäudeenergetik, Thermotechnik und Energiespeicherung

der Universität Stuttgart

2021

'You cannot hope to build a better world without improving the individuals.
To that end each of us must work for his own improvement,
and at the same time share a general responsibility for all humanity,
our particular duty being to aid those to whom we think
we can be most useful.'

Marie Skłodowska Curie

Acknowledgement

Firstly, I want to express my gratitude to Prof. Dr. K. **Andreas Friedrich** for giving me the opportunity to conduct research on the presented - in my opinion - important, challenging but fascinating topic. I am grateful that you gave me the chance to may slightly contribute in hopefully making the world a better place. You always provided sophisticated and inventive advice. Thank you!

Additionally, I want to thank Prof. Dr.-Ing. **Elias Klemm** for being my co-supervisor and beyond of that the most motivational person I know yet. It was always a pleasure to work and discuss with you.

Furthermore, I want to thank Dr. **Norbert Wagner** for being my group head and always finding 'some money' whenever I wanted to build up new test set-ups or hire students. Thank you for putting up with me, I know it must have been a little challenge.

Beyond of that, I want to express my gratitude to Dr. **Armin Löwe**, **Joachim Hildebrand** and **Dennis Kopljar** who were perfect sparing's partners for scientific discussions. Not to be forgotten, Dr. **Simon Geiger** who always broadened my vision with creative inputs.

Finally, I want to thank all the members of the battery group for being so supportive and sympathetic. Therefore, I want to thank **Jan Majchel**, my office mate, for the innumerable discussions and funny moments. I know that I will not forget the time we shared together in the office. Especially, I want to thank **Joachim Häcker** who also became more than a colleague in this tough time and always giving empathic advice in work and private related topics and introducing me to 'Klettersteige'. Also, I want to thank **Alexander Kube, Christina Schmitt and Diana Maria Amaya Duenas** for their helpfulness and for always having an open door whenever I was in need to talk or discuss.

I also want to thank **Werner Seybold** who was always ready to get work done and to build homemade electrochemical cells or other test-benches. Furthermore, I want to thank **Ina Plock** who supplied high-quality SEM pictures and EDX analysis.

Declaration

I certify that the dissertation entitled:

„ *Characterization of the degradation of carbon-supported tin and bismuth gas-diffusion electrodes applied in alkaline CO_2 electrolysis* “

is entirely my own work. Passages and ideas from other sources have been clearly marked.

Erklärung

Ich versichere, dass ich die vorliegende Dissertation mit dem Titel:

„ *Characterization of the degradation of carbon-supported tin and bismuth gas-diffusion electrodes applied in alkaline CO_2 electrolysis* “

selbständig verfasst und keine anderen als die angegebenen Quellen und Hilfsmittel benutzt habe. Passagen und Gedanken aus fremden Quellen sind als solche kenntlich gemacht.

Fabian Bienen

Stuttgart, 2021.06.10

Abstract

The continuously rising CO_2 concentration in the atmosphere and the associated climate change resulting in a steady increase in the planets' temperature requires immediate counteraction and mitigation of CO_2 emissions. Possible CO_2 mitigation concepts are carbon capture and storage or in the best-case carbon utilization. Renewable energy can be used to power CO_2 electrolysis devices in which CO_2 is used as feed stock and converted to value-added products (CO, CH_4, C_2H_4, HCOOH / $HCOO^-$, …) guiding the route to a circular carbon economy. Therefore, traditional synthesis routes for carbonaceous species might be substituted by environmental friendlier CO_2 electrolysis. Consequently, the role of CO_2 can be changed from a harmful species to a valuable resource.

This thesis focuses on the tin catalyzed electrochemical conversion of CO_2 to formate which is principally close to be economically feasible due to the already achieved performance targets (activity, selectivity) for this half-cell reaction. Nevertheless, long-term operation and full cell setups are rarely reported since most of the scientists focus on the development of suitable catalysts for a specific target product. Consequently, the degradation of CO_2 converting electrodes is an underrepresented topic in literature. Therefore, this thesis provides an elaborated fundamental electrochemical impedance spectroscopic (EIS) study which can be used to identify degradation mechanisms during operation of an CO_2 electrolysis cell.

Firstly, tin foil was investigated via EIS by varying temperature, electrolyte as well as current density. In combination with the analysis of the measured Faraday efficiencies (FE) the results pointed out that the observed impedance spectrum is determined not only by the CO_2 reduction reaction (CO_2RR) - the reaction of interest - but also the parasitic aqueous electrolyte decomposition: the hydrogen evolution reaction (HER). The superposition of contributions of both reactions to the measured features in the impedance spectrums was supported by equivalent circuit modelling. However, it was suggested that the two observed features in the EIS spectrum are determined by a proton coupled charge transfer reaction and ionic migration of HCO_3^- (aq).

Building on the foil measurements, a fundamental EIS study for tin gas-diffusion electrodes, which are due to their sufficient activity more relevant than tin foil electrodes, was conducted by changing CO_2 volume fraction, electrolyte, temperature and current density. Considering the measured FEs it could be concluded that, depending on the reaction conditions, the CO_2RR or HER determines the spectrum shape. In the spectrum, features arise due to the ionic and

electrical conductivity inside the porous system, homogeneous conversion of CO_2 with OH^-, a charge transfer onto CO_2 to form $CO_2^{\bullet -}$ and the liquid phase diffusion of CO_2 to the active sites. Interestingly, it could be stated that for unfavorable CO_2 electrolysis (CO_2EL) conditions (low CO_2 volume fraction in feed-gas) the impedance spectra shape dominating reaction switches from CO_2RR to HER. The proposed information in this study can help other scientists to identify degradation mechanisms of GDEs.

The generated fundamental knowledge about EIS for GDEs in CO_2EL was then transferred into an applied study were the degradation of tin- and bismuth- based GDEs was investigated. In particular, the effect of wetting on the electrode's performance was the aim of these investigations. Therefore, the wetting state was measured operando in terms of differential double layer capacitance via EIS and additionally evaluated post mortem with energy dispersive X-ray microscopy. The electrolyte was tested for diluted catalyst species using inductively coupled plasma mass spectrometry. For the tin-based GDE a revealed catalyst leaching prevented a clear assignment of the observed degradation to one single process as it was aimed for. Obviously, these GDEs degraded due to a loss of catalyst whereas this might be not the sole reason. The bismuth-based GDEs did not show a net catalyst leaching, but a catalyst aggregation induced by a dissolution / reduction process could be suggested. This catalyst aggregation and probably an ongoing electrode wetting lead to a marginal electrode degradation.

Lastly, an alternative field of application for the produced formate solution was demonstrated in a proof of concept study: the generated formate containing electrolyte was transferred into a direct formate fuel cell or in a polymer electrolyte membrane fuel cell after formate was decomposed to H_2. Within this study formate was re-electrified and its usage as energy carrier demonstrated.

Zusammenfassung

Die in der Atmosphäre stetig ansteigende Konzentration von CO_2, welches maßgeblich für den Klimawandel verantwortlich ist, führt zu einem kontinuierlichen Anstieg der Temperatur auf der Erde und zeigt, dass unmittelbar Maßnahmen zur Vermeidung von CO_2-Emissionen ergriffen werden müssen. Als mögliche Konzepte zur Verminderung von CO_2-Emissionen werden typischerweise die CO_2 -Abscheidung (carbon capture and storage) und im besten Falle die CO_2 -Nutzung (carbon utilization) genannt. CO_2-Elektrolyseure können mit erneuerbarer Energie und CO_2 als Rohstoff betrieben werden und erzeugen wertvolle Kohlenwasserstoffe (CO, CH_4, C_2H_4, HCOOH / $HCOO^-$, …). Im Idealfall kann dies zu einer Kohlenstoffkreislaufwirtschaft führen. Auf diese Weise können traditionelle, CO_2 intensive, Herstellverfahren von Kohlenwasserstoffen durch die CO_2 -Elektrolyse substituiert werden. Folglich ändert sich die Rolle des CO_2 von einem schädlichen Treibhausgas hin zu einem wertvollen Rohstoff.

Die in dieser Dissertation dargestellten Arbeiten konzentrieren sich auf die mit Zinn katalysierte elektrochemische Umwandlung von CO_2 zu Formiat, welche aufgrund der bereits heutzutage in Halbzellenmessungen erzielten Leistungskenndaten (Selektivität, Aktivität) an der Schwelle zur ökonomischen Realisierbarkeit steht. Nichtsdestotrotz wurden bisher nur wenige Langzeitstudien oder der Betrieb von Vollzellen demonstriert. Dies liegt daran, dass die meisten Wissenschaftler sich auf die Entwicklung von maßgeschneiderten Katalysatoren für die selektive Herstellung eines Zielproduktes beschäftigt haben. Folglich, ist die Degradation von CO_2 umwandelnden Elektroden ein unterrepräsentiertes Thema in der Forschungsgemeinschaft und diese Arbeit füllt eine entsprechende wissenschaftliche Lücke. In dieser Dissertation wurden grundlegende elektrochemische Impedanz spektroskopische (EIS) Studien durchgeführt, deren Erkenntnisse bei der Identifizierung von Degradationsmechanismen während des Elektrolysebetriebes herangezogen werden können.

Zunächst wurde eine einfache Elektrodengeometrie, Zinnfolie, mittels EIS untersucht, indem die Temperatur, der Elektrolyt und die applizierte Stromdichte variiert wurde. Es konnte unter Heranziehung der gemessenen Faraday-Effizienzen (FE) beobachtet werden, dass der Verlauf des Impedanzspektrums nicht nur von der CO_2 Reduktionsreaktion (engl. CO_2 reduction reaction CO_2RR), sondern gleichzeitig auch von der parasitär, durch Zersetzung des wässrigen Elektrolyten, stattfindenden Wasserstoffentwicklungsreaktion (engl. Hydrogen evolution reaction, HER) überlagert wird. Die Überlagerung von zwei verschiedenen parallel ablaufenden

Reaktionen im Impedanzspektrum konnte auch mittels Ersatzschaltbildmodellierung bestätigt werden. Für die beiden erkennbaren Prozesse im Impedanzspektrum wurden ein Protonen gekoppelter Ladungsdurchtritt und die Bewegung (Migration/Diffusion) von HCO_3^-(aq) in der Flüssigphase vorgeschlagen.

Aufbauend auf den vorherigen Messungen wurden Zinn basierte Gasdiffusionselektroden (GDEs), welche im Vergleich zur Zinnfolie aufgrund ihrer hohen Aktivität von höherer praktischer Bedeutung sind, untersucht. EIS Messungen erfolgten unter Variation der CO_2-Volumenkonzentration, Elektrolytzusammensetzung, Temperatur und Stromdichte. Unter Betrachtung der parallel gemessenen FEs (HER vs. CO_2RR) konnte gezeigt werden, dass bei diesen Elektroden das gemessene Impedanzspektrum je nach Reaktionsbedingungen entweder durch die CO_2RR oder HER dominiert wird. Die im Impedanzspektrum abgebildeten Verläufe werden hervorgerufen durch die elektrische und ionische Leitfähigkeit im Porensystem, die Reaktion von CO_2 und OH^-, den Ladungsdurchtritt auf CO_2 unter Bildung von $CO_2^{\bullet -}$ und die Diffusion von CO_2 in der Flüssigphase hin zu den aktiven Zentren. Interessanterweise wurde für ungünstige CO_2-Elektrolyse (CO_2EL)-Bedingungen (niedrige CO_2 -Volumenkonzentration im Zustrom) beobachtet, dass im Impedanzspektrum die bestimmende Reaktion von der CO_2RR hin zur HER wechselt. Mit Hilfe der vorgeschlagenen im Impedanzspektrum abgebildeten Prozesse können interessierte Wissenschaftler die Degradation ihrer für die CO_2EL hergestellten GDEs nun einfacher untersuchen.

Die Erkenntnisse aus den EIS Messungen für die CO_2 umwandelnden GDEs wurde dann in einer anwendungsnahen Untersuchung von Zinn- und Bismut basierten GDEs vertieft. Speziell sollte der Einfluss der GDE Benetzung auf die Elektrodenleistungsfähigkeit untersucht werden. Dafür wurde im Betrieb die Benetzung der Elektrode über die differentielle Doppelschichtkapazität (ermittelt via EIS) und *post mortem* die Eindringtiefe des Elektrolyten über Energiedispersive Röntgenspektroskopie evaluiert. Der Elektrolyt wurde auf gelöste Katalysatorspezies mittels Massenspektrometrie mit induktiv gekoppeltem Plasma geprüft. Es wurde ein Auflösen des Zinn-Katalysators aus der GDE festgestellt und dieser Effekt verhindert, dass weitere Degradationsmechanismen zugeordnet werden konnten, da die Auflösung des Katalysators die möglicherweise vorliegenden weiteren Effekte überlagert. Beim Betrieb der Bismut GDE konnte keine Netto-Auflösung beobachtet werden, wohingegen eine Aggregation von Katalysatorpartikeln, induziert durch einen Auflösungs- / Reduktionsprozess, beobachtet werden konnte. Jedoch haben die Aggregation und eine fortschreitende Benetzung nur zu einer minimalen Degradation der Elektrode geführt.

Zuletzt wurde eine alternative Anwendungsmöglichkeit für die bei der CO_2-Elektrolyse erhaltenen Formiatlösung vorgeschlagen. Dafür wurde die Formiatlösung in eine Direkt Formiat Brennstoffzelle oder Polymerelektrolytbrennstoffzelle, nachdem Formiat katalytisch zu H_2 zersetzt wurde, überführt und re-elektrifiziert. Auf diese Weise wurde in einer Machbarkeitsstudie die Verwendung von Formiat als Energieträger demonstriert.

List of publications

This is a cumulative doctoral thesis based on four articles which were published after a peer-review process.

Article I:

'Investigation of CO_2 Electrolysis on Tin Foil by Electrochemical Impedance Spectroscopy'

Fabian Bienen, Dennis Kopljar, Simon Geiger, Norbert Wagner, K. Andreas Friedrich

ACS Sustainable Chemistry and Engineering, **2020**, 8 (13), 5192-5199, doi: 10.1021/acssuschemeng.9b07625.

Contribution Fabian Bienen: concept, experiments, evaluation and writing. Rebuttal during peer-review process.

Article II:

'Revealing Mechanistic Processes in Gas-Diffusion Electrodes During CO_2 Reduction via Impedance Spectroscopy'

Fabian Bienen, Dennis Kopljar, Armin Löwe, Simon Geiger, Norbert Wagner, Elias Klemm. K. Andreas Friedrich

ACS Sustainable Chemistry and Engineering, **2020,** *8* (36), 13759-13768, doi: 10.1021/acssuschemeng.0c04451.

Contribution Fabian Bienen: concept, GDE manufacturing (except: SnO_2 / C synthesis) and experiments (except: XRD, XPS, SEM, Hg-Porosimetry), evaluation and writing. Rebuttal during peer-review process.

Article III:

'Degradation study on tin- and bismuth-based gas-diffusion electrodes during electrochemical CO_2 reduction in highly alkaline media'

Fabian Bienen, Armin Löwe, Joachim Hildebrand, Sebastian Hertle, Dana Schonvogel, Dennis Kopljar, Norbert Wagner, Elias Klemm. K. Andreas Friedrich

Journal of Energy Chemistry, **2021,** 62, 367–376, doi: 10.1016/j.jechem.2021.03.050.

Contribution Fabian Bienen: concept, GDE manufacturing (except: SnO_2 / C and Bi_2O_3 / C synthesis) experiments (except: ICP-MS, TEM, XRD, XPS, SEM, Hg-Porosimetry), evaluation and writing. Rebuttal during peer-review process.

A**rticle IV:**

'Utilizing Formate as an Energy Carrier by Coupling CO_2 Electrolysis with Fuel Cell Devices'

Fabian Bienen, Dennis Kopljar, Armin Löwe, Pia Assmann, Marvin Stoll, Paul Rössner, Norbert Wagner, K. Andreas Friedrich, Elias Klemm.

Chemie Ingenieur Technik, **2019**, 91 (6), 872-882, doi: 10.1002/cite.201800212.

Contribution Fabian Bienen: concept, experiments regarding direct formate fuel cell (DFFC), evaluation and writing DFFC concerned sections (state of art, experimental, results & discussion). Rebuttal during peer-review process.

Table of Content

List of abbreviations

Abbreviation	Description
AB	acetylene black
ATR-IR	attenuated total reflectance infrared spectroscopy
ATR-SEIRAS	attenuated total reflectance surface-enhanced infrared absorption spectroscopy
BSE	back scattered electrons
CO_2EL	CO_2 electrolysis
CO_2RR	CO_2 reduction reaction
CPE	constant phase element
DFFC	direct formate fuel cell
DFT	density functional theory
ECSA	electrochemical surface area
EDX	energy dispersive X-ray spectroscopy
EIS	electrochemical impedance spectroscopy
FE	Faraday efficiency
GC	gas chromatography
GDE	gas-diffusion electrode
GDL	gas-diffusion layer
HER	hydrogen evolution reaction
HPLC	high performance liquid chromatography
KPI	key performance indicators
LSV	linear sweep voltammetry
MEA	membrane electrode assembly
MIP	mercury intrusion porosimetry
NMR	nuclear magnetic resonance spectroscopy
OER	oxygen evolution reaction
ORR	oxygen reduction reaction
PEMFC	polymer electrolyte membrane fuel cell
SDS	sodium dodecyl sulphate
SE	secondary electrons
SEM	scanning electron microscopy
SHE	standard hydrogen electrode
TEM	transmission electron microscopy

TFFA	thin-film flooded agglomerate
TGA	thermal gravimetric analysis
TPB	triple phase boundary
XPS	X-ray photoelectron spectroscopy
XRD	X-ray diffractometry

List of symbols

Symbol	Description	Unit
a	activity	mol L^{-1}
A	surface	m^2
c	concentration	mol L^{-1}
$C_{d.}$	differential capacitance	F
$C_{G.C.}$	differential capacitance Gouy-Chapman model	F
C_H	differential capacitance Helmholtz model	F
C_S	specific capacitance	F
D	diffusion coefficient	m^2 s^{-1}
d	distance	m
d_{hkl}	plane spacing	m
E	energy or electric potential	J or V
G	Gibbs free energy	J mol^{-1}
I	current	A
j	current density	A m^{-2}
j_0	exchange current density	A m^{-2}
j_{limit}	limiting current density	A m^{-2}
J	diffusion flux	mol m^{-2} s^{-1}
k	reaction rate constant	s^{-1}
K	equilibrium constant	diverse
L	inductance	H
n	number of moles	mol
$\dot{n}_{i,exp.}$	experimental molar flow component i	mol s^{-1}

$\dot{n}_{i,theor.}$	theoretical molar flow component i	mol s^{-1}
Ox	oxidized species	-
p	pressure	Pa
pH	pH value	-
pK_a	negative decadic acid constant	-
q	excess charge	C
Q	electric charge or admittance	C or s^{α} Ω^{-1}
r	pore radius	m
R	resistance	Ω
R_{ct}	charge transfer resistance	Ω
Red	reduced species	-
R_{Ω}	ohmic resistance	Ω
T	temperature	K
t	time	s
U	voltage	V
$\dot{V}_{catholyte}$	catholyte volume flow	L s^{-1}
$\dot{V}_t$	total gaseous volume flow	L s^{-1}
$\dot{V}_{i,exp.}$	volume flow component i experimental	L s^{-1}
$\dot{V}_{i,theor.}$	volume flow component i theoretical	L s^{-1}
w	work	J
x	distance	m
z	number of transferred electrons	-
Z	impedance	Ω
Z_{im}	imaginary part impedance	Ω
Z_{real}	real part impedance	Ω
α	constant phase exponent or symmetry factor	-
β_i	volume fraction component i	%
γ	surface energy	J m^{-2}
γ_{LV}	surface energy liquid vapor interface	J m^{-2}
Γ	surface excess concentration	mol m^{-2}
$\Delta_r G$	Gibbs free reaction energy	J mol^{-1}
$\Delta_r H$	reaction enthalpy	J mol^{-1}

δ_N	Nernst diffusion layer thickness	m
ε_r	relative permittivity	-
η_{ac}	activation overpotential	V
η_{conc}	concentration overpotential	V
η_{diff}	diffusion overpotential	V
η_Ω	ohmic overpotential	V
θ	incident angle	°
θ_{SL}	contact angle solid liquid interface	°
κ	ionic conductivity	S m^{-1}
λ	wave length	m
μ	chemical potential	J mol^{-1}
$\bar{\mu}$	electrochemical potential	J mol^{-1}
ν	stochiometric coefficient or frequency or sweep rate	- or Hz or V s^{-1}
ϕ	Galvani potential	V
Φ	work function or phase shift	J or °
ω	angular frequency	s^{-1}

List of constants

Symbol	Description	Value	Unit
c	speed of light	299,792,458	m s^{-1}
F	Faraday constant	96,485	C mol^{-1}
h	Planck constant	6.62607015×10^{-34}	J s
i	imaginary unit	$i^2 = -1$	-
R	Ideal gas constant	8.3145	J K^{-1} mol^{-1}
ε_0	Vacuum permittivity	8.854187812810^{-12}	F m^{-1}

List of figures

1 Introduction

The concentration of CO_2 in air, which is besides CH_4 and N_2O one of the harmful greenhouse gases responsible for climate change, rose from the beginning of the industrial era (1750) from ~ 277 ppm up to ~ 416 ppm until today (2021).[1, 2] Mainly, electricity production, industry, and transport sector are responsible for the vast amount of emitted CO_2.[3] To hit the target which was manifested in the Paris Agreement to keep the global warming well below 2 °C (referenced to preindustrial times) substantial effort has to be made in these sectors to mitigate extensive CO_2 emitting.[4] Preferably, the average global temperature should not rise more than 1.5 °C until 2100. Unfortunately, it is already clear that a temperature rise of 1.5 °C will be surpassed before 2100 and cannot be prevented anymore. Nevertheless, in order to achieve the target of a maximum temperature rise of 1.5 °C in the long run (2100) it is necessary to embed carbon dioxide removal technologies to neutralize CO_2 emissions for applications where no mitigation strategies are proposed yet. Unfortunately, it is also postulated that the greenhouse gas emissions around 2030 must not exceed 25 - 30 $GtCO_2e$ per year to achieve the 1.5 °C target. Contradictory, when sticking to the present behavior of mankind these emissions are forecasted to be 52-58 $GtCO_2e$ per year which is about twice of the aimed value and again points out that mankind needs to act urgently.[5]

However, besides the transition to renewable energies the concepts to reduce or at least not further increase the concentration of CO_2 in the atmosphere can be summarized in two approaches: carbon capture with subsequent storage and carbon utilization. For example, a typical carbon capture process is the conversion of CO_2 with CaO to form $CaCO_3$ which is then stored. On the other hand, using CO_2 as a feedstock to produce carbonaceous chemicals is defined as carbon utilization. Following, depending on the CO_2 source and the CO_2 emissions attributed to the utilization process it is possible to establish a circular carbon economy.[6]

9 % of the greenhouse gas emissions in the EU-27 must be ascribed to industrial processes and product use, emphasizing that a beneficial noticeable impact can be achieved if whenever possible industrial processes in the EU-27 are substituted by innovative routes with smaller carbon footprints.[7] Due to the expansion of renewable energy technologies their share in the total amount of provided energy increases steadily.[8] Therefore, electrochemical processes are charming as carbon utilization technologies since they can directly, without conversion to heat, use the provided low carbon electricity source to utilize CO_2.

When combining water, CO_2 and electricity in an electrolysis cell it is possible to activate the stable CO_2 molecule ($E_{C=O}$ = 391 kJ mol^{-1}) to form hydro carbonaceous species.[6] Due to the excessive amount of provided energy and the existence of a sufficient amount of hydrogen, oxygen and carbon, a variety of chemicals such as CO, CH_4, HCOOH / $HCOO^-$, C_2H_4, CH_3CH_2OH can be produced at the CO_2 converting cathode. In a parasitic side reaction, H_2 is produced via decomposition of the aqueous electrolyte.[9] The obtained product spectrum is mainly determined by the chosen catalyst and reaction conditions.[6, 10] Nonetheless, the production of CO or HCOOH / $HCOO^-$ via CO_2 electrolysis was already postulated to be close to inherent economic feasibility whereas the electrolysis process cannot yet compete with the traditional synthesis route.[11, 12] While CO or a mixture of CO and parasitically generated H_2 (syn gas) can be used to produce diverse chemicals, i.e., acetic acid or methanol, formic acid (FA) and formate (FM) are mainly directly used for silage (FA), tanning (FA), pharmaceuticals (FA) or as de-icing agent (FM).[13, 14] The usage of formate as hydrogen or energy carrier was recently demonstrated.[15]

Yet, this work focuses on the electrochemical conversion of CO_2 to formate. A substantial effort for the development of suitable catalysts and electrode engineering can be observed in the associated literature: novel catalysts, optimized reaction conditions (i.e., temperature, electrolyte) and different electrode architectures are the subject of the published works. Consequently, the numeric targets (suggested by industry) for the key performance indicators selectivity and current density for this reaction are already accomplished.[16, 17] On the other hand, due to typical short testing times, long-term stability and the observable degradation phenomena are insufficiently explored.[18] Therefore, electrochemical impedance spectroscopy (EIS) can be used as an operando tool to assign the degradation to specific altered microscopic processes. But first, the nature of the resembled processes in the impedance spectrum must be identified before conclusions of the present degradation mechanisms can be drawn. The assignment of microscopic processes to features observable in the impedance spectra is the central objective of the presented work and ultimately enables the CO_2 electrolysis community to perform a knowledge-based analysis of measured impedance spectra. These findings are not necessarily limited to the conversion of CO_2 to formate but can be transferred to CO_2 electrolysis processes with different target products. Finally, the degradation of tin- and bismuth-based electrodes is investigated via EIS and physical post mortem characterization.

2 CO_2 electrolysis

CO_2 is a remarkable stable molecule due to the linear double bonds of carbon with oxygen. The bonding energy of the C=O bond is approximately 391 kJ mol^{-1} which is noticeably higher compared to i.e., C=C bonds (303 kJ mol^{-1}). To utilize CO_2 via conversion to valuable carbonaceous species a bond breaking of C=O is necessary for which the required energy can be provided in chemical, electrochemical and photochemical processes.[6] The electrochemical conversion of CO_2, often abbreviated as CO_2EL (CO_2 electrolysis), is charming owing to the fact that the main driving force for the conversion - the electrochemical potential - is easily controllable. Additionally, the electrical energy can be provided by renewables indicating that no additional CO_2 is produced during the necessary energy generation to operate the electrolyzer. Furthermore, the scale-up is relatively simple since it is usually just a numbering up of electrochemical cells.[6] The dream production would be that CO_2 is taken from the atmosphere and converted to carbonaceous species. In the very end of life, this species will be naturally converted to CO_2 again and emitted into the air which will then represent a new start of the life cycle of the considered carbon atom. Also, CO_2 from concentrated sources like power or cement plants can be used as feed stock for CO_2EL to generate refined chemicals. The drawback of this approach, when not using CO_2 from the atmosphere, is that at the end of life of the refined carbon containing chemical CO_2 is emitted again and the problem is just postponed to a later date.[19, 20] However, in the best case, electrochemical CO_2 conversion can be used to create a carbon cycle in which intermediate steps CO_2 is refined to valuable chemicals.

Already in 1870, Royer et al. published an article with the original title '*Réduction de l'acide carbonique en acide formique*' in which the electrochemical conversion of carbonic acid to formic acid was reported. [21] Approximately 30 years later, Coehn et al. further investigated this reaction in aqueous bicarbonate containing solutions and concluded the importance of the existence of the HCO_3^- ion. They already proposed the necessity of an inherent high hydrogen overvoltage of the CO_2 converting electrodes. Otherwise, due to the extremely negative potentials the electrolyte will be decomposed via the hydrogen evolution reaction (HER) and by that decreasing the charge efficiency for CO_2 reduction reaction (CO_2RR). Furthermore, they solely observed formic acid as reaction product.[22] Contrary, in 1954 Teeter et al. proposed that in case of a mercury electrode dissolved CO_2 adsorbs at the electrodes surface before the reduction process occurs. Following, they concluded that dissolved CO_2 is the electroactive species.[23, 24] However, several years later in 1994, the very detailed pioneer work of Hori et al.

regarding CO_2 reduction in bicarbonate solutions at various metal electrodes has generated a lot of interest and is of high importance for the CO_2EL community. They proposed that the investigated metal electrodes could be divided in two groups, while the first group (Cu, Au, Ag, Zn, Pd, Ga, Ni, Pt) mainly produces CO, the second group (Pb, Hg, In, Sn, Cd) preferentially produces formic acid / formate. Furthermore, traces of CH_4, C_2H_4, EtOH and PrOH, predominantly at copper electrodes, were observed during their experiments.[25] An even more distributed product spectrum was reported from Kuhl et al. in 2012 who investigated a copper electrode in 0.1 M $KHCO_3$ aqueous solution and analyzed the liquid phase products with nuclear magnetic resonance spectroscopy (NMR) which due to the sensitivity of the method was capable to detect traces of even more species than proposed for copper by Hori et al.. They divided the measurable products in three categories: the main products were hydrogen, methane, formate, carbon monoxide, ethylene; intermediate amounts of ethanol, n-propanol and allyl alcohol were measured; to a minor extent methanol, glycolaldehyde, acetaldehyde, acetate, ethylene glycol, propionaldehyde, acetone and hydroxyacetone were observed. This demonstrates that up to 15 carbonaceous species are produced when electrolyzing CO_2 at copper electrodes.[26] The main challenge in CO_2EL is to achieve high conversion rates (current densities) and simultaneously a high selectivity for a desired product. The extent of the parasitic HER should be reduced to a minimum.

2.1 Electrochemical CO_2 conversion to formate

This work focuses on the investigation of electrodes converting CO_2 to formate in alkaline media. In most studies presented in literature Sn[27-30], In[31, 32], Bi[33-35] and Pb[32, 36, 37] catalysts were used as electrode material for production of formate / formic acid. Carbon monoxide is usually observed in a minor extent as a side reaction product whereas hydrogen as a result of the parasitic HER is observed in a higher amount. The fraction of the total introduced charge into the electrolyzer which is used to convert CO_2 to a specific product is called Faraday efficiency (FE) and desirably as high as possible. A schematic representation of the formate formation in an alkaline CO_2 electrolyzer is depicted in Figure 1 including the oxygen evolution reaction (OER) which takes place as counter reaction at the anode. The corresponding electrochemical reactions, including the undesired CO and hydrogen formation, can be seen in (1) - (4). The electrochemical standard potentials are referenced to the standard hydrogen electrode (SHE) at 25 °C and p = 101.3 kPa:[6]

Cathode:

HCOO$^-$: $2\,CO_2 + 2\,H_2O + 4\,e^- \rightleftharpoons 2\,HCOO^- + 2\,OH^-$ $\Delta\phi^0 = -1.078\,V$ (1)

CO: $2\,CO_2 + 2\,H_2O + 4\,e^- \rightleftharpoons 2\,CO + 4\,OH^-$ $\Delta\phi^0 = -0.934\,V$ (2)

HER: $4\,H_2O + 4\,e^- \rightleftharpoons 2\,H_2 + 4\,OH^-$ $\Delta\phi^0 = -0.826\,V$ (3)

Anode:

OER: $4\,OH^- \rightleftharpoons 2\,H_2O + O_2 + 4\,e^-$ $\Delta\phi^0 = +0.404\,V$ (4)

Total reaction (assuming 100% FE for formate):

$2\,CO_2 + 2\,KOH \rightleftharpoons 2\,HCOOK + O_2$ $U_{cell} = -1.482\,V$ (5)

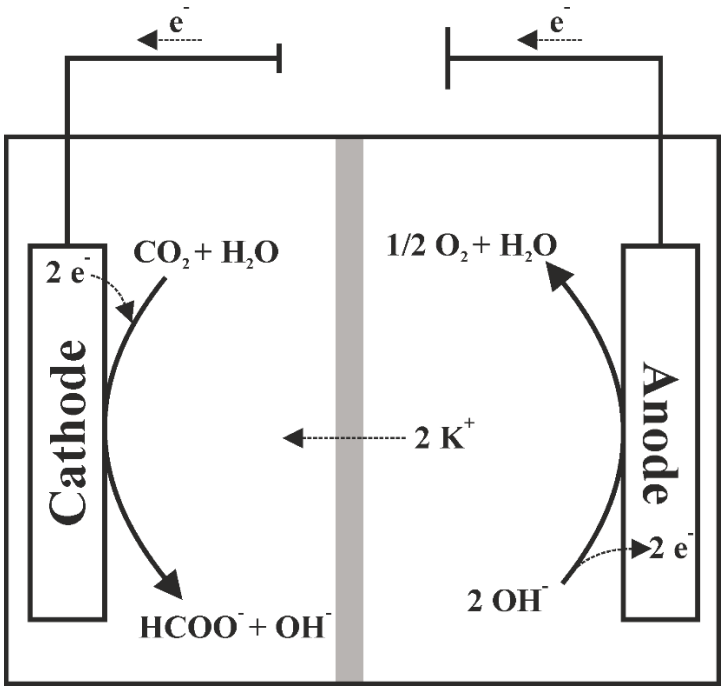

Figure 1 Principle of the cathodic conversion of CO_2 + H_2O to $HCOO^-$ + OH^- and anodic oxygen evolution reaction.

The proximity of the standard potentials for the HER and CO_2RR points out from a thermodynamic point of view why hydrogen is usually observed as a parasitic reaction product and emphasizes the necessity to use suitable catalysts with high HER overpotential to suppress the electrolyte's decomposition. Considering the cell voltage, it becomes evident that alkaline conditions are beneficial for CO_2 to formate converting systems since the half-cell potentials of the formate producing cathode and oxygen generating anode move away from each other as a result of different pH dependencies of the standard potentials. For each pH unit shift towards acidic conditions, the cathodes potential increases by 0.059/2 V whereas the anodes electrode potential raises with 0.059 V. The same holds true for the HER and formate formation, lower pH values increase the standard potential of the HER to a higher extent and by that making it less favorable compared to CO_2 to formate conversion.

Compared to possible target products like CH_3OH (6 e^-), CH_4 (8 e^-) or C_2H_4 (12 e^-) only two electrons need to be transferred to convert CO_2 into formate or CO.[6] This fact implies that these reactions follow a less complex reaction mechanism making them more facile and easier to investigate for principle studies which go beyond an empirical understanding of the CO_2RR.[38-40] However, several techno economic analysis demonstrated that the electrochemical production of CO and formic acid is close to become economically feasible.[12, 19, 41, 42] Unfortunately, these analysis consider formic acid as the final product of CO_2EL which usually does not hold true due to the in the CO_2EL community mainly used slightly alkaline bicarbonate solution as electrolyte. A necessary subsequent acidification is not examined in these analyses and would dramatically reduce the feasibility of the CO_2EL process with formate as the obtained product. However, formate solution is mainly used as de-icing agent (small market volume) in situations where chloride containing chemicals would be to corrosive (airplane de-icing) or as drilling-fluid.[14] In the scope of this thesis a contribution with the title '*Utilizing Formate as an Energy Carrier by Coupling CO_2 Electrolysis with Fuel Cell Devices*' (**Article IV**) was published as a proof of concept study and demonstrates the usage of the obtained potassium formate solution as fuel for a direct formate fuel cell or conventional polymer electrolyte membrane fuel cell (PEMFC) after decomposition of formate to hydrogen.[15]

Following a brief overview of the state of research for CO_2EL with formate as target product will be given.

2.2 Tin and bismuth catalysts

In the literature and also in this work mainly tin is used as a catalyst material due to the attributed high electrochemical performance for CO_2EL to formate, low toxicity and cheap raw material price.[43] Therefore, substantial effort was made in the CO_2EL community to identify the active species of tin catalysts: Chen et al. compared the CO_2EL performance of freshly etched and untreated tin foil with an native oxide layer and concluded, as evidenced by significantly lower partial current densities for CO_2RR products, that not metallic tin but tin oxide is the active species without further specifying the oxidation state of tin.[44] Considering the Pourbaix diagram of tin (cf. Figure 2 a)) it becomes evident that in strong alkaline solutions, which are present during the experiments for this thesis, and negative applied potentials (< - 1.0 V vs. SHE) SnO_x is not stable from a thermodynamic point of view and will be reduced to metallic tin which is barely active for CO_2EL. Fortunately, it was shown by several authors that the stability region of SnO_x is extended due to a kinetic hindrance of the reduction to potentials regions (down to ~ - 1.6 V vs. SHE) which are commonly needed when reducing CO_2.[45-48] In detail, Dutta et al. used operando Raman spectroscopy to monitor the oxidation state of tin and proposed that SnO_2 is the present species at the catalyst surface even at reducing conditions.[46] In accordance, Baruch et al. demonstrated via operando attenuated total reflectance infrared spectroscopy (ATR-IR) the existence of a native SnO_x layer under reducing conditions and suggested furthermore the presence of a surface bound tin-carbonate species as reaction intermediate.[49]

Contradictory, Pander et al. demonstrated via operando ATR-IR that bismuth metal does not show a meta stable oxide layer under reducing conditions which in combination with potentiostatic electrolysis experiments and evaluation of the obtained reaction product FEs lead to the conclusion that metallic bismuth is the active species for CO_2EL. Fortunately, bismuth is the stable phase in highly alkaline media and - the for CO_2EL necessary - negative potentials (cf. Figure 2 b)) making it a promising electrode material.

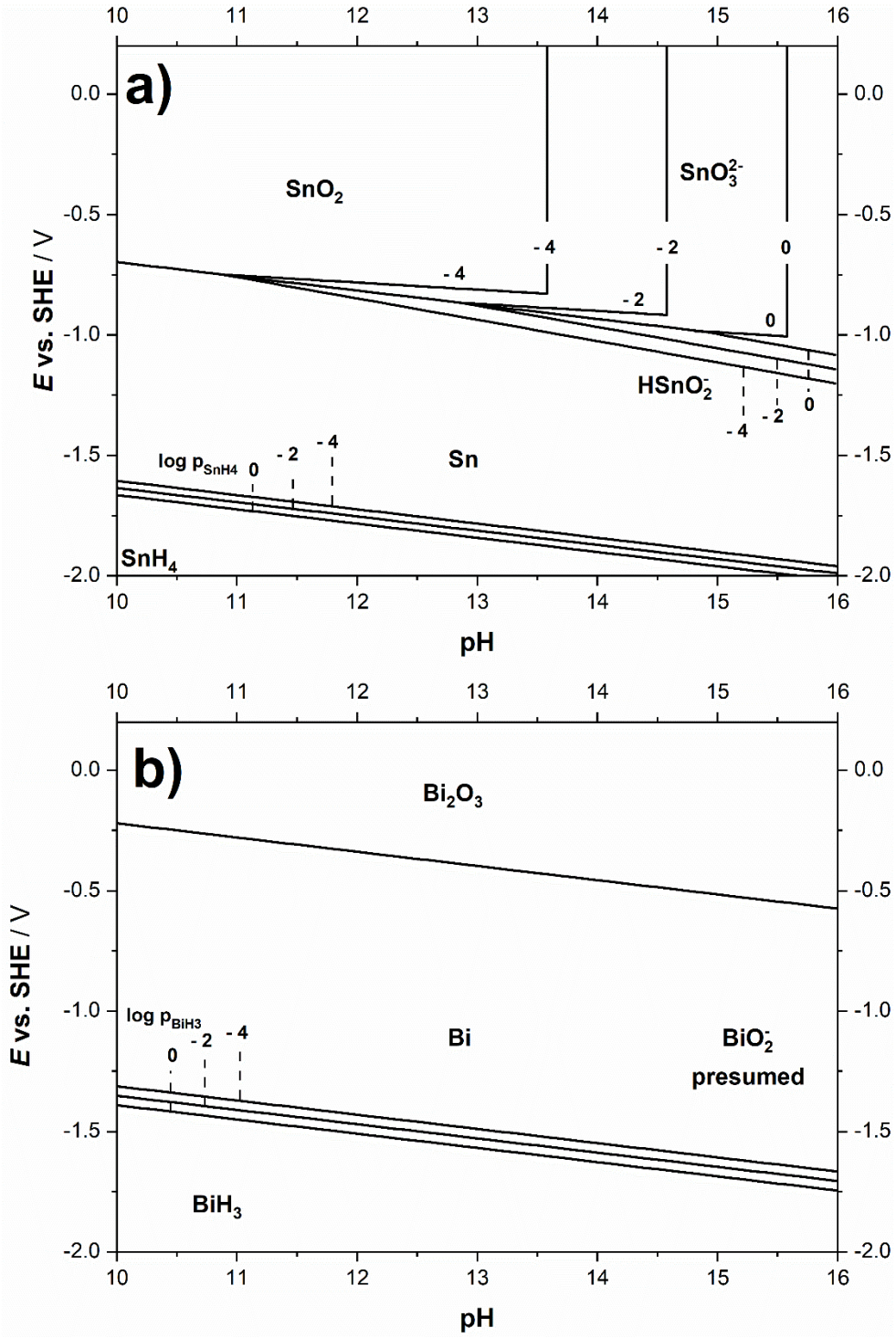

Figure 2 Pourbaix diagram for tin and bismuth calculated in accordance with Pourbaix.[50]

2.3 Reaction mechanisms

Due to its widely usage for the conversion of CO_2 to formate, tin is the material which is mainly used to investigate the associated CO_2RR mechanism. In principle, the underlying reaction steps can be described as:[51]

$$CO_2\ (aq)\ \rightleftharpoons CO_2\ (ad) \tag{6}$$

$$CO_2\ (ad) + \ e^-\ \rightleftharpoons CO_2^{\cdot -}(ad) \tag{7}$$

$$CO_2^{\cdot -}\ (ad) + \ H_2O\ \rightleftharpoons HCOO^{\cdot}\ (ad) + \ OH^- \tag{8}$$

$$HCOO^{\cdot}\ (ad) + \ \ e^-\ \rightleftharpoons HCOO^-\ (ad) \tag{9}$$

$$HCOO^-\ (ad)\ \rightleftharpoons HCOO^-\ (aq) \tag{10}$$

After surface-adsorption, CO_2 is activated with an electron to form the CO_2 anion radical. Subsequently, this radical is protonated by free or adsorbed water which yields an adsorbed formate radical and a hydroxide ion. A second electron is then transferred to the adsorbed formate radical which finally leads to the adsorbed formate anion which can be desorbed and transported into the bulk.[38, 45] While a few authors proposed the protonation[39, 44, 51] (cf. (8)) as rate-determining step, mostly the CO_2 anion radical formation[52-55] (cf. (7)) is suggested as the rate-determining reaction. Interestingly, a redox potential of - 1.9 V vs. SHE[56] is attributed to the CO_2 anion radical formation which is more negative than the typically observed onset potentials for CO_2EL. This puzzle is suggested to be solved by the stabilizing effect of the catalyst for the CO_2 anion radical which then reduces the necessary reduction potential for the activation of CO_2.[10]

However, density functional theory (DFT) studies strongly indicate that two reaction intermediates can be present at the tin surface: *COOH or *OCHO$^{(*)}$, * denotes the atom bonded to the surface. *OCHO$^{(*)}$ can be bonded in mono (*OCHO) or bidentate (*OCHO*) configuration.[38] These oxygen bonded intermediates cannot only be formed by direct CO_2 adsorption on the catalyst surface but subsequently after insertion of CO_2 into the hydroxylated

tin surface forming an intermediate surface bound carbonate as proposed by several authors.[49, 52] The valuable study of Feaster et al. proposed that *COOH is the key intermediate in the reduction of CO_2 to CO whereas *OCHO(*) is the crucial intermediate for formate generation. Their argumentation was based on the fact that Volcano plots obtained from DFT calculations for metals like Sn, Au, Ag, Zn could only describe the experimentally observed partial current densities for CO respectively $HCOO^-$ if *COOH (for CO) or *OCHO(*) (for formate) binding energies were used as descriptors in the Volcano plot.[57] In accordance, a DFT study by Cui et al. proposed that for hydroxylated tin electrodes the formation of *OCHO(*) is energetically favored compared to *COOH which fits to the observation that formate is the predominant reaction product for tin electrodes.[52] Additionally, a DFT study combined with experiments from Koh et al. suggests that the *OCHO(*) pathway for formate generation is also observable for bismuth electrodes.[58] In accordance, the corresponding suggested reaction pathways for $HCOO^-$ and CO generation are depicted in Figure 3.

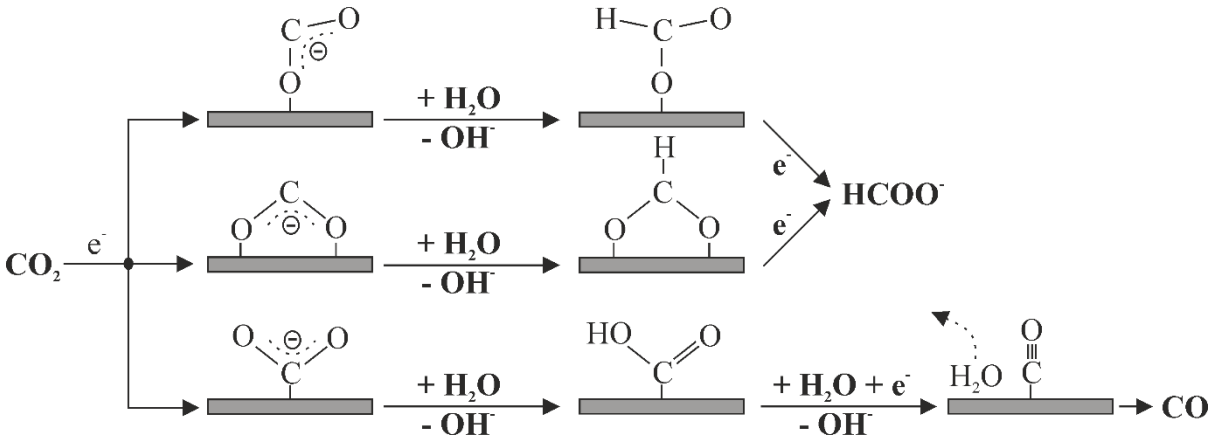

Figure 3 Suggested reaction pathways for $HCOO^-$ and CO generation. Adapted and combined from Kortlever et al. and Zhu et al..[38, 59]

2.4 Electrolyte

Commonly, aqueous supporting electrolytes are used in CO_2 electrolysis. Besides the mainly used alkali bicarbonate[27, 28, 60-62] electrolyte, solutions of KCl[63-65], K_2SO_4[66-68] or KOH[64, 69-71] are often used. When using plane electrodes, CO_2 is provided via bubbling into the electrolyte which will result in alterations of the electrolyte. These alterations were studied in a very valuable contribution of Zhong et al. who investigated the effect of CO_2 bubbling into $KHCO_3$,

K_2CO_3, HCl, KCl, and KOH electrolytes and monitored the resulting concentrations of H_2CO_3 (aq) / CO_2 (aq), HCO_3^- (aq), CO_3^{2-} (aq). The concentrations of H_2CO_3 (aq) and CO_2 (aq) were reported as a sum parameter while the H_2CO_3 (aq) concentration is expected to be much lower compared to CO_2 (aq). Using (12) and (13) with the corresponding pK_a values in accordance with Zhong et al. the pH dependent above mentioned equilibrium concentrations of a solution with a total carbon value of 1 mol L^{-1} are exemplarily calculated and illustrated in Figure 4.[72]

$$CO_2\,(\mathrm{g}) \rightleftharpoons CO_2\,(\mathrm{aq}) \tag{11}$$

$$CO_2\,(\mathrm{aq}) + H_2O\,(\mathrm{l}) \overset{K_1}{\rightleftharpoons} H^+\,(aq) + HCO_3^-\,(aq) \qquad \mathrm{p}K_1 = 6.35 \tag{12}$$

$$H^+\,(aq) + HCO_3^-\,(aq) \overset{K_2}{\rightleftharpoons} 2\,H^+\,(aq) + CO_3^{2-}\,(aq) \qquad \mathrm{p}K_2 = 10.33 \tag{13}$$

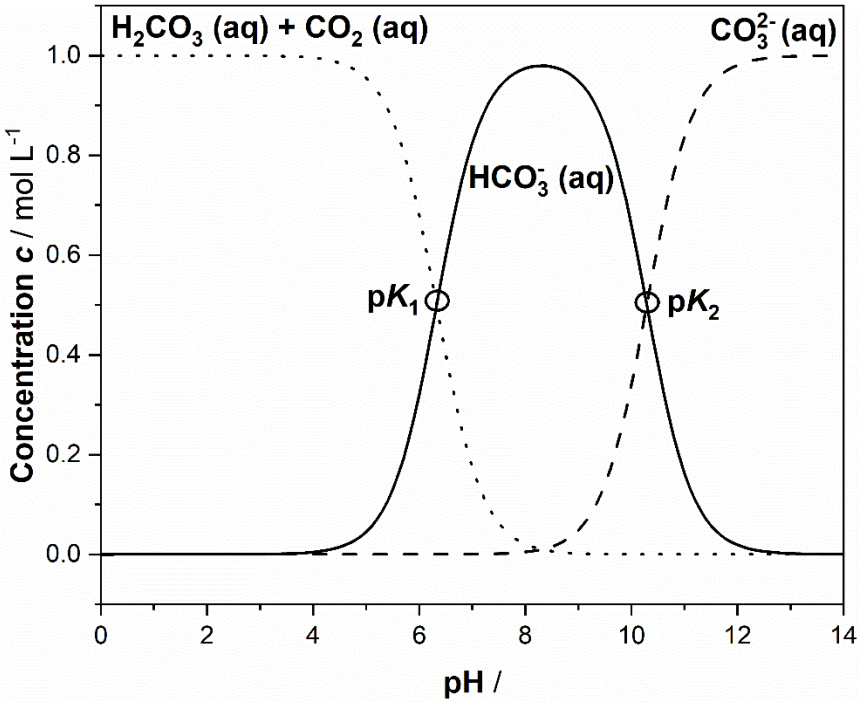

Figure 4 Calculated equilibrium concentrations assuming a total carbon value of 1 mol L^{-1} for the CO_2 / H_2CO_3 / HCO_3^- / CO_3^{2-} equilibrium according to Zhong et al. and using the pK_a values calculated in on the report of Harned et al..[72-74]

In this work, 0.1 M and 1.0 M $KHCO_3$ solutions as well as 1.0 M KOH were used as electrolyte. It is important to mention that for all of these electrolytes, even for 1.0 M KOH, CO_2 (aq) is available in the solution.[72] This dissolved CO_2 species is of utmost importance since it is often proposed to be the active species in CO_2EL.[53, 75, 76] Furthermore, Dunwell et al. discovered via isotopic labelling that the majority of CO_2 (aq) at the electrode's surface originates from HCO_3^- (aq) due to a quick equilibration of this anion with CO_2 (aq) which is compared to the conversion of CO_2 (g) to CO_2 (aq) much faster and is suggested to follow a Grotthus like mechanism. The role of CO_2 (g) is then to 'refill' the consumed CO_2 (aq) and maintain the HCO_3^- (aq) equilibrium concentration.[76]

As it was discussed above, the pH value not just influences the equilibrium potential or catalyst stability (cf. 2.2) but also affects the equilibrium concentration of CO_2 (aq). Therefore, a description of the local pH value in close proximity to the electrode's surface is of great interest. Thus, in tortuous porous systems (cf. 4.4) where the removal of the OH^- ions produced during HER and CO_2RR (cf. (1) + (3)) is hindered, a high local pH value is expected especially at higher current densities. Several modelling studies demonstrated that the local pH value will be higher in the reaction zone compared to the bulk, i.e. Gupta et al. showed that for low concentrated $KHCO_3$ solutions (< 0.1 M) at 150 mA cm^{-2} and an assumed 100 µm thick boundary layer the discrepancy of the bulk and surface pH can be about 6 units.[77] Furthermore, Varela et al. as well as Burdyny et al. postulated the correlation that a low buffer capacity (low $KHCO_3$ concentrations) and high current densities will lead to substantially higher local pH values. When 1.0 M KOH is used as electrolyte the modelled local pH values changes only slightly (< 1).[78, 79]

A noticeable amount of work was done to investigate the impact of different cations and anions onto the CO_2EL performance. While it is widely accepted that, at least for alkali cations, larger cations facilitate the CO_2RR there is still some discrepancy of the effect of different anions. However, Thorson et al. rated the facilitation of the CO_2RR by cations as: $Li^+ < Na^+ < K^+ < Rb^+ < Cs^+$ and attributed the radius dependent facilitation to two phenomena. Firstly, compared to smaller cations larger cations have less water molecules in their hydration shell which leads to a less distinct charge neutralization and therefore resulting in a stronger adsorption at the negative charged cathode. These cations could stabilize reaction intermediates like the above-mentioned CO_2 anion radical. A DFT study by Resasco et al. supports this theory of a stronger dipole field induced by a higher number of adsorbed large cations which then stabilizes charged reaction intermediates.[80] Secondly, they stated that compared to smaller cations larger cations

show a higher tendency to adsorb on the electrodes surface which will result in a less negative potential in the outer Helmholtz layer and decrease the H^+ concentration at the electrodes surface. Consequently, the parasitic HER is hindered due to the necessity of H^+ ions for the reaction.[45, 81] Another explanation was suggested by Bell et al. who proposed that the size of the cation affects the pK_a value of the cations acid-base reaction in a manner that larger cations have a much smaller pK_a value compared to smaller cations in close proximity to the negatively charged cathode (pK_a Li^+: 11.6; pK_a Cs^+: 4.3) and by that show a better buffer capacitance and maintain high local CO_2 concentrations.[82] Cuesta et al. showed experimental evidence for this phenomenon via in-situ attenuated total reflectance surface-enhanced infrared absorption spectroscopy (ATR-SEIRAS) measurements and postulated that the local pH value at the electrolyte-electrode interface indeed depends on the provided cation.[83]

Regarding the effect of the anion two phenomena must be distinguished: the first one is dealing with the buffering effect of the anion while the second one takes anion induced electrolyte-electrode interface modifications into account. It is common sense that in general buffering anions are beneficial for the CO_2RR due to the maintenance of high local CO_2 concentrations, i.e. the extensively used bicarbonate system is capable to buffer local pH changes induced by the produced OH^- ions during the reaction.[84] On the other hand, it was proposed by Resasco et al. that a high buffer concentration might be contra productive because of the ability to provide hydrogen at the electrodes surface which is beneficial for the parasitic HER.[85] However, non-buffered systems like KOH could be useful from the point of view that high local pH values result in low proton concentrations which in consequence will hinder the hydrogen formation due to the necessity of protons for the HER.[86] The second effect of anion induced electrolyte-electrode interface modifications was mainly studied for halide anions. A ranking which halide anion provides the best conditions for CO_2RR is not straight forward due to inconsistencies observed in the published literature which were traced back to the different electrolysis set-ups and testing protocols of the publishing groups.[45, 86] However, there is still a lot of ongoing research regarding the origin of the beneficial effects of halides.[87-89] Exemplarily, it is suggested that halides specifically adsorb at the electrodes surface and stabilize adsorbing CO_2 due to the attraction of the anions of the positively polarized carbon evoked by the inductive effect. Gao et al. suggested that adsorbed halides can even change the electronic structure of i.e., copper electrodes by stabilizing Cu_2O at the electrodes surface (despite extremely negative applied potentials) which is known to effectively support C-C coupling. Additionally, the specific adsorbed halides could sterically hinder the proton adsorption which consequently leads to a higher HER overvoltage.[88-90]

2.5 Degradation mechanisms

The experimental work in CO_2 electrolysis mainly focuses on the optimization of - from an academical point of view - key performance indicators (KPI), which are: a high Faraday efficiency (high selectivity) for the target product, decreasing overpotential (high energy efficiency) and high current densities (high activity).[18] While for the conversion of CO_2 to formic acid / formate high selectivities (> 80 %) at industrial relevant current densities (> 200 mA cm^{-2}) are already achieved it is common sense in the community that another KPI, the durability of the CO_2 electrolysis system, which is of utmost importance for commercialization is very rarely studied.[16, 17, 91] For the electrochemical conversion of CO_2, porous electrodes are widely used due to their superior performance compared to plane electrodes. Gaseous CO_2 penetrates into the porous electrode from the back side while the electrolyte penetrates into the system from the opposite side. Both phases meet inside the electrode at a solid catalyst particle, forming the triple phase boundary where the reaction takes place. Further information about the structure of these porous, often carbon containing, electrodes is discussed in more detail in 4.4. However, a very comprehensive review about the possible occurring degradation mechanisms for this type of electrodes was published by Nwabara et al. and is highly recommended for further reading. In a first step, they pointed out that most of the studies investigating the degradation of the electrolysis systems were operated for less than 30 hours which means that degradation phenomena occurring at longer time frames are usually not considered. Additionally, a few contributions presented operation times of more than 30 h up to 1000 h in which the underlying phenomena of the observed degradation were not investigated in detail, solely the KPIs were monitored.[18]

Nwabara et al. summarized the possible degradation phenomena for CO_2 electrolyzers in accordance to already known phenomena from PEMFC, which partially uses similar types of electrodes, as:[18]

Concerning the catalyst:

- **Aggregation** of catalyst particles induced by Ostwald ripening, dissolution and re-deposition or coalescence during operation leading to a reduced electrochemical surface area which in consequence reduces the achievable current densities at a constant potential.[91-93]
- Catalyst **leaching** resulting in a loss of active material.[94]

- **Poisoning** of the catalyst induced by electrolyte impurities or reaction intermediates. Both especially investigated for copper- and palladium-based electrodes.[95, 96]
- **Alteration** in **chemical composition** (oxidation state) of oxide-based catalysts induced by strong reductive potentials.[46, 93, 97]

Concerning the carbon-based porous electrode architecture:

- **Erosion** of the gas-diffusion layer (GDL) due to the provided gas flow which in consequence facilitates GDL flooding and by that hindering the transport of the gaseous reactant as shown by Ha et al. for PEMFC.[98]
- **Binder (Nafion®, PTFE) degradation** by decomposition via radicals: HO● provided by H_2O_2 generated in parasitic oxygen (traces diluted in electrolyte) reduction reaction and / or H● as a product of the direct conversion of O_2 and H_2 at the catalyst surface. This binder decomposition makes the catalyst vulnerable for leaching and the porous architecture less hydrophobic which may result in flooding of the electrode.[99, 100] Furthermore, the adsorption of less hydrophobic hydrocarbons at the binder surface will reduce the hydrophobicity and result in electrode flooding.[101]
- **Carbonate precipitation** according to (14) - (15) due to high local pH values (cf. 2.4) resulting in impeded reactant supply and at the same time promoting electrode flooding due to its hygroscopic properties.[102, 103]

$$CO_2 + \text{KOH} \rightleftharpoons KHCO_3 \tag{14}$$

$$KHCO_3 + \text{KOH} \rightleftharpoons K_2CO_3 + H_2O \tag{15}$$

Especially, the degradation phenomenon of electrode flooding attracted a significant amount of interest. It is expected that a flooded electrode facilitates the parasitic HER due to the excessive accessible number of protons while at the same time the diffusion length of CO_2 in the liquid phase is elongated resulting in aggravated mass transport.[66, 102] The undesirable effect of electrode flooding is already known from PEMFC and silver based gas-diffusion electrodes (GDE) for the oxygen reduction reaction (ORR).[104-107]

However, electrochemical impedance spectroscopy is a powerful operando method which can be used to monitor time-dependent alterations of the involved microscopic processes of an

electrochemical system. Therefore, this technique can be used to specifically identify which sub-step (i.e., charge transfer, mass transport, electrodes conductivity) occurring during reactant conversion is impeded with time. This information is very useful and helps to reveal possible degradation phenomena, i.e., an increasing charge transfer resistance may indicate a catalyst leaching or poisoning and can be employed for a targeted electrode optimization. Unfortunately, the interpretation of the impedance spectra is not straight-forward and requires careful analysis of the obtained data.[108-110] In literature, a few studies used EIS, among other methods, in CO_2EL as an additional characterization tool to evaluate synthesized catalysts. These works did not include an elaborated EIS study to identify the underlying processes which points out the necessity of the presented work in this thesis.[111, 112] A more detailed summary of works using EIS for CO_2EL is presented for tin foil in **Article I** and tin-based GDEs in **Article II**.

The careful analysis of impedance spectra for tin foil and tin-based GDEs is the main content of this thesis. Ultimately, the goal is to suggest which underlying phenomena can be observed in the impedance spectrum and therefore enabling the CO_2EL community to use EIS as an advanced tool to characterize CO_2 converting electrodes.

3 Motivation and interrelation between the studies

As it was pointed out in the sections before, the electrochemical conversion of CO_2 to formate can be used to convert renewable energy to valuable carbonaceous species and guide a way to a circular carbon economy. While for systems using GDEs the KPIs of a sufficient selectivity and current density are already achieved, the stability is rarely studied and the underlying degradation phenomena are insufficiently investigated. Therefore, EIS is a promising tool for operando monitoring of the degradation of inherent sub-steps (i.e., charge transfer, mass transport) which occur at an CO_2 converting cathode. To be able to assign the observed features in EIS to specific underlying processes, the obtained EIS spectra need to be carefully analyzed before proposing which microscopic processes are resembled in the spectrum. This is where this doctoral thesis tries to create scientific merit:

In a first step, as a benchmark, electrodes with a simple geometry - tin foil - were investigated in terms of EIS to get a basic understanding of the obtained EIS spectra which resemble a superposition of contributions of the parasitic HER and desired CO_2RR (**Article I**).

Building on this, the EIS investigations were extended to GDEs which, due to their higher achieved current densities and selectivity for formate, have a higher practical significance. Consequently, an assignment of the underlying processes to features obtained in the EIS spectrum was proposed (**Article II**).

Finally, the generated knowledge for GDEs was used in a degradation study of tin- and bismuth-based GDEs. A possibly occurring flooding induced degradation process was analyzed by monitoring the electrode's wetting state via EIS and physical post mortem characterization of the GDE. Additionally, a possible catalyst leaching was examined by analyzing the electrolyte for traces of the catalyst (**Article III**).

Furthermore, a possible field of application for the generated formate solution was investigated in a proof of concept study. Therefore, formate was applied as an energy carrier by using it as a fuel for a direct formate fuel cell, or as hydrogen source for PEMFC after catalytic decomposition (**Article IV**).

The successive structure of the published scientific articles is illustrated in Figure 5.

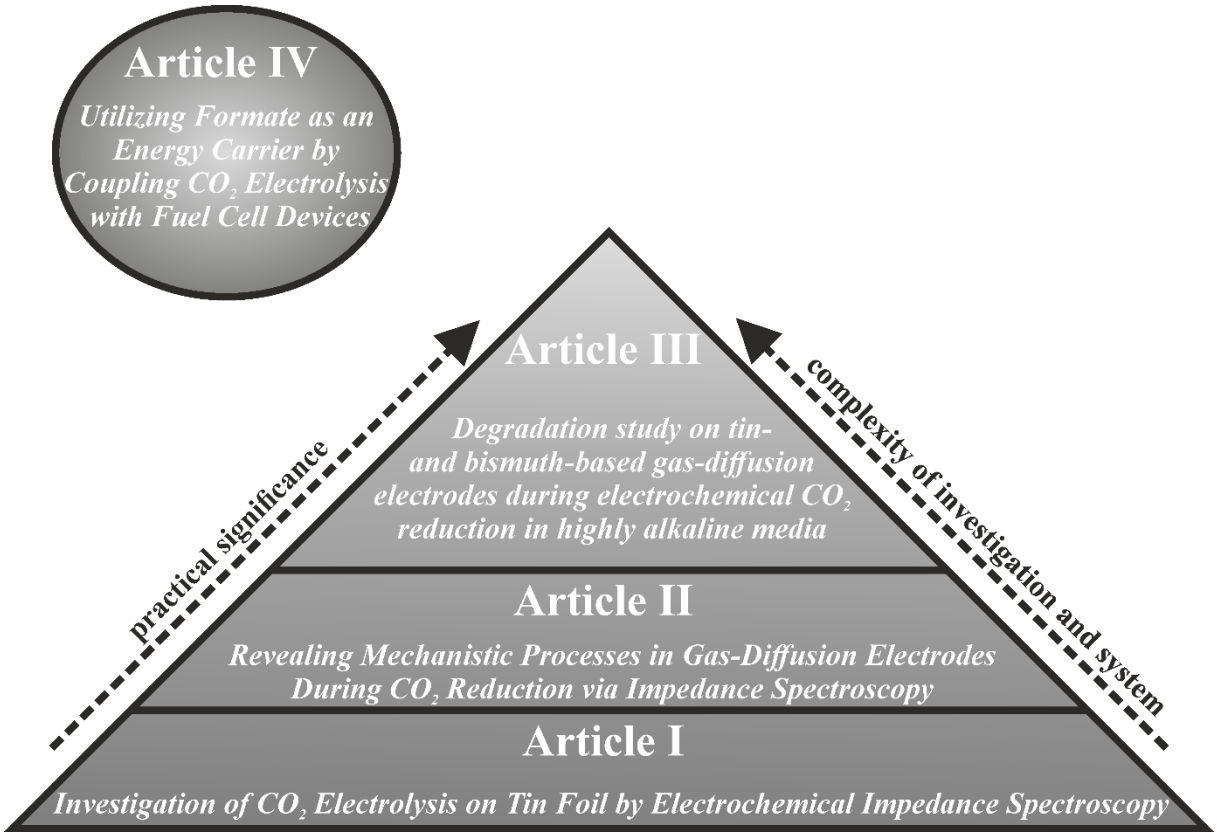

Figure 5 Content of the cumulative doctoral thesis in a nutshell.

The classification of the results presented in the articles in the overall context is discussed in the following paragraphs.

Figure 6 illustrates a comparison of the measured impedance spectra for the operation with pure CO_2 or N_2 feed for the tin foil (**Article I**) and SnO_x / C GDE system (**Article II**). For the operation of the GDE system with CO_2 three arcs could be observed in the impedance spectrum whereas only one depressed arc is observable when operating the same system with N_2. The difference was assigned to a switch from HER to CO_2RR, which then determines the shape of the spectrum, when using CO_2 as feed gas as evidenced by the substantially decreased H_2 FE. In contrast, the shape of the impedance spectrum for tin foil operated with CO_2 and N_2 remains the same only the diameters of the two observed arcs increase when introducing CO_2 instead of N_2 into the system. This fact indicates that the underlying processes resembled in the spectrum are the same no matter if the system is operated with N_2 or CO_2. Since the H_2 FE for the operation of the tin foil system with CO_2 is about 85% it is obvious that the underlying processes must be mainly assigned to the HER and not CO_2RR as it was further evidenced by kinetic isotope effect experiments. Additionally, equivalent circuit simulations (**Article I**) demonstrate

that for parallel occurring charge transfer reactions (HER and CO_2RR) only one arc will be observed in the impedance spectrum which diameter will be dominated by the favored reaction. Naturally, due to the porous nature of the GDE (resembled in the high frequency region of the spectrum) the number of active sites is significantly increased compared to the foil electrode which results in lower polarization resistances independent on the shape determining reaction. However, besides the possibility that the impedance spectrum shape determining reaction might change with variation of experimental parameters, differences in the semi-circle diameters can be used for interpretation unless the spectrum shape does not dramatically change with the varied parameter.

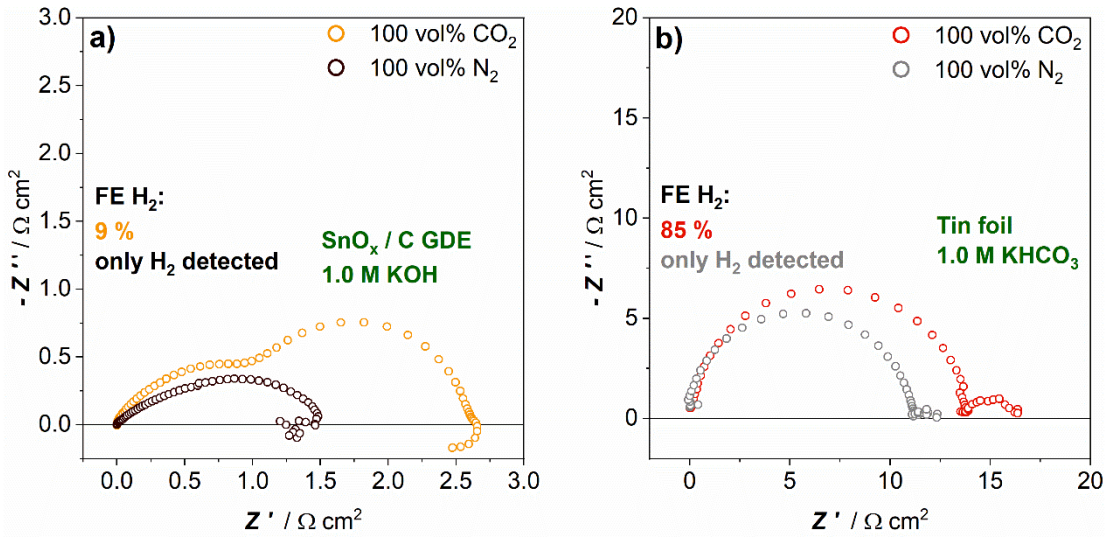

Figure 6 Comparison of impedance spectra measured for the operation with CO_2 and N_2 for **a)** SnO_x / C GDE in 1.0 M KOH and **b)** tin foil electrode in gas saturated 1.0 M $KHCO_3$. Diagram adapted from supporting information of **Article II**.[112]

Ultimately, the interpretation of the EIS investigation for the GDE system (**Article II**) is based on the microscopic processes derived from model studies (cf. Figure 7 a)). The medium frequency process was assigned to a charge transfer related to the formation of the CO_2 anion radical. Therefore, after conversion of the admittance via Brugs equation (cf. (88)), the extracted capacitance value can be correlated with the wetted surface area of the GDE. This knowledge was used in **Article III** to monitor the wetting state of the GDE and for correlation of the degradation with the degree of wetting. Unfortunately, it was not possible to identify a clear correlation of the GDE degradation and wetting state due to a superimposed observed catalyst leaching. Nevertheless, the characteristic curves for the time dependent C_{dl} values of the SnO_x / C GDE and tin foil are depicted in Figure 7 b). It can be seen that the C_{dl} values for the tin foil system are instantly constant and are significantly smaller compared to the GDE

system. Both observations are the results of the non-porous architecture of the tin foil electrode which will arise in a low accessible surface area while simultaneously no wettable pores are provided leading to constant C_{dl} values. On the other hand, a time dependent wetting process is observable for the GDE system which is induced by the applied potential lowering the surface energy of the electrolyte / electrode interface favoring electrolyte imbibition into the porous electrode architecture. Since the impedance spectra and extracted resistances highly depend on the number of wetted active sites, it becomes obvious that it is important to analyze the obtained data at similar wetting states. This was considered in the qualitative and quantitative evaluations of **Article I+II** by performing the same pre-conditioning protocol for all experiments and analyzing the spectra after a fixed time of operation.

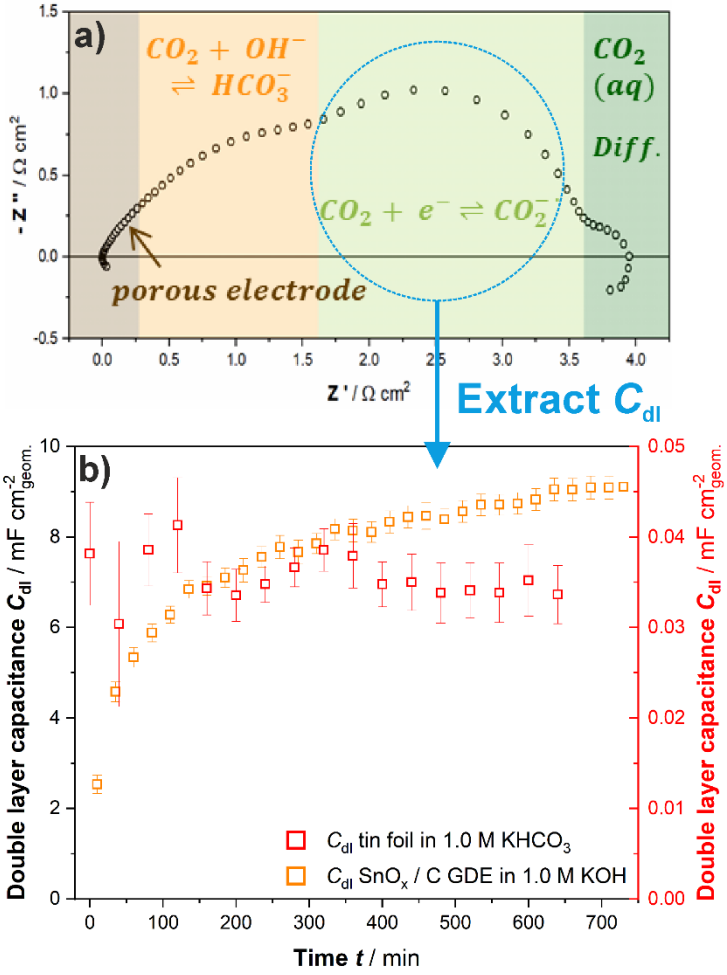

Figure 7 a) On the basis of **Article II** suggested microscopic processes observable in impedance spectrum for GDEs[112] and **b)** application of the generated knowledge by extracting the double layer capacitance as descriptor for the GDEs wetting state as investigated in **Article III**. Exemplary C_{dl} values for the tin foil system are added for comparison.

4 Fundamentals

4.1 Thermodynamics: Electrochemical Potential

The electrochemical potential is the key parameter in electrochemical devices since this quantity determines from a thermodynamic point of view which reactions possibly occur at the electrode / electrolyte interface. In contrast to the well-known chemical potential, the electrochemical potential takes the necessary work for the transport of charged species inside an electric field into account.[113] (16) points out the definition of the chemical potential for a component *i* in phase α at constant *T*, *p* and moles of all other components. (17) shows the extension of the traditional definition considering the electrical work due to the movement of charged species inside an electric field:

$$\mu_i^\alpha = \left(\frac{\partial G}{\partial n_i}\right)_{T,p,j\neq i} = \mu_i^{\alpha,0} + R \cdot T \cdot \ln a_i^\alpha \tag{16}$$

$$\bar{\mu}_i^\alpha = \mu_i^\alpha + z_i F \phi^\alpha \tag{17}$$

It can be seen directly that the electrical work is proportional to the charge per mole and the existing electric potential. Depending on the signs of the moved charge and the present potential the extension term must be added or subtracted from the chemical potential.

However, for a simple equilibrated reaction of a metal in solid phase *s* and its ion in the liquid phase *l*

$$Me\,(s) \rightleftharpoons Me^{z+}(l) + z \cdot e^- \tag{18}$$

one can write:

$$\bar{\mu}_{Me}^s = \bar{\mu}_{Me^{z+}}^l + z \cdot \bar{\mu}_{e^-}^s \tag{19}$$

Introducing (17) into (19) and respecting that the metallic species is neutral so that the electrochemical potential can be substituted with the chemical potential we obtain:[113, 114]

$$\mu_{Me}^{s,0} + R \cdot T \cdot \ln a_{Me}^{s} = \mu_{Me^{z+}}^{l,0} + R \cdot T \cdot \ln a_{Me^{z+}}^{l} + z \cdot F \cdot \phi^{l} + \mu_{e^-}^{s,0} + z \cdot R \cdot T \cdot \ln a_{e^-}^{s} - z \cdot F \cdot \phi^{s} \quad (20)$$

The quantity of interest is the difference of the Galvani potentials $\Delta\phi$ which is the potential difference between the solid and liquid phase. Considering that the activity of the metal and charge in the solid phase is assumed to be constant, $\Delta\phi$ can be expressed by:

$$\Delta\phi = \phi^{s} - \phi^{l} = \frac{\mu_{Me^{z+}}^{l,0} + \mu_{e^-}^{s,0} - \mu_{Me}^{s,0}}{z \cdot F} + \frac{R \cdot T}{z \cdot F} \cdot \ln a_{Me^{z+}}^{l} = \Delta\phi^{0} + \frac{R \cdot T}{z \cdot F} \cdot \ln a_{Me^{z+}}^{l} \quad (21)$$

$\Delta\phi^0$ is the potential difference of the observed system at 298.15 K and an activity of 1 mol L^{-1}. The fact that the terms including the activity of the species in the liquid phase cannot be measured without creating an additional interphase with an own potential difference, points out the inevitable necessity to measure the Galvani potential versus a well-defined reference system. Typically, the hydrogen evolution reaction at standard conditions, proton activity of 1 mol L^{-1}, hydrogen fugacity of 1 atm and 298.15 K, is used as reference system and set to a value of 0 V.[115]

However, for other reactions than metal dissolution and deposition the activity of the reduced species cannot be neglected. Therefore, the activity of both, the reduced and oxidized form of the active species, has to be taken into account. Consequently, a more general equation describing the situation is the Nernst equation showing the activity and temperature dependence of the Galvani potential (ν is the stoichiometric coefficient):

$$\Delta\phi = \Delta\phi^{0} + \frac{R \cdot T}{z \cdot F} \cdot \ln\left(\frac{\prod a_{ox}^{\nu_{ox}}}{\prod a_{red}^{\nu_{red}}}\right) \quad (22)$$

Exemplarily, the Nernst equation for the conversion of gaseous carbon dioxide and liquid water to carbon monoxide and hydroxide ions (cf. (2)) can be written as:

$$\Delta\phi = \Delta\phi^{0} + \frac{R \cdot T}{2 \cdot F} \cdot \ln\left(\frac{a_{CO_2}^{l} \cdot a_{H_2O}^{l}}{a_{CO}^{l} \cdot a_{OH^-}^{2,l}}\right) \quad (23)$$

The activity of water can be neglected due to its excess availability whereas the activity of hydroxide ions can be approximated with the concentration of hydroxide ions. The gaseous species are related to the partial pressure of the component so that a more practical equation can be derived:

$$\Delta\phi = \Delta\phi^{0`} + \frac{R \cdot T}{2 \cdot F} \cdot \ln\left(\frac{p_{CO_2}}{p_{CO} \cdot c_{OH^-}^2}\right) \tag{24}$$

$\Delta\phi^{0`}$ is the standard Galvani potential at $p_i = p_0$, 298.15 K and an activity for the liquid phase species of 1.[113]

4.1.1 Relationship between $\Delta\phi$ and $\Delta_R\overline{G}$

To understand the fundamental meaning of the electrochemical potential, as reaction direction determining measure, the relationship of $\Delta\phi$ and $\Delta_R\overline{G}$ should be derived. In classical thermodynamics it is defined that the maximum usable work of a system at constant *p* and *T* is equal to the free reaction enthalpy $\Delta_R\overline{G}$ of the underlying chemical reaction. This maximum usable chemical energy is converted in electrochemical systems to electrical energy so that we can write:[116]

$$w_{max} = \Delta_R\overline{G} = w_{electric} \tag{25}$$

The provided electrical work of an energy generating system from a system egoistic point of view is defined as the product of charge and voltage:[116]

$$w_{electric} = -Q \cdot U \tag{26}$$

Q can be further specified by Faraday's law which correlates the number of converted moles of a species with the introduced or extracted charge into / out of a system. For a system with a constant applied current, Faraday's law can be expressed:[114]

$$Q = I \cdot t = n \cdot z \cdot F \tag{27}$$

Combining equation (25) - (27) with n = 1 mol (necessary since $\Delta_R\overline{G}$ is normalized for 1 mol) and substituting U with $\Delta\phi$ finally leads to:[116]

$$\Delta_R\overline{G} = -z \cdot F \cdot \Delta\phi \tag{28}$$

With equation (28), the standard potential of a specific reaction can be calculated from the free Gibbs reaction energy. Consequently, the electrochemical potential can be used to control the direction of a specific electrochemical conversion. Depending on the applied potential, the electroactive species can be oxidized or reduced. This equation does not consider kinetic effects which may prevent the occurrence of a reaction.

4.2 The kinetics of a simple electrochemical reaction

In the previous section we solely looked at the thermodynamic description of an electrochemical system at equilibrium. However, when it comes to a mass transfer due to a turnover of chemical species at the electrode the kinetics of a reaction has to be considered to properly describe the system. Typically, a rate determining first order reaction with one transferred electron is assumed for an easy fundamental review of the electrochemical conversion. O and R represent the oxidized and reduced species while k_{ox} and k_{red} are the rate constants for the oxidation- and reduction reaction:[116]

$$Ox + e^- \underset{k_{ox}}{\overset{k_{red}}{\rightleftharpoons}} Red \tag{29}$$

The rate law for the first order forward and backward reaction can be written with the help of Faraday's law as:

$$\left(\frac{dc_{Red}}{dt}\right) = k_{red} \cdot c_{Ox} = \frac{I_{red}}{z \cdot F} \tag{30}$$

$$\left(\frac{dc_{Ox}}{dt}\right) = k_{ox} \cdot c_{Red} = \frac{I_{ox}}{z \cdot F} \tag{31}$$

The chemical reaction can be further treated in a quantitative manner applying the transition state theory. The transition state is an unstable activated state of the reactant which will further

decompose to the desired product. With the help of the Arrhenius equation the rate constant for the generation of the activated complex can be expressed as:[115]

$$k = k_0 \cdot \exp\left(-\frac{\Delta G^{\#}}{R \cdot T}\right) \tag{32}$$

The $\Delta G^{\#}$ denotes the standard free Gibbs energy of activation for the activated complex and k_0 is the rate constant at standard conditions. As shown in (28) the free Gibbs reaction energy can be correlated with the electrochemical potential leading to (z = 1):[115]

$$\Delta_R \overline{G} \equiv \Delta G^{\#} = -F \cdot \Delta\phi \tag{33}$$

However, a symmetry factor α must be introduced and can be interpreted as the fraction of the total change of Gibbs energy in the system which is used to change the Gibbs energy of activation. Naturally, α takes values between 0 and 1. Additionally, in non-equilibrium state $\Delta\phi$ is the sum of the reversible potential $\Delta\phi^0$ and the overpotential η which will be discussed later in detail. With these considerations, we obtain for the reduction and oxidation reaction:[114]

$$\Delta G_{red}^{\#} = \Delta G_{red}^{\#,0} + \alpha \cdot F \cdot \eta \tag{34}$$

$$\Delta G_{ox}^{\#} = \Delta G_{ox}^{\#,0} - (1 - \alpha) \cdot F \cdot \eta \tag{35}$$

(34) and (35) can be combined with (32) to get an expression for the rate constant of the anodic (oxidation) and cathodic (reduction) rate constants:[114]

$$k_{red} = k_{0,red} \cdot \exp\left(-\frac{\Delta G_{red}^{0,\#}}{R \cdot T}\right) \cdot \exp\left(-\frac{\alpha \cdot F \cdot \eta}{R \cdot T}\right) \tag{36}$$

$$k_{ox} = k_{0,ox} \cdot \exp\left(-\frac{\Delta G_{ox}^{0,\#}}{R \cdot T}\right) \cdot \exp\left(\frac{(1-\alpha) \cdot F \cdot \eta}{R \cdot T}\right) \tag{37}$$

The rate constants are then inserted into (30) and (31) to gain the expression for the anodic and cathodic current of an electrode (z = 1). It has to be noted that the current *I* is substituted with the surface normalized current, the current density *j*, since electrochemical processes occur at the electrode's surface.[114]

$$j_{red} = F \cdot k_{0,red} \cdot c_{Ox} \cdot \exp\left(-\frac{\Delta G_{red}^{0,\#}}{R \cdot T}\right) \cdot \exp\left(-\frac{\alpha \cdot F \cdot \eta}{R \cdot T}\right) \tag{38}$$

$$j_{ox} = F \cdot k_{0,ox} \cdot c_{Red} \cdot \exp\left(-\frac{\Delta G_{ox}^{0,\#}}{R \cdot T}\right) \cdot \exp\left(\frac{(1-\alpha) \cdot F \cdot \eta}{R \cdot T}\right) \tag{39}$$

In equilibrium, both reactions occur at equal velocity which means that both current densities have the same value. The overpotential must be zero with $c_{Ox} = c_{ox}^0$, $c_{Red} = c_{red}^0$ leading to:[113]

$$\begin{aligned} j_{red} = j_{ox} &= F \cdot k_{0,red} \cdot c_{ox}^0 \cdot \exp\left(-\frac{\Delta G_{red}^{0,\#}}{R \cdot T}\right) \\ &= F \cdot k_{0,ox} \cdot c_{red}^0 \cdot \exp\left(-\frac{\Delta G_{ox}^{0,\#}}{R \cdot T}\right) \\ &= j_0 \end{aligned} \tag{40}$$

j_0 is known as the exchange current density and describes the rate at which the reduction and oxidation occur in equilibrium without a net current flow. Typically, j_0 is a measure for the catalytic activity of a material and describes the anodic and cathodic reaction rate in equilibrium. The applied current in non-equilibrium conditions is the difference between the cathodic and anodic current density. Using the definition of the exchange current density and neglecting the transport processes so that the equilibrium concentrations c_{ox}^0 and c_{red}^0 are equal to c_{ox} and c_{red}, the famous Butler - Volmer equation can be derived by subtracting (39) from (38):[114]

$$j = j_{red} - j_{ox} = j_0 \cdot \left[\exp\left(-\frac{\alpha \cdot F \cdot \eta}{R \cdot T}\right) - \exp\left(\frac{(1-\alpha) \cdot F \cdot \eta}{R \cdot T}\right)\right] \tag{41}$$

4.2.1 The limiting cases of the Butler-Volmer equation

Two limiting cases of the Butler -Volmer equation are often used for quantitative evaluation of electrochemical systems. The first and most famous derivate of the Butler - Volmer equation is the simplification for high overpotentials ($|\eta| \geq 118$ mV). One term of the bracket in (41) can be neglected depending on the sign of the overpotential. In the case of a high negative overpotential, the first term in the bracket of (41) can be neglected which results in:[113, 114]

$$j = j_0 \cdot \left[\exp\left(-\frac{\alpha \cdot F \cdot \eta}{R \cdot T}\right)\right] \tag{42}$$

For the evaluation of the exchange current density and the symmetry factor, the equation is written in the Tafel form:[114]

$$\log_{10}(|j|) = \log_{10}(j_0) - \frac{\alpha \cdot F}{2.303 \cdot R \cdot T} \cdot \eta \tag{43}$$

As it can be seen from Figure 8, the exchange current density and the Tafel slope can be derived from the plot of the Tafel equation. The exchange current density is a measure for the catalytic performance of a material while the Tafel slope can give mechanistic insides about the observed reaction.[115]

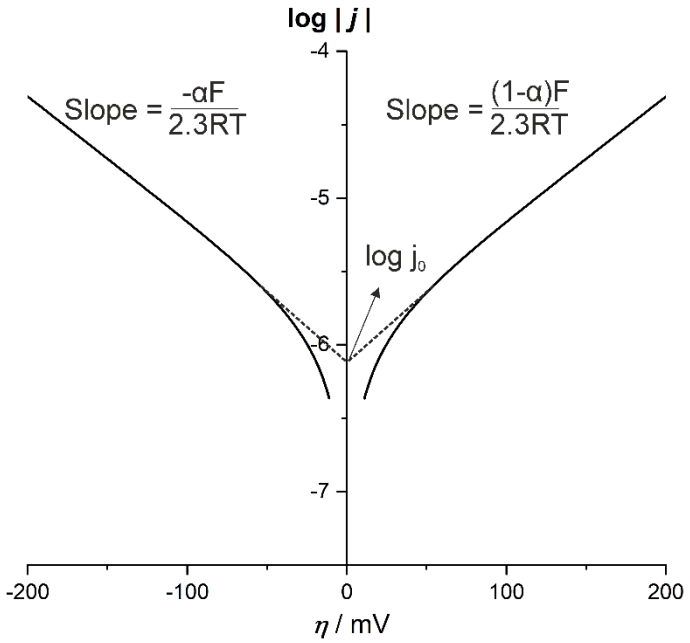

Figure 8 Exemplary Tafel plot to extract the exchange current density and Tafel slope from kinetic measurements. Adapted from Bard et al..[114]

The second limiting case of the Butler - Volmer equation corresponds to a situation where the overpotential is very small ($|\eta| \leq 10$ mV).[113] Therefore, e^x can be approximated via Taylor series expansion:[117]

$$e^x = 1 + \sum_{n=1}^{n<\infty} \frac{x^n}{n!} = 1 + x + \frac{x^2}{2!} + \frac{x^3}{3!} + \cdots \tag{44}$$

Applied to (41) and neglecting terms of $n > 1$ due to the assumed small overpotentials we obtain:[117]

$$j \approx j_0 \cdot \left[\left(1 - \frac{\alpha \cdot F \cdot \eta}{R \cdot T}\right) - \left(1 + \frac{(1-\alpha) \cdot F \cdot \eta}{R \cdot T}\right)\right] \approx - j_0 \cdot \frac{F}{R \cdot T} \cdot \eta \tag{45}$$

A linear correlation between the current density and the overpotential can be observed. This equation is often used to determine the charge transfer resistance R_{ct} when the potential is close to the equilibrium value. The ratio of the overpotential to the current density leads to the value of the surface normalized R_{ct} which can be used to rate catalyst materials:[114]

$$R_{ct} \approx \frac{R \cdot T}{F \cdot j_0} \tag{46}$$

4.2.2 Additional types of overpotentials and their description

The discussed relationship between current density and overpotential was restricted to the activation overpotential η_{ac}. Commonly, in electrolysis systems at least two additional overpotentials must be considered: the concentration overpotential η_{conc} and the ohmic overpotential η_{Ω}.

η_{conc} must be taken into account due to a depletion of the concentration of the active species at the electrode surface when a current is applied. Then, the assumption that the bulk and surface concentration are equal is not reasonable anymore $c \neq c^0$. Exemplarily, this means $c^0_{ox} \neq c_{ox}$ for the cathodic current density and (41) is written as:[113]

$$j_{red} = j_0 \cdot \frac{c_{ox}}{c^0_{ox}} \left[\exp\left(-\frac{\alpha \cdot F \cdot \eta}{R \cdot T}\right)\right] \tag{47}$$

with:

$$\eta = \eta_{act} + \eta_{conc} \tag{48}$$

Re-arranging (47) with respect to η and performing a coefficient comparison with (48) the following equation for η_{conc} can be derived:

$$\eta_{conc} = -\frac{R \cdot T}{\alpha \cdot F} \cdot \ln\left(\frac{c_{ox}^0}{c_{ox}}\right) \tag{49}$$

It can easily be seen that η_{conc} becomes zero if the bulk concentration is equal to the surface concentration. For extremely high current densities, the surface concentration approaches zero $c_{ox} \rightarrow 0$ and $\eta_{conc} \rightarrow \infty$.

A special case exists if the mass transport to the electrode's surface is determined by diffusion. The surface concentration c can be calculated from the bulk concentration c^0 via Fick's first law.[113]

$$J = \frac{j}{n \cdot F} = D\left(\frac{\partial c}{\partial x}\right)_{x=0} = D\left(\frac{c^0 - c}{\delta_N}\right) \tag{50}$$

J represents the flux of the electroactive species, D is the diffusion coefficient and δ_N is the thickness of the Nernst diffusion layer. It is obvious that the highest flux, and therefore the highest current density can be achieved if the surface concentration is zero $c = 0$ (immediate reactant consumption). The obtained current density is the limiting current density evoked by mass transport due to diffusion.[117]

$$j_{limit} = n \cdot F \cdot D \cdot \left(\frac{c^0}{\delta_N}\right) \tag{51}$$

Rolling back to (22) a diffusion overpotential η_{diff} can be defined as:[113]

$$\eta_{diff} = \frac{R \cdot T}{n \cdot F} \cdot \ln\left(\frac{c}{c^0}\right) \tag{52}$$

Finally, introducing (50) and (51) into (52) leads to the desired equation for the concentration overpotential determined by diffusion:

$$\eta_{diff} = \frac{R \cdot T}{n \cdot F} \cdot \ln\left(1 - \frac{j}{j_{limit}}\right) \tag{53}$$

The ohmic overpotential accounts for all occurring resistances which behave like a classical ohmic resistor. Typically, these resistances are caused by the electrical conductivity in the solid phase of the electrode, the ionic conductivity of the electrolyte and contact resistances of the current collector. The most prominent phenomenon is the overpotential induced by the voltage drop evoked from the limited conductivity of the electrolyte. This specific overpotential can be described via:[114]

$$\eta_{\Omega} = I \cdot \frac{x}{\kappa \cdot A} = R_{\Omega} \cdot I \tag{54}$$

I represents the flowing current during electrolysis, x is the distance of the electrodes, *A* represents the electrode's surface and κ is the solution's conductivity. For electrochemical measurements, the potentials are usually '*iR*-corrected'. This means that R_{Ω} was determined via electrochemical techniques and that the observed potentials during further electrochemical characterizations are corrected by $R_{\Omega} \cdot I$. This work flow is mandatory to rule out inconsistent performances of the same electrode in different set-ups (distance electrodes, conductivity electrolyte etc.).

4.3 Electrochemical double layer theory

Electrochemical processes typically occur at the electrode - electrolyte interface, and therefore, it is useful to have a basic understanding of the nature of the interface region. This interface region is called electrochemical double layer. In this section, three basic concepts for the description of the electrochemical double layer are briefly introduced.

Helmholtz was the first scientist who tried to describe the charge arrangement at the electrode - electrolyte interface. As it can be seen in Figure 9 a), an excess charge of positively charged ions (electrode) and solvated negatively charged ions (electrolyte) is present at the interface of a metallic electrode immersed in an electrolyte. The total charge of the interface region is electroneutral.[115] The charge in the solid electrode and the solvated ions approach the surface as close as possible which is in the case of the solvated ions half of their diameter

(including H_2O shell). Both charges are strongly attached to the surface which will result in separated charges on straight planes with a distance of $d/2$.[114]

It becomes obvious that the change of excess space charge density of the metal, q_m, with applied voltage drop (potential) can be described via the model equation of a parallel-plate capacitor:

$$\frac{\partial q_m}{\partial \phi} = C_H = \varepsilon \cdot \varepsilon_0 \cdot \frac{A}{d} \tag{55}$$

C_H corresponds to the Helmholtz differential capacitance while ε_0 is the permittivity of vacuum and ε is the relative permittivity of the electrolyte referenced to ε_0. A denotes the area and d represents the distance of the 'plates'.[114] It must be mentioned that d in (55) is equal to $d/2$ presented in Figure 9 a). Unfortunately, this model does not consider that the charge density will be affected by the electrochemical potential and concentration of the solvated ions. Typically, experimentally obtained differential capacitance values show a dependence on the potential and electrolyte concentration. Furthermore, thermally induced movement of the solvated ions was neglected which will in consequence lead to a non-fixed arrangement of the solvated charge as it was assumed in the Helmholtz model.[113, 115]

These inaccuracies were tackled by Gouy and Chapman. They proposed the existence of a diffuse double layer. In principle, the model considers the attracting forces of the charged electrode onto the solvated ions fixing them close to the surface and the random thermal movement of the ions which will counteract and lead to a diffuse distribution of the solvated ions. As shown in Figure 9 b), an accumulation of the solvated ions close to the surface can be observed since the electrostatic forces prevail the thermally induced movement of the solvated ions. Depending on the distance to the electrode, the association of the ions will decay. The extent to which the charge species is fixed and the diffuse double layer will expand depends on the potential of the electrode and the concentration of the solvated ions. Gouy and Chapman derived an equation to describe the change of the space charge density depending on the potential level and ion concentration:[114, 115]

$$\left(\frac{\partial q_m}{\partial \phi_0}\right)_{\mu} = C_{G.C.} = |z| \cdot F \cdot \left(\frac{2 \cdot \varepsilon \cdot \varepsilon_0}{R \cdot T} \cdot c\right)^{\frac{1}{2}} \cdot \cosh\left(\frac{|z| \cdot F}{2 \cdot R \cdot T} \cdot \phi_0\right) \tag{56}$$

ϕ_0 represents the potential at the electrode's surface, all other variables are already defined. However, the predicted capacitance values still deviate from the experimentally observed ones. The introduced errors can be traced back to three assumptions which are made in the derivation of (56): ion-ion interactions are neglected; the ions are assumed to be point charges and ε is assumed to be independent of the distance of the electrode.[115]

Otto Stern was the one who combined the two existing unsatisfactory models and combined them to a model which predicts capacitance values which are in good agreement with experimental values. Stern pointed out that the Helmholtz and the Gouy-Chapman description exist simultaneously. This indicates that a compact fixed layer of solvated ions exists close to the interface while a diffuse layer can be expected at increasing distance from the electrode's surface. The total predicted differential capacitance C_d for a polarized electrode can be described mathematically as:

$$\frac{1}{C_d} = \frac{1}{C_H} + \frac{1}{C_{G.C.}} \tag{57}$$

$$\frac{1}{C_d} = \left[\frac{\varepsilon \cdot \varepsilon_0}{d}\right]^{-1} + \left[|z| \cdot F \cdot \left(\frac{2 \cdot \varepsilon \cdot \varepsilon_0}{R \cdot T} \cdot c\right)^{\frac{1}{2}} \cdot \cosh\left(\frac{|z| \cdot F}{2 \cdot R \cdot T} \cdot \phi_0\right)\right]^{-1} \tag{58}$$

Figure 9 c) summarizes all three presented models and illustrates the arrangement of the charged species depending on the distance to the electrode surface. Additionally, the potential drop as a function of the distance is depicted.

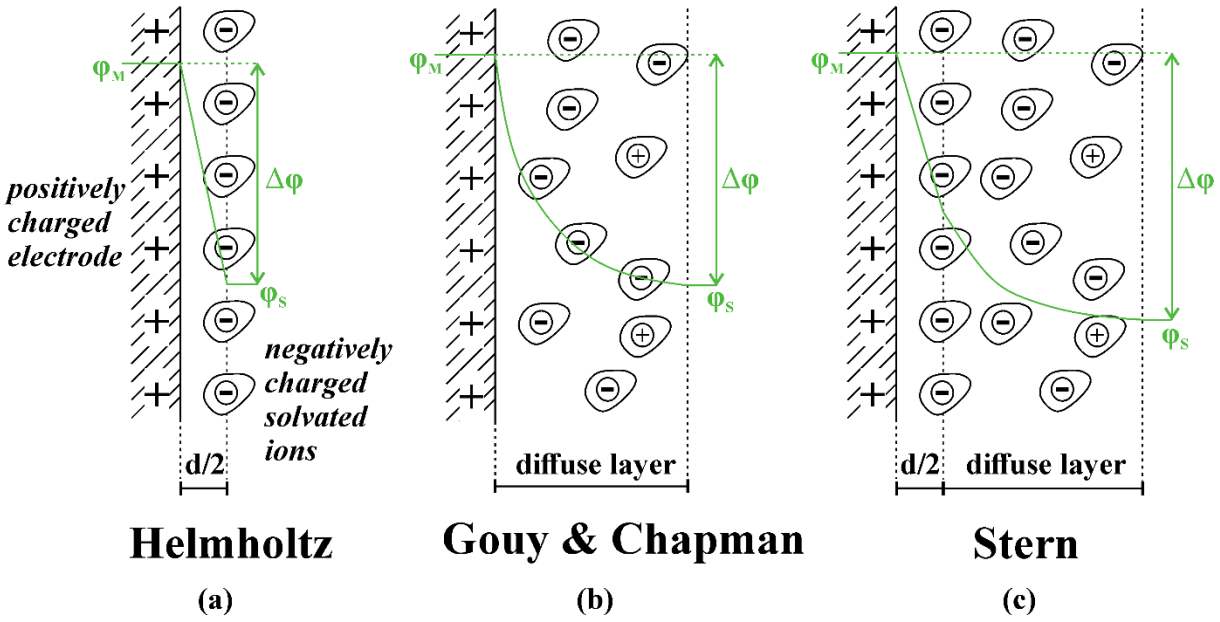

Figure 9 Overview of the presented models for the description of the electrode - electrolyte interface: a) Helmholtz- b) Gouy & Chapman- c) Stern- model

From an experimental point of view, measured values of the differential capacitance C_d are often evaluated with Helmholtz model (55) - besides the shown inaccuracy - to determine the area of the parallel-plate capacitor which is typically interpreted as the electrochemical surface area (ECSA) of an electrode. This approach requires the knowledge of ε and d which are hard to estimate. To get around this, the measured differential capacitance of a well-defined surface (not rough, known surface area) of the desired material in the specific electrolyte is set as specific capacitance (C_s / mF cm^{-2}) and used to convert differential capacitance values of the same material in the same electrolyte under operating conditions to a surface area. This surface area is of high importance when it comes to catalyst evaluation since the electrodes performance highly depends on the number of accessible active sites which are proportional to the ECSA.

$$ECSA = \frac{C_d}{C_S} \tag{59}$$

4.3.1 Electrocapillarity

Let us now consider a metal electrode which is in contact with aqueous electrolyte. As explained before, a double layer of opposite charged species will be formed at the electrode - electrolyte interface. This situation at the interface can be described quantitatively from classical thermodynamics with the Gibbs adsorption isotherm:[114]

$$-d\gamma = \sum_i \Gamma_i \cdot d\bar{\mu}_i \tag{60}$$

γ represents the surface energy to create a unit amount of interface, Γ_i and $\bar{\mu}_i$ represent the surface excess concentration and electrochemical potential of the component *i*. This abstract equation can be transformed to a more useful form from the electrochemical point of view:[115]

$$-d\gamma = q_m \cdot d\phi + \sum_i \Gamma_i \cdot d\mu_i \tag{61}$$

(61) points out that if the composition of the electrolyte is assumed to be constant ($d\mu_i$ = const.) the change of the work induced by a change of the electrochemical potential is balanced by the surface energy. Since in experimental science changes of quantities can be measured more convenient compared to absolute values, the first and second order derivative of $d\gamma$ is calculated with respect to the electrochemical potential with $d\mu_i$ = const.:[113]

$$-\left(\frac{\partial\gamma}{\partial\phi}\right)_{\mu_i} = q_m \tag{62}$$

$$-\left(\frac{\partial^2\gamma}{\partial\phi^2}\right)_{\mu_i} = \left(\frac{\partial q_m}{\partial\phi}\right)_{\mu_i} = C_d \tag{63}$$

(62) is the famous Lippmann equation. It becomes evident from (63) that the change of surface energy can be correlated with the double layer capacitance which was introduced in the foregoing section. To be more precise, the double layer capacitance as shown before should be named differential capacitance since this quantity describes the change of the surface charge

for a potential perturbation. For further insights, the integration of the first order derivative of (63) was performed setting the upper boundary ϕ and the lower boundary to ϕ_{pzc} which is called the potential of zero charge where the excess charge q_m at the interface is equal to 0:

$$q_m = C_i \cdot (\phi - \phi_{pzc}) \tag{64}$$

It must be noted that the subscript of the capacitance changes to i since this value now corresponds to the integral capacitance. Because the determination of ϕ_{pzc} is a challenging task, the differential capacitance is the quantity which is of practical interest for the description of the capacitive behavior of an electrode and relatively easy measurable. The relationship of C_i and C_d is nicely shown by Bard et al. and depicted in Figure 10:[114]

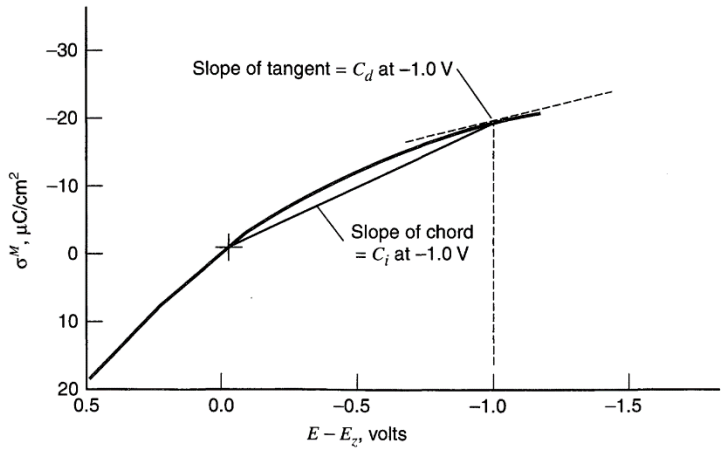

Figure 10 Plot of the surface charge vs. (ϕ - ϕ_{pzc}). C_i is the average change of the excess surface charge q_m with a potential perturbation referenced to ϕ_{pzc}. C_d is the slope of the plotted curve for an infinitesimal perturbation of the potential at ϕ. Reproduced from Bard et al..[114]

Now that we know an expression for the excess surface charge q_m, we can introduce (64) into the Lippmann equation (62) and integrate to get a correlation between the surface energy of the interface and the integral capacitance.

$$\gamma = \gamma_{pzc} - C_i \cdot \frac{(\phi - \phi_{pzc})^2}{2} \tag{65}$$

An exemplary plot of (65) is shown in Figure 11: it can directly be seen that the shape of the γ vs. ϕ curve is an inverted parabola with its maximum γ_{pzc} at $\phi = \phi_{pzc}$. Independent of the sign,

the necessary energy to create a unit amount of interface surface will be reduced when a potential - relative to ϕ_{pzc} - is applied. From a phenomenological point of view this behavior can be explained as following: at ϕ_{pzc} no excess charge is present at the interface, the aqueous phase shows the lowest tendency to wet the hydrophobic electrode surface. If a potential $\phi \neq \phi_{pzc}$ is applied the electrodes will be polarized and the double layer will form. The accumulation of equally charged species at the interface will result in repelling forces which in consequence will lead to a tendency to increase the area of the interface. This is the underlying phenomenon for the electrowetting effect which results in a more pronounced wetting of polarized surfaces / electrodes.[113]

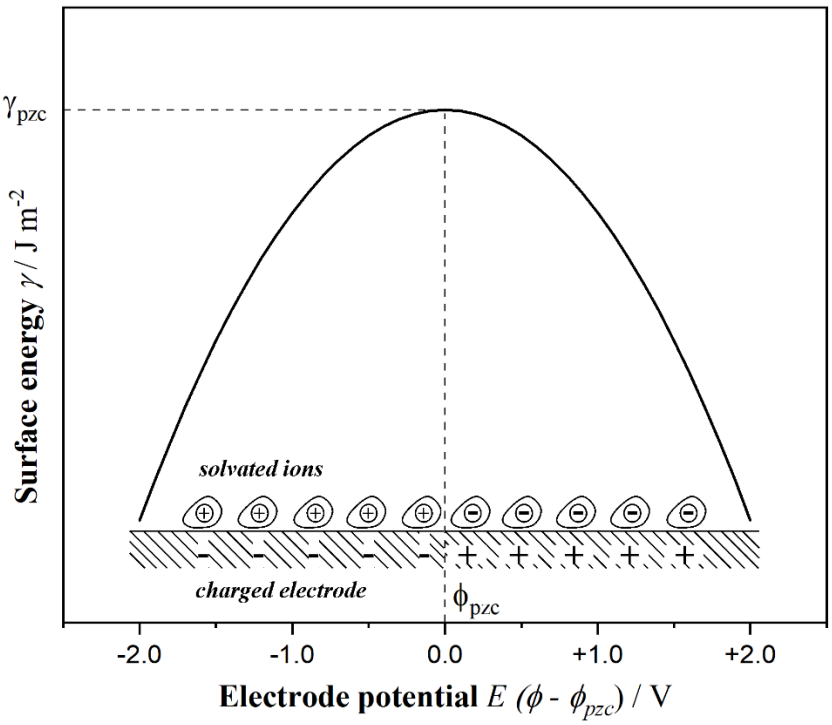

Figure 11 Schematic plot of the potential dependent interface surface energy according to (65), inspired by Hamann et al..[113] At more negative or positive potentials referenced to ϕ_{pzc} a surface energy reduction is observable. At ϕ_{pzc} the excess charge is equal to zero and the surface energy reaches a maximum due to the absence of repelling charge carriers of the same sign.

4.4 Gas-diffusion electrodes

Besides the electrochemical conversion of CO_2, several electrochemical applications, for example zinc-air batteries, fuel cells, chlor-alkali electrolysis, include the reaction of gaseous educts with protons provided from a liquid electrolyte.[118-120] Therefore, the reactant gas must

be dissolved in the liquid phase and diffuse to the electrode where electrons are transferred (cf. Figure 12 a)). It is not surprising that due to the low solubility of gases (O_2, CO_2) in aqueous electrolytes[6, 121] and slow diffusion velocity of the dissolved gas, the mass transport limits the applicable current densities.[27, 122] For the most part, these limitations can be circumvented when using gas-diffusion electrodes (GDE). These electrodes consist of a porous architecture which faces the liquid electrolyte on one side and the gaseous reactant at the opposite side. Both reactants penetrate into the GDE while the reaction takes places at the spot where the liquid electrolyte, gaseous reactant and solid catalyst meet. This region is often referred to as the triple phase boundary (TPB) which is a widely accepted terminus despite it does not sufficiently describe the conditions inside the GDE as it will be discussed later in this section.[118, 123] Besides the obvious tremendous amount of provided active sites inside the porous GDE, a significant reduction of the diffusion length of the gaseous species through the liquid phase is the reason GDEs are superior, especially at high conversion rates, compared to plain electrodes.[124-126] A simplified representation of the discussed conditions is illustrated in Figure 12 b).

Taking a short digression to the historical point of view: GDEs were already described by Reid in a patent in 1902. He used porous carbon to convert H_2 and O_2 in aqueous KOH to electricity, today known as alkaline fuel cell. He already described that the liquid electrolyte can only partially penetrate into the porous carbon while the gaseous reactant will diffuse through the porous system.[127] Furthermore, in 1925 Heise patented porous carbon-based electrodes for the usage as cathodes in zinc-air batteries including an intermediate paste layer. This intermediate layer was introduced to prevent the electrode from flooding. Heise postulated that batteries in which the intermediate layer was included were more durable compared to air electrodes without this hydrophobic layer.[128, 129] As stated by Kubannek et al. a breakthrough of GDE engineering was achieved by introducing polytetrafluoroethylene (PTFE) as electrochemical stable hydrophobic agent and binder for GDEs applied in alkaline electrolytes.[129] Furthermore, in the 1960s Grot patented wettable PTFE - today known as Nafion® - which is one of the key components in membrane electrode assemblies (MEA) in PEMFC.[130]

However, considering Figure 12 a): at high conversion rates the depleted concentration of gaseous reactant will be replenished by diffusion of dissolved gas from the bulk to the electrode's surface; the thickness of the depletion layer and by that the diffusion length of the reactant depends on the conversion rate. The achievable conversion rate will be limited by the mass transport of the gaseous educt.[6] On the other hand, Figure 12 b) points out the simplified conditions inside a GDE: the electrolyte will form a thin liquid film on the pore walls and wets

the catalyst particle, the gaseous reactant will diffuse quickly in the gas phase and dissolves in the thin liquid film. The distance the reactant has to diffuse in the liquid phase, which is much slower compared to gas phase diffusion, is significantly reduced. Consequently, a facile educt mass transport will be achieved.[79, 124] It cannot be stressed enough that the illustrated GDE representation only demonstrates a simplified viewpoint on the present conditions inside the GDE.

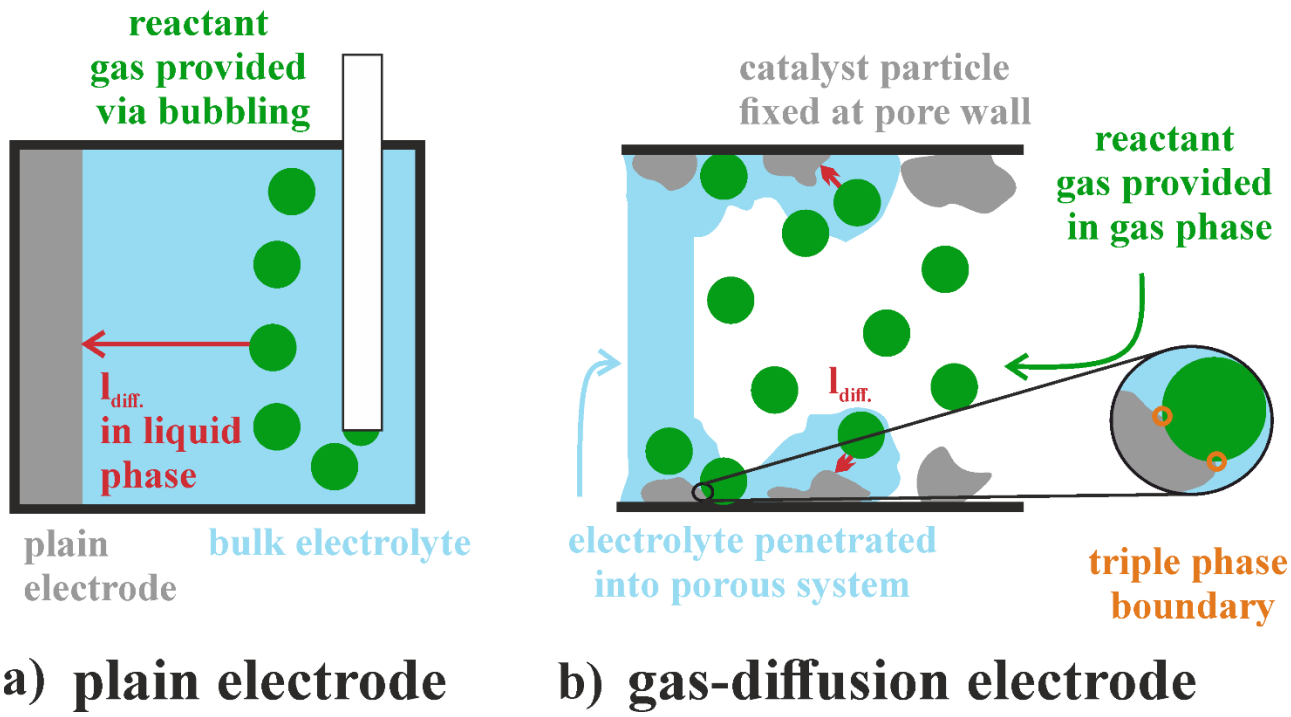

Figure 12 Schematic representation for the electrochemical conversion of gaseous educts at a) plain electrode and b) gas-diffusion electrode revealing a significantly reduced liquid phase diffusion length $l_{diff.}$ for the gaseous reactant. Besides the reduction of $l_{diff.}$, an increased number of active sites - caused by the porous nature of the GDE - is the reason why GDEs are superior compared to plain electrodes.

However, to emphasize the role of a small diffusion length to achieve high current densities, a rough estimation of the limiting current depending on the diffusion layer thickness δ_N for CO_2 converting electrodes can be made via (51). The following parameters (25 °C) were assumed: $D_{CO2/H2O} = 1.92 \times 10^{-5}$ cm^2 s^{-1} [131], $c_{CO2/H2O} = 0.0336$ mol L^{-1} [6], $z = 2$, $F = 96485$ A s mol^{-1}. The calculated results are depicted in Figure 13 and demonstrate a steep rise of j_{limit} for small diffusion layer thicknesses. For CO_2EL at a plain electrode where CO_2 is provided via bubbling into the bulk electrolyte, the diffusion layer thickness is estimated to be around 40 - 100 µm

which will result in $j_{limit} \approx 30$ mA cm^{-2}. [60, 79, 132] On the other hand, the diffusion layer thickness for a GDE was estimated from Weng et al. via modelling to be approximately 0.01 – 10 µm which - considering Figure 13 - explains why it is possible to achieve significantly higher current densities with GDE set-ups compared to plain electrodes (cf. Figure 12).[133] It must be mentioned that for industrial applications a current density of ~ 200 mA cm^{-2} is mandatory to achieve desired space-time yields.[41, 79]

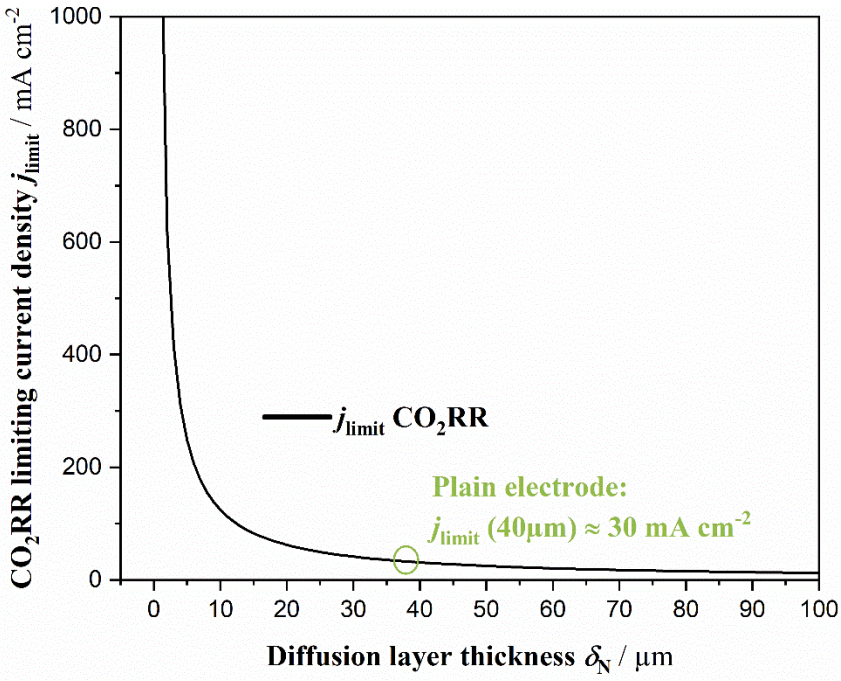

Figure 13 Modelled limiting current density j_{limit} for CO_2EL as function of diffusion layer thickness δ_N. Calculation based on (51).

The contact intensification of the three existing phases is not the sole task of the GDE. These porous architectures should also provide a high electrical conductivity (reduce ohmic losses), sufficient mechanical stability and a suitable wetting behavior so that a GDE flooding or dry out can be prevented.[124, 134] These versatile requirements onto the GDEs properties indicate that GDE engineering is a crucial task on the way to industrial realization of a CO_2 electrolysis system.

Two GDE designs, depicted in Figure 14, have prevailed: a multi-layer approach[60, 135] where each layer fulfills a specific task or in contrast the single-layer GDE design[27, 66] with a homogeneous architecture. The multi-layer GDE consists of a hydrophobic gas-diffusion-layer (GDL) and a hydrophilic catalyst layer. The GDL (~ 100 – 300 µm) itself is a combination of a macroporous- and a microporous-layer: while the macroporous-layer ensures a facile gas transport of the gaseous educt inside the GDE, the microporous layer prevents excessive flooding of the GDL.[136, 137] The top of the GDL is coated with the catalytic layer (5 - 50 µm) which includes the electrocatalyst and Nafion® as hydrophilic binding agent. Therefore, this layer is more or less flooded and represents the reaction zone in which CO_2 is provided through the GDL and diffuses in the flooded catalyst layer to the active sites.[60, 138] On the other hand, the single-layer GDE combines the gas-diffusion- and catalytic-layer in one homogeneous phase. The catalyst powder (or supported catalyst) is mixed with a hydrophobic agent - almost exclusively PTFE powder - and consecutively pressed or rolled to obtain the GDE. In the case of single-layer GDEs, PTFE is not solely used to control the hydrophobicity but also as binder to provide mechanical stability. For advanced GDE engineering, additional functional layers can be coated onto the single-layer GDE or pore-forming agents can be used to custom tailor the porous structure. Commonly, the GDE is fixed to a metallic current collector to improve the current distribution inside the GDE. A famous example for a single-layer GDE is the PTFE bonded silver-based oxygen-depolarized-cathode which is used in industrial scale in chlor-alkali electrolysis. [27, 119, 121, 139]

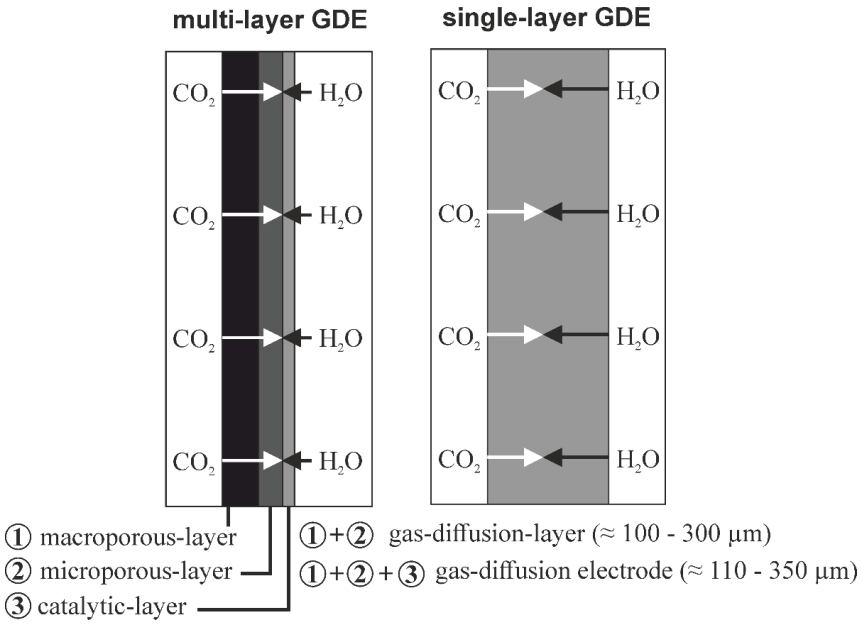

Figure 14 Schematic representation of the architectures of single- and multi-layer GDE designs.

A considerable amount of work was done from a modelling point of view to understand the operation principle of GDEs. The first models were quite simple assuming that the pores of the GDE will be filled to a specific extent at which end a meniscus will be formed. Unsatisfactorily, this model predicts low j_{limit} due to the small triple phase area as consequence of the assumed wetting characteristics.[129, 140] This model was then extended separately by two different approaches: the first concept was to introduce a liquid electrolyte film which forms on the pore walls[129, 141, 142] while the second optimization was to assume the parallel existence of completely dry hydrophobic and flooded hydrophilic pores.[129, 143, 144] However, the puzzle was more or less solved by Cutlip who combined both above mentioned approaches to set up the famous *thin-film flooded agglomerate* (TFFA) model which in contrast to the previous approaches can be used to describe experimentally observed limiting current densities of GDEs as shown from Pinnow et al. for Ag-GDEs in NaOH for the oxygen reduction reaction. The TFFA model suggests the parallel existence of flooded catalyst agglomerates and hydrophobic gas transport pores. At the transition of flooded and dry regions a liquid film is formed at the pore walls.[129, 145, 146]

Considering the knowledge provided via modelling the terminus TPB needs to be re-evaluated. As indicated in Figure 12 b), the triple phase boundary is restricted to a single point or a line which would result in small ECSAs and not sufficiently explain the high observable activity of GDEs. Following, the TPB might be interpreted as a reaction zone (cf. Figure 15 a)): to a certain extent the GDE is flooded up to a point where the macropores are dry and only adjacent smaller pores are filled due to the higher capillary forces. Additionally, a liquid film is formed on the pore walls at the exit of a flooded small (< 100 nm) macropore.[79] The existence of dry macropores close to flooded or wetted significantly smaller pores is the most important characteristic of the GDE since this is the reason for the short diffusion lengths of CO_2 in the liquid phase. Consequently, a bimodal pore system is mandatory for a properly working GDE.[138]

4.4.1 GDEs wetting behavior

As pointed out in the previous section the interplay of wetted and non-wetted regions inside the GDE is a major characteristic for highly active GDEs. The hydrophobicity of the GDE determines the wetting behavior and can be adjusted by varying the mass fraction of the hydrophobic agent.[124] Furthermore, if a catalyst support is used the hydrophobic characteristic of the support affects the hydrophobicity of the GDE. The hydrophobicity of carbon support can be adjusted by oxidizing the support's surface.[18] However, three wetting scenarios must be

distinguished to properly understand the importance of GDE wetting during operation. These scenarios are illustrated in Figure 15.

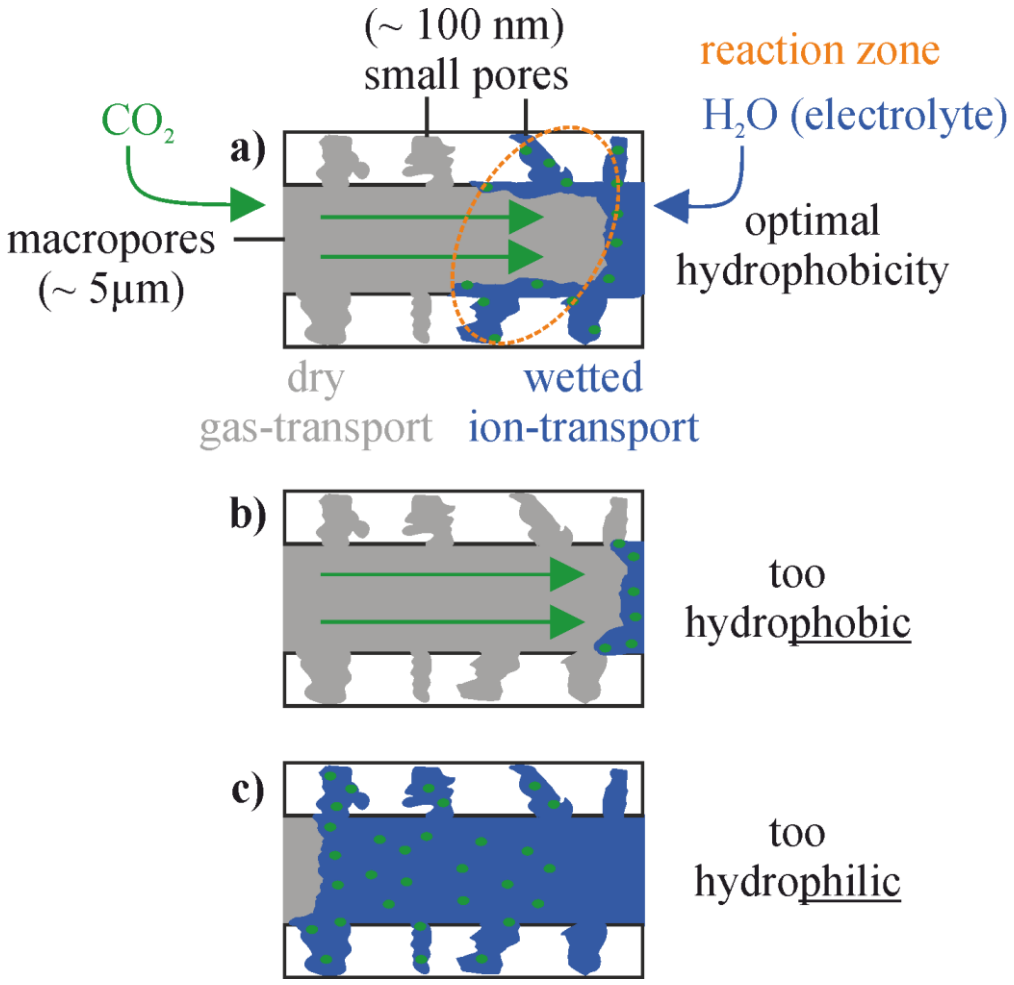

Figure 15 Possible scenarios of GDE wetting during operation: a) optimal hydrophobicity resulting in small diffusion lengths for CO_2 b) too hydrophobic pore system leading to a small ECSA and therefore to unsatisfactorily activity c) too hydrophilic pore system which will be flooded and dramatically increase the diffusion length of CO_2 in the liquid phase.

The desired wetting behavior is depicted in Figure 15 a): the macropores of the GDE are partially flooded while the adjacent smaller pores are completely flooded due to the higher capillary forces. At the connection points of the small flooded pores and the dry macropores a liquid film is formed. The flooded adjacent pores and the wetted pore walls of a macropore can be suggested to be the reaction zone where the reaction takes place. This scenario is a compromise of a high ECSA while the diffusion length of CO_2 in the liquid phase is kept to a minimum. It must be mentioned that it is not yet clear with certainty that the location of the reaction is inside the liquid film and smaller pores or if the reaction takes place at the very TPB.[126] Nonetheless, for a highly hydrophobic GDE the scenario in Figure 15 b) can be

expected. The electrolyte penetrates only slightly into the GDE which will result in a low ECSA and activity. The other extreme case is a highly hydrophilic GDE which will be (nearly) completely flooded and have a high ECSA. Unluckily, the diffusion length of CO_2 in the liquid phase to a sufficient number of active sites is significantly increased. Especially, at higher current densities this will lead to a mass transport limitation of CO_2 and favor the undesired HER.[27, 60]

It is noteworthy, that the GDEs used in this thesis are extremely hydrophobic which is not just a result of the hydrophobic PTFE but also due to the inherent remarkable hydrophobicity of the used acetylene black support.[147] Thus, it is legitimate to question why the hydrophobic GDEs show a high activity for CO_2EL despite the expected insufficient wetting (cf. Figure 15 b)). This can be answered by recalling the fundamentals of electrowetting shown in Figure 11. As soon as a potential - relative to ϕ_{PZC} - is applied the surface energy of the liquid and solid interface is reduced and a wetting process will be induced. This is the reason why the extremely hydrophobic GDEs show a decent activity for CO_2EL. However, the wetting behavior of a GDE can be altered by several reasons (degradation porous system, catalyst alteration, precipitation of electrolyte salts inside GDE) resulting in flooding and by that in a degradation of the electrode's performance as noticeable in decreasing CO_2RR FE and increasing HER FE.[18, 102]

5 Methods

5.1 GDE preparation

In this thesis, carbon supported tin- and bismuth-based GDEs were investigated. Therefore, the catalyst powder was mixed with the binding agent PTFE and dry-pressed in a hydraulic press. A more detailed description of the catalyst powder synthesis and the GDE manufacturing process will be presented in the following subsections. Exemplary results of the material characterization of the catalyst material and GDE will be presented in the sub section where the basic principles of the characterization techniques are briefly explained.

Both catalyst powders used in this dissertation were provided from a collaboration partner from the Institute of Technical Chemistry from the University of Stuttgart. For both powders acetylene black (AB) was used as supporting material since it was tested in previous works to be the most suitable carbon black - among the tested ones - for the desired application due to its high electrical conductivity and noticeable hydrophobicity.[147, 148] Furthermore, the agglomerates and aggregates of AB provide a sufficient number of mesopores.[45, 149] Interestingly, the BET surface of the used AB, 75 m^2 g^{-1}, (Alfa Aesar, 100 % compressed, 99.9+ %) was quite low for a carbon black material.[147] However, the synthesis routes for both catalyst powders will be described.

5.1.1 Tin-based catalyst powder

A homogeneous precipitation method was adapted from Kang et al. to precipitate SnO_2 on acetylene black.[27, 150] Therefore, 9.0 g AB and 0.577 g of sodium dodecyl sulfate (SDS, improves dispersion of hydrophobic AB in water) were dispersed in 200 mL of deionized water and vigorously stirred overnight. Following, the dispersion was ultra-sonicated for 1 h while consecutively 0.451 g of the precursor, $SnCl_2 \times 2\ H_2O$, and 6.0 g of urea were added to the dispersion. The mixture was heated up to 90 °C were urea starts to slowly decompose to ammonia, carbon dioxide and hydroxide ions which carefully raises the pH value.[150] The hydrolysis was carried out for 4 h under total reflux of the evaporated water. The dispersion was filtered and thoroughly washed to remove chloride salts and SDS. Lastly, the powder was dried at 100 °C overnight in air. The approximate Sn loading determined via thermal gravimetric analysis (TGA) was 2.6 wt%. As suggested by Kang et al., the slow and uniform rise of the pH is the reason for the precipitation of evenly sized nano particles.[150]

5.1.2 Bismuth-based catalyst powder

The Bi_2O_3 catalyst was synthesized according to Yuan et al. and precipitated on AB via a slightly modified protocol of the above shown homogeneous precipitation method.[151, 152] 13.6 g of AB and 0.865 g of SDS were dispersed in 300 mL of deionized water stirred overnight and ultra-sonicated as described above. The dispersion was then acidified with 22.5 mL of conc. HCl and the precursor, 3.0 g $Bi(NO_3)_3 \times 5\ H_2O$, was added. The pH value was raised to a value of 11 by carefully pouring 1.0 M NaOH to the dispersion. Thereafter, the dispersion was stirred for 2 h at room temperature and 3 h at 90 °C under total reflux. Analogously, the powder was filtered, washed and dried at 100 °C overnight in air. The Bi loading was 4.5 wt% as determined with TGA. Due to the higher molar weight of Bi, the loading on a molar base was the same as in the Sn-based catalyst powder.

5.1.3 GDE manufacturing

The GDEs were prepared via dry-pressing. A schematic procedure of the manufacturing process is illustrated in Figure 16. In a first step, the catalyst powder is mixed in a knife-mill with the hydrophobic agent PTFE (Dyneon, TF 2053Z) in a ratio of 65 wt% : 35 wt% referenced to pure carbon. This chosen mixing ratio is an outcome of previous work.[148] The mixture is then transferred into a cylindrical mask with $d = 39$ mm and $h = 10$ mm. The excess powder is removed with a doctor blade to achieve a macroscopic flat surface. Following, a cylindrical stamp is put in the mask and the arrangement is transferred to a hydraulic dry-pressing unit. A pressure of 10.5 kN cm^{-2} was applied for 60 s. After the pressing step the electrode was thermally treated for 60 min in air at 340 °C (ramp: ~ 5 °C min^{-1}), which is slightly above the PTFE melting point.[153] During the thermal treatment PTFE partially melts and generates hydrophobic macropores and increases the mechanical stability.[45] As stated in 4.4, the existence of a bimodal pore structure is of utmost importance for properly working GDEs.

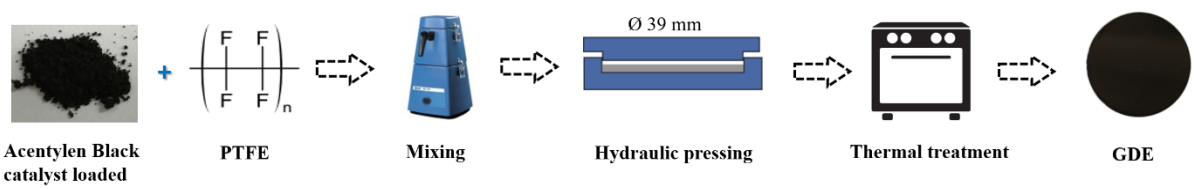

Figure 16 Principal processing steps for GDE manufacturing.

5.2 Material characterization

5.2.1 Scanning electron microscopy

Scanning electron microscopes (SEM) are widely used to analyze and picture the structure of the surface of materials. The achievable magnification ranges from about 20x up to 100,000x. Principally, an electron gun generates an electron beam which is accelerated with an acceleration voltage of up to 40 kV, subsequently focused by lenses and finally scans over the surface of the probe. The electrons will hit the surface of the sample and produce inelastic or elastic scattering whereas the scattered electrons are collected with a detector to generate the image.

Inelastic scattering will result in secondary electrons (SE) which are detected with the SE detector and used to reveal the topographic information about the sample. SE contain a depth information of about 5 - 50 nm.

Elastic scattered electrons are typically called back scattered electrons (BSE) containing a depth information of about 50 - 300 nm and are detected with the corresponding BSE detector. The ratio of the number of incident electrons and back scattered electrons is called backscatter coefficient and depends on the atomic number of the material the sample is made of. Typically, the backscatter coefficient increases with increasing atomic number. A higher number of back scattered electrons will increase the number of electrons hitting the BSE detector and result in bright spots in the picture. Depending on the atomic number varying gray levels can be observed giving information about the distribution of different species inside the sample.[154]

In this thesis, a Zeiss ULTRA PLUS SEM was used to characterize the topography of the porous GDE (using SE) and to analyze the catalyst distribution via material contrast images (using BSE). Exemplary SEM images of the SnO_2 GDE are illustrated in Figure 17.

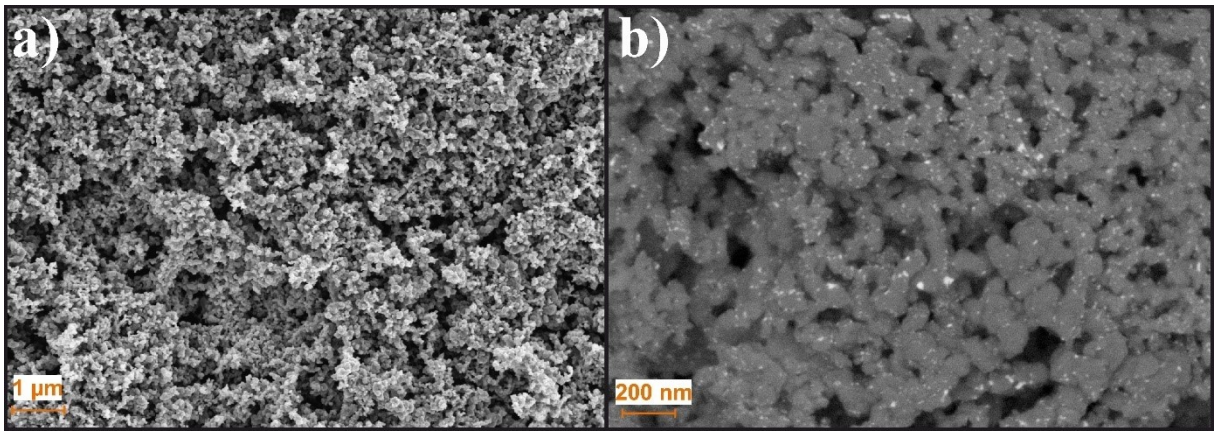

Figure 17 a) SEM picture obtained with secondary electrons showing the porous architecture of the SnO_2 GDE. b) Material contrast image generated by back-scattered electrons revealing the homogeneous dispersion of the SnO_2 catalyst.

5.2.1.1 Energy dispersive X-ray spectroscopy

Energy dispersive X-ray spectroscopy (EDX) can be used for qualitative and quantitative elemental analysis of the investigated sample. Usually, EDX is an extension of SEM: the electron beam of the SEM excites an electron in an inner shell of an atom which will result in a vacancy. This vacancy will be refilled by an electron which drops from an outer shell and simultaneously emitting an X-ray photon with a specific energy. This phenomenon is illustrated in Figure 18. For example, if an electron from the K shell is knocked-out from the atom, the vacancy can be refilled by electrons from the L and M shell. The energy of the emitted X-ray photon - released during the refilling of the vacancy - depends on the energy difference of the vacancy shell and the shell from where the refilling electrons drops. To clearly specify the energy levels the Siegbahn notation was introduced. However, it is important to mention that the emitted characteristic X-ray energy depends on the atomic number as stated in Moseley's law when combined with the wavelength - energy correlation ($E = h\,c\,\lambda^{-1}$):

$$E = \frac{h \cdot c}{B} \cdot (Z - \sigma)^2 \tag{66}$$

E denotes the characteristic energy of the emitted photon. h and c represent Planck's constant and the speed of light. B and σ are constants which are characteristic for the specific shells while Z is the atomic number.[154] This dependence of the characteristic X-ray on the atomic number is essential in EDX to qualitatively distinguish between different elements. For example, the $K\alpha_1$ values for potassium and platinum are 3.314 keV and 66.83 keV. Typically,

EDX spectra show the intensity as an auxiliary unit as a function of the energy in keV. Since the energy levels are specific for an element, the present species can be identified.

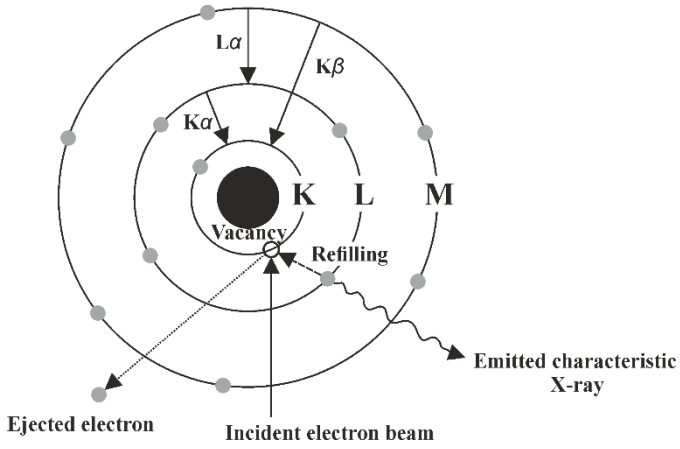

Figure 18 Schematic representation of the generation of characteristic X-rays during EDX.

In this work, the elemental distribution in the cross-section of an GDE is used to evaluate the penetration depth of the electrolyte into the GDE. A surface EDX analysis is often referred to as an element mapping. An exemplary element map of potassium distributed inside the GDE after operation is depicted in Figure 19 and was recorded with a Bruker XFlash 5010 device.

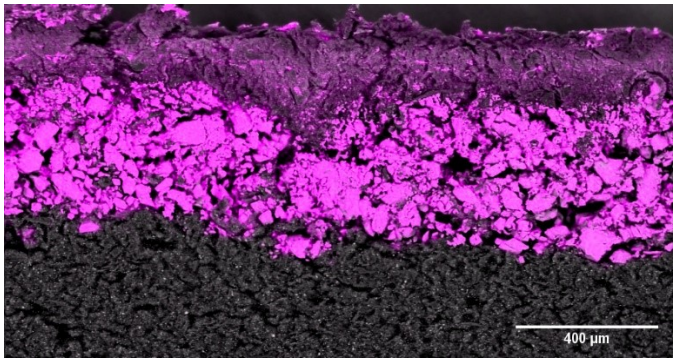

Figure 19 Potassium element map for the cross section of a GDE after operation.

5.2.2 Transmission electron microscopy

Transmission electron microscopes (TEM) can be used to generate high-resolution images of samples. Analogously to SEM, an electron gun provides an electron beam but in contrast to SEM it is accelerated with much higher voltages of 200 kV or even 1000 kV in high-resolution TEM. A typical resolution of a TEM operated with 200 kV as acceleration voltage is about 0.24 nm which demonstrates the main difference of TEM to SEM: a higher resolution can be

achieved with TEM. Due to the underlying principle of electron transmission, the samples must be thin enough (< 100 nm) to transmit a suitable number of electrons which can be analyzed by a detector. Therefore, the sample preparation includes several steps (grinding, electrolytic thinning or ion milling) to achieve sufficient thin samples. The image is generated by the deflection of electrons relative to their initial transmission direction. The scattered electrons lead to a lower number of electrons, relative to the initial beam, reaching the detector which will result in an observable contrast. There are two underlying phenomena responsible for the electron scattering during transmission: mass-density contrast which represents the scattering due to interaction of electrons with the nuclei, and diffraction contrast which is a result of constructive interference of scattered electrons (cf. 5.2.3).[154] For the sake of simplicity, further explanation of the underlying scattering phenomena is omitted.

TEM measurement were performed from the collaboration partners from the Institute of Technical Chemistry from the University of Stuttgart. Dark field TEM pictures, in which the contrast is inverted so that heavy elements appear as bright spots, of the bismuth-based catalyst powder are depicted in Figure 20. These pictures illustrate the homogeneous catalyst distribution and that aggregates of a few nm are precipitated onto the acetylene black support.[152]

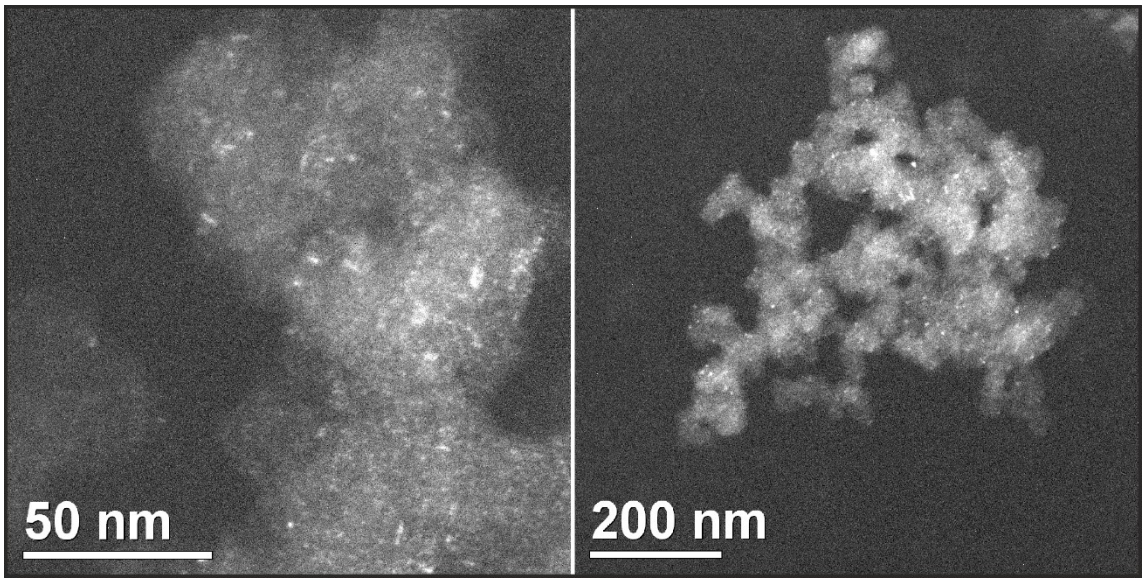

Figure 20 TEM images of the bismuth-based catalyst powder revealing a homogeneous catalyst distribution and the existence of catalyst aggregates of a few nm on the acetylene black support.

5.2.3 X-ray diffractometry

X-ray diffractometry (XRD) is the most widespread technique to characterize the crystallographic structure of materials. Compared to other material characterization methods, XRD identifies a material by its crystalline structure and not by its composition, and therefore, it can be used to reveal the existence of different phases of a material with the same composition.[154]

The underlying phenomenon in XRD is the constructive or deconstructive interference of diffracted X-rays as it will be explained in the following with the help of Figure 21. Two X-rays with the wavelength λ travelling in the direction of the sample interfere constructive when their phase shift is $n\lambda$ while n is an integer. These beams are termed in phase. On the other hand, the beams interfere destructive and are out of phase if their phase shift is $n\lambda/2$. Two incidents in phase beams which are diffracted on the crystallographic planes are only in phase after diffraction if *Bragg's law* (cf. (69)) is fulfilled. Out of phase diffracted beams will interfere destructive and cannot be detected. From a geometrical point of view, the incident and diffracted beams can only be in phase, considering Figure 21, if:

$$n \cdot \lambda = SQ + QT \tag{67}$$

SQ and QT can be calculated via trigonometry (θ = incident angle) and yield:

$$SQ + QT = 2 \cdot PQ \cdot \sin(\theta) \tag{68}$$

Introducing (68) into (67) and substituting PQ with the plane spacing d_{hkl}, *Bragg's law* can be formulated as:

$$n \cdot \lambda = 2 \cdot d_{hkl} \cdot \sin(\theta) \tag{69}$$

The detector can only detect X-rays when the diffracted beams are in phase. A diffractogram is a plot of the detector signal in dependence of the incident angle. This incident angle is varied in a specific range and the diffracted X-rays are detected in the case of constructive interference. Therefore, the different plane spacing of a material can be identified. Typically, the evaluation procedure consists of an alignment of library data and the measured diffractograms to specify the material at hand. It must be mentioned that XRD is a bulk sensitive method, depending on

the material of the sample, incident angle and X-Ray source the penetration depth of the radiation is in the range from 2 - 160 µm.[154]

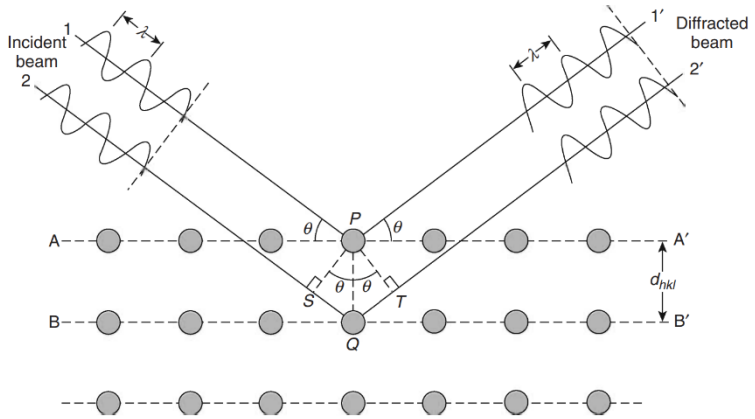

Figure 21 X-ray diffraction on parallel crystallographic planes graphically emphasizing Bragg's law. Reproduced from Leng et al..[154]

The XRD device used in this work is a Bruker D8 Discover GADDS with an CuK_{α} X-ray source. The measurements were conducted in the *Bragg-Brentano arrangement* of the device. An exemplary diffractogram of the precipitated tin catalyst is depicted in Figure 22. To properly analyze the crystalline structure of the catalyst, the precipitation was performed without a carbon support to improve the signal to noise ratio for the material of interest. The diffractogram reveals that SnO_2 is the present species in the bulk phase.

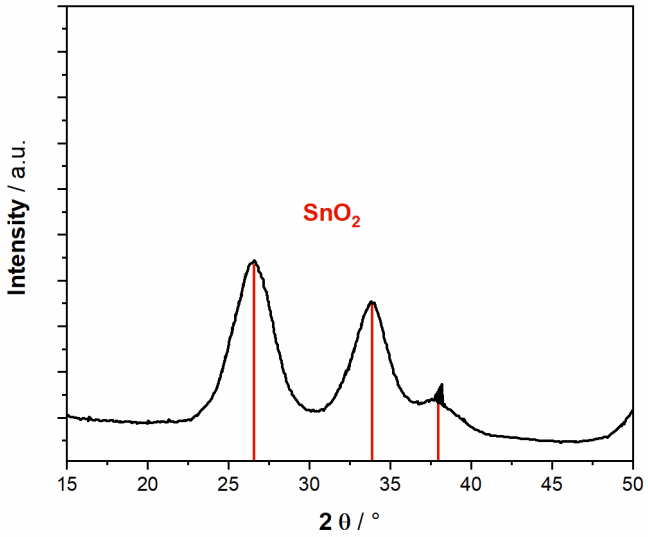

Figure 22 Exemplary diffractogram for the precipitated tin catalyst without carbon support.

5.2.4 X-ray photoelectron spectroscopy

X-ray photoelectron spectroscopy (XPS) is a powerful tool to characterize the nature of a species at the surface of a sample. The basic principle of XPS is illustrated in Figure 23: An incident X-ray photon - with an energy of hν - hitting the surface of a sample can knock out electrons from the inner shell of the present elements. Typically, the emitted electrons have a low energy of 20 - 2000 eV (which is the reason why this technique is surface sensitive, depth information < 10 nm) and are called X-ray photoelectrons. These photoelectrons are analyzed by a detector in terms of their kinetic energies E_k. With the help of the equation describing the photoelectric effect (cf. (70)), the binding energies E_b of the surface species can be correlated with the measured kinetic energies E_k and the energy of the incident beam. The incident beam energy is the product of Planck's constant h and the frequency ν of the X-ray. Φ denotes the work function of the spectrometer and can be calibrated for the specific device.[155]

$$E_b = h \cdot \nu - E_k - \Phi \tag{70}$$

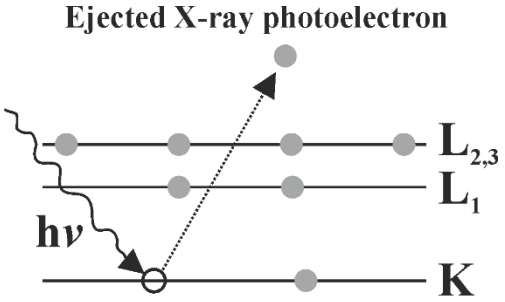

Figure 23 Scheme illustrating the principles of photoelectron generation. Adapted from Leng et al..[154]

A typical plot of an XPS spectrum shows the binding energy on the x-axis and the signal intensity on the y-axis. The observable peaks reveal the element binding energies at the surface which, considering metal and metal oxide catalysts, correlate with the oxidation state of the material. One cannot overemphasize the importance of XPS for catalyst evaluation due to the fact that catalyzed electrochemical processes take place at the electrodes surface and not in the bulk phase. Therefore, operando XPS can be used to characterize the catalytic active species at the surface which often differs from the bulk material.[155]

The surface of the Sn-based GDE was analyzed with XPS using a Thermo Scientific ESCALAB 250 ultra-high vacuum (1 x 10^{-9} bar base pressure) X-Ray photoelectron spectrometer with an Al K (alpha) source (Thermo Scientific XR4). The XPS spectrum (cf. Figure 24) reveals that

SnO_x and not Sn (0) is the present species at the GDEs surface. It must be mentioned that because of the proximity of the binding energies (SnO: $Sn3d_{3/2}$ = 494.7 eV, $Sn3d_{5/2}$ = 486.3 eV ; SnO_2: $Sn3d_{3/2}$ = 495.4 eV, $Sn3d_{5/2}$ = 486.9 eV)[156, 157] and the available resolution of the XPS at hand, it was not possible to distinguish between Sn (+I) and Sn (+II) - oxide. Furthermore, the measurement was not performed during operation of the GDE in which the surface species is very likely partially reduced to metallic tin at the applied negative potentials.[47] The carbon and fluorine signal are caused by the acetylene black support respectively PTFE which was used as binder in the GDE manufacturing process.

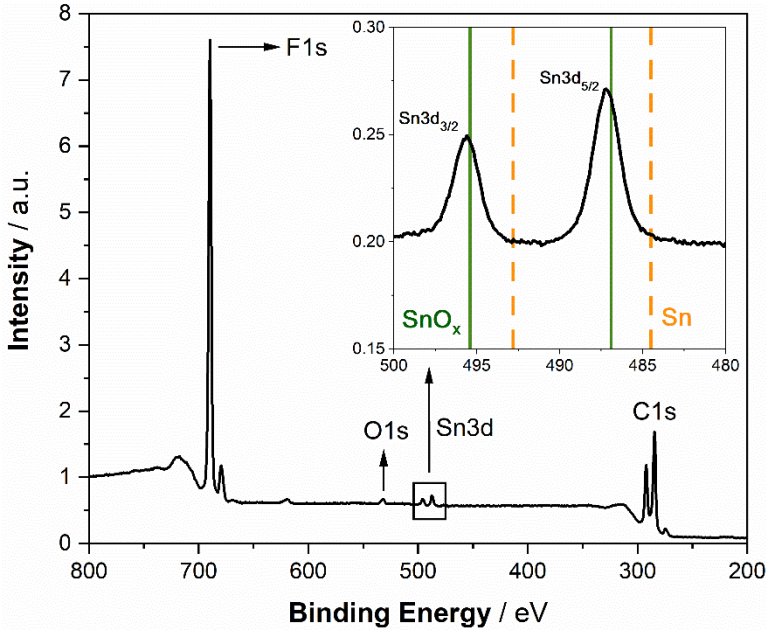

Figure 24 XPS spectrum of the Sn-based GDE revealing that SnO_x and not Sn (0) is the present species at the catalyst surface before operation.[112]

5.2.5 Mercury intrusion porosimetry

As it was shown in 4.4 the porous architecture of a GDE is of utmost importance for a properly working electrode. Therefore, mercury intrusion porosimetry (MIP) is widely accepted to characterize porous architectures containing meso (d = 2 nm - 50 nm, measurable down to 3.6 nm) and macropores (d > 50 nm).[158] Usually, the pore size distribution and the cumulative pore volume are of interest, the latter one can be measured via MIP and used to calculate the pore size distribution. The principle of MIP was first postulated in 1921 by Edward Washburn. He stated that the required pressure for mercury to penetrate into a porous material is inverse

proportional to the pore radius. For the assumption of cylindrical pores and a non-wetting fluid, the following equation can be used to calculate the smallest radius r_{min} of pores which can be filled at the applied pressure p:[159]

$$r_{min} = -\left(\frac{2 \cdot \gamma_{LV}}{p}\right) \cdot \cos(\theta_{SL}) \tag{71}$$

γ_{LV} represents the surface energy for the liquid / vapor interface of mercury while θ_{SL} denotes the contact angle between liquid mercury and the solid sample. It is crucial that mercury does not spontaneously imbibe into the porous sample ($\theta_{SL} > 90°$) so that the intruded mercury volume (for constant γ_{LV} and θ_{SL}) only depends on the applied pressure. Typically, 484 mN m^{-1} is assumed for γ_{LV} while 140° is used for θ_{SL}. It must be mentioned that θ_{SL} depends on the material's surface roughness and composition and is usually not measurable for each specific sample. For this reason, a standard value of 140° for θ_{SL} is assumed for the calculation of r_{min}.[158]

In principle, a change of the observable mercury volume induced by penetration into the porous sample is measured versus a step-wise increase of the applied pressure (0.003 - 400 MPa). With this information, the cumulative pore volume can be plotted versus the applied pressure or when using (71) versus the pore radius respectively diameter. Due to the large range of pore diameters, it is useful to plot the calculated diameter on a logarithmic (decadic) scale. The differential quotient $\Delta V \, (\Delta \log_{10}(d))^{-1}$ yields the pore size distribution which is of high interest in GDE engineering.[158] A typical MIP plot for the manufactured Sn-based GDE is depicted in Figure 25 and reveals the necessary bimodal pore size distribution as stated in 4.4. A pore size regime at ~ 4 µm and 90 nm was observed. Additionally, the existence of mesopores (< 50 nm) can be seen in the plotted data.

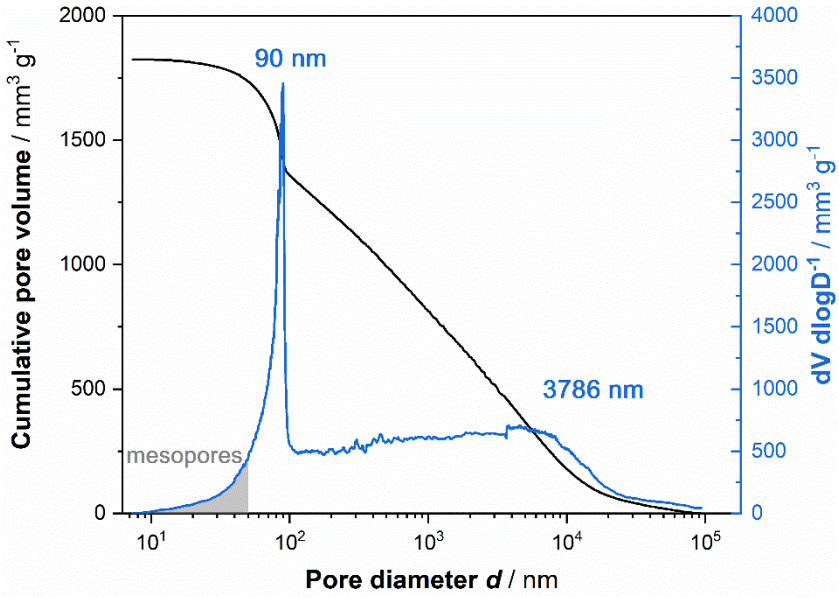

Figure 25 Mercury intrusion porosimetry for a Sn-based GDE revealing a bimodal pore size distribution and the existence of mesopores.

5.3 Reaction product quantification

Due to the parallel occurring reactions in electrochemical CO_2 conversion (cf. 2.1), it is necessary for a GDE performance evaluation to quantify the fraction of the total introduced charge which is used to produce the desired product. This fraction is called Faraday efficiency (FE), i.e., FE CO denotes the fraction of charge which was used to produce CO referring to the total introduced charge into the system. The total introduced charge depends on the applied current and polarization time and can be calculated via (27) for constant current. Furthermore, (27) can be used to derive a theoretical molar flow for a reaction with z transferred electrons. To calculate the FE, it is necessary to determine the amounts of the observed reaction products. For the gas-phase products (H_2, CO) gas chromatography (GC) was used while the liquid product ($HCOO^-$) was quantified via high performance liquid chromatography (HPLC). A brief explanation of the quantification methods is provided below.

5.3.1 Gas chromatography

A GC is used to separate the reaction gas into its components and subsequently quantify the amount of a component in the gas mixture. The underlying phenomenon for the separation of the components is the distribution of the analyte in two immiscible phases. In the case of GC, these two phases are the gaseous phase and the solid phase. The mobile gas phase contains the analyte and is injected into the GC with subsequent flowing through the stationary solid phase,

a capillary column. The equilibrium concentration of the analyte in both phases will be determined by the equilibrium constant of the distribution equilibrium:[160]

$$K = \frac{c_{i,stationary}}{c_{i,mobile}} . \tag{72}$$

A strong interaction of the analyte with the stationary phase (high $c_{\mathrm{i,stationary}}$) will lead to a retarded flow of a specific component relative to the flow of the mobile phase through the stationary phase. Miscellaneous components interact in a varying extent with the stationary phase which will result in different retention times for each specific component. The extent to which a component interacts with the stationary phase depends on several parameters, i.e., nature of the analyte component, material of the column etc. Typically, the careful selection of the column material is the key process to solve a separation problem. The fine-tuning of the separation process is conducted by adjusting the pressure or temperature inside the column. The dependence of the distribution equilibrium constant on the temperature can be described with the Van't Hoff equation and points out that the retention time of the analyte can be manipulated by adjusting the temperature: [160]

$$\left(\frac{\partial \ln K}{\partial T}\right) = \frac{\Delta H}{R \cdot T^2} \tag{73}$$

The quantification of the separated components in the mobile phase at the end of the column is in the used device realized by a thermal conductivity detector. In the obtained chromatogram, the detector's signal is plotted versus the time. Due to the different retention times of the components the chromatogram contains several signal peaks. A calibration of the GC with external standards containing the analytes of interest is necessary to get quantitative results. Commonly, the calibrated amount is correlated with the peak area of the peak at the component's retention time. In an analysis run, the obtained peak areas of the sample with unknown quantitative composition is then used to calculate the concentration of each component.

With the measured concentrations β (in vol%) of the gas phase products and the total exhaust gas volume flow leaving the electrolyzer, the partial volume flow of each component can be quantified as:

$$\dot{V}_{i,exp.} = \dot{V}_t \cdot \beta_i \tag{74}$$

The theoretical flow of the component *i* is calculated by a combination of Faraday's (27) and the ideal gas-law, yielding:

$$\dot{V}_{i,theor.} = \frac{R \cdot T \cdot I}{p \cdot z \cdot F} \tag{75}$$

Finally, the FE for the component *i* is then calculated as:

$$FE_i = \frac{\dot{V}_{i,exp.}}{\dot{V}_{i,theor.}} \tag{76}$$

The device used in this thesis was a Varian® µ-GC equipped with a thermal conductivity detector and two molecular sieves (5 Å). The channel containing a molecular sieve using helium as mobile phase was used to quantify CO whereas the channel with the molecular sieve operated with argon was used to quantify hydrogen. Theoretically, both components would be detectable on the same column but due to the close proximity of the thermal conductivity of hydrogen and helium, the sensitivity for the hydrogen detection would not be sufficient in the channel using helium as mobile phase.

5.3.2 High performance liquid chromatography

High performance liquid chromatography (HPLC) was performed to quantify the amount of produced formate. Analogously to GC, the liquid phase components are separated in an HPLC and subsequently quantified by means of a calibrated external standard. In contrast to GC, the mobile phase including the analyte is a liquid solvent which flows through the stationary phase. The interaction of the analyte with the stationary phase while flowing through it has two underlying different mechanisms: on the one hand, the separation can be based on an adsorption process in which the components are separated due to their varying ad- and desorption characteristic on the columns surface. On the other hand, the components can be separated via an absorption process which is comparable to the separation process in GC and includes a change of phase of the analyte. Due to the different extent of component retardation via one of the above-mentioned mechanisms, the mixture is separated and a chromatogram is obtained. Typically, the choice of the stationary- and mobile phase as well as the applied volume flow of

the mobile phase are optimization parameters to solve the separation problem. As mentioned above, the concentration c_i of the separated components can be determined after the device was calibrated with an external standard of the components of interest.[160]

During electrolysis experiments, samples were taken at the in- and outlet of the electrolyzer to determine the respective concentrations of formate. The produced molar flow of the component of interest, formate, can be calculated using the measured concentrations and the catholyte flow rate:

$$\dot{n}_{i,exp.} = \dot{V}_{catholyte} \cdot \left(c_{i,outlet} - c_{i,inlet}\right) \tag{77}$$

The ratio of the experimental and theoretical (calculated with (27)) molar flow rate yields the FE:

$$FE_i = \frac{\dot{n}_{i,exp.}}{\dot{n}_{i,theor.}} \tag{78}$$

A HPLC 1260 Infinity II system from Agilent Technologies was used in this thesis. The system consisted of a quaternary pump, auto sampler, column oven and a refractive index detector which was used to quantify the analyte by measuring the changes in the refractive index of the analyte loaded mobile phase referenced to the refractive index of the pure mobile phase. Aqueous 0.005 M H_2SO_4 was used as a mobile phase with a flow rate of 0.6 mL min^{-1} while an Agilent Technologies Hi-Plex H column with a diameter of 6.5 mm was chosen as stationary phase and operated at 60 °C. This column contained sulfonated cross-linked styrene / divinylbenzene gel.

5.4 Electrochemical methods

5.4.1 Linear sweep voltammetry

Linear sweep voltammetry (LSV) is a basic potential sweep method which was reported in 1938 by Randles and Sevcik.[161] The principle of LSV measurements will be explained on the basis of a scheme depicted in Figure 26 which was reproduced from Bards famous textbook.[114]

A simple reaction of anthracene which takes up an electron to form an anion radical is considered:

$$A + e^- \underset{k_{ox}}{\overset{k_{red}}{\rightleftharpoons}} A^{*-} \tag{79}$$

At the initial potential E_i, the resulting current is zero. The potential is then linearly swept with a constant sweep-rate of v which can range from 0.1 mV s^{-1} up to 1000 V s^{-1} (cf. Figure 26 a)). Up to the potential $E^{0'}$ only non-faradaic current, so-called capacitive current, is measurable which is evoked by the time-dependent change of the excess charge at the surface of the electrode. The potential is further moved beyond $E^{0'}$ and a flow of a faradaic current as a result of the reduction of anthracene can be observed (cf. Figure 26 b)). An increasing potential will result in an increase of the faradaic current due to the provided enhanced driving force (cf. (28)) up to the point where a peak current is achieved. Now it is important to consider the concentration profile of anthracene in the vicinity of the electrode (cf. Figure 26 c)): the anthracene concentration will decrease due to the consumption during the reaction whereas the anion radical concentration will increase. At a specific current - the peak current - the mass transport of anthracene from the bulk to the vicinity of the electrode cannot keep up with the reaction rate and an educt depletion at the electrode's surface will be observed with ongoing time / potential sweep. This depletion will reduce the surface concentration and the resulting current will decrease.[114, 115]

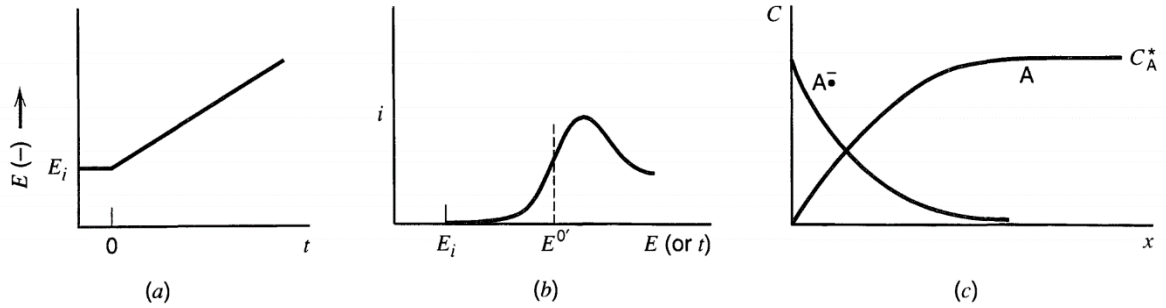

Figure 26 Illustration of the LSV method: a) linear potentials sweep with time, starting at $t = 0$. b) resulting potential and time-dependent current. c) concentration profile of the reaction's educt and product. Figure reproduced from Bard.[114]

The correlation between the capacitive current I_c and the applied sweep rate v is of high practical significance. As it can be seen from (80), a measurement series for varying sweep-rates can

lead to the differential double layer capacitance via a plot of the resulting capacitive currents vs. sweep-rates. As stated in 4.3, the C_d value can be correlated with the ESCA and provides valuable information about the wetted surface area.

$$i_c = C_d \cdot \frac{dE}{dt} = C_{dl} \cdot \nu \tag{80}$$

However, LSVs are mainly used to determine the reactivity of an electrode. A high current density at low applied overpotential is desired. The resulting current density of different electrodes at a defined overpotential or vice versa is taken as an evaluation parameter. It must be mentioned that the expressiveness of LSVs in CO_2 electrolysis is very limited. The measured current is the sum of all CO_2RR reactions and the parasitic HER. The partial current densities of the reactions are more meaningful and can be calculated as the product of the total current density with the faradaic efficiency for the reaction product of the desired reaction at the specific potential. Furthermore, the postulated occurrence of a peak (cf. Figure 26 b)) will not be observed in LSVs due to the excess availability of water which is the educt for HER. The mass transport limitation of CO_2 cannot be observed when solely looking at an LSV due to the replacement of the decreasing partial CO_2RR current with an increasing partial HER current. The mass transport limitation of CO_2 is only noticeable in a decreasing FE for CO_2EL reaction products and an increasing FE for H_2.

5.4.2 Electrochemical impedance spectroscopy

Electrochemical impedance spectroscopy is a powerful advanced electrochemical characterization method to identify the nature and quantify the extent of occurring loss-resistances during operation of an electrochemical device. It is obvious that electrochemical devices dealing with currents and potentials can also be described in terms of resistances. These loss-resistances correlate with the corresponding overpotentials and can be used to rate the velocity of a single sub-process, i.e., charge transfer or mass transport. The knowledge of the magnitude of a specific loss-resistance is a valuable information since it can be used as a guidance for a targeted optimization of the electrochemical device. Furthermore, a time-dependent evaluation of the loss-resistances can yield important information about degradation processes, i.e., an increasing charge transfer resistance (= increasing activation overpotential η_{ac}) with time indicates catalyst alteration. This valuable information points out that the catalyst has to be optimized.[162]

The principle of EIS will be explained on the basis of Figure 27 which depicts a typical current voltage relationship of a cathode during electrolysis:

Considering the operation of a working electrode at a stationary state marked as direct current (DC) operation point. Depending on the parameter which is controlled to be constant, the operation mode is called potentiostatic (E = const.) or galvanostatic (j = const.). The EIS principle is the same for both types of operation, thus the further explanation will exemplarily consider potentiostatic EIS. The system, which is in a stationary state, will be disturbed and excited by a sinusoidal change of the potential (cf. (81)) with a specific frequency (cf. Figure 27) which will result in a phase shifted sinusoidal answer (cf. (82)) of the resulting current (cf. Figure 27). It is of utmost importance that the excitation due to the alternating potential will result in the same amount of change of current for both directions of perturbation. However, the impedance Z, as resistances in alternating current circuits are called, can be calculated analogously to Ohm's law as the fraction of voltage and current (cf. (83)), and therefore describe the slope of the E - j curve at the specific point of operation. It cannot be stressed enough that the slope of the curve is a complex partial derivate of the underlying physical processes affecting the E - j curve. [108, 114]

$$E(t) = E_0 \cdot \sin(\omega \cdot t) \tag{81}$$

$$I(t) = I_0 \cdot \sin(\omega \cdot t + \Phi) \tag{82}$$

$$Z(\omega) = \frac{E(t)}{I(t)} = \frac{E_0}{I_0} \cdot e^{(i \cdot \Phi)} = |Z| \cdot e^{(i \cdot \Phi)} = Z_{Re} + i \cdot Z_{Im} \tag{83}$$

ω represents the angular frequency, Φ is the phase shift between the waves of the excitation and resulting signal while i denotes the imaginary unit. It can be seen that the total impedance contains a real and imaginary part. Ohmic resistances affect the value of the real part while i.e., capacitive or inductive contributions of the impedance are represented in the imaginary part.

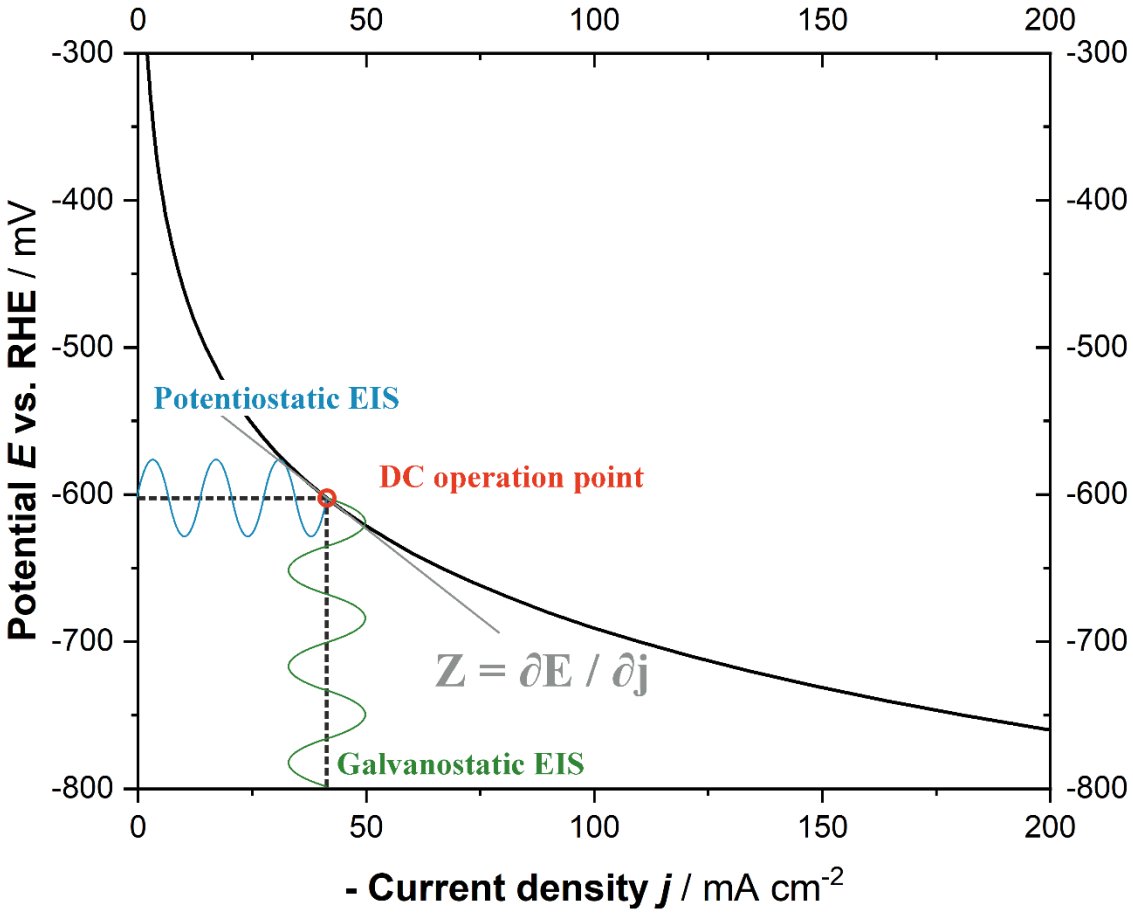

Figure 27 Schematic representation of the principles of EIS.

An impedance measurement at a single frequency is not very meaningful since the measured impedance value contains information on all processes occurring at this specific and higher frequencies. To get information about the specific underlying processes and to separate them from each other, the impedance measurement is repeated in a wide range of frequencies to obtain an impedance spectrum. Impedance spectra are commonly plotted in the Bode form (cf. Figure 28 a)) which is $|Z|$ (y_1 axis) and phase shift (y_2 axis) vs. logarithm of the frequency f (not angular) or in the Nyquist (cf. Figure 28 b)) representation where Z_{Im} is plotted vs. Z_{Re}.

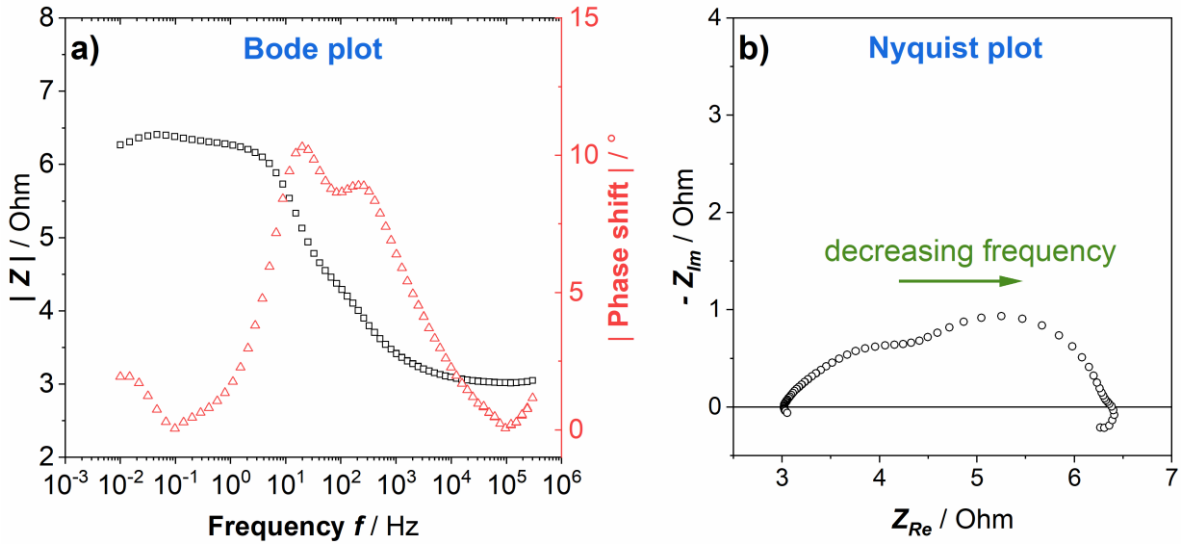

Figure 28 a) Bode and b) Nyquist representation of an impedance spectrum.

The exploited phenomenon is exemplarily depicted in Figure 29 for the operation of a fuel cell: every single process which is involved during the operation possesses a specific time-constant which can, i.e., for a charge transfer process be interpreted as the rate constant of the reaction. It is well known that frequency is the reciprocal time, and therefore, point out how the frequency dependent impedance measurement can be correlated with processes at different time scales. The recording of an EIS spectrum starts at high frequencies, the measured impedance value will then be - considering Figure 29 - determined by the double-layer charging of the electrode. When reducing the frequency, the measured impedance contains contributions of the double-layer charging and the charge transfer. Since the contribution of the double-layer was already estimated at higher frequencies it is possible to deconvolute the information at the lowered frequency containing contributions of both processes. This procedure can be continued to low frequencies where, i.e., mass transport in gas- or liquid phase and degradation effects are observed in the impedance spectrum. Typically, EIS devices operate in the frequency range of 1 mHz - 1 MHz.[108, 162] Unfortunately, as it can be seen in Figure 29, the frequency ranges of the processes overlap and it is not possible from a single EIS measurement to safely determine which type of processes affect the measured impedance value. Therefore, it is necessary to perform a series of experiments varying experimental parameters (*T*, potential, educt concentration, etc.). For example, a diffusion process can be identified by reducing the educt concentration since the mass transport resistance (cf. (52)) increases which will result in a growing impedance value at lower frequencies. These considerations point out the complexity

of EIS: the measurement is simple, but the interpretation is challenging. The first step must always be to identify the underlying processes in the EIS spectrum at the desired operation point. Therefore, as mentioned above, a series of experiments is necessary to get a clue of the nature of the observed processes.

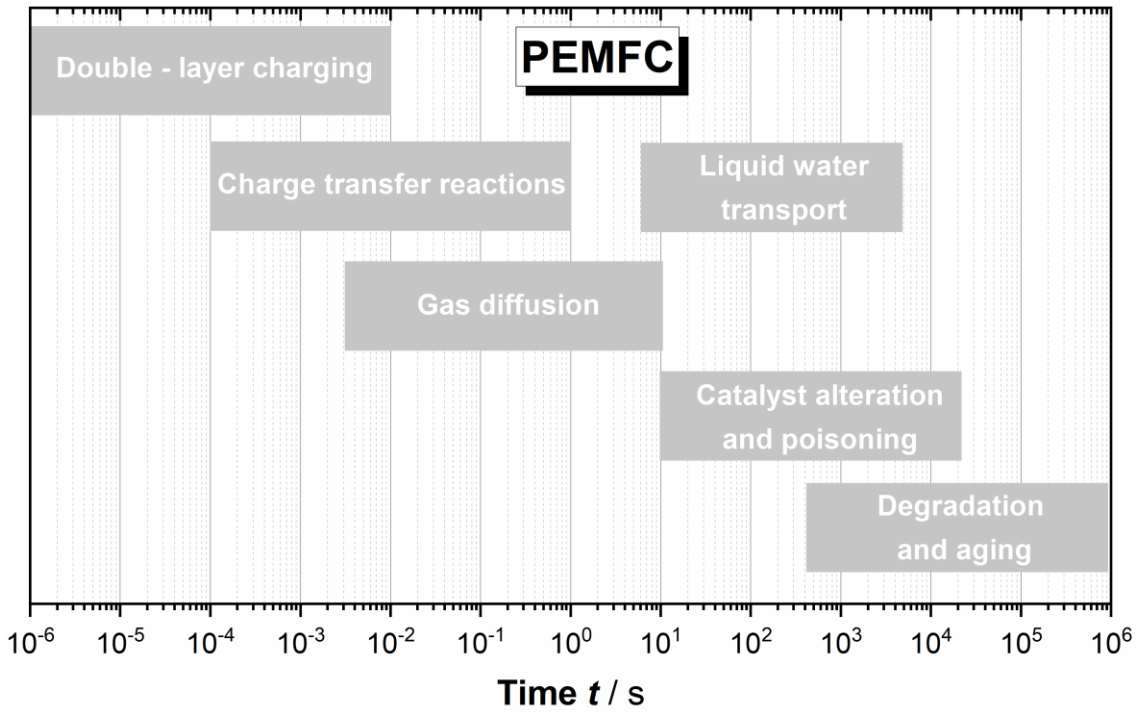

Figure 29 Exemplary time-constants in PEMFC for the occurring microscopic processes. Figure adapted from Friedrich et al.[163]

The quantitative information of the EIS spectrum is usually evaluated via equivalent circuit modelling (EQCM): The measured spectrum is fitted to an equivalent circuit which commonly consists of resistors, capacitors and inductors. The components can be connected in serial and parallel configurations and yield an equation describing the equivalent circuit. Unfortunately, the corresponding equivalent circuit which is able to describe the measured spectrum is not necessarily unique. To get a meaningful equivalent circuit the underlying processes should be already known. The chosen equivalent circuit should be as simple as possible due to the fact that with increasing components in the equivalent circuit the number of fitting parameters increases which naturally increases the quality of the fit. The most relevant equivalent circuit components will be presented below.

Resistor:

Electric conductivity of the electrolyte or inside the electrode is typically modelled with a resistor while the impedance of a resistor is simply the value of the ohmic resistance. There is no observable time dependence:

$$Z_R = R \tag{84}$$

Inductor:

Inductive effects occur at high frequencies (kHz), i.e. due to the current flow in the connection cables. Twisting the current carrying cables can reduce the extent of this undesired effect. The phase angle has a value of + 90°. Thus, the impedance can be calculated as (L = Inductance):

$$Z_I(\omega) = i \cdot \omega \cdot L \tag{85}$$

Capacitor:

The capacitor is used to describe the time-dependent behavior of the impedance as a result of, i.e., charging the double-layer at the electrode - electrolyte interface. It is assumed that the double-layer at the electrodes surface behaves like a parallel plate capacitor with the capacitance C. The phase angle has a value of - 90°.

$$Z_C(\omega) = \frac{1}{i \cdot \omega \cdot C} \tag{86}$$

Constant phase element (CPE):

In reality, classic capacitors fail to describe the capacitive behavior of the investigated electrodes. This is due to irregularities of the electrode's surface, roughness of the electrode leading to a dispersion of time-constants along the electrode. This phenomenon was experimentally discovered since the capacitance of a real electrode is not a vertical line but has a slope indicating that the phase angle is not constantly - 90°. The CPE can be described via the following equation:[108, 162]

$$Z_{CPE}(\omega) = \frac{1}{Q \cdot (i \cdot \omega)^{\alpha}} \tag{87}$$

Q is the value of the admittance and α is the constant phase exponent which can take values between 0 and 1. For $\alpha = 1$, the electrode's surface behaves like an ideal capacitor. It must be mentioned that Q is not equal to the interfacial capacitance which is often of interest due to its correlation with the ECSA. Brug et al. suggested that the Q value for an ideal polarizable electrode can be transferred to a meaningful interfacial capacitance according to:[164]

$$C = \sqrt[\alpha]{\frac{Q}{R_{\Omega}^{(\alpha-1)}}} \tag{88}$$

R_{Ω} denotes the sum of the ohmic resistances recognizable at $\omega \rightarrow \infty$.

R - CPE element:

Commonly, a parallel combination of a resistor and CPE element are used as one equivalent circuit component to describe a time-dependent microscopic process. All impedance spectra which fulfil the Kramers - Kronig relation can always be described by a connection of n R - CPE elements.[165, 166] Consequently, this means that EIS spectra can always be fitted by a serial combination of n R - CPE elements. As already mentioned, by increasing n unsurprisingly the quality of the fit of the model will be better due to the higher number of fitting parameters. On the other hand, each R - CPE element corresponds to one time-constant and by that to one physical process indicating that choosing the value for n should be conducted very cautiously regarding a realistic number of underlying processes. The R - CPE element can be described via:[108]

$$Z_{R-CPE}(\omega) = \frac{R}{1 + (i \cdot \omega \cdot R \cdot Q)^{\alpha}} \tag{89}$$

Porous electrode:

Electrochemical processes often take advantage of porous electrodes because of the tremendous provided surface area. The distribution of the local current and potential inside the porous electrode is not uniform due to the geometry of the pores and will result in a time-constant dispersion affecting the impedance spectrum. Furthermore, not just the geometry of the pores but also the surface concentration gradients along the pore length will lead to an additional distribution of the local current and potential inside the GDE along the pore length. Commonly, this time-constant dispersion is mathematically described by transmission line models which

consider gradients of resistances and capacitances inside the porous GDE.[108, 109, 162] Depending on the assumed pore geometries and boundary conditions regarding current flow, electrolyte and electrode conductivity and origin of the processes occurring inside the porous system (charge transfer reaction or solely double-layer charging) a variety of models exists. A typical equivalent circuit for a transmission line model adapted from Göhr[167] is depicted in Figure 30. The illustration emphasizes that the total impedance of the porous electrode is composed of impedance contributions by:[108, 167]

Z_e: outer surface layer of the porous electrode

Z_m: ground surface of the porous electrode

Z_p: electrolyte resistance inside the pore

Z_s: electrical resistance of the porous electrode

Z_q: surface processes occurring at the pore walls

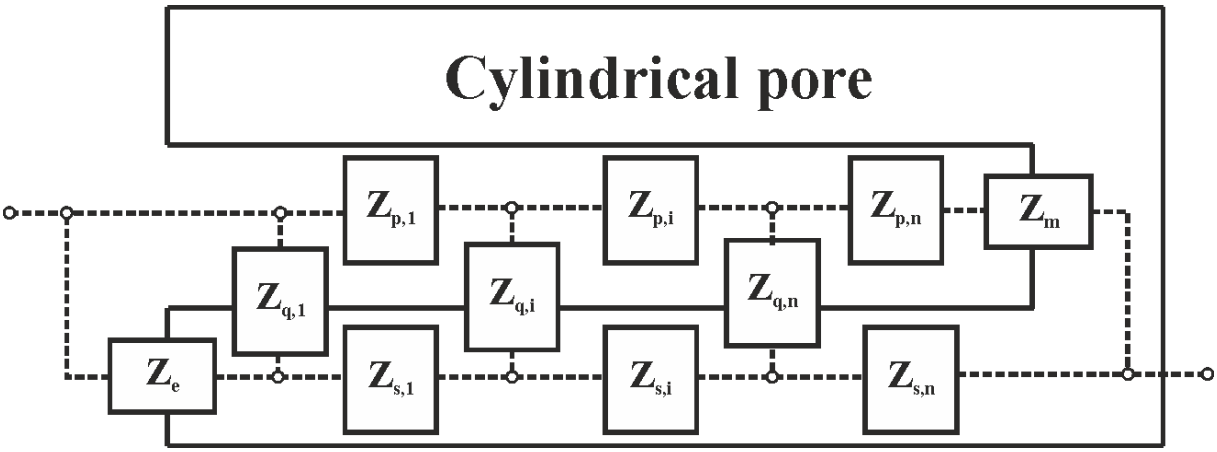

Figure 30 Illustration of a transmission line model for a cylindrical pore. Adapted from Göhr.[167]

The special case of a blocking outer and ground surface layer (Z_e & $Z_m \rightarrow \infty$) with additional neglection of either the impedance evoked by the limited conductivity of the electrodes bulk phase ($Z_s = 0$) or electrolytes conductivity inside the pore ($Z_p = 0$) can be described with (90) or (91). Z_q denotes the impedance at the pore walls which is often assigned to an R - CPE element describing the charge transfer inside the porous system. These equations are used in the evaluation software Thales® from ZAHNER-Elektrik GmbH & CoKG which potentiostats were used in this thesis.[167]

$$Z_{porous} = \frac{(Z_p \cdot Z_q)^{\frac{1}{2}}}{\tanh\left[\left(\frac{Z_p}{Z_q}\right)^{\frac{1}{2}}\right]} \tag{90}$$

$$Z_{porous} = \frac{(Z_s \cdot Z_q)^{\frac{1}{2}}}{\tanh\left[\left(\frac{Z_s}{Z_q}\right)^{\frac{1}{2}}\right]} \tag{91}$$

6 Conclusions and Outlook

6.1 Conclusions

This cumulative doctoral thesis consists of four peer reviewed research articles and contributes to the understanding of the degradation of tin- and bismuth-based gas-diffusion electrodes (GDEs) which are employed in alkaline CO_2 electrolysis to generate formate. Electrochemical impedance spectroscopy (EIS) was identified as a powerful operando characterization method to ascribe the degradation to specific microscopic processes. For that reason, elaborated EIS studies on tin foil and tin-based gas-diffusion electrodes were conducted to carefully interpret which processes determine the shape of the impedance spectra. This cautious analysis is challenging but mandatory before using EIS for degradation studies. Following, the generated knowledge was used for the investigation of tin- and bismuth-based GDEs via EIS. Apart from that an additional field of application for the usage of the obtained formate solution was encountered: in a proof of concept study formate was used as an energy carrier for the re-electrification in a direct formate fuel cell (DFFC) or polymer electrolyte membrane fuel cell (PEMFC) after decomposition to H_2. The main findings reported in the four articles are summarized below:

Article I:

The impedance spectrum of tin foil electrodes operated in $KHCO_3$ aqueous solutions yield two observable processes. While the process in the low frequency region cannot be assigned with certainty, our results suggest that the ionic movement of HCO_3^- is described in this time domain. The high frequency process is determined by a charge transfer reaction which contains inseparable information about the CO_2 reduction reaction (CO_2RR) and the parallel occurring parasitic hydrogen evolution reaction (HER). The reasonability of this conclusion was supported by equivalent circuit modelling which predicts that two charge transfer processes happening simultaneously at the same surface will lead to only one observable process in the impedance spectrum. Finally, this means that for tin foil electrodes (intermediate Faraday efficiencies (FE) for HER and CO_2RR) EIS cannot be used to evaluate a specific reaction, due to the superposition of the contributions of HER and CO_2RR. Interestingly, kinetic isotope experiments suggested that the observed charge transfer includes a proton transfer since the corresponding resistance increases when using D_2O instead of H_2O as solvent. This fact indicates that the charge transfer might be mainly determined by the HER since it is widely

accepted that in CO_2RR the electron transfer onto CO_2 to form $CO_2^{\bullet -}$ is the rate-determining step and does not involve a proton.

Article II:

Tin-based gas-diffusion electrodes were operated in aqueous 1.0 M KOH. An elaborated EIS study was conducted by varying several parameters such as temperature, CO_2 volume fraction, current density and electrolyte. Four underlying microscopic processes were suggested to determine the shape of the impedance spectrum, listed in descending velocity: ionic and electronic conductivity inside the porous GDE, homogeneous reaction of CO_2 with OH^- to form bicarbonate, charge transfer from the electrode onto CO_2 to form $CO_2^{\bullet -}$, liquid phase diffusion of CO_2. The exact specification of the charge transfer was achieved by kinetic isotope experiments which suggested that no proton is involved during the charge transfer reaction. Interestingly, it was shown that the spectrum was mainly determined by CO_2RR and that the shape determining reaction can change when applying unfavorable conditions. In particular, when changing the CO_2 volume fraction to values below 20 vol%, the characteristic shape of the spectrum changes and surprisingly the polarization resistance decreases which can only be explained by a switch of the spectrum determining reaction towards the HER. This hypothesis was supported by the observation that the new spectrum shape looked like a spectrum obtained for the same electrode operating with N_2 where the HER is the sole observable reaction.

Article III:

The provided knowledge of the above described EIS investigations was used to characterize the degradation of tin- and bismuth-based GDEs in aqueous 1.0 M KOH. Therefore, EIS was used to monitor the degradation with a specific focus on electrodes wetting and catalyst leaching. The wetting of the GDE was monitored in terms of differential double layer capacitance which is proportional to the wetted surface area and could be - due to the investigations of foregoing work (**Article I + II**) - extracted from the EIS spectra. Additionally, post mortem characterization of GDEs via SEM EDX was used to reveal progressing time-dependent wetting of the GDEs. However, it could be shown that for tin-based GDEs the alteration induced by wetting cannot be quantified because of an observable superimposed catalyst leaching. Consequently, catalyst leaching was identified as a degradation process but simultaneous degradation due to GDE flooding cannot be excluded. Finally, a bismuth-based GDE was used as a promising alternative catalyst material considering its thermodynamic stability according

to the Pourbaix diagram. Indeed, no bismuth leaching was detected, but a slight degradation could be observed. This degradation might be assigned to an ongoing wetting of the electrode or a catalyst aggregation induced by a dissolution / redeposition mechanism resulting in no net bismuth loss but reduction of accessible catalyst surface.

Article IV:

Herein, an additional field of application for formate solutions generated via CO_2 electrolysis was demonstrated in a proof of concept study. Therefore, the obtained solution was transferred into a DFFC and successfully re-electrified. The poor numerical results were attributed to a non-optimized fuel cell system and lower operation temperatures. Another successfully demonstrated approach was the re-electrification via PEMFC after formate was decomposed to H_2 in an autoclave using a carbon supported palladium catalyst.

6.2 Outlook

The shown evaluation of impedance spectra helps to understand the degradation of CO_2 converting GDEs. In future works, it should be tested if the suggested interpretation, assignment of microscopic process to features observed in the impedance spectrum, can be transferred to different electrode compositions, architectures and extended operation conditions to identify the limitations of the proposed interpretation of EIS spectra. Furthermore, it would be interesting to pass the knowledge of the advised processes to physical (non-equivalent circuit-based modelling) impedance spectra modelling to check if the results are in good agreement. However, as stated in **Article III** of this cumulative thesis, EIS can be employed as a powerful operando characterization method to monitor the degradation of the investigated cathode. In general, besides evaluating catalyst stability special attention regarding the investigation of degradation phenomena should be paid to two additional phenomena. Firstly, flooding of the electrode which impedes facile CO_2 supply. Secondly, the precipitation of carbonate salts (reaction CO_2 with OH^-) which block the pore system and increase the GDEs wetting which both lead to an altered CO_2 transport to the active sites. The undesired conversion of CO_2 with OH^- is a natural constituent when using alkaline electrolytes, alternatively, acidic CO_2 electrolysis can be a remedy for this issue and consequently should attract the focus of researchers besides the drawback of high accessibility of protons which is beneficial for the parasitic HER.

Moreover, the degradation study of tin- and bismuth-based GDEs indicated that bismuth is a promising catalyst material which can, at least for the tested times of operation, surpass the

performance of tin while simultaneously indicating a less distinct degradation. Therefore, the bismuth-based GDE should be investigated more intensively with a focus on long-term operation.

In general, while it is already possible to achieve outstanding performance parameters such as, current densities of 1.8 A cm^{-2} at Faraday efficiency of ~ 70 % for the conversion of CO_2 to formate, the used set-ups are almost exclusively not optimized to reduce the total voltage drop and the operation times are quite short (< 30 h). Therefore, promising electrodes like the demonstrated bismuth-based GDE should be tested in optimized full cell set-ups and longer durations to get more insights about the full cell performance and possible occurring electrode or system degradation. These investigations are mandatory for the commercialization of CO_2 electrolyzers.

7 Bibliography

1. Joos, F.; Spahni, R., *Proc. Natl. Acad. Sci. U.S.A.* **2008**, *105* (5), 1425, doi: 10.1073/pnas.0707386105.
2. Dlugokencky, E.; Tans, P. *Trends in atmospheric carbon dioxide, National Oceanic & Atmospheric Administration*. Earth System Research Laboratory (NOAA/ESRL), **2021**, http://www.esrl.noaa.gov/gmd/ccgg/trends/global.html (accessed 2021.03.14).
3. Ritchie, H. *Sector by sector: where do global greenhouse gas emissions come from?* Global Change Data Lab, **2018**, https://ourworldindata.org/ghg-emissions-by-sector (accessed 2021.03.14).
4. Smith, P.; Davis, S. J.; Creutzig, F.; Fuss, S.; Minx, J.; Gabrielle, B.; Kato, E.; Jackson, R. B.; Cowie, A.; Kriegler, E.; van Vuuren, D. P.; Rogelj, J.; Ciais, P.; Milne, J.; Canadell, J. G.; McCollum, D.; Peters, G.; Andrew, R.; Krey, V.; Shrestha, G.; Friedlingstein, P.; Gasser, T.; Grübler, A.; Heidug, W. K.; Jonas, M.; Jones, C. D.; Kraxner, F.; Littleton, E.; Lowe, J.; Moreira, J. R.; Nakicenovic, N.; Obersteiner, M.; Patwardhan, A.; Rogner, M.; Rubin, E.; Sharifi, A.; Torvanger, A.; Yamagata, Y.; Edmonds, J.; Yongsung, C., *Nat. Clim. Chang.* **2015**, *6* (1), 42–50, doi: 10.1038/nclimate2870.
5. IPCC, Masson-Delmotte, V., P. Zhai, H.-O. Pörtner, D. Roberts, J. Skea, P.R. Shukla, A. Pirani, W. Moufouma-Okia, C. Péan, R. Pidcock, S. Connors, J.B.R. Matthews, Y. Chen, X. Zhou, M.I. Gomis, E. Lonnoy, T. Maycock, M. Tignor, and T. Waterfield (eds.) *Global warming of 1.5°C An IPCC Special Report on the impacts of global warming of 1.5°C above pre-industrial levels and related global greenhouse gas emission pathways, in the context of strengthening the global response to the threat of climate change, sustainable development, and efforts to eradicate poverty*; 2018; p 630.
6. Qiao, J.; Liu, Y.; Zhang, J., *Electrochemical Reduction of Carbon Dioxide: Fundamentals and Technologies*. CRC Press **2016**.
7. Eurostat *Greenhouse gas emissionstatistics - emissioninventories*. **2020**, https://ec.europa.eu/eurostat/statistics-explained/pdfscache/1180.pdf (accessed 2021.03.14).
8. Murdock, H.; Gibb, D.; Andre, T. *Key findings of the Renewables 2020 Global Status Report*. REN21, **2020**, (accessed 2021.03.14).

9. Kibria, M. G.; Edwards, J. P.; Gabardo, C. M.; Dinh, C.-T.; Seifitokaldani, A.; Sinton, D.; Sargent, E. H., *Adv. Mater.* **2019**, *31* (31), 1807166, doi: 10.1002/adma.201807166.
10. Birdja, Y. Y.; Pérez-Gallent, E.; Figueiredo, M. C.; Göttle, A. J.; Calle-Vallejo, F.; Koper, M. T. M., *Nat. Energy* **2019**, *4*, 732–745, doi: 10.1038/s41560-019-0450-y.
11. Masel, R. I.; Liu, Z.; Yang, H.; Kaczur, J. J.; Carrillo, D.; Ren, S.; Salvatore, D.; Berlinguette, C. P., *Nat. Nanotechnol.* **2021**, *16* (2), 118-128, doi: 10.1038/s41565-020-00823-x.
12. Spurgeon, J. M.; Kumar, B., *Energy Environ. Sci.* **2018**, *11* (6), 1536-1551, doi: 10.1039/c8ee00097b.
13. Bierhals, J., Carbon Monoxide. In *Ullmann's Encyclopedia of Industrial Chemistry*, **2001**, doi: 10.1002/14356007.a05_203.
14. Hietala, J.; Vuori, A.; Johnsson, P.; Pollari, I.; Reutemann, W.; Kieczka, H., Formic Acid. In *Ullmann's Encyclopedia of Industrial Chemistry*, John Wiley and Sons **2016;** 1-22, doi: 10.1002/14356007.a12_013.pub3.
15. Bienen, F.; Kopljar, D.; Löwe, A.; Assmann, P.; Stoll, M.; Rössner, P.; Wagner, N.; Friedrich, A.; Klemm, E., *Chem. Ing. Tech.* **2019**, *91* (6), 872–882, doi: 10.1002/cite.201800212.
16. Löwe, A.; Schmidt, M.; Bienen, F.; Kopljar, D.; Wagner, N.; Klemm, E., *ACS Sustainable Chem. Eng.* **2021**, *9* (11), 4213-4223, doi: 10.1021/acssuschemeng.1c00199.
17. Yang, H.; Kaczur, J. J.; Sajjad, S. D.; Masel, R. I., *J. CO2 Util.* **2020**, *42*, doi: 10.1016/j.jcou.2020.101349.
18. Nwabara, U. O.; Cofell, E. R.; Verma, S.; Negro, E.; Kenis, P. J. A., *ChemSusChem* **2020**, *13* (5), 855–875, doi: 10.1002/cssc.201902933.
19. Jouny, M.; Luc, W.; Jiao, F., *Ind. Eng. Chem. Res.* **2018**, *57* (6), 2165–2177, doi: 10.1021/acs.iecr.7b03514.
20. Rumayor, M.; Dominguez-Ramos, A.; Perez, P.; Irabien, A., *J. CO2 Util.* **2019**, *34*, 490-499, doi: 10.1016/j.jcou.2019.07.024.
21. Royer, M. E., **1870**, *1870*, 731-732, doi: -.
22. Coehn, A.; Jahn, S., *Berichte der deutschen chemischen Gesellschaft* **1904**, *37* (3), 2836-2842, doi: 10.1002/cber.19040370358.
23. Teeter, T. E.; Van Rysselberghe, P., *Chem. Phys.* **1954**, *22* (4), 759-760, doi: 10.1063/1.1740178.

24. Russell, P. G.; Kovac, N.; Srinivasan, S.; Steinberg, M., *J. Electrochem. Soc.* **1977**, *124* (9), 1329-1338, doi: 10.1149/1.2133624.
25. Hori, Y.; Wakebe, H.; Tsukamoto, T.; Koga, O., *Electrochim. Acta* **1994**, *39* (11-12), 1833-1839, doi: 10.1016/0013-4686(94)85172-7.
26. Kuhl, K. P.; Cave, E. R.; Abram, D. N.; Jaramillo, T. F., *Energy Environ. Sci.* **2012**, *5*, 7050-7059, doi: 10.1039/C2EE21234J.
27. Löwe, A.; Rieg, C.; Hierlemann, T.; Salas, N.; Kopljar, D.; Wagner, N.; Klemm, E., *ChemElectroChem* **2019**, *6* (17), 4497–4506, doi: 10.1002/celc.201900872.
28. Jeong, J.; Kang, J. S.; Shin, H.; Lee, S. H.; Jang, J.; Hyeon, T.; Park, H. S.; Sung, Y.-E., *ChemComm* **2021**, doi: 10.1039/d1cc00927c.
29. Lv, W.; Zhang, R.; Gao, P.; Lei, L., *J. Power Sources* **2014**, *253*, 276 - 281, doi: 10.1016/j.jpowsour.2013.12.063.
30. Daiyan, R.; Lu, X.; Saputera, W. H.; Ng, Y. H.; Amal, R., *ACS Sustainable Chem. Eng.* **2018**, *6* (2), 1670-1679, doi: 10.1021/acssuschemeng.7b02913.
31. Kapusta, S.; Hackerman, N., *J. Electrochem. Soc.* **1983**, *130* (3), 607-613, doi: 10.1149/1.2119761.
32. Ikeda, S.; Takagi, T.; Ito, K., *Bull. Chem. Soc. Jpn.* **1987**, *60* (7), 2517-2522, doi: 10.1246/bcsj.60.2517.
33. Deng, P.; Wang, H.; Qi, R.; Zhu, J.; Chen, S.; Yang, F.; Zhou, L.; Qi, K.; Liu, H.; Xia, B. Y., *ACS Catal.* **2019**, *10* (1), 743-750, doi: 10.1021/acscatal.9b04043.
34. Lv, W.; Zhou, J.; Bei, J.; Zhang, R.; Wang, L.; Xu, Q.; Wang, W., *Appl. Surf. Sci.* **2017**, *393*, 191 - 196, doi: 10.1016/j.apsusc.2016.10.017.
35. Zhang, Y.; Zhang, X.; Ling, Y.; Li, F.; Bond, A. M.; Zhang, J., *Angew. Chem. Int. Ed.* **2018**, *57* (40), 13283-13287, doi: 10.1002/anie.201807466.
36. Köleli, F.; Balun, D., *Appl. Catal. A-Gen.* **2004**, *274* (1-2), 237-242, doi: 10.1016/j.apcata.2004.07.006.
37. Wang, J.; Wang, H.; Han, Z.; Han, J., *Front Chem. Sci. Eng.* **2016**, *9* (1), 57-63, doi: 10.1007/s11705-014-1444-8.
38. Kortlever, R.; Shen, J.; Schouten, K. J. P.; Calle-Vallejo, F.; Koper, M. T. M., *J. Phys. Chem. Lett.* **2015**, *6* (20), 4073-4082, doi: 10.1021/acs.jpclett.5b01559.
39. Dunwell, M.; Luc, W.; Yan, Y.; Jiao, F.; Xu, B., *ACS Catal.* **2018**, *8* (9), 8121-8129, doi: 10.1021/acscatal.8b02181.
40. Daiyan, R.; Lu, X.; Ng, Y. H.; Amal, R., *Catal. Sci. Technol* **2017**, *7* (12), 2542-2550, doi: 10.1039/c7cy00246g.

41. Verma, S.; Kim, B.; Jhong, H.-R. M.; Ma, S.; Kenis, P. J. A., *ChemSusChem* **2016**, *9* (15), 1972–1979, doi: 10.1002/cssc.201600394.
42. Masel, R.; Ni, R.; Liu, Z.; Chen, Q.; Kutz, R.; Nereng, L.; Lutz, D.; Lewinski, K., *Energy Procedia* **2014**, *63*, 7959-7962, doi: 10.1016/j.egypro.2014.11.832.
43. Oloman, C.; Li, H., *ChemSusChem* **2008**, *1* (5), 385–391, doi: 10.1002/cssc.200800015.
44. Chen, Y.; Kanan, M. W., *J. Am. Chem. Soc.* **2012**, *134* (4), 1986–1989, doi: 10.1021/ja2108799.
45. Löwe, A. *Development and investigation of an efficient electrolysis process for the conversion of carbon dioxide to formate.* Dissertation, University of Stuttgart, Stuttgart, **2020**, doi: 10.18419/opus-11462.
46. Dutta, A.; Kuzume, A.; Rahaman, M.; Vesztergom, S.; Broekmann, P., *ACS Catal.* **2015**, *5* (12), 7498–7502, doi: 10.1021/acscatal.5b02322.
47. Lee, S.; Ocon, J. D.; Son, Y.-i.; Lee, J., *J. Phys. Chem. C* **2015**, *119* (9), 4884–4890, doi: 10.1021/jp512436w.
48. Pander, J. E.; Baruch, M. F.; Bocarsly, A. B., *ACS Catal.* **2016**, *6* (11), 7824–7833, doi: 10.1021/acscatal.6b01879.
49. Baruch, M. F.; Pander, J. E.; White, J. L.; Bocarsly, A. B., *ACS Catal.* **2015**, *5* (5), 3148–3156, doi: 10.1021/acscatal.5b00402.
50. Pourbaix, M., *Atlas of Electrochemical Equilibria in Aqueous Solutions*. Pergamon Press **1966**.
51. Zhang, Y.; Chen, L.; Li, F.; Easton, C. D.; Li, J.; Bond, A. M.; Zhang, J., *ACS Catal.* **2017**, *7* (7), 4846-4853, doi: 10.1021/acscatal.7b01305.
52. Cui, C.; Han, J.; Zhu, X.; Liu, X.; Wang, H.; Mei, D.; Ge, Q., *J. Catal.* **2016**, *343*, 257-265, doi: 10.1016/j.jcat.2015.12.001.
53. Wuttig, A.; Yoon, Y.; Ryu, J.; Surendranath, Y., *J. Am. Chem. Soc.* **2017**, *139* (47), 17109-17113, doi: 10.1021/jacs.7b08345.
54. Luc, W.; Collins, C.; Wang, S.; Xin, H.; He, K.; Kang, Y.; Jiao, F., *J. Am. Chem. Soc.* **2017**, *139* (5), 1885-1893, doi: 10.1021/jacs.6b10435.
55. Won, D. H.; Choi, C. H.; Chung, J.; Chung, M. W.; Kim, E.-H.; Woo, S. I., *ChemSusChem* **2015**, *8* (18), 3092-3098, doi: 10.1002/cssc.201500694.
56. Schwarz, H. A.; Dodson, R. W., *J. Phys. Chem.* **1989**, *93* (1), 409-414, doi: 10.1021/j100338a079.

57. Feaster, J. T.; Shi, C.; Cave, E. R.; Hatsukade, T.; Abram, D. N.; Kuhl, K. P.; Hahn, C.; Norskov, J. K.; Jaramillo, T. F., *ACS Catal.* **2017**, *7* (7), 4822-4827, doi: 10.1021/acscatal.7b00687.

58. Koh, J. H.; Won, D. H.; Eom, T.; Kim, N.-K.; Jung, K. D.; Kim, H.; Hwang, Y. J.; Min, B. K., *ACS Catal.* **2017**, *7* (8), 5071-5077, doi: 10.1021/acscatal.7b00707.

59. Zhu, D. D.; Liu, J. L.; Qiao, S. Z., **2016**, *28* (18), 3423-52, doi: 10.1002/adma.201504766.

60. Xing, Z.; Hu, L.; Ripatti, D. S.; Hu, X.; Feng, X., **2021**, *12* (1), 136, doi: 10.1038/s41467-020-20397-5.

61. Wang, X.; Klingan, K.; Klingenhof, M.; Moller, T.; Ferreira de Araujo, J.; Martens, I.; Bagger, A.; Jiang, S.; Rossmeisl, J.; Dau, H.; Strasser, P., *Nat. Commun.* **2021**, *12* (1), 794, doi: 10.1038/s41467-021-20961-7.

62. Mou, S.; Wu, T.; Xie, J.; Zhang, Y.; Ji, L.; Huang, H.; Wang, T.; Luo, Y.; Xiong, X.; Tang, B.; Sun, X., *Adv. Mater.* **2019**, *31* (36), e1903499, doi: 10.1002/adma.201903499.

63. Zhou, Y.; Che, F.; Liu, M.; Zou, C.; Liang, Z.; De Luna, P.; Yuan, H.; Li, J.; Wang, Z.; Xie, H.; Li, H.; Chen, P.; Bladt, E.; Quintero-Bermudez, R.; Sham, T.-K.; Bals, S.; Hofkens, J.; Sinton, D.; Chen, G.; Sargent, E. H., *Nat. Chem.* **2018**, *10* (9), 974-980, doi: 10.1038/s41557-018-0092-x.

64. Verma, S.; Lu, X.; Ma, S.; Masel, R. I.; Kenis, P. J. A., *Phys. Chem. Chem. Phys.* **2016**, *18* (10), 7075-7084, doi: 10.1039/c5cp05665a.

65. Natsui, K.; Iwakawa, H.; Ikemiya, N.; Nakata, K.; Einaga, Y., *Angew. Chem. Int. Ed.* **2018**, *57* (10), 2639-2643, doi: 10.1002/anie.201712271.

66. Jeanty, P.; Scherer, C.; Magori, E.; Wiesner-Fleischer, K.; Hinrichsen, O.; Fleischer, M., *J. CO2 Util.* **2018**, *24*, 454–462, doi: 10.1016/j.jcou.2018.01.011.

67. Kortlever, R.; Tan, K. H.; Kwon, Y.; Koper, M. T. M., *J. Solid State Chem.* **2013**, *17* (7), 1843-1849, doi: 10.1007/s10008-013-2100-9.

68. Vennekötter, J.-B.; Scheuermann, T.; Sengpiel, R.; Wessling, M., *J. CO2 Util.* **2019**, *32*, 202-213, doi: 10.1016/j.jcou.2019.04.007.

69. Song, Y.; Junqueira, J. R. C.; Sikdar, N.; Ohl, D.; Dieckhofer, S.; Quast, T.; Seisel, S.; Masa, J.; Andronescu, C.; Schuhmann, W., *Angew. Chem. Int. Ed.* **2021**, doi: 10.1002/anie.202016898.

70. Zhang, J.; Luo, W.; Züttel, A., *J. Catal.* **2020**, *385*, 140–145, doi: 10.1016/j.jcat.2020.03.013.

71. Ma, M.; Clark, E. L.; Therkildsen, K. T.; Dalsgaard, S.; Chorkendorff, I.; Seger, B., *Energy Environ. Sci.* **2020**, 977-985, doi: 10.1039/D0EE00047G.
72. Zhong, H.; Fujii, K.; Nakano, Y.; Jin, F., *J. Phys. Chem. C* **2015**, *119* (1), 55-61, doi: 10.1021/jp509043h.
73. Harned, H. S.; Scholes, S. R., *J. Am. Chem. Soc.* **1941**, *63* (6), 1706-1709, doi: 10.1021/ja01851a058.
74. Harned, H. S.; Davis, R., *J. Am. Chem. Soc.* **1943**, *65* (10), 2030-2037, doi: 10.1021/ja01250a059.
75. Hori, Y.; Murata, A.; Takahashi, R., *J. Chem. Soc. Faraday Trans.* **1989**, *85*, 2309-2326, doi: 10.1039/F19898502309.
76. Dunwell, M.; Lu, Q.; Heyes, J. M.; Rosen, J.; Chen, J. G.; Yan, Y.; Jiao, F.; Xu, B., *J. Am. Chem. Soc.* **2017**, *139* (10), 3774-3783, doi: 10.1021/jacs.6b13287.
77. Gupta, N.; Gattrell, M.; MacDougall, B., *J. Appl. Electrochem.* **2006**, *36* (2), 161–172, doi: 10.1007/s10800-005-9058-y.
78. Varela, A. S.; Kroschel, M.; Reier, T.; Strasser, P., *Catal. Today* **2016**, *260*, 8 - 13, doi: 10.1016/j.cattod.2015.06.009.
79. Burdyny, T.; Smith, W. A., *Energy Environ. Sci.* **2019**, *12* (5), 1442-1453, doi: 10.1039/c8ee03134g.
80. Resasco, J.; Chen, L. D.; Clark, E.; Tsai, C.; Hahn, C.; Jaramillo, T. F.; Chan, K.; Bell, A. T., *J. Am. Chem. Soc.* **2017**, *139* (32), 11277-11287, doi: 10.1021/jacs.7b06765.
81. Thorson, M. R.; Siil, K. I.; Kenis, P. J. A., *J. Electrochem. Soc.* **2012**, *160* (1), F69-F74, doi: 10.1149/2.052301jes.
82. Singh, M. R.; Kwon, Y.; Lum, Y.; Ager, J. W., 3rd; Bell, A. T., *J. Am. Chem. Soc.* **2016**, *138* (39), 13006-13012, doi: 10.1021/jacs.6b07612.
83. Ayemoba, O.; Cuesta, A., *ACS Appl. Mater. Interfaces* **2017**, *9* (33), 27377-27382, doi: 10.1021/acsami.7b07351.
84. König, M.; Vaes, J.; Klemm, E.; Pant, D., *iScience* **2019**, *19*, 135-160, doi: 10.1016/j.isci.2019.07.014.
85. Resasco, J.; Lum, Y.; Clark, E.; Zeledon, J. Z.; Bell, A. T., *ChemElectroChem* **2018**, *5* (7), 1064-1072, doi: 10.1002/celc.201701316.
86. Sa, Y. J.; Lee, C. W.; Lee, S. Y.; Na, J.; Lee, U.; Hwang, Y. J., *Chem. Soc. Rev.* **2020**, *49* (18), 6632-6665, doi: 10.1039/d0cs00030b.
87. Varela, A. S.; Ju, W.; Reier, T.; Strasser, P., *ACS Catal.* **2016**, *6* (4), 2136-2144, doi: 10.1021/acscatal.5b02550.

88. Gao, D.; Scholten, F.; Roldan Cuenya, B., *ACS Catal.* **2017**, *7* (8), 5112-5120, doi: 10.1021/acscatal.7b01416.

89. Nguyen, D. L. T.; Jee, M. S.; Won, D. H.; Oh, H.-S.; Min, B. K.; Hwang, Y. J., *Catal. Commun.* **2018**, *114*, 109-113, doi: 10.1016/j.catcom.2018.06.020.

90. Ogura, K.; Ferrell, J. R.; Cugini, A. V.; Smotkin, E. S.; Salazar-Villalpando, M. D., *Electrochim. Acta* **2010**, *56* (1), 381-386, doi: 10.1016/j.electacta.2010.08.065.

91. Popovic, S.; Smiljanic, M.; Jovanovic, P.; Vavra, J.; Buonsanti, R.; Hodnik, N., *Angew. Chem. Int. Ed.* **2020**, *59* (35), 14736–14746, doi: 10.1002/anie.202000617.

92. Rogers, C.; Perkins, W. S.; Veber, G.; Williams, T. E.; Cloke, R. R.; Fischer, F. R., *J. Am. Chem. Soc.* **2017**, *139* (11), 4052-4061, doi: 10.1021/jacs.6b12217.

93. Park, S.; Wijaya, D. T.; Na, J.; Lee, C. W., *Catalysts* **2021**, *11* (2), doi: 10.3390/catal11020253.

94. Kim, Y. E.; Lee, W.; Youn, M. H.; Jeong, S. K.; Kim, H. J.; Park, J. C.; Park, K. T., *J. Ind. Eng. Chem.* **2019**, *78*, 73-78, doi: 10.1016/j.jiec.2019.05.042.

95. Zhou, F.; Li, H.; Fournier, M.; MacFarlane, D. R., *ChemSusChem* **2017**, *10* (7), 1509-1516, doi: 10.1002/cssc.201601870.

96. Hori, Y.; Konishi, H.; Futamura, T.; Murata, A.; Koga, O.; Sakurai, H.; Oguma, K., *Electrochim. Acta* **2005**, *50* (27), 5354-5369, doi: 10.1016/j.electacta.2005.03.015.

97. Dutta, A.; Zelocualtecatl Montiel, I.; Kiran, K.; Rieder, A.; Grozovski, V.; Gut, L.; Broekmann, P., *ACS Catal.* **2021**, 4988-5003, doi: 10.1021/acscatal.0c05317.

98. Ha, T.; Cho, J.; Park, J.; Min, K.; Kim, H.-S.; Lee, E.; Jyoung, J.-Y., *Int. J. Hydrog. Energy* **2011**, *36* (19), 12436-12443, doi: 10.1016/j.ijhydene.2011.06.098.

99. Ghassemzadeh, L.; Kreuer, K.-D.; Maier, J.; Müller, K., *J. Phys. Chem. C* **2010**, *114* (34), 14635-14645, doi: 10.1021/jp102533v.

100. Sanchez, D. G.; Ruiu, T.; Biswas, I.; Schulze, M.; Helmly, S.; Friedrich, K. A., *J. Power Sources* **2017**, *352*, 42-55, doi: 10.1016/j.jpowsour.2017.03.057.

101. Terzyk, A. P.; Bryk, P.; Korczeniewski, E.; Kowalczyk, P.; Zawadzka, A.; Plociennik, P.; Wisniewski, M.; Wesolowski, R. P., *Langmuir* **2019**, *35* (2), 420-427, doi: 10.1021/acs.langmuir.8b03790.

102. Leonard, M. E.; Clarke, L. E.; Forner-Cuenca, A.; Brown, S. M.; Brushett, F. R., *ChemSusChem* **2020**, *13* (2), 400–411, doi: 10.1002/cssc.201902547.

103. Verma, S.; Hamasaki, Y.; Kim, C.; Huang, W.; Lu, S.; Jhong, H.-R. M.; Gewirth, A. A.; Fujigaya, T.; Nakashima, N.; Kenis, P. J. A., *ACS Energy Lett.* **2017**, *3* (1), 193-198, doi: 10.1021/acsenergylett.7b01096.

104. Forner-Cuenca, A.; Manzi-Orezzoli, V.; Biesdorf, J.; Kazzi, M. E.; Streich, D.; Gubler, L.; Schmidt, T. J.; Boillat, P., *J. Electrochem. Soc.* **2016**, *163* (8), F788-F801, doi: 10.1149/2.0271608jes.

105. Gostick, J. T.; Ioannidis, M. A.; Fowler, M. W.; Pritzker, M. D., *J. Power Sources* **2009**, *194* (1), 433 - 444, doi: 10.1016/j.jpowsour.2009.04.052.

106. Wagner, N.; Schulze, M.; Gülzow, E., *J. Power Sources* **2004**, *127* (1–2), 264 - 272, doi: 10.1016/j.jpowsour.2003.09.022.

107. Paulisch, M. C.; Gebhard, M.; Franzen, D.; Hilger, A.; Osenberg, M.; Kardjilov, N.; Ellendorff, B.; Turek, T.; Roth, C.; Manke, I., *Materials* **2019**, *12* (17), doi: 10.3390/ma12172686.

108. Raistrick, I. D.; Macdonald, J. R.; Franceschetti, D. R., *Impedance Spectroscopy: Theory, Experiment, and Applications, Third Edition*. John Wiley and Sons **2018**; p 21-105.

109. Lasia, A., Electrochemical Impedance Spectroscopy and its Applications. In *Modern Aspects of Electrochemistry*, Kluwer Academic Publishers **1999;** 143-248, doi.

110. Wagner, N.; Friedrich, K. A., *Fuel Cells* **2009**, *9* (3), 237-246, doi: 10.1002/fuce.200800071.

111. Bienen, F.; Kopljar, D.; Geiger, S.; Wagner, N.; Friedrich, K. A., *ACS Sustainable Chem. Eng.* **2020**, *8* (13), 5192-5199, doi: 10.1021/acssuschemeng.9b07625.

112. Bienen, F.; Kopljar, D.; Löwe, A.; Geiger, S.; Wagner, N.; Klemm, E.; Friedrich, K. A., *ACS Sustainable Chem. Eng.* **2020**, *8* (36), 13759–13768, doi: 10.1021/acssuschemeng.0c04451.

113. Hamann, C. H.; Hamnett, A.; Vielstich, W., *Electrochemistry*. 2nd ed.; Wiley-VCH Weinheim, **2007**.

114. Bard, A. J.; Faulkner, L. R., *Electrochemical Methods: Fundamentals and Applications, 2nd Edition*. John Wiley & Sons, Incorporated **2000**.

115. Eliaz, N.; Gileadi, E., *Physical Electrochemistry: Fundamentals, Techniques, and Applications*. 2nd ed.; Wiley-VC **2018**.

116. Schmidt, V. M., *Elektrochemische Verfahrenstechnik*. Wiley-VCH **2003**.

117. Atkins, P.; De Paula, J.; Keeler, J., *Atkins' physical chemistry*. 9 ed.; Oxford University Press London, England, **2009**.

118. Li, Y.; Dai, H., *Chem. Soc. Rev.* **2014**, *43* (15), 5257-75, doi: 10.1039/c4cs00015c.

119. Bidault, F.; Brett, D. J. L.; Middleton, P. H.; Brandon, N. P., *J. Power Sources* **2009**, *187* (1), 39-48, doi: 10.1016/j.jpowsour.2008.10.106.

120. Moussallem, I.; Jörissen, J.; Kunz, U.; Pinnow, S.; Turek, T., *J. Appl. Electrochem.* **2008**, *38* (9), 1177-1194, doi: 10.1007/s10800-008-9556-9.
121. Rohe, M.; Kubannek, F.; Krewer, U., *ChemSusChem* **2019**, *12* (11), 2373-2384, doi: 10.1002/cssc.201900312.
122. Bultel, Y.; Wiezell, K.; Jaouen, F.; Ozil, P.; Lindbergh, G., *Electrochim. Acta* **2005**, *51* (3), 474-488, doi: 10.1016/j.electacta.2005.05.007.
123. Danner, T. a. b.; Eswara, S. c. d.; Schulz, V. P. e.; Latz, A. a. b. f., *J. Power Sources* **2016**, *324*, 646-656, doi: 10.1016/j.jpowsour.2016.05.108.
124. Hernandez-Aldave, S.; Andreoli, E., *Catalysts* **2020**, *10* (6), doi: 10.3390/catal10060713.
125. Liu, K.; Smith, W. A.; Burdyny, T., *ACS Energy Lett.* **2019**, *4* (3), 639-643, doi: 10.1021/acsenergylett.9b00137.
126. Nguyen, T. N.; Dinh, C. T., *Chem. Soc. Rev.* **2020**, *49* (21), 7488–7504, doi: 10.1039/d0cs00230e.
127. Reid, J. H. US736016: Process of generating electricity. US736016A, **1902**.
128. Heise, G. W. US1899615: Air-depolarized primary battery. US1899615A, 1925, **1925**.
129. Kubannek, F.; Turek, T.; Krewer, U., *Chem. Ing. Tech.* **2019**, *91* (6), 720-733, doi: 10.1002/cite.201800181.
130. Grot, W. G. US3702267: Electrochemical cell containing a water-wettable polytetrafluoroethylene separato. **1970**.
131. Cussler, E. L., *Diffusion Mass Transfer in Fluid Systems*. Cambridge University Press New York, **2009**.
132. Clark, E. L.; Resasco, J.; Landers, A.; Lin, J.; Chung, L. T.; Walton, A.; Hahn, C.; Jaramillo, T. F.; Bell, A. T., *ACS Catal.* **2018**, *8* (7), 6560-6570, doi: 10.1021/acscatal.8b01340.
133. Weng, L. C.; Bell, A. T.; Weber, A. Z., *Phys. Chem. Chem. Phys.* **2018**, *20* (25), 16973-16984, doi: 10.1039/c8cp01319e.
134. Alfath, M.; Lee, C. W., *Catalysts* **2020**, *10* (8), doi: 10.3390/catal10080859.
135. Dinh, C.-T.; García de Arquer, F. P.; Sinton, D.; Sargent, E. H., *ACS Energy Lett.* **2018**, *3* (11), 2835-2840, doi: 10.1021/acsenergylett.8b01734.
136. Pollet, B. G.; Franco, A. A.; Su, H.; Liang, H.; Pasupathi, S., Proton exchange membrane fuel cells. In *Compendium of Hydrogen Energy*, **2016;** 3-56, doi: 10.1016/b978-1-78242-363-8.00001-3.

137. Gostick, J. T.; Ioannidis, M. A.; Fowler, M. W.; Pritzker, M. D., *Electrochem. commun.* **2009**, *11* (3), 576-579, doi: 10.1016/j.elecom.2008.12.053.
138. Zhang, J., *PEM Fuel Cell Electrocatalysts and Catalyst Layers*. **2008**.
139. Kintrup, J.; Millaruelo, M.; Trieu, V.; Bulan, A.; Mojica, E. S., *Electrochem. Soc. Interface.* **2017**, *26* (2), 73-76, doi: 10.1149/2.f07172if.
140. Austin, L. G.; Ariet, M.; Walker, R. D.; Wood, G. B.; Comyn, R. H., *Ind. Eng. Chem. Fundam.* **1965**, *4* (3), 321-327, doi: 10.1021/i160015a015.
141. Srinivasan, S.; Hurwitz, H. D., *Electrochim. Acta* **1967**, *12* (5), 495-512, doi: 10.1016/0013-4686(67)80019-7.
142. Iczkowski, R. P., *J. Electrochem. Soc.* **1964**, *111* (9), 1078, doi: 10.1149/1.2426320.
143. Newman, J. S.; Tobias, C. W., *J. Electrochem. Soc.* **1962**, *109* (12), 1183, doi: 10.1149/1.2425269.
144. Giner, J.; Hunter, C., *J. Electrochem. Soc.* **1969**, *116* (8), 1124, doi: 10.1149/1.2412232.
145. Cutlip, M. B., *Electrochim. Acta* **1975**, *20* (10), 767-773, doi: 10.1016/0013-4686(75)85013-4.
146. Pinnow, S.; Chavan, N.; Turek, T., *J. Appl. Electrochem.* **2011**, *41* (9), 1053-1064, doi: 10.1007/s10800-011-0311-2.
147. Tomantschger, K.; Kordesch, K. V., *J. Power Sources* **1989**, *25* (3), 195-214, doi: 10.1016/0378-7753(89)80004-7.
148. Kopljar, D. *unpublished Dissertation.* University of Stuttgart, Stuttgart, doi.
149. Singh, M.; Vander Wal, R., *C* **2018**, *5* (1), doi: 10.3390/c5010002.
150. Song, K. C.; Kang, Y., *Mater. Lett.* **2000**, *42* (5), 283 - 289, doi: 10.1016/S0167-577X(99)00199-8.
151. Miao, C.-C.; Yuan, G.-Q., *ChemElectroChem* **2018**, *5* (23), 3741–3747, doi: 10.1002/celc.201801036.
152. Bienen, F.; Löwe, A.; Hildebrand, J.; Hertle, S.; Schonvogel, D.; Kopljar, D.; Wagner, N.; Klemm, E.; Andreas Friedrich, K., *J. Energy Chem.* **2021**, doi: 10.1016/j.jechem.2021.03.050.
153. Kopljar, D.; Wagner, N.; Klemm, E., *Chem. Eng. Technol.* **2016**, *39* (11), 2042-2050, doi: 10.1002/ceat.201600198.
154. Leng, Y., *Materials Characterization*. **2013**.
155. Che, M.; Vedrine, J. C., *Characterization of Solid Materials and Heterogeneous Catalysts, 2 Volume Set: From Structure to Surface Reactivity*. Wiley **2012**.

156. Ma, H.; Teng, K.; Fu, Y.; Song, Y.; Wang, Y.; Dong, X., *Energy Environ. Sci.* **2011**, *4* (8), 3067-3074, doi: 10.1039/C1EE01095F.
157. Wang, C.; Wu, Q.; Ge, H. L.; Shang, T.; Jiang, J. Z., *Nanotechnology* **2012**, *23* (7), 075704, doi: 10.1088/0957-4484/23/7/075704.
158. Rouquerol, J.; Baron, G.; Denoyel, R.; Giesche, H.; Groen, J.; Klobes, P.; Levitz, P.; Neimark, A. V.; Rigby, S.; Skudas, R.; Sing, K.; Thommes, M.; Unger, K., *Pure Appl. Chem.* **2011**, *84* (1), 107-136, doi: 10.1351/pac-rep-10-11-19.
159. Washburn, E. W., *Proc. Natl. Acad. Sci. U.S.A.* **1921**, *7* (4), 115-116, doi: 10.1073/pnas.7.4.115.
160. Rouessac, F.; Rouessac, A., *Chemical Analysis: Modern Instrumentation Methods and Techniques*. Wiley **2007**.
161. Christensen, P.; Hamnett, A., *Techniques and Mechanisms in Electrochemistry*. Blackie Academic & Professional Glasgow, **1993**.
162. Orazem, M. E.; Tribollet, B., *Electrochemical Impedance Spectroscopy*. Wiley **2011**.
163. Wagner, N.; Friedrich, K. A., Fuel Cells – Proton-Exchange Membrane Fuel Cells | Dynamic Operational Conditions. In *Encyclopedia of Electrochemical Power Sources*, Garche, J., Ed. Elsevier Amsterdam, **2009;** 912-930, doi: 10.1016/B978-044452745-5.00239-2.
164. Brug, G. J.; van den Eeden, A. L. G.; Sluyters-Rehbach, M.; Sluyters, J. H., *J. Electroanal. Chem.* **1984**, *176* (1), 275–295, doi: 10.1016/S0022-0728(84)80324-1.
165. Schichlein, H.; Müller, A. C.; Voigts, M.; Krügel, A.; Ivers-Tiffée, E., *J. Appl. Electrochem.* **2002**, *32* (8), 875-882, doi: 10.1023/A:1020599525160.
166. Steinhauer, M. *Untersuchung von Anoden/Elektrolyt-Grenzflächen (Solid Electrolyte Interphase SEI) zur Verbesserung der Zyklenstabilität und Sicherheit von Lithium-Ionen-Batterien.* Dissertation, University of Stuttgart, Stuttgart, **2017**.
167. Göhr, H. *Impedance Modelling of Porous Electrodes*. **1997**, http://zahner.de/pdf/ea1997.pdf (accessed 09.03.2021).

8 Additional publications

8.1 Articles

1. *'Importance of Time-Dependent Wetting Behavior of Gas-Diffusion Electrodes for Reactivity Determination'*

   Fabian Bienen, Joachim Hildebrand, Dennis Kopljar, Norbert Wagner, Elias Klemm, K. Andreas Friedrich

   Chemie Ingenieur Technik, **2021**, doi: 10.1002/cite.202000192.

2. *'Optimizing Reaction Conditions and Gas Diffusion Electrodes Applied in the CO_2 Reduction Reaction to Formate to Reach Current Densities up to 1.8 A cm^{-2}'*

   Armin Löwe, Maximilian Schmidt, Fabian Bienen, Dennis Kopljar, Norbert Wagner, Elias Klemm

   ACS Sustainable Chemistry & Engineering, **2021**, 9 (11), 4213-4223, doi: 10.1021/acssuschemeng.1c00199.

8.2 Talks

First author = presenting author.

1. *'Examination of gas-diffusion electrodes applied in CO_2 electrolysis employing electrochemical impedance spectroscopy (EIS).'*

   Fabian Bienen, Dennis Kopljar, Norbert Wagner, Armin Löwe, Elias Klemm, K. Andreas Friedrich

   Symposium on Insights into Gas Diffusion Electrodes: From Fundamentals to Industrial Applications, 23. - 25. September **2019**, Magdeburg, Germany.

2. *'Examination of gas-diffusion electrodes applied in CO_2 electrolysis employing electrochemical impedance spectroscopy (EIS).'*

   Norbert Wagner, Fabian Bienen, Dennis Kopljar, Armin Löwe, Elias Klemm, K. Andreas Friedrich

   Sofia Electrochemical Days (SED), 16. - 19. Ocotber **2019**, Sofia, Bulgaria.

3. *On the applicability of the capillary rise method for determining the internal wettability of gas-diffusion electrodes.'*

   Fabian Bienen, Norbert Wagner, Dennis Kopljar, Armin Löwe, Elias Klemm, K. Andreas Friedrich

   22nd Topical Meeting of the International Society of Electrochemistry, 15. - 18. April **2018**, Tokyo, Japan.

4. *'Production and characterization of gas diffusion electrodes for CO_2 reduction to formic acid.'*

   Norbert Wagner, Fabian Bienen, Dennis Kopljar, Elias Klemm, K. Andreas Friedrich

   20th Romanian International Conference on Chemistry and Chemical Engineering, 06. - 08. September **2017**, Brasov, Romania.

8.3 Posters

First author = presenting author.

1. *'Investigation of gas-diffusion electrodes applied in alkaline CO_2 electrolysis by electrochemical impedance spectroscopy (EIS).'*

   Norbert Wagner, Fabian Bienen, Dennis Kopljar, Armin Löwe, Elias Klemm, K. Andreas Friedrich

   11th International Symposium on Electrochemical impedance Spectroscopy, 2. - 7. June **2019**, Lège-Cap-Ferret, France.

2. *'Exploring electrochemical CO_2 conversion to potassium formate and its application as energy storage technology.'*

Fabian Bienen, Norbert Wagner, Dennis Kopljar, Pia Assmann, Armin Löwe, Marvin Stoll, Elias Klemm, K. Andreas Friedrich

2. Jahrestagung der GDCh Fachgruppe Chemie und Energie, 30. September - 02. October **2018**, Mülheim an der Ruhr.

3. *'Sophisticated Electrode Design and Characterization for Gas Diffusion Electrodes in the Reduction of CO_2.'*

Dennis Kopljar, Fabian Bienen, Elias Klemm, Norbert Wagner, K. Andreas Friedrich

Electrochemistry, 24. - 26. September **2018**, Ulm, Germany

4. *'Electrochemical and structural investigation of metal-electrodes for an energy-efficient CO_2 - reduction process.'*

Fabian Bienen, Norbert Wagner, Dennis Kopljar, Armin Löwe, Elias Klemm, K. Andreas Friedrich

231st Meeting of The Electrochemical Society, 28. May- 01. June **2017**, New Orleans, USA

9 Scientific articles

ACS Sustainable Chemistry & Engineering

pubs.acs.org/journal/ascecg

Research Article

Investigation of CO_2 Electrolysis on Tin Foil by Electrochemical Impedance Spectroscopy

Fabian Bienen,* Dennis Kopljar, Simon Geiger, Norbert Wagner, and Kaspar Andreas Friedrich*

Cite This: *ACS Sustainable Chem. Eng.* 2020, 8, 5192–5199

Read Online

ACCESS | Metrics & More | Article Recommendations | Supporting Information

ABSTRACT: The conversion of CO_2 on tin catalysts via electrolysis leads to valuable chemicals like CO and formate and can help to close the carbon cycle. In the current literature, catalysts for the electrochemical CO_2 reduction reaction (CO_2RR) are amongst other methods characterized via electrochemical impedance spectroscopy (EIS) in terms of charge transfer resistances while neglecting the parallelly occurring hydrogen evolution reaction (HER). This may lead to an inapt assignment of the catalyst properties to the CO_2RR, whereas the impedance spectrum displays features of the parasitic HER or mixed information of both the reactions. This circumstance is tackled systematically in this work by analyzing linear sweep voltammograms and impedance spectra under various experimental conditions to get more insights into the processes displayed in the respective impedance spectra. The main finding is that the observed high-frequency process displays a charge transfer reaction, which contains contributions of the HER and CO_2RR and is not appropriate for evaluating catalysts for the CO_2RR. This ambiguity was observed for experimental conditions where the HER or CO_2RR prevailed. Additionally, equivalent circuit model (EQCM) simulations confirmed the occurrence of just one arc in the EIS spectrum for the parallelly occurring charge transfer reactions on the same electrode.

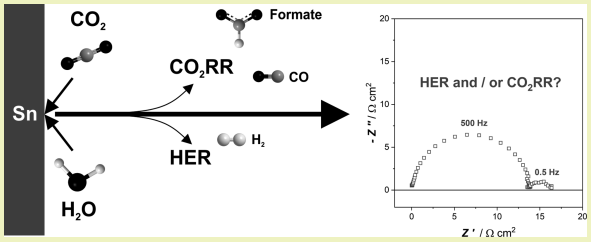

KEYWORDS: *CO_2 electrolysis, CO_2RR, electrochemical impedance spectroscopy, tin, formate, carbon dioxide, CO_2*

INTRODUCTION

To achieve reduction of CO_2 emissions on the order necessary to comply with the goals defined in the Paris agreement, all countries and sectors have to substantially increase their efforts. Beyond other measures, particularly for the carbon footprint of the industry, it is mandatory to develop technologies that can substitute processes that are based on fossil feedstock and which emit CO_2 and other greenhouse gases as a consequence.[1,2] In that respect, the electrochemical conversion of CO_2 off-gas from industrial plants, biorefineries, or, in the long term, even from the atmosphere to useful chemicals using renewable energy can help to change the role of CO_2 from a harmful waste to a valuable feedstock for the production of a variety of carbon-based chemicals, which are nowadays mainly derived from fossil resources.[1−4] The electrochemical CO_2RR can lead to several reaction products such as CO, formate/formic acid, methane, ethylene, or methanol. At the same time, the most important parasitic reaction in aqueous electrolytes is the HER.[5,6] The significance of the HER and the distribution between the CO_2RR products highly depends on the catalyst, electrolyte, reaction conditions, and electrode potential.[7,8] In this work, we focus on the conversion of CO_2 on tin foil electrodes to formate, which is used in a variety of different applications, e.g., as a deicing agent, drilling fluid, or for silage and tanning if subsequently protonated to formic acid.[9,10] Most of the CO_2RR research papers focus on the conversion of CO_2 to CO or formate since only two electrons are needed for this conversion thus making the reaction mechanisms less complex and achieving better performance.[6,11] Accordingly, it was shown that the electrochemical conversion of CO_2 to formic acid and CO is already close to being competitive with the traditional fossil-based production process.[6,12] However, there is still a lack of knowledge on the conversion of CO_2 to formate on tin electrodes, especially regarding the reaction mechanism and degradation phenomena.[6,8] Electrochemical impedance spectroscopy (EIS) can approach this lack of information with its ability for *operando* quantifying the resistances of the microscopic processes (e.g., charge transfer, mass transport of educts, adsorption of species) displayed in the impedance spectrum.[13] The challenges are to identify the respective processes that are displayed in the impedance spectrum and to assign these features to the correct physical phenomena.

Received: December 20, 2019
Revised: February 4, 2020
Published: March 13, 2020

Several authors used EIS as an additional tool among other methods to compare catalysts presented in their papers and substantiate their arguments. However, there is no study focusing on a detailed analysis of the impedance spectrum itself to clearly elucidate the different contributions observable in the spectra and assign them to specific physicochemical processes.[14] Specifically for Sn-based electrodes, various authors have performed EIS with different appearances of the spectra suggesting a significant influence of the exact composition of the electrocatalyst, reaction conditions, and the chemical environment. Choi et al. performed EIS measurements for Sn and Sn−Pb alloys in a CO_2-saturated 0.5 M aqueous $KHCO_3$ solution. They observed two arcs in the frequency range of 1 MHz to 100 mHz. The presented interpretation focused on the high-frequency process, which was dependent on the alloy composition, without further specifying the underlying chemical process.[15] Two arcs were also observed in the impedance spectrum by Lv et al., who conducted EIS measurements in CO_2-saturated 0.1 M $KHCO_3$ in the frequency range of 40 kHz to 10 mHz for Sn deposited on a Cu foil and Sn.[16] On the other hand, Daiyan et al., who analyzed SnO_2-based electrodes in a CO_2-saturated 0.1 M aqueous $KHCO_3$ solution, observed only one semicircle in the Nyquist plot, which was used for the comparison of the investigated catalysts with regard to their reaction kinetics.[17] Comprehensibly, all of the above-mentioned authors did not investigate the origin of the observed processes displayed in the impedance spectrum in detail since their papers focused on the investigation of catalyst materials and EIS was merely employed to compare the kinetics of the reaction on the specific catalyst. Zeng et al. conducted a slightly more detailed investigation on their EIS measurements for Cu and Cu−Sn foams. The electrolyte was N_2- or CO_2-saturated 0.1 M $KHCO_3$, and the frequency was varied in the range of 10 kHz down to 100 mHz. For both types of foam and purging gas, the spectra showed two arcs with one of them highly dependent on the applied potential, indicating that this arc represents a charge transfer process. An important result is that in contrast to bare Cu foam, the Cu−Sn foam exhibits lower charge transfer resistance values in the CO_2-saturated 0.1 M $KHCO_3$ solution compared to the N_2-saturated electrolyte, which was then interpreted that the Cu−Sn foam is more active for CO_2RR compared to the HER.[18]

Since the HER and CO_2RR occur in a competing way parallelly on the same electrode, we want to emphasize how important it is to be sure about which reaction dominates the processes displayed in the impedance spectrum before taking the results of EIS to evaluate catalysts. To the best of our knowledge, no elaborate EIS study exists for the CO_2RR on tin foil in aqueous $KHCO_3$ solution, or for the CO_2RR in general. Therefore, a detailed investigation, as described in this contribution, is necessary to get more insights into the processes displayed in the impedance spectrum.

EXPERIMENTAL SECTION

All experiments were performed in a classic three-electrode setup. The working electrode was tin foil (99.998%, Alfa Aesar, 0.1 mm thickness) with a diameter of 2 cm and a geometrical surface area of π cm^2. Before assembling the cell, the tin foil electrode was immersed for 30 s in 1.0 M HNO_3 (Pan Reac AppliChem 1N) to remove surface impurities followed by rinsing with deionized water. In all experiments, the reversible hydrogen electrode (RHE) was used as the reference electrode, whereas a platinum foil served as the counter electrode. If not stated otherwise, the temperature of the electrolyte was 303 K. $KHCO_3$ solutions were obtained by mixing solid $KHCO_3$ (≥99%, Roth) with pure water (resistivity >18 MΩ). For some of the experiments, deuterium oxide (99.9 atom % D, Sigma-Aldrich) was used as the solvent for $KHCO_3$. Before starting the experiments, the electrolytes were purged in situ at a flow rate of 0.05 slm for at least 1 h with N_2 (5.0, Linde) or CO_2 (4.5, Linde), depending on the desired experimental parameters. During the tests, the bubbling of the desired gas into the electrolyte continued at the above-mentioned flow rate. If mentioned, the pH value was measured by using a pH electrode (InLab Flex-Micro, Mettler Toledo) in combination with an evaluation unit (S7 Seven2GoTM Pro, Mettler Toledo). For all electrochemical tests, a ZAHNER-elektrik GmbH & Co. KG Zennium electrochemical workstation and the corresponding evaluation software Thales were used.

Electrochemical Characterization. Electrochemical impedance spectra for tin foil were recorded in the range of 10 mHz to 300 kHz in galvanostatic operation mode. The excitation current for every experiment was 5 mA. The benchmark conditions were 303 K and a load of −4.77 mA cm^{-2} for measurement in a 1 M $KHCO_3$ aqueous solution saturated with CO_2. By conducting experiments at −3.18, −4.77, −6.37, and −7.96 mA cm^{-2}, the current dependency of the impedance spectra of tin could be observed. To investigate the thermal behavior of the impedance spectra of tin, a temperature series was carried out for 303, 313, 323, and 333 K. The effect of different electrolytes was tested using 0.1, 0.2, 0.5, and 1.0 M aqueous $KHCO_3$ solutions. All solutions were purged with N_2 or CO_2 before starting impedance measurements. To identify the processes involving hydrogen-containing species, deuterium oxide was used as a solvent to generate $KHCO_3$ solutions. For all of the experiments, the cell was polarized for 10 min at the desired experimental conditions as a preconditioning procedure before immediately—with no current interruption—recording the impedance spectra. At least three consecutive spectra (∼ 7 min relaxation time under load between each run) were recorded for each experimental parameter set whereby the second spectrum was used for evaluation. In contrast to the first spectrum, the second spectrum has reached a steady state and the observed changes during the following consecutive spectra were marginal. Experiments were repeated for at least one more time to guarantee reproducible results. For an easier comparison, the Nyquist data were shifted to the same origin by subtracting the ohmic resistance.

Linear sweep voltammetry (LSV) was performed to compare the activity of tin foil in different electrolytes. The potential was shifted from +50 to −1300 mV versus RHE with a sweep rate of 1 mV s^{-1}. The electrolytes were 1.0 and 0.1 M $KHCO_3$ solutions purged with CO_2 or N_2. For *iR* compensation, an impedance measurement was conducted after recording the LSV to determine the ohmic resistance.

The faradic efficiency (FE) was measured during galvanostatic EIS measurements applying a constant current of −4.77 mA cm^{-2} at 303 K. The concentration of the gaseous products H_2 and CO in the purging gas stream was quantified by a micro-gas chromatograph and averaged over time for at least 60 min with a measurement resolution of 5 min. The averaged concentrations were then multiplied by the volume flow of the purging gas stream to obtain the gas flow of the reaction products. By calculating the ratio of the experimental and theoretical product flows (applying Faraday's law), the FE was determined. The FE for formate was calculated as the difference from 100% and the FEs of H_2 and CO since tin is known to exclusively produce H_2, CO, and formate in aqueous alkaline media.[19,20] Nevertheless, to prove this assumption, exemplarily formate was determined to close the mass balance. This was done via UV spectroscopy after converting formate to formic acid and expelling dissolved CO_2 and bicarbonate from the liquid sample (interference on detection peak at ca. 220 nm) using H_2SO_4 (cf. Figure S1).[21]

RESULTS AND DISCUSSION

EIS is a powerful tool to elucidate rate-determining processes in a specific time domain during electrochemical reactions. However, the analysis of impedance spectra is not trivial and

https://dx.doi.org/10.1021/acssuschemeng.9b07625
ACS Sustainable Chem. Eng. 2020, 8, 5192−5199

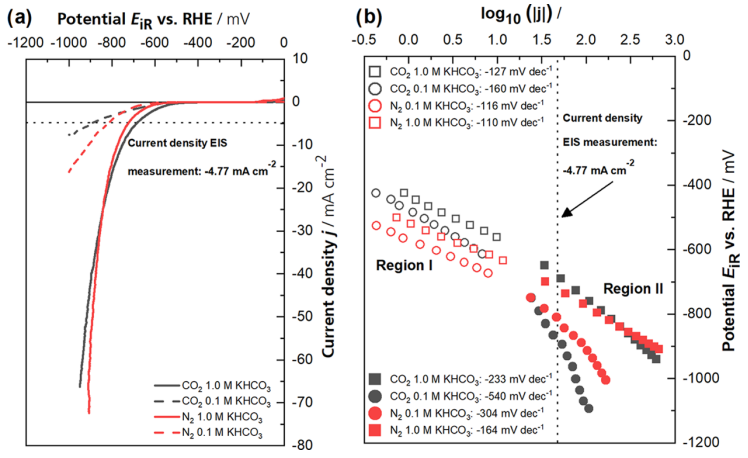

Figure 1. (a) Linear sweep voltammetry at 1 mV s^{-1} for tin foil in N_2- and CO_2-saturated 0.1 and 1.0 M $KHCO_3$ aqueous solutions and (b) the corresponding Tafel analysis based on total current ($I_{CO_2RR} + I_{HER}$).

one needs to have detailed knowledge on the contributions that can be observed in the spectra. However, performing a literature survey on this topic, it becomes clear that the origins of the processes displayed in the impedance spectra obtained for tin foil during CO_2 electrolysis are not well understood as—to the best of our knowledge—no detailed analysis has been conducted so far. Combining linear sweep voltammetry (LSV), faradic efficiency, and impedance measurements, we want to give insights into the nature of the processes during CO_2 reduction on tin foil in $KHCO_3$ aqueous solution.

Linear Sweep Voltammetry and Apparent Tafel Analysis. As a starting point to introduce the system that is being studied, LSV measurements were made in CO_2- and N_2-saturated 0.1 and 1.0 M $KHCO_3$ electrolytes with a sweep rate of 1 mV s^{-1} and are depicted in Figure 1a. For both concentrations, tin foil shows a higher activity in the CO_2-saturated environment at lower potentials, whereas the activity in the high overpotential region is superior in the N_2-saturated electrolyte. This might be explained as due to the mass transportation effects of CO_2 and a hindrance to the HER at higher current densities. The LSVs were used to perform apparent (not taking partial current densities into account) Tafel analysis, which can be seen in Figure 1b. For each combination of purging gas and electrolyte concentration, one can distinguish two regions in the diagram. The increase of the Tafel slopes observed at higher potentials indicates that mass transport effects or other processes contribute to the slope and determine the shape of the plot in this region.[22] The slopes in both the N_2-saturated and CO_2-saturated 1.0 M $KHCO_3$ electrolytes in the low potential region are close to −118 mV dec^{-1}, which is as expected for the HER where the Volmer step is rate limiting.[23] A rate-limiting electron transfer in the CO_2RR (cf. eq 5) would result in a Tafel slope of −118 mV dec^{-1} as well.[24,25] When analyzing the FE for the HER, which was determined at a constant potential of −550 mV versus RHE (region I in Tafel plot), one can see that hydrogen evolution prevails in CO_2-saturated 0.1 and 1.0 M $KHCO_3$ solutions (FE H_2: 83% and 85%) at this potential. This fact indicates that the apparent Tafel slope in the CO_2-saturated electrolyte might be mainly determined by the HER in region I. On the other hand, in the CO_2-saturated 0.1 M $KHCO_3$ solution, the Tafel slope is −160 mV dec^{-1}, which significantly deviates from −118 mV dec^{-1} as expected for the HER and a rate-limiting electron transfer during the CO_2RR. This higher Tafel slope indicates a change in the reaction mechanism for the HER (the deactivation of active sites induced by CO_2) or an increasing contribution of the CO_2RR (assuming a mechanism with a Tafel slope greater than 118 mV dec^{-1} for this reaction with an uncertain mechanism) to the apparent Tafel slope.

Electrochemical Impedance Spectroscopy. FEs for H_2 and CO were determined during galvanostatic impedance measurements using gas chromatography. The received results and additional information regarding potential and pH values after 1 h of bubbling with N_2 and CO_2, respectively, are shown in Table 1.

Table 1. FE for Tin Foil in N_2- and CO_2-Saturated 0.1 and 1.0 M $KHCO_3$ Solutions at −4.77 mA cm^{-2}

Purging Gas	Electrolyte	Potential E_{iR} vs RHE/ mV	FE H_2	FE CO	FE $HCOO^-$	pH after 1 h bubbling
CO_2	1.0 M $KHCO_3$	−682	87%	3%	10%[a]	8.0
CO_2	0.1 M $KHCO_3$	−879	43%	5%	52%[a]	7.1
N_2	1.0 M $KHCO_3$	−722	only H_2 detected			8.9
N_2	0.1 M $KHCO_3$	−821	only H_2 detected			9.2

[a]Calculated using FE_{H_2} and FE_{CO} and mass balance closing condition.

As described above, impedance measurements were conducted at a current density of −4.77 mA cm^{-2} (15 mA) in galvanostatic operation mode with an excitation signal of 5 mA. After saturating the electrolyte for 1 h with N_2 or CO_2, the preconditioning phase was 10 min at the desired experimental parameter set. Figure 2 shows the Nyquist and imaginary part versus the frequency plot. In general, the spectra reveal at least two processes during electrolysis with a low-frequency process occurring at a characteristic frequency around 0.1 Hz and a high-frequency process at around 500 Hz. The spectra recorded in N_2-saturated electrolytes are dominated by the HER, as no CO_2RR products were detected via μ-GC. In general, changing the purging gas to CO_2 results in larger

https://dx.doi.org/10.1021/acssuschemeng.9b07625
ACS Sustainable Chem. Eng. 2020, 8, 5192−5199

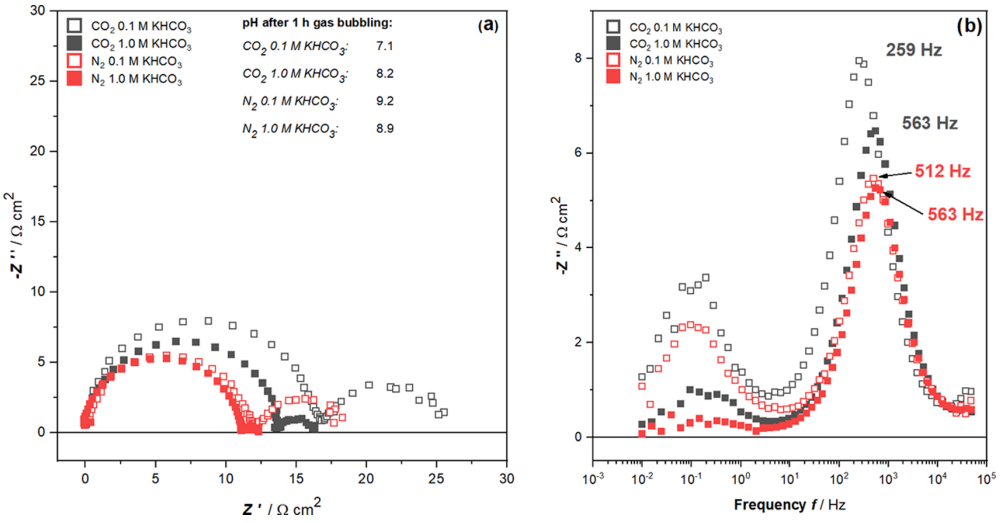

Figure 2. (a) Nyquist plot for tin foil obtained in CO_2- and N_2-saturated 0.1 and 1.0 M $KHCO_3$ at galvanostatic operation, −4.77 mA cm^{-2}, with an amplitude of 5 mA, ohmic resistance subtracted, and (b) the corresponding imaginary part versus frequency plot.

diameters for both semicircles and, as a consequence, to an increased total faradic impedance. When bubbling CO_2 into the electrolyte, in addition to the HER, the CO_2RR must also be taken into account. Accordingly, the increased impedance values might be a result of the sluggish CO_2RR becoming more accented or that the CO_2-saturated environment slows down the HER. To reveal the origin of the processes, we introduce the investigation regarding thermal activation and potential activation of the two processes.

Temperature- and Current-Dependent Behavior. To identify thermal- and current-activated processes, the impedance spectra for the temperature series were recorded at 303, 313, 323, and 333 K in CO_2-saturated 1.0 and 0.1 M $KHCO_3$ solutions at a current density of −4.77 mA cm^{-2}, while for the current series, spectra were recorded at −3.18, −4.77, −6.37, and −7.96 mA cm^{-2} at 303 K (Figure S2 for 1.0 M $KHCO_3$ and Figure S3 for 0.1 M $KHCO_3$).

Taking the obtained results of the current density and temperature variation into account, it is very likely that the high-frequency process that is activated by increasing the temperature and current density displays a charge transfer.[13,26] Consequently, a plot of the R_{Ct} values versus the reciprocal current should result in a straight line, whereas the slope represents the Tafel slope (cf. eq 1 and insets in Figures S2 and S3).[27]

$$R_{Ct} = b \cdot \frac{1}{2.303 \cdot I} \tag{1}$$

It is important to mention that the plotted reciprocal current is the total current and not a partial current for the HER or CO_2RR. The slopes of these plots for 0.1 and 1.0 M $KHCO_3$ are −163 and −132 mV dec^{-1}, which are in agreement with the Tafel slopes obtained via LSV. As a consequence, the shape of the curve for CO_2-saturated electrolytes in region 1 in Figure 1a is determined by an electron transfer. The fact that plotting the reciprocal total current versus R_{Ct} leads to the expected straight line and comparable Tafel slopes to the values found via LSV evaluation suggests that the R_{Ct} arc in the EIS spectrum is a mixed quantity consisting of contributions of the HER and CO_2RR. Because of the contribution of both the reactions to the Tafel slope in the kinetic region, two different explanations exist for an increased Tafel slope in the CO_2-saturated electrolyte compared to the N_2-saturated electrolyte. On the one hand, the presence of CO_2 could slow down the HER, increasing its magnitude and resulting in an increased mixed Tafel slope; on the other hand, the presence of CO_2 obviously results in the CO_2RR taking place at the electrode, which might have a significantly higher Tafel slope than in the HER and thus pushing the mixed Tafel slope to a higher value.

The low-frequency process cannot be attributed to a charge transfer process since it is not activated with increasing temperature and current density in the probed current density range (cf. Figures S2 and S3). To gain further insights into the high- and low-frequency processes, additional experiments with varying $KHCO_3$ concentrations and isotope-labeled water were conducted.

Kinetic Isotope Effect. Impedance spectra were recorded in CO_2-saturated 0.1 and 1.0 M $KHCO_3$ solutions using ultrapure water or deuterium oxide (D_2O) as solvent (303 K, −4.77 mA cm^{-2}). This should give an insight into the mechanism of the processes, as slower kinetics of proton-involved processes are expected due to the additional neutron in the deuterium core. A simplified reaction mechanism for the HER in alkaline media including the Volmer, Heyrovsky, and Tafel reactions is given in eqs 2−4, which points out the involvement of hydrogen in the charge transfer reactions 2 and 3.[23]

$$M + H_2O + e^- \rightleftharpoons MH_{ads} + OH^- \tag{2}$$

$$MH_{ads} + H_2O + e^- \rightleftharpoons M + OH^- + H_2 \tag{3}$$

$$2MH_{ads} \rightleftharpoons 2M + H_2 \tag{4}$$

Regarding the reaction mechanism of the conversion of CO_2 to formate or CO, there is no unequivocal and conclusive consensus in the scientific community yet. Typically, the first step is considered to be the activation of CO_2 through a direct electron transfer followed by a protonation with a simultaneous electron transfer (cf. eqs 5 and 6).[8,28] The fact that the CO_2 radical formation is often referred to be the rate-determining step suggests that a possible displayed charge

https://dx.doi.org/10.1021/acssuschemeng.9b07625
ACS Sustainable Chem. Eng. 2020, 8, 5192−5199

ACS Sustainable Chemistry & Engineering pubs.acs.org/journal/ascecg Research Article

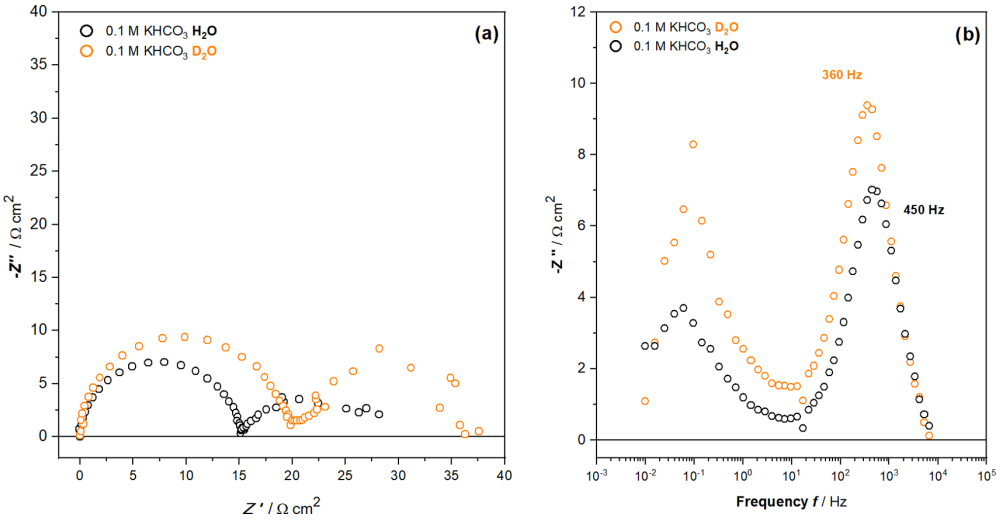

Figure 3. (a) Impedance spectra and (b) imaginary part versus frequency plot for tin foil obtained in CO_2-saturated 0.1 M $KHCO_3$ solution comparing H_2O and D_2O as solvents. Galvanostatic operation at −4.77 mA cm^{-2} with an amplitude of 5 mA, ohmic resistance subtracted.

transfer in the impedance spectrum, which is attributed to the CO_2RR, must then represent a nonconcerted proton and electron transfer to CO_2.[5,29]

$$CO_2 + e^- \rightleftharpoons CO_2^{-\bullet} \quad (5)$$

$$CO_2^{-\bullet} + H_2O + e^- \rightleftharpoons HCOO^- + OH^- \quad (6)$$

As a result of the above considerations, we expect, in contrast to the HER, that a CO_2RR-attributed charge transfer process shown in the spectrum will not be decelerated, resulting in a higher resistance and lower characteristic frequency, when substituting hydrogen with deuterium.[30,31] We would expect quite the contrary—an acceleration of the CO_2RR because the solubility of CO_2 increases from 33.8 mmol L^{-1} in H_2O to 38.1 mmol L^{-1} in D_2O.[32]

However, the high- and low-frequency processes are both slowed down when using D_2O as the solvent in 1.0 M $KHCO_3$ and in 0.1 M $KHCO_3$ where CO_2RR prevails (cf. Figures 3 and S4 for 1.0 M $KHCO_3$). This fact can be seen in the larger diameters of the arcs in the high- and low-frequency regions and a reduction of the characteristic frequencies. Since the high-frequency process displays a charge transfer reaction affected by CO_2, one can now be little more specific that this charge transfer process involves hydrogen or a hydrogen-containing species. This observation rules out that the observed charge transfer is dominated by the conversion of CO_2 to the $CO_2^{\bullet-}$ radical (cf. eq 5), leading to the suggestion that this process might be ascribed to the HER. On the other hand, since the mechanism of CO_2RR to $HCOO^-$ and CO is not fully understood yet, it might be that (in contrast to eq 5) a hydrogen-containing species is involved in the rate-limiting CO_2RR charge transfer reaction. For example, Baruch et al. suggested the involvement of hydrogen-containing tin carbonate species in the rate-limiting CO_2RR charge transfer. Analogous to the involvement of hydrogen in the HER, the unlikely, but not completely excluded, participation of a bicarbonate species during the CO_2RR would result in an increase of the high-frequency resistance as well when substituting H_2O with D_2O.[33] As will be shown later, the low-frequency arc correlates with the HCO_3^- concentration so that a slowed-down low-frequency process in D_2O-based electrolytes might be explained by the impeded movement of HCO_3^- and DCO_3^- ions in D_2O.

$KHCO_3$ Concentration Series in N_2- and CO_2-Saturated Electrolytes. To investigate the influence of the electrolyte concentration, impedance measurements were conducted in N_2- and CO_2-saturated 0.1, 0.2, 0.5, and 1.0 M $KHCO_3$ solutions. It can be seen that in the N_2-saturated electrolyte, the high-frequency process, the charge transfer, seems to be independent of the $KHCO_3$ concentration, while the low-frequency process becomes slower at lower $KHCO_3$ concentrations (cf. Figure 4a,b). In N_2-saturated electrolyte, only hydrogen is detected, which means that all displayed features might be linked with the HER. However, a slight increase in the charge transfer resistance with decreasing $KHCO_3$ concentration might be a result of an increasing pH value and a slowing down of the HER kinetics. The observed deceleration of the low-frequency process with decreasing HCO_3^- concentration may be explained by the fact that HCO_3^- can be reduced to hydrogen at the applied potentials, as it was shown by Wuttig et al. for Au catalysts, and contribute to the total polarization resistance so that the low-frequency arc may display the diffusion of HCO_3^- ions.[34] Recording the impedance spectra for CO_2-saturated solutions with different $KHCO_3$ concentrations reveals that both processes are accelerated when increasing the $KHCO_3$ concentration, as shown in Figure 4c,d. The increased charge transfer resistance can be explained taking eq 1 and Figure 1b into account: The Tafel slope (calculated with total current) increases with reduced $KHCO_3$ concentrations and consequently results in higher R_{Ct} values. As shown above, the R_{Ct} values of the $KHCO_3$ concentration series in the N_2-saturated electrolyte remain more or less constant, which was also observed in the LSV evaluation. However, the change of the nearly independent charge transfer in the N_2-saturated electrolyte regarding the HCO_3^- concentration to a distinct HCO_3^--concentration-dependent charge transfer in the CO_2-saturated electrolyte indicates a contribution of the CO_2RR as a reaction itself (higher Tafel slope compared to the HER) or a decelerated HER in the CO_2-saturated electrolyte to the

https://dx.doi.org/10.1021/acssuschemeng.9b07625
ACS Sustainable Chem. Eng. 2020, 8, 5192−5199

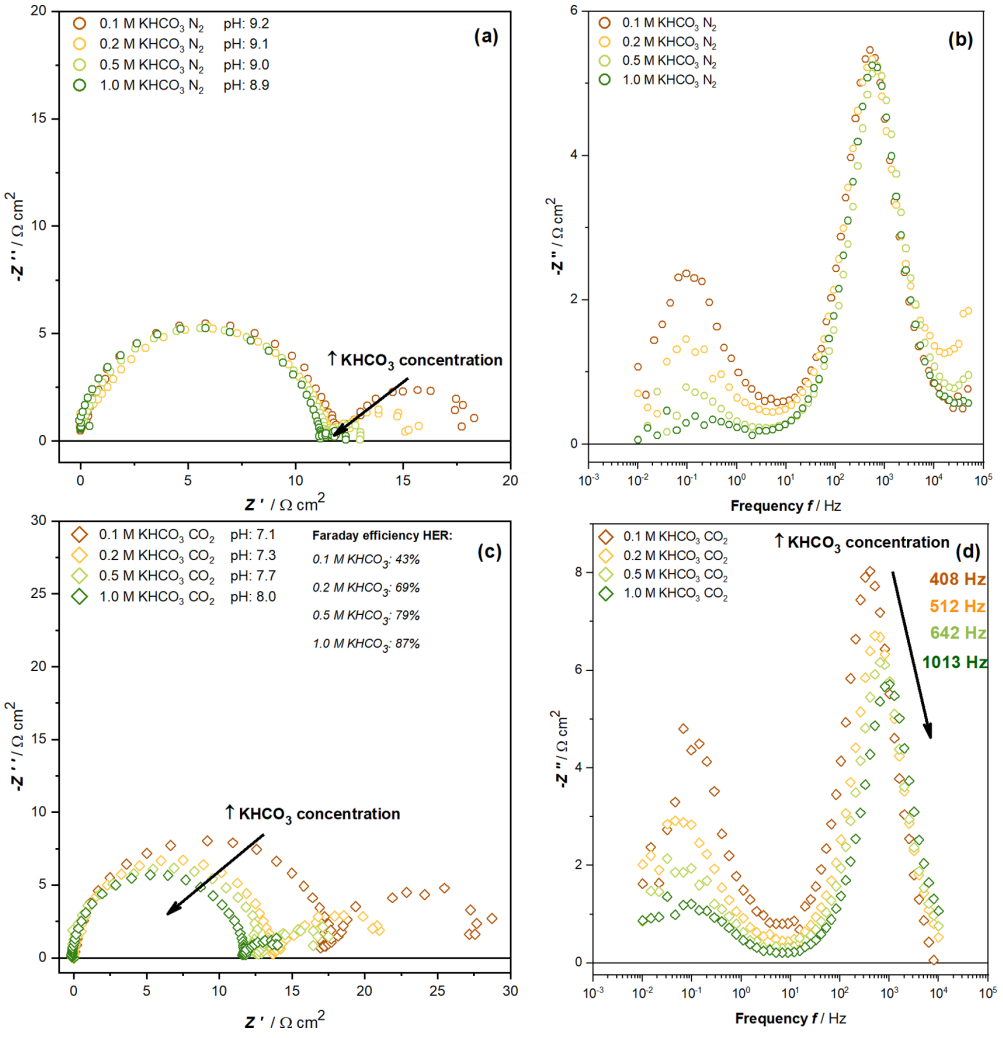

Figure 4. Impedance spectra obtained for tin foil in aqueous solutions with varying $KHCO_3$ concentrations saturated with (a) N_2 or (c) CO_2 and their corresponding imaginary part versus frequency plots (b, d). Galvanostatic operation at −4.77 mA cm^{-2} with an amplitude of 5 mA, ohmic resistance subtracted.

charge transfer arc in the impedance spectrum. The increase of the charge transfer arc in lower-concentration CO_2-saturated electrolytes is not a pH effect of the HER since this reaction should be favored at more acidic conditions (cf. pH values Figure 4c).[35] The increasing low-frequency arc in low-concentration CO_2-saturated electrolytes can also be explained via a possible HCO_3^- diffusion process.

Simulating Independent Parallelly Occurring Charge Transfer Reactions. The results indicate that the high-frequency process displays a charge transfer, which is the sum of the contributions traced back to the HER and the CO_2RR. The reactions occur parallelly on the same electrode. Figure 5a shows an equivalent circuit model (EQCM) simulation for the high-frequency process generated with Thales from ZAHNER-elektrik GmbH & Co. KG assuming one RC element for each reaction (inserted parameters are listed in Table S6). Consequently, the RC elements were combined in parallel since the reactions occur parallelly.[36] A parameter study regarding the corresponding time constants τ_{HER} and τ_{CO_2RR} (regardless of which reaction is slowed down) illustrates that for parallel reactions, only one arc will be observed in the impedance spectrum no matter how dissimilar the time constants are. When applying the rules of electrical engineering by converting the two resistors and capacitors to one mixed RC element, one can see that the simulated Nyquist plot is identical no matter if the EQCM contains two separate RC elements or one combined RC element (cf. Figure 5b). This finding supports our theory that the observed charge transfer cannot be exclusively ascribed to the HER or the CO_2RR since the parallelly occurring reactions will result in one mixed arc during EIS.

CONCLUSIONS

Impedance spectroscopy reveals at least two observable processes during electrolysis on tin foil in CO_2-saturated aqueous $KHCO_3$ solutions. In 1.0 M $KHCO_3$ solution, the HER prevailed while in the 0.1 M $KHCO_3$ solution, the CO_2RR products dominated the product distribution. A parameter study was carried out to identify the origin of the observed processes for these two cases. Our results indicate

https://dx.doi.org/10.1021/acssuschemeng.9b07625
ACS Sustainable Chem. Eng. 2020, 8, 5192−5199

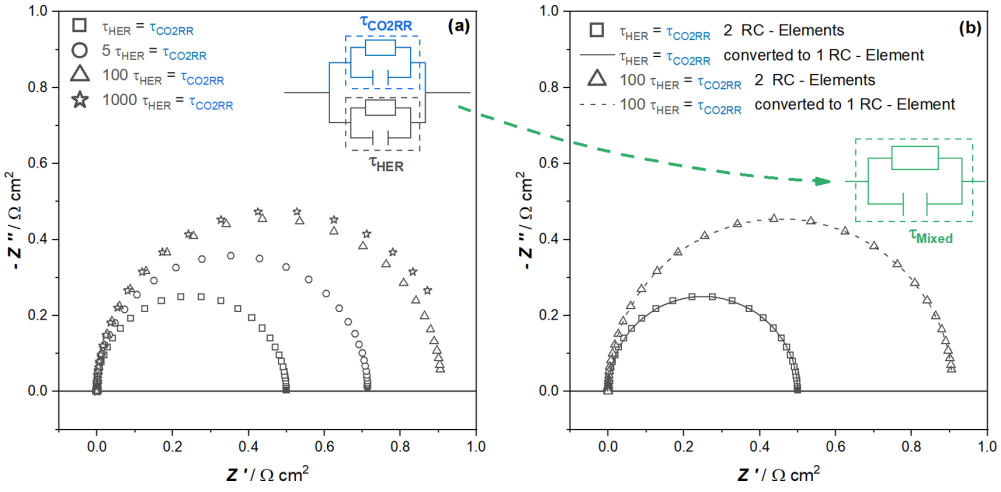

Figure 5. (a) Simulated EIS spectra for two parallel connected RC elements, representing HER and CO_2RR charge transfers on the same electrode surface, with varying time constants showing only one semicircle regardless of how distinct the time constants are. (b) Nyquist plot of one combined RC element, displaying one mixed time constant for the HER and CO_2RR, calculated from the parameters of the two RC elements shown in (a).

that the high-frequency process around 500 Hz displays a charge transfer reaction, which is determined by the HER and CO_2RR no matter if the faradic efficiency for the HER is about 87% (1.0 M $KHCO_3$) or 43% (0.1 M $KHCO_3$). The reactions occur in parallel, which we showed in an EQCM simulation will result in one mixed time constant (RC element) in the EIS spectrum no matter how distinct the differences of the corresponding time constants of the two reactions are. The second process in the low-frequency region around 0.1 Hz cannot be reliably identified. Our results suggest that this process may describe the ionic movement in the electrolyte since the resistance of this process scales with the $KHCO_3$ concentration (higher concentration, lower resistance). With our study, we wanted to help identify the observed processes in the EIS spectrum during CO_2 electrolysis on tin foil in aqueous $KHCO_3$ solution. Since the HER and CO_2RR occur in parallel on the same electrode, we showed that the charge transfer resistance measured via EIS is affected by both the reactions and cannot easily be used to evaluate catalyst materials. The widely used chronopotentiometry or chronoamperometry in combination with the determination of the FEs for CO_2RR products is suitable and sufficient to evaluate catalysts for CO_2RR.

■ ASSOCIATED CONTENT

Supporting Information

The Supporting Information is available free of charge at https://pubs.acs.org/doi/10.1021/acssuschemeng.9b07625.

Determination of faradic efficiencies on tin foil for galvanostatic electrolysis in CO_2-saturated 1.0 M $KHCO_3$ solution; EIS spectra for tin foil depending on temperature, applied current, and solvent (H_2O vs D_2O) for CO_2-saturated 0.1 and 1.0 M $KHCO_3$ solutions (PDF)

■ AUTHOR INFORMATION

Corresponding Authors

Fabian Bienen − *Institute of Engineering Thermodynamics, German Aerospace Center, 70569 Stuttgart, Germany; Institute of Building Energetics, Thermal Engineering and Energy Storage, University of Stuttgart, 70569 Stuttgart, Germany;* orcid.org/0000-0002-4660-8826; Email: Fabian.Bienen@dlr.de

Kaspar Andreas Friedrich − *Institute of Engineering Thermodynamics, German Aerospace Center, 70569 Stuttgart, Germany; Institute of Building Energetics, Thermal Engineering and Energy Storage, University of Stuttgart, 70569 Stuttgart, Germany*; Email: Andreas.Friedrich@dlr.de

Authors

Dennis Kopljar − *Institute of Engineering Thermodynamics, German Aerospace Center, 70569 Stuttgart, Germany*

Simon Geiger − *Institute of Engineering Thermodynamics, German Aerospace Center, 70569 Stuttgart, Germany*

Norbert Wagner − *Institute of Engineering Thermodynamics, German Aerospace Center, 70569 Stuttgart, Germany*

Complete contact information is available at: https://pubs.acs.org/10.1021/acssuschemeng.9b07625

Author Contributions

The manuscript was written through contributions of all authors. All authors have given approval to the final version of the manuscript.

Notes

The authors declare no competing financial interest.

■ ACKNOWLEDGMENTS

Parts of this work were funded by the Federal Ministry for Economic Affairs and Energy (FKZ 03ET1379A/B − EnElMi2.0).

■ REFERENCES

(1) Abanades, J. C.; Rubin, E. S.; Mazzotti, M.; Herzog, H. J. On the climate change mitigation potential of CO2 conversion to fuels. *Energy Environ. Sci.* **2017**, *10*, 2491−2499.

(2) Smith, P.; Davis, S. J.; Creutzig, F.; Fuss, S.; Minx, J.; Gabrielle, B.; Kato, E.; Jackson, R. B.; Cowie, A.; Kriegler, E.; van Vuuren, D. P.; Rogelj, J.; Ciais, P.; Milne, J.; Canadell, J. G.; McCollum, D.; Peters, G.; Andrew, R.; Krey, V.; Shrestha, G.; Friedlingstein, P.; Gasser, T.;

Grübler, A.; Heidug, W. K.; Jonas, M.; Jones, C. D.; Kraxner, F.; Littleton, E.; Lowe, J.; Moreira, J. R.; Nakicenovic, N.; Obersteiner, M.; Patwardhan, A.; Rogner, M.; Rubin, E.; Sharifi, A.; Torvanger, A.; Yamagata, Y.; Edmonds, J.; Yongsung, C. Biophysical and economic limits to negative CO2 emissions. *Nat. Clim. Change* **2016**, *6*, 42−50.
(3) Jouny, M.; Luc, W.; Jiao, F. General Techno-Economic Analysis of CO2 Electrolysis Systems. *Ind. Eng. Chem. Res.* **2018**, *57*, 2165−2177.
(4) Zhang, W.; Hu, Y.; Ma, L.; Zhu, G.; Wang, Y.; Xue, X.; Chen, R.; Yang, S.; Jin, Z. Progress and Perspective of Electrocatalytic CO2 Reduction for Renewable Carbonaceous Fuels and Chemicals. *Adv. Sci.* **2017**, *5*, No. 1700275.
(5) Kortlever, R.; Shen, J.; Schouten, K. J. P.; Calle-Vallejo, F.; Koper, M. T. M. Catalysts and Reaction Pathways for the Electrochemical Reduction of Carbon Dioxide. *J. Phys. Chem. Lett.* **2015**, *6*, 4073−4082.
(6) Kibria, M. G.; Edwards, J. P.; Gabardo, C. M.; Dinh, C.-T.; Seifitokaldani, A.; Sinton, D.; Sargent, E. H. Electrochemical CO 2 Reduction into Chemical Feedstocks: From Mechanistic Electrocatalysis Models to System Design. *Adv. Mater.* **2019**, No. 1807166.
(7) Scibioh, M. A.; Viswanathan, B. Electrochemical Reduction of CO2. In *Carbon Dioxide to Chemicals and Fuels*; Elsevier, 2018; pp 307−371.
(8) Birdja, Y. Y.; Pérez-Gallent, E.; Figueiredo, M. C.; Göttle, A. J.; Calle-Vallejo, F.; Koper, M. T. M. Advances and challenges in understanding the electrocatalytic conversion of carbon dioxide to fuels. *Nat. Energy* **2019**, 732−745.
(9) Bienen, F.; Kopljar, D.; Löwe, A.; Assmann, P.; Stoll, M.; Rössner, P.; Wagner, N.; Friedrich, A.; Klemm, E. Utilizing Formate as an Energy Carrier by Coupling CO 2 Electrolysis with Fuel Cell Devices. *Chem. Ing. Tech.* **2019**, 872−882.
(10) Hietala, J.; Vuori, A.; Johnsson, P.; Pollari, I.; Reutemann, W.; Kieczka, H. Formic Acid. In *Ullmann's Encyclopedia of Industrial Chemistry*; John Wiley and Sons, 2016; pp 1−22.
(11) Verma, S.; Kim, B.; Jhong, H.-R. M.; Ma, S.; Kenis, P. J. A. A Gross-Margin Model for Defining Technoeconomic Benchmarks in the Electroreduction of CO2. *ChemSusChem* **2016**, *9*, 1972−1979.
(12) Agarwal, A. S.; Zhai, Y.; Hill, D.; Sridhar, N. The Electrochemical Reduction of Carbon Dioxide to Formate/Formic Acid: Engineering and Economic Feasibility. *ChemSusChem* **2011**, *4*, 1301−1310.
(13) Raistrick, I. D.; Macdonald, J. R.; Franceschetti, D. R. *Impedance Spectroscopy: Theory, Experiment, and Applications*, 3rd ed.; John Wiley and Sons, 2018; pp 21−105.
(14) Sacco, A. Electrochemical impedance spectroscopy as a tool to investigate the electroreduction of carbon dioxide: A short review. *J. CO2 Util.* **2018**, *27*, 22−31.
(15) Choi, S. Y.; Jeong, S. K.; Kim, H. J.; Baek, I.-H.; Park, K. T. Electrochemical Reduction of Carbon Dioxide to Formate on Tin−Lead Alloys. *ACS Sustainable Chem. Eng.* **2016**, *4*, 1311−1318.
(16) Lv, W.; Zhou, J.; Kong, F.; Fang, H.; Wang, W. Porous tin-based film deposited on copper foil for electrochemical reduction of carbon dioxide to formate. *Int. J. Hydrogen Energy* **2016**, *41*, 1585−1591.
(17) Daiyan, R.; Lu, X.; Saputera, W. H.; Ng, Y. H.; Amal, R. Highly Selective Reduction of CO2 to Formate at Low Overpotentials Achieved by a Mesoporous Tin Oxide Electrocatalyst. *ACS Sustainable Chem. Eng.* **2018**, *6*, 1670−1679.
(18) Zeng, J.; Bejtka, K.; Ju, W.; Castellino, M.; Chiodoni, A.; Sacco, A.; Farkhondehfal, M. A.; Hernandez, S.; Rentsch, D.; Battaglia, C.; Pirri, C. F. Advanced Cu-Sn foam for selectively converting CO 2 to CO in aqueous solution. *Appl. Catal., B* **2018**, *236*, 475−482.
(19) Qiao, J.; Liu, Y.; Zhang, J. *Electrochemical Reduction of Carbon Dioxide: Fundamentals and Technologies*; CRC Press, 2016.
(20) Azuma, M.; Hashimoto, K.; Hiramoto, M.; Watanabe, M.; Sakata, T. Electrochemical Reduction of Carbon Dioxide on Various Metal Electrodes in Low-Temperature Aqueous KHCO 3 Media. *J. Electrochem. Soc.* **1990**, *137*, 1772−1778.
(21) Narayanan, S. R.; Haines, B.; Soler, J.; Valdez, T. I. Electrochemical Conversion of Carbon Dioxide to Formate in Alkaline Polymer Electrolyte Membrane Cells. *J. Electrochem. Soc.* **2011**, *158*, A167−A173.
(22) Reier, T.; Oezaslan, M.; Strasser, P. Electrocatalytic Oxygen Evolution Reaction (OER) on Ru, Ir, and Pt Catalysts: A Comparative Study of Nanoparticles and Bulk Materials. *ACS Catal.* **2012**, *2*, 1765−1772.
(23) Lasia, A. Hydrogen Evolution Reaction. In *Handbook of Fuel Cells*; John Wiley and Sons, 2010; pp 416−440.
(24) Chen, Y.; Kanan, M. W. Tin Oxide Dependence of the CO2 Reduction Efficiency on Tin Electrodes and Enhanced Activity for Tin/Tin Oxide Thin-Film Catalysts. *J. Am. Chem. Soc.* **2012**, *134*, 1986−1989.
(25) Zhang, Y.; Chen, L.; Li, F.; Easton, C. D.; Li, J.; Bond, A. M.; Zhang, J. Direct Detection of Electron Transfer Reactions Underpinning the Tin-Catalyzed Electrochemical Reduction of CO2 using Fourier-Transformed ac Voltammetry. *ACS Catal.* **2017**, *7*, 4846−4853.
(26) Orazem, M. E.; Tribollet, B. Model-Based Graphical Methods. In *Electrochemical Impedance Spectroscopy*; John Wiley and Sons, 2008; pp 353−362.
(27) Orazem, M. E.; Tribollet, B. Kinetic Models. In *Electrochemical Impedance Spectroscopy*; John Wiley and Sons, 2008; pp 163−181.
(28) Chen, Y.; Li, C. W.; Kanan, M. W. Aqueous CO2 reduction at very low overpotential on oxide-derived Au nanoparticles. *J. Am. Chem. Soc.* **2012**, *134*, 19969−19972.
(29) Chen, Z.; Fan, T.; Zhang, Y.-Q.; Xiao, J.; Gao, M.; Duan, N.; Zhang, J.; Li, J.; Liu, Q.; Yi, X.; Luo, J.-L. Wavy SnO2 catalyzed simultaneous reinforcement of carbon dioxide adsorption and activation towards electrochemical conversion of CO2 to HCOOH. *Appl. Catal., B* **2020**, *261*, No. 118243.
(30) Wuttig, A.; Yoon, Y.; Ryu, J.; Surendranath, Y. Bicarbonate Is Not a General Acid in Au-Catalyzed CO2 Electroreduction. *J. Am. Chem. Soc.* **2017**, *139*, 17109−17113.
(31) Lee, J. H.; Tackett, B. M.; Xie, Z.; Hwang, S.; Chen, J. G. Isotopic Effect on Electrochemical CO2 Reduction Activity and Selectivity in H2O- and D2O-based Electrolytes over Palladium. *Chem. Commun.* **2019**, *56*, 106−108.
(32) Pocker, Y.; Bjorkquist, D. W. Stopped-flow studies of carbon dioxide hydration and bicarbonate dehydration in water and water-d2. Acid-base and metal ion catalysis. *J. Am. Chem. Soc.* **1977**, *99*, 6537−6543.
(33) Baruch, M. F.; Pander, J. E.; White, J. L.; Bocarsly, A. B. Mechanistic Insights into the Reduction of CO2 on Tin Electrodes using in Situ ATR-IR Spectroscopy. *ACS Catal.* **2015**, *5*, 3148−3156.
(34) Wuttig, A.; Yaguchi, M.; Motobayashi, K.; Osawa, M.; Surendranath, Y. Inhibited proton transfer enhances Au-catalyzed CO2-to-fuels selectivity. *Proc. Natl. Acad. Sci. U.S.A.* **2016**, *113*, E4585−E4593.
(35) Dubouis, N.; Grimaud, A. The hydrogen evolution reaction: from material to interfacial descriptors. *Chem. Sci.* **2019**, *10*, 9165−9181.
(36) Sluyters-Rehbach, M. Impedances of electrochemical systems: Terminology, nomenclature and representation - Part I: Cells with metal electrodes and liquid solutions (IUPAC Recommendations 1994). *Pure Appl. Chem.* **1994**, *66*, 1831−1891.

https://dx.doi.org/10.1021/acssuschemeng.9b07625
ACS Sustainable Chem. Eng. 2020, 8, 5192−5199

Supporting Information

Investigation of CO_2 electrolysis on tin foil by electrochemical impedance spectroscopy

Fabian Bienen[*†‡], *Dennis Kopljar*[†], *Simon Geiger*[†], *Norbert Wagner*[†] *and Kaspar Andreas Friedrich*[*†‡]

†Institute of Engineering Thermodynamics, German Aerospace Center, Pfaffenwaldring 38-40, 70569 Stuttgart, Germany

‡Institute of Building Energetics, Thermal Engineering and Energy Storage, University of Stuttgart, Pfaffenwaldring 31, 70569 Stuttgart, Germany

Corresponding Author

*Fabian Bienen, E-mail: Fabian.Bienen@dlr.de

*Kaspar Andreas Friedrich, E-mail: Andreas.Friedrich@dlr.de

Number of pages: 7

Number of figures: 5

Number of tables: 1

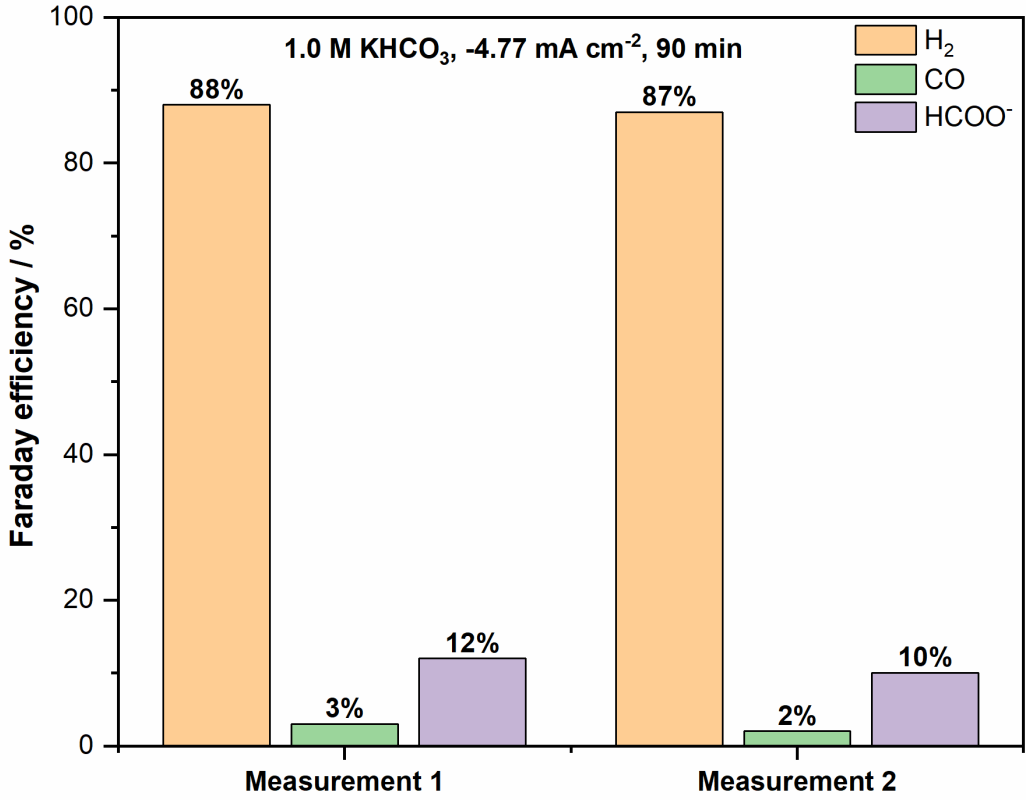

Figure S1 Faraday efficiency determination of H_2, CO and $HCOO^-$ after galvanostatic operation at - 4.77 mA cm^{-2} in CO_2 saturated 1.0M $KHCO_3$ aqueous solution showing reproducible results and by that validating the test set-up. During EIS measurements shown in the primary paper further liquid phase $HCOO^-$ determination was skipped due to the lack of possibility to quantify $HCOO^-$ online. H_2 and CO were quantified online via µ-GC and used to calculate the faraday efficiency for formate via the mass balance closing condition.

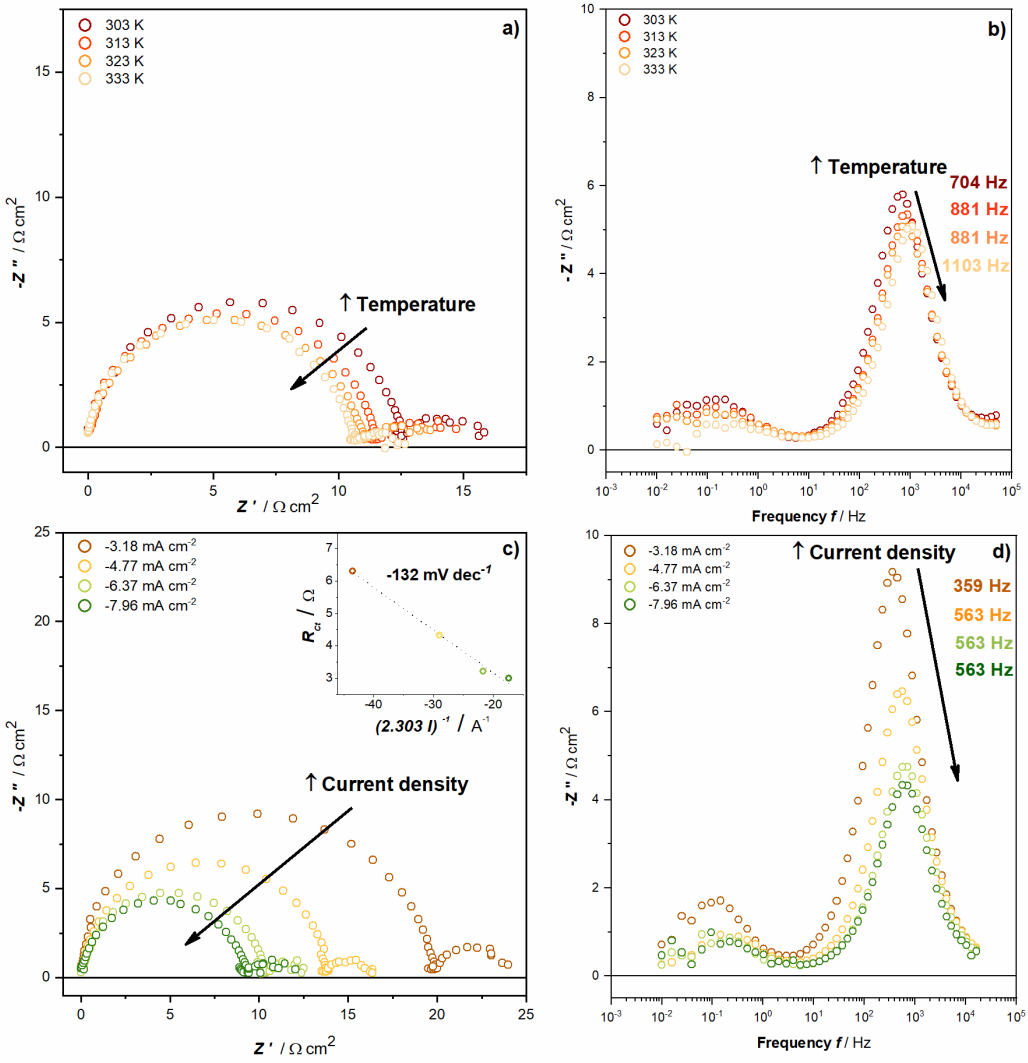

Figure S2 –Nyquist plots for tin foil (ohmic resistance subtracted) of **a)** temperature and **c)** current density parameter series to identify thermal and current activated processes in 1.0 M $KHCO_3$ solution and their corresponding imaginary part vs. frequency plots **b), d)**. Inset **c)** Tafel slope determination via R_{Ct} vs. I^{-1} plot.

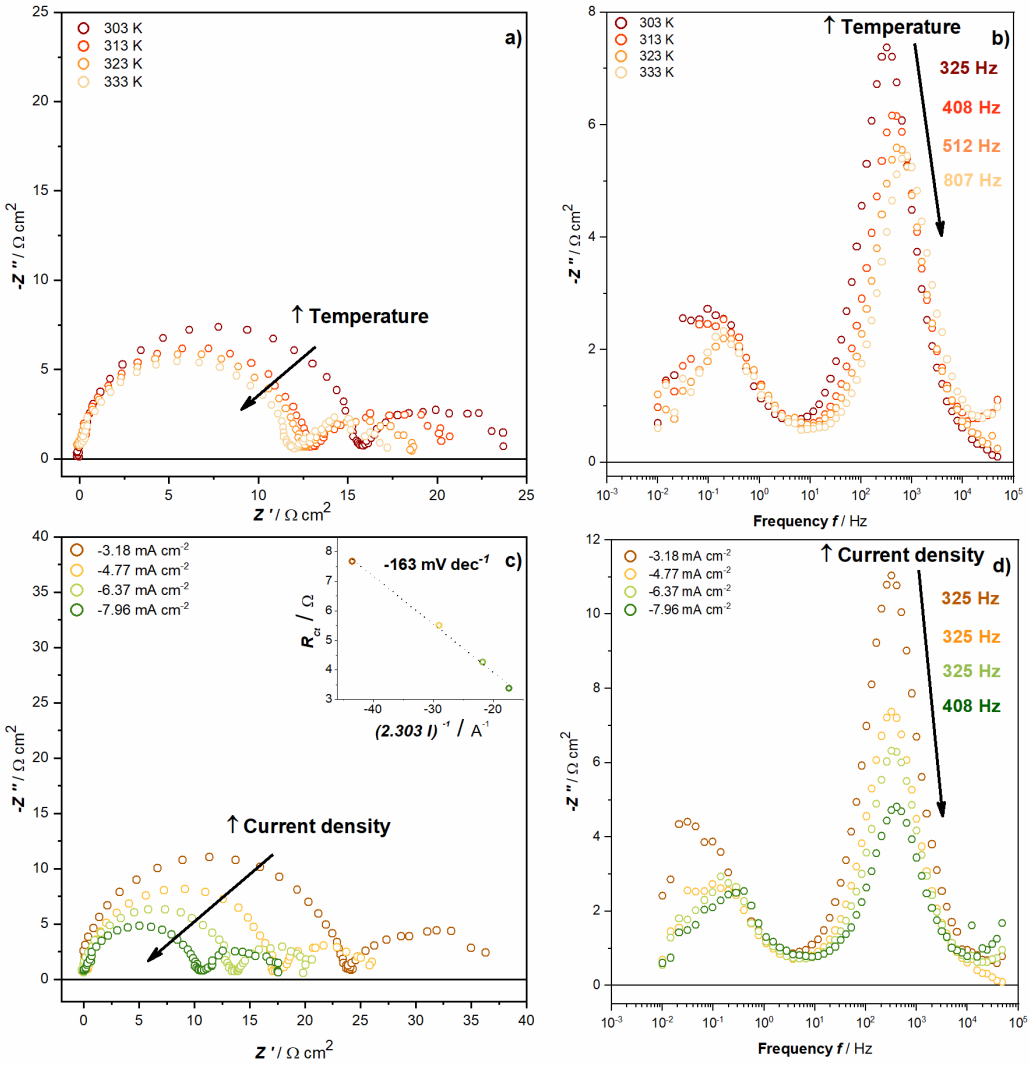

Figure S3 –Nyquist plots for tin foil (ohmic resistance subtracted) of **a)** temperature and **c)** current density parameter series to identify thermal and current activated processes in 0.1 M $KHCO_3$ solution and their corresponding imaginary part vs. frequency plots **b), d)**. Inset **c)** Tafel slope determination via R_{Ct} vs. I^{-1} plot.

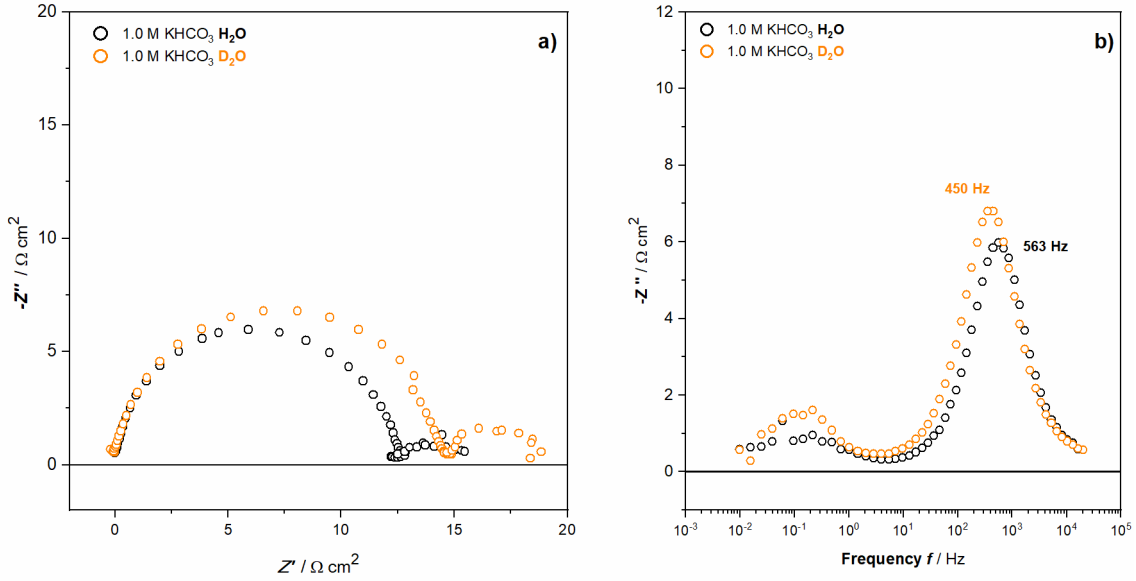

Figure S4 Impedance spectra **a)** and **b)** imaginary part vs. frequency plot for tin foil obtained in CO_2 saturated 1.0 M $KHCO_3$ solution comparing H_2O and D_2O as solvent. Galvanostatic operation at – 4.77 mA cm^{-2} with an amplitude of 5mA, ohmic resistance subtracted.

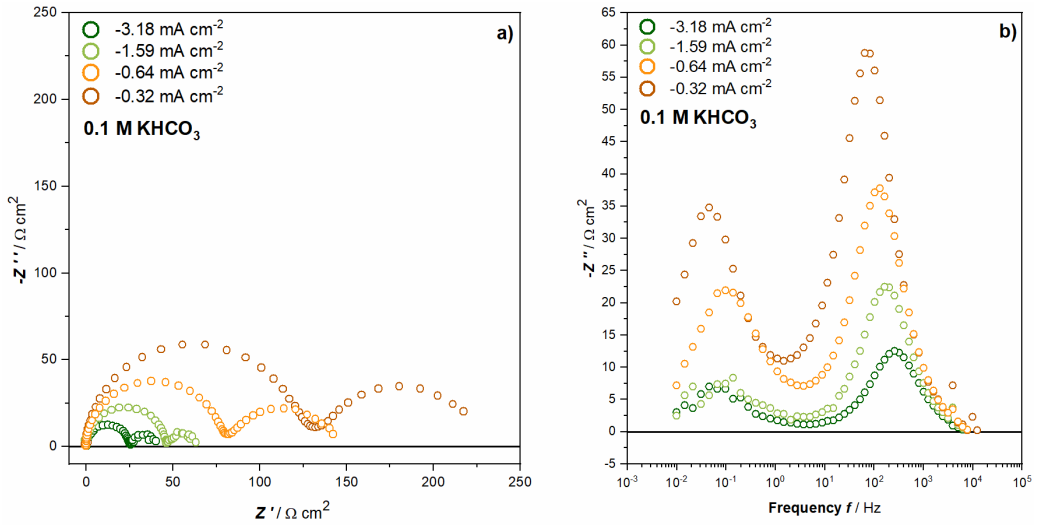

Figure S5 Impedance spectra **a)** and **b)** imaginary part vs. frequency plot for tin foil obtained in CO_2 saturated 0.1 M $KHCO_3$ solution for low current densities. Galvanostatic operation at desired current densities with an amplitude of 5mA, ohmic resistance subtracted.

In contrast to S3 c) and d) the low frequency process clearly depends on the applied current for extremely low current levels. However, further investigation would go beyond the scope of this contribution since at these low current densities, respectively potentials, the EIS response is almost completely determined by HER and the product analysis unreliable (due to low current densities resulting in low conversion rates). Therefore, the faraday efficiency for CO_2RR is almost negligible, thus, with low relevance to the target of this investigation.

Table S1 Resistance and Capacitor values inserted into Thales® EQCM modelling tool. Time constant τ, R_{mixed} and C_{mixed} calculated via Equation S1-S3.

Ratio time constants	R_{HER} / Ω	C_{HER} / F	τ_{HER} / s	R_{CO2RR} / Ω	C_{CO2RR} / F	τ_{CO2RR} / s	R_{mixed} / Ω	C_{mixed} / F	τ_{mixed} / s
$\tau_1 = \tau_2$	1	0.01	0.01	1	0.01	0.01	0.5	0.02	0.01
5 $\tau_1 = \tau_2$	1	0.01	0.01	2.5	0.02	0.05	0.714	0.03	0.021
100 $\tau_1 = \tau_2$	1	0.01	0.01	10	0.1	1	0.909	0.11	0.100
1000 $\tau_1 = \tau_2$	1	0.01	0.01	20	0.5	10	0.952	0.510	0.486

$$\tau = R \bullet C \tag{S1}$$

$$\frac{1}{R_{mixed}} = \frac{1}{R_{HER}} + \frac{1}{R_{CO2RR}} \tag{S2}$$

$$C_{mixed} = C_{HER} + C_{CO2RR} \tag{S3}$$

ACS Sustainable Chemistry & Engineering

pubs.acs.org/journal/ascecg

Research Article

Revealing Mechanistic Processes in Gas-Diffusion Electrodes During CO_2 Reduction via Impedance Spectroscopy

Fabian Bienen,* Dennis Kopljar, Armin Löwe, Simon Geiger, Norbert Wagner, Elias Klemm, and Kaspar Andreas Friedrich*

Cite This: *ACS Sustainable Chem. Eng.* 2020, 8, 13759−13768

Read Online

ACCESS | Metrics & More | Article Recommendations | Supporting Information

ABSTRACT: The use of gas-diffusion electrodes (GDEs) as CO_2 converting electrodes increases the achieved current densities for the CO_2 reduction reaction (CO_2RR) by a multiple (>100 mA cm^{-2}) compared to planar electrodes (10 mA cm^{-2}), whereas the long-time stability of the employed GDEs is a crucial factor for the industrial realization of this technology. We investigated carbon-supported tin-based GDEs by electrochemical impedance spectroscopy with the goal to identify the underlying physical processes by varying the applied current density, temperature, CO_2 partial pressure, and electrolyte, an unexplored task so far. The spectrum displays four features which we interpreted as (i) ionic and electronic conductivity in the porous system, (ii) reaction of CO_2 with OH^- to form bicarbonate, (iii) charge transfer converting CO_2 (aq) to $CO_2^{\bullet-}$, and (iv) liquid phase diffusion of CO_2 (aq). Besides the assignment of the physical processes to the features obtained in the spectrum, we conclude that the observed spectrum shape is affected by CO_2RR and hydrogen evolution reaction, whereby the shape dominating reaction switches with varying experimental conditions such as temperature, CO_2 volume fraction, current density, and electrolyte.

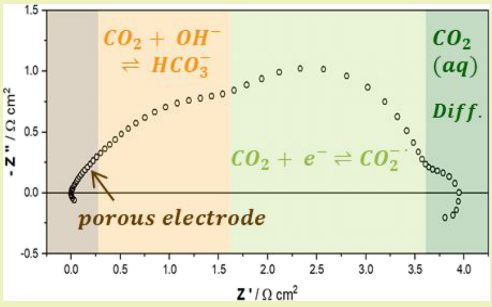

KEYWORDS: *CO_2 electrolysis, CO_2RR, electrochemical impedance spectroscopy, tin, gas-diffusion electrode, GDE, CO_2*

INTRODUCTION

All countries that signed the Paris agreement have committed to reduce greenhouse gas emissions according to the target to keep global warming well below 2 °C with regard to preindustrial values. This entails significant efforts to reduce the carbon footprint of all sectors in the following decades. Because industrial processes significantly contribute to the overall emissions of industrialized countries, for example, in the EU-28 with 8%, the development of innovative routes with lower or negligible CO_2 emissions that can substitute traditional processes based on fossil resources can make a contribution to achieve the desired targets.[1−3] The electrochemical conversion of CO_2 using renewable energy not only substitutes conventional CO_2-intensive processes based on fossil resources but also utilizes CO_2 itself as a feedstock, thereby making it a valuable carbon source.[4−6] Depending on the catalysts and reaction conditions, several carbon-based products can be obtained by the cathodic electrochemical reduction of CO_2.[7,8]

This work focuses on the tin-catalyzed conversion of CO_2 to obtain formate as the target product. Typically, CO_2 is not solely converted to formate (eq 1) on tin catalysts but also to carbon monoxide to a lower extent (eq 2), while the aqueous electrolyte is reduced to hydrogen (eq 3) in a parasitic side reaction, reducing the charge efficiency with respect to formate formation, according to the following equations

$$CO_2 + H_2O + 2e^- \rightleftharpoons HCOO^- + OH^- \quad (1)$$

$$CO_2 + H_2O + 2e^- \rightleftharpoons CO + 2OH^- \quad (2)$$

$$2H_2O + 2e^- \rightleftharpoons H_2 + 2OH^- \quad (3)$$

Formate can be used as a deicing agent or drilling fluid as well as for tanning and silage when protonated to formic acid.[9] In a proof-of-concept study, it was also shown that formate obtained via CO_2 reduction reaction (CO_2RR) can be utilized as energy carrier and fed into a direct formate fuel cell to produce electricity or after catalytic decomposition to hydrogen with subsequent re-electrification in a typical polymer electrolyte membrane fuel cell.[10,11]

Unfortunately, the conversion of dissolved CO_2 on planar electrodes is limited to a maximum current density of well below 10 mA cm^{-2} because of mass transport constraints evoked by the low solubility of CO_2 in the aqueous electrolyte (33 mM L^{-1} in H_2O, 25 °C, 1 atm) and the diffusion of dissolved CO_2 from the bulk electrolyte to the electrode

Received: June 17, 2020
Revised: August 6, 2020
Published: August 20, 2020

surface.[7,12,13] This limitation can be circumvented by the use of so-called gas-diffusion electrodes (GDEs) providing a porous architecture and intensifying the contact between the gas-, liquid-, and solid phases. Their use entails a substantial increase in the number of active sites while the diffusion length of dissolved CO_2 to the catalyst surface is reduced. Accordingly, gaseous CO_2 can be employed as the substrate and, due to the above effects; the macroscopic mass transport of the reactant is substantially accelerated.[14−16] As a result, the achievable current densities when using GDEs for CO_2 electrolysis can be increased by more than an order of magnitude compared to planar electrodes without sacrificing selectivity toward CO_2RR products.[17−19] The so far achieved current densities which are already on industrially relevant orders are the reason why GDEs have gained increasing interest in recent years for the investigation of CO_2 electrolysis systems.[15,19−21] Nevertheless, long-term stability of these GDEs is an under-represented research topic in the literature. Besides potential catalyst degradation, GDEs might suffer from a change of their hydrophobic properties over time, resulting in flooding, efficiency losses, and in a shift of the product selectivity toward the undesired hydrogen evolution.[22,23] In that respect, electrochemical impedance spectroscopy (EIS) is a powerful tool to deconvolute contributions of specific physical and (electro)chemical processes to the overall resistance during operation of electrochemical devices. The knowledge which process (e.g., charge-transfer, mass transport of reactants) determines the polarization resistance gives valuable insights required for the rational optimization of the employed GDEs and can aid in revealing possible degradation mechanisms. To use EIS as an electrochemical diagnostic tool, it is crucial to know which physical phenomena are observed in the measured impedance spectra. As described in one of our previous contributions on the use of EIS to investigate planar tin electrodes during CO_2RR, there is a lack of knowledge on how to analyze and interpret EIS measurements for CO_2 reduction. This is because most authors use EIS solely as an additional tool to characterize their catalyst materials or electrodes without a detailed investigation of the underlying processes observed in the spectrum.[24−26] However, as we have shown, because of the competitive nature of the reaction [hydrogen evolution reaction (HER) vs CO_2RR], single features in the spectrum cannot unequivocally be assigned to one specific reaction and used as argument to compare catalytic performance as such. Only a few studies in the literature perform a more elaborate analysis of the EIS spectra. Wang et al. for example used EIS as an additional characterization method to investigate their tin-based GDEs in the aqueous $KHCO_3$ electrolyte. They observed two arcs in the Nyquist spectrum and assigned the lower frequency arc to a not further specified charge transfer because the diameter of the arc decreases with increasing overpotential. The high-frequency process was correlated with the ionic migration in the liquid film inside the GDE.[27−29] In another contribution, Verma et al. recorded impedance spectra in different concentrations of aqueous KOH electrolytes in a flow reactor with a Ag-based GDE cathode and IrO_2 as an anode in the frequency range of 10 kHz to 0.1 Hz. They observed one semicircle and found that the cell resistance and the charge transfer, described by the observed semicircle, decrease with increasing KOH concentrations.[30] The fact that the HER occurs in parallel to the CO_2RR on the same electrode competing for the same active sites and by that affecting the obtained impedance spectrum is usually not considered in reports using EIS as a characterization method. In this contribution, we want to expand our previous rather fundamental investigation for tin foil electrodes to the industrially more relevant GDEs.[31] The aim is to identify the underlying physical and chemical processes observed in the impedance spectrum for GDEs used in CO_2 electrolysis to provide information for the sophisticated optimization of CO_2 converting GDEs and reveal possible degradation mechanisms.

EXPERIMENTAL SECTION

Preparation of Gas-Diffusion Electrodes. The catalyst powder was prepared, as reported previously.[19] Briefly, SnO_x was precipitated onto acetylene black (AB) (Alfa Aesar, 100% compressed, 99.9+%) from aqueous solution using $SnCl_2 \times 2H_2O$ (Carl Roth, >98%) as a precursor. The slurry contained urea (Carl Roth, >99.5%) as a precipitating agent, which was hydrolyzed at 90 °C. Thereby, formed ammonia gives a homogeneous raise to the pH value, inducing the $Sn(OH)_x$ precipitation process. The catalyst powder was filtered, washed, and dried in air at 100 °C. The catalyst loading was 2.5 wt % referred to be metallic Sn on AB (determined by thermogravimetric analysis). The electrode preparation is based on a previous reported procedure.[32] The catalyst powder was mixed in a knife mill with polytetrafluoroethylene (PTFE) (Dyneon, TF 92070Z) at a C/PTFE ratio of 65:35. The powder was then filled in a cylindrical mask with a diameter of 39 mm and a height of 10 mm. The mask was completely filled with the powder mixture while the overlapping excess powder was removed via doctor blading. Afterward, the corresponding counterpart of the cylindrical mask was carefully inserted into the mask, followed by a hydraulic pressing step for 1 min at 10.5 kN cm^{-2}. Thermal treatment for 60 min at 340 °C (heating ramp 5.3 K min^{-1}) complemented the GDE manufacturing process.

Physical Characterization. The GDEs morphology and the catalyst dispersion were studied using a scanning electron microscope (SEM, Zeiss ULTRA PLUS) with an acceleration voltage of 2.00 kV and a magnification of 20k and 50k. The angle-selective back scattered electron detector was used to obtain material contrast images and by that showing the catalyst dispersion. Furthermore, mercury intrusion porosimetry (MIP) was applied to obtain information about the porosity and the pore size distribution of the GDE. The surface of the GDE was investigated by X-ray photoelectron spectroscopy (XPS) using a Thermo Scientific ESCALAB 250 ultra-high vacuum (1×10^{-9} bar base pressure) X-ray photoelectron spectrometer with a Al Kα source (Thermo Scientific XR4).

Electrochemical Characterization. All experiments were performed in a common three-electrode setup (cf. Figure S1). The geometrical surface of GDE exposed to the electrolyte was 1 cm^2. In all experiments, the reversible hydrogen electrode was used as the reference electrode, whereas platinum foil served as the counter electrode. If not stated otherwise, the temperature of the electrolyte, 1.0 M KOH, was 30 °C. The backpressure of the GDE was adjusted to 3 mbar g using a dip tube and water column. The KOH electrolyte was obtained by mixing solid KOH pellets (Chemsolute ≥85%) with in-house purified water (ion-exchange, resistivity > 18 MΩ). For designated experiments, deuterium oxide (99.9 atom % D, Sigma-Aldrich) was used as solvent for KOH, whereas the KOH pellets for these experiments had a purity of 99.98% (Acros Organics). The gas supply consisting of CO_2 (4.5, Linde), N_2 (5.0, Linde), or a mixture of both was introduced at a flow rate of 50.0 mLn min^{-1} toward the back side of the GDE. The mixtures of N_2 and CO_2 were obtained via mixing in T-fitting using mass-flow controllers (Bronkhorst EL-FLOW Select). For all electrochemical tests, a ZAHNER-elektrik GmbH & Co. KG Zennium electrochemical workstation and the corresponding evaluation software Thales were used.

EIS were recorded in the range of 10 mHz to 300 kHz in a galvanostatic operation mode while the excitation current for every experiment was 10 mA. The reference parameter set at 30 °C was a load of −50 mA cm^{-2} for a measurement in 1.0 M KOH aqueous

https://dx.doi.org/10.1021/acssuschemeng.0c04451
ACS Sustainable Chem. Eng. 2020, 8, 13759−13768

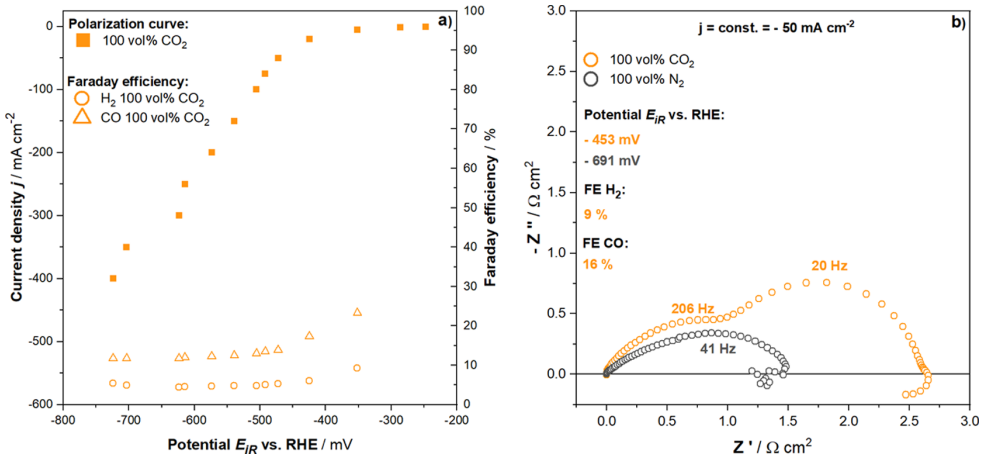

Figure 1. (a) Polarization curve and FEs obtained during CO_2 electrolysis using aqueous 1.0 M KOH as the electrolyte and (b) impedance spectra recorded in a galvanostatic operation mode employing pure CO_2 and N_2 as feed gas.

solution and a pure CO_2 feed with a flow rate of 50.0 mLn min^{-1}. The current dependent behavior of the GDE was investigated by conducting EIS measurements at −25, −50, −75, −100, and −125 mA cm^{-2}, the thermal-dependent characteristic of the GDE was studied at 30, 40, 50, and 60 °C. To identify CO_2 volume fraction-dependent processes, the partial pressure of CO_2 varied by mixing N_2 into the feed gas, maintaining a total gas flow of 50.0 mLn min^{-1}. Consequently, the impedance spectra were recorded for 100, 70, 50, 30, 20, and 0 vol % CO_2. Additionally, a current series was conducted at the abovementioned loads for a gas feed containing 20 vol % CO_2 and 80 vol % N_2. To identify processes involving hydrogen containing species, deuterium oxide was used as solvent to prepare 1.0 M KOH solutions. Before recording any impedance spectra, the system was polarized for 10 min at the desired experimental parameter set. Immediately after these 10 min, the measurement started without current interruption. At least three consecutive spectra (approx. 7 min relaxation time under load between each run) were recorded for each experimental parameter set of which the second spectrum was used for evaluation. In contrast to the first spectrum, the second spectrum is close to steady-state conditions, and the observed changes during the following consecutive spectra were significantly smaller compared to the changes from the first to the second spectrum. Experiments were repeated for at least one more time to ensure reproducible results. To make the comparison more straightforward, the Nyquist data were shifted to the same origin by subtracting the ohmic resistance.[31]

The Faraday efficiencies (FEs) were measured during the EIS measurements at the given parameter set. The volume fractions of the gaseous products H_2 and CO in the gas stream were quantified by a micro gas chromatograph (μ-GC, Varian) with a resolution of 5 min. The obtained gaseous product volume fractions during the recording of the second impedance spectrum (used for evaluation) were averaged. The averaged volume fractions were then multiplied with the inlet volume flow of the feed gas to obtain the gas flow of the reaction products (the error of the CO_2 flow rate, used for the calculation of the FEs, induced by the conversion of CO_2 with OH^- of the electrolyte and OH^- produced during the electrochemical reaction is estimated in the Supporting Information). By calculating the ratio of the experimental and theoretical product flows (applying Faraday's law), the FE was determined. The FE for formate was calculated as difference from 100% and the FEs of H_2 and CO since tin is known to exclusively produce H_2, CO, and formate in aqueous alkaline media.[7,33] Additionally, we showed in a previous work that only these three products are generated in a significant amount during CO_2RR using our in-house manufactured GDEs.[19]

A polarization curve was obtained for pure CO_2 as feed gas by a stepwise increase of the current load (−0.5 mA cm^{-2} to −400 mA cm^{-2}). Each current retained for 15 min whereas the corresponding potential was logged after these 15 min before changing to the next current. Simultaneously measured volume fractions of the gas phase products via μ-GC were averaged (three data points) and used to calculate the FE. After each current step, before changing to the new current, the high-frequency resistance was measured at the present current to calculate the *iR*-drop at the specific current. Before recording these polarization curves, the GDEs were preconditioned at −50 mA cm^{-2} for 10 min to achieve a reproducible wetting at the beginning of the polarization curve measurement. The experiments were reproduced at least once.

RESULTS AND DISCUSSION

EIS is a powerful tool to analyze rate-determining processes during electrochemical reactions. However, the evaluation of the impedance spectra is not trivial and one needs to have detailed knowledge on the contributions that can be observed in the spectra. By recording impedance spectra as a function of the applied current, temperature, CO_2 partial pressure, and electrolyte composition, we want to elucidate the nature of the observed features and the underlying processes during electrochemical reduction of CO_2 on tin-based GDEs. The physical characterization of the GDE is depicted in the Supporting Information (Figure S2).

Electrochemical Impedance Spectroscopy. Before discussing the results of the EIS measurement, it is useful to get a general understanding of CO_2 reduction employing the GDEs manufactured in our laboratory. A polarization curve for the GDE operated with 100 vol % CO_2 in 1.0 M KOH at 30 °C is depicted in Figure 1a. The curve was recorded via a stepwise increase of the current and logging the corresponding potential after 15 min at each value. At the maximum current, −400 mA cm^{-2}, the potential is approx. −725 mV with a FE for CO and H_2 of about 12 and 5%, respectively. The remaining 83% is attributed to the production of formate. A slight scattering of the potentials at higher currents is induced due to the gas evolution at the GDE surface making a precise potential determination impossible. The observed FEs for CO (~12%) and H_2 (~5%) remain nearly constant for potentials of −450 mV to −725 mV. This fact indicates that even at a current density of −400 mA cm^{-2}, no mass transport limitation for CO_2 is observed because otherwise the FE for H_2 would increase. For 1 and 0.5 mA cm^{-2}, the FEs were not determined

https://dx.doi.org/10.1021/acssuschemeng.0c04451
ACS Sustainable Chem. Eng. 2020, 8, 13759−13768

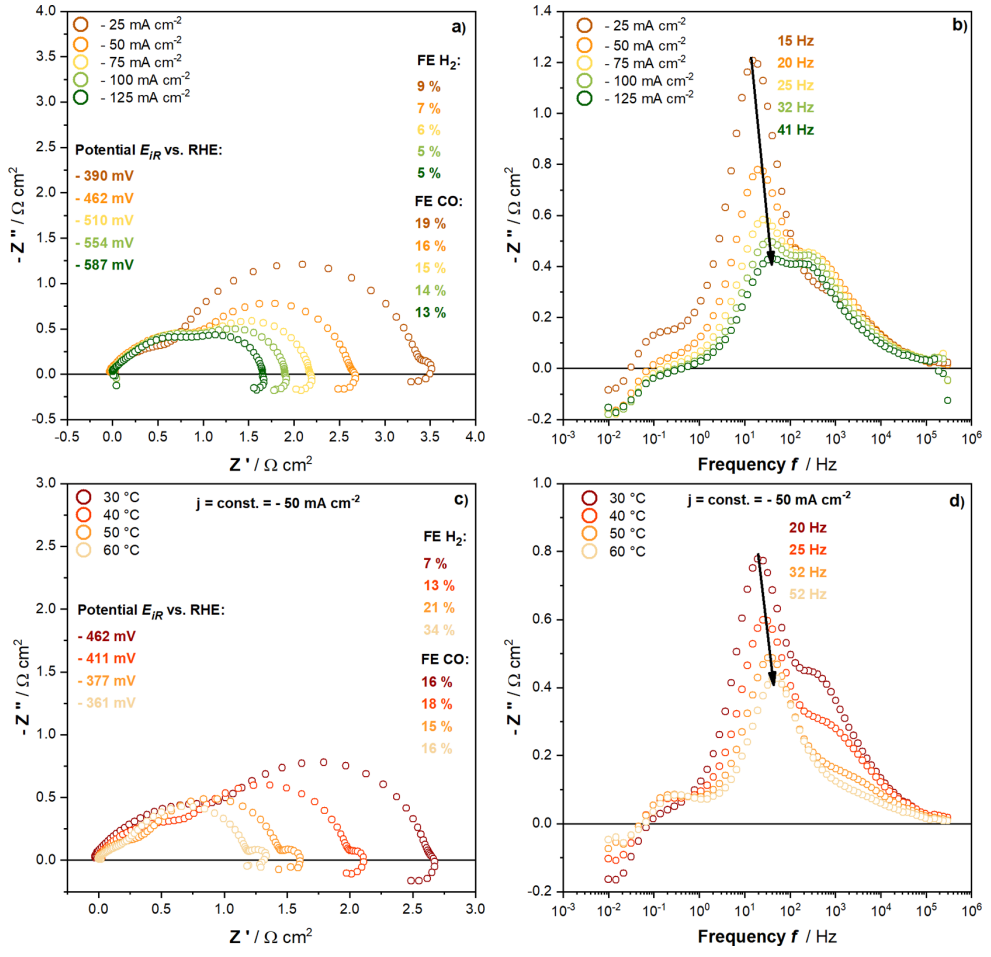

Figure 2. Impedance spectra obtained during CO_2 electrolysis for (a) current density and (c) temperature parameter series to identify current- and thermal-activated processes and their corresponding imaginary part vs frequency plots (b,d).

because the quantification error would be too high due to the low amount of charge involved.

Impedance spectra recorded at −50 mA cm^{-2} in 1.0 M KOH at 30 °C for 100 vol % CO_2 and 100 vol % N_2, respectively, are shown in Figure 1b in the so-called Nyquist representation in which the negative of the imaginary impedance is plotted over its real part. The measurement frequency decreases from left to right. The spectrum obtained for N_2 displays two features: in the high-frequency range (left part of the figure), a 45° slope is observed which is determined by the ionic and electrical conductivity inside the porous electrode.[34] The second feature occurs at around 41 Hz and represents at least one process. The EIS spectrum for pure CO_2 is more complex and shows a higher polarization resistance compared to the operation with pure N_2. This observation, which is important for later interpretation, shows that at conditions where only HER takes place, that is, in the absence of gaseous CO_2, the polarization resistance is significantly smaller compared to the case when CO_2RR is contributing to charge conversion. This fact suggests that the existence of CO_2 inside the GDE increases the resistance for the HER because otherwise CO_2 conversion would be barely observed due to the higher polarization resistance. However, the spectrum obtained for pure CO_2 gas feed shows that at high frequencies, the ionic and electrical conductivity determine the shape of the spectrum in a similar way observed for the EIS data obtained in a N_2 atmosphere. Significant features occur at approximately 206 and 20 Hz and indicate the existence of at least two faradaic processes. At even lower frequencies, a small shoulder can be recognized where the curve intersects with the *x*-axis again, denoting the existence of another process in the low-frequency regime. An inductive contribution in the low-frequency region—which we observe as well—is a wide discussed topic in fuel cell science and cannot be explained unequivocally until today. Typically, this feature is attributed to slow adsorption/desorption processes of reaction intermediates, the blocking of active sites with catalyst poison, or the migration of charged species inside a porous electrode.[35,36] However, this part of the spectrum will not be further discussed in the following because we will focus on the elucidation of the high- and medium-frequency process and a potential low-frequency process. The identification of the corresponding underlying physical processes is the overarching target of the experiments shown in this contribution. First of all, we analyzed the thermal- and current-dependent behavior of the impedance spectrum.

Temperature- and Current-Dependent Behavior. In Figure 2, the current- and temperature-dependent Nyquist and

https://dx.doi.org/10.1021/acssuschemeng.0c04451
ACS Sustainable Chem. Eng. 2020, 8, 13759−13768

ACS Sustainable Chemistry & Engineering pubs.acs.org/journal/ascecg Research Article

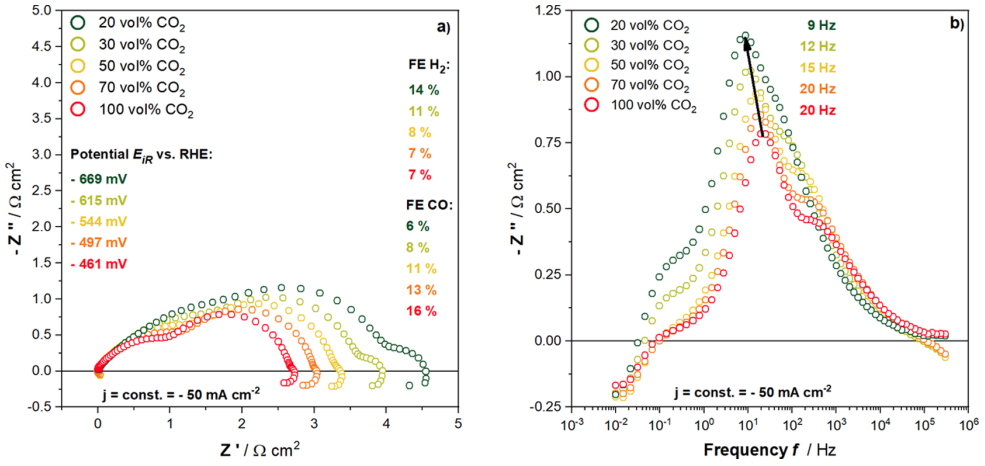

Figure 3. (a) Impedance spectra recorded during CO_2 electrolysis for varying CO_2 volume fractions in the feed gas and (b) corresponding imaginary part vs frequency plots.

imaginary impedance versus frequency plots are shown. The obtained FEs for H_2 and CO during the EIS measurements are in good agreement with the observed values for the FE acquired during the measurement of the polarization curve. The medium-frequency process around 20 Hz shows a distinct dependence on the applied current. A higher current leads to an exponential decrease of the corresponding medium-frequency resistance (cf. Figure 2a). Additionally, Figure 2b reveals that the characteristic frequency of this resistance shifts to higher values when increasing the current. The exact same trends can be observed for the medium-frequency process for an increase of temperature (cf. Figure 2c,d). This temperature- and current-dependent behavior is commonly associated with a charge-transfer process and strongly indicates that the medium-frequency process displays a charge-transfer reaction.[34,37] A process in the low-frequency region (on the right in the Nyquist plot) can be observed for the lowest current density of −25 mA cm^{-2} (cf. Figure 2a). On the other hand, this process becomes already visible at −50 mA cm^{-2} when increasing the temperature to above 30 °C (cf. Figure 2c). Typically, diffusion processes are displayed at low frequencies which we will be investigating in the following sections.[34] The process in the high-frequency domain is slightly activated with an increase of the current load. This behavior is further manifested in the difference plots of the imaginary parts of the spectra referenced for the one at −50 mA cm^{-2} (except for −25 mA cm^{-2}) (cf. Figure S4a). This high-frequency process is also activated with a temperature increase (cf. Figures 2d and S4b). Interestingly, the FEs obtained during EIS at more or less similar potential for the current and temperature series (comparing spectrum −25 mA cm^{-2} with the spectrum at 50 °C) differ from each other showing that the shift of FEs during the temperature series is not just a result of different applied potentials. The activation energies for the thermal-activated high- and medium-frequency processes are determined via the Arrhenius plot (cf. Figure S6). The corresponding activation energy for the high-frequency process is about 43.0 ± 2.2 kJ mol^{-1}, while for the medium-frequency process, a charge transfer, an activation energy of 16.2 ± 1.4 kJ mol^{-1} was calculated. In the next step, the CO_2 partial pressure varied to reveal processes affected by the CO_2 volume fraction.

Effect of CO_2 Partial Pressure. The impact of the CO_2 partial pressure on the shape of the EIS spectra at −50 mA cm^{-2} is depicted in Figure 3. It is evident that the polarization resistance increases when the CO_2 partial pressure is reduced. The resistance of the medium-frequency process, which has been ascribed to the charge transfer, increases with the decreasing CO_2 volume fraction, and the characteristic frequency shifts to lower values (cf. Figure 3b). This indicates that this charge-transfer process is positively affected by high CO_2 volume fractions in the gas phase which determine the concentration of dissolved species in the electrolyte according to Henry's law. As a result, this process can be ascribed to a rate-limiting charge transfer occurring in the CO_2RR mechanism which is improved according to the concentration of active species. The process observed in the high-frequency region exhibits a lower resistance by higher CO_2 partial pressures as well. According to the results presented in the following, we suggest that this process represents the equilibrium reaction between dissolved CO_2 with hydroxide ions in the alkaline electrolyte according to

$$CO_2 + OH^- \rightleftharpoons HCO_3^- \quad (4)$$

It was shown in a kinetic study by Pohorecki et al. that the activation energy for this reaction is about 45.1 kJ mol^{-1} in 0.85 mol L^{-1} KOH which fits to our calculated activation energy for this process of 43.0 ± 2.2 kJ mol^{-1} (see above).[38] A density functional theory study by Cui et al. supports this as well since at the hydroxylated tin surface, which we expect to be present in our GDE, the conversion of CO_2 to HCO_3^- is an integral part of the reaction mechanism and has an activation energy of 0.47 eV ≙ 45.4 kJ mol^{-1}.[39] The aforementioned decrease of the high-frequency resistance with increasing current densities (as shown in the differential plots of Figure S4a) can now be explained because of the increased local OH^- concentration at high current densities (cf. eqs 1−3) accelerating the homogeneous reaction of CO_2 and OH^- to form bicarbonate.

The volume fraction of CO_2 can be reduced to 50 vol % without having any effect onto the low-frequency process. The indicated small arc at low frequencies remains the same size as well as the FE for H_2. This behavior changes when reducing the CO_2 volume fraction below 50 vol % to 30 vol %. A low-

https://dx.doi.org/10.1021/acssuschemeng.0c04451
ACS Sustainable Chem. Eng. 2020, 8, 13759−13768

ACS Sustainable Chemistry & Engineering pubs.acs.org/journal/ascecg Research Article

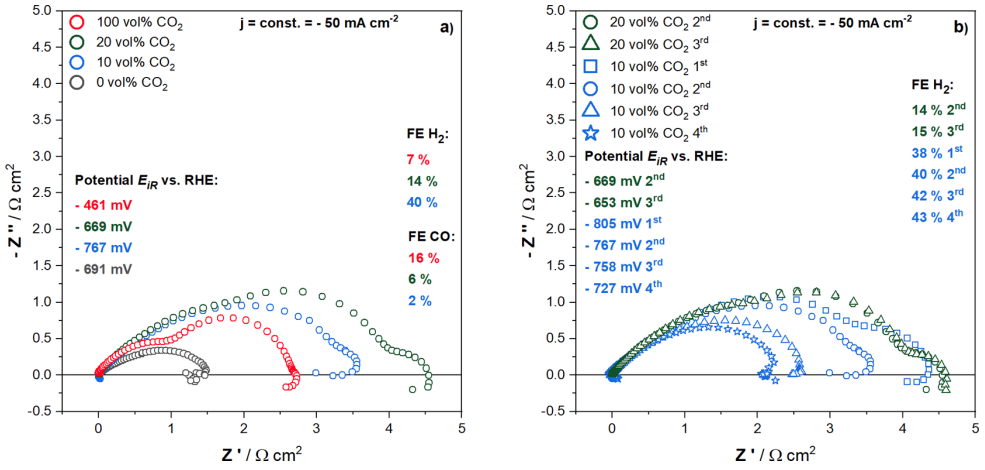

Figure 4. (a) Impedance spectra recorded during electrolysis for varying CO_2 volume fractions in the feed gas and (b) time-dependent behavior of the impedance spectra for the operation with 20 and 10 vol % CO_2 in the feed gas.

frequency arc becomes more pronounced which is intensified when the CO_2 volume fraction is further decreased to 20 vol %. In contrast to CO_2 volume fractions of 100, 70, and 50 vol % where the FE for H_2 is constant (~7%), the values are now increased to 11 and 14% which we think is a result of the depletion of the carbon containing active species due to the low CO_2 partial pressure. These observations indicate that the low-frequency process corresponds to the diffusion of the carbon containing active species to the active site. When taking the shape of the diffusional process into account, it can be further specified as a finite-length diffusion process with a characteristic finite diffusion layer thickness.[40] As shown before, the observed arc in the low-frequency region increases with rising temperatures (cf. Figure 2c) which seems to be counter intuitive to our interpretation because diffusion processes are usually accelerated at higher temperatures, but on the other hand, the CO_2 solubility is significantly reduced at higher temperatures which might be overcompensating the accelerated diffusion.[7]

Figure 4a displays the already known EIS spectra recorded for 100 and 20 vol % and the now introduced spectra recorded for 10 and 0 vol % CO_2 in the feed gas. This figure shows that decreasing the CO_2 volume fraction beyond a certain volume fraction, in our specific case 10 vol %, the above trend becomes reversed and the polarization resistance decreases. The presented behavior points toward the complexity of analyzing EIS data for CO_2RR as it demonstrates how the HER becomes the dominant process in the impedance spectrum because the total resistance of the HER for the operation with 10 vol % CO_2 in the feed gas is lower compared to the CO_2RR resistance. The fact that the FE for H_2 dramatically increases from 14 to 40% when reducing the CO_2 volume fraction from 20 to 10 vol % supports this theory. We recently demonstrated for tin foil electrodes that parallel occurring reactions like HER and CO_2RR during CO_2 electrolysis will both affect the shape of the impedance spectrum.[31] Following the rules of electrical engineering for parallel resistors, it can be assumed that the process with lower total resistance dominates the spectrum. The dynamic shape of the impedance spectrum recorded for GDEs supplied with 10 vol % CO_2 in the feed gas stream becomes even more evident when taking a look at the time-dependent change of the spectrum (cf. Figure 4b). Typically, the EIS measurements are recorded at steady-state, that is, the first spectrum is always discarded due to conditioning effects. This holds true for operation at 20 vol % for which the second and third spectrum look almost identical. However, it can be observed for the measurements with 10 vol % CO_2 that the appearance of the spectrum is significantly changed with time and that it becomes more similar to the shape of the spectrum obtained for pure N_2 as feed gas. Accordingly, the polarization resistance is reduced significantly. The very first spectrum reveals a vast diffusional arc which is more pronounced compared to the spectrum recorded for 20 vol % CO_2. This indicates that at the beginning, the spectrum is still dominated by CO_2RR and that the HER becomes increasingly dominant due to a lasting depletion of the carbon containing active species for the CO_2RR inside the GDE. As a result, no diffusional arc can be observed in the 3rd and 4th spectrum and the polarization resistance approaches values comparable to the operation with pure N_2. The same can be observed for a current series with 20 vol % CO_2 (cf. Figure S7): the impedance spectra have a similar shape for currents between −25 and −100 mA cm^{-2} while only a slight change of the FE for H_2 can be observed. When further reducing the current to −125 mA cm^{-2}, the FE toward hydrogen increases by around 9% and the spectrum is changing its shape. In particular, the diffusional process of the carbon containing active species which should be accented at higher currents vanishes and the spectrum looks more like the spectrum obtained for the operation with pure N_2 where the HER is the sole reaction (cf. Figure 1b).

For a better classification of the results, we added a brief comparison in the Supporting Information where the above shown spectra for GDEs are compared with the spectra recorded for the operation of tin foil electrodes (cf. Figure S9). The results for the tin foil electrode were published in a previous publication of our group.[31]

Kinetic Isotope Effect. In the literature, there is still ongoing debate about whether CO_2 (aq) or HCO_3^- (aq) is the active species during the rate-limiting step of the CO_2RR.[8,41−44] To gain further insights into this matter, we will present experiments related to kinetic isotope effects (KIEs) in the following in which D_2O is employed as solvent for the electrolyte. Processes which are affected by hydrogen

https://dx.doi.org/10.1021/acssuschemeng.0c04451
ACS Sustainable Chem. Eng. 2020, 8, 13759−13768

ACS Sustainable Chemistry & Engineering pubs.acs.org/journal/ascecg Research Article

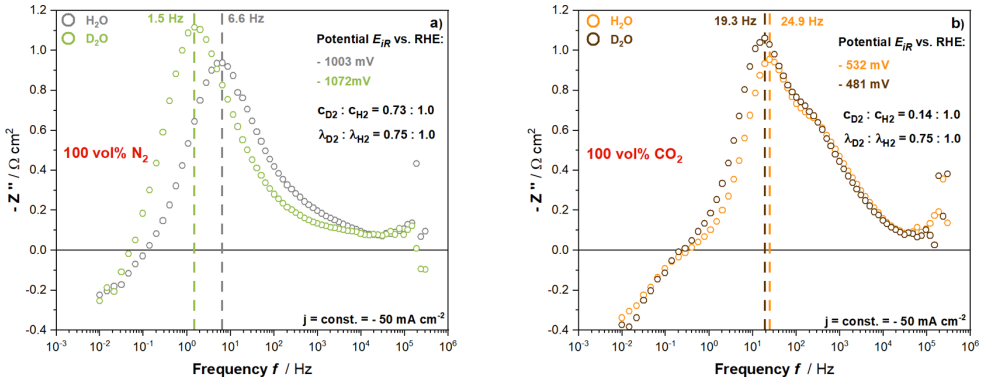

Figure 5. Imaginary part vs frequency plots obtained from EIS measurements during electrolysis using pure (a) N_2 and (b) CO_2 as feed gas and H_2O- or D_2O-based 1.0 M KOH as the electrolyte.

atoms are expected to be slowed down when substituting hydrogen with heavier deuterium which should shed light on the species involved in the reaction.[45]

The changes when substituting H_2O with D_2O become evident comparing the data in the imaginary part versus frequency part representation of the results. These plots for pure N_2 and CO_2 gas feed in H_2O- and D_2O-based KOH electrolytes are depicted in Figure 5 and partially reveal significant differences in the characteristic frequencies of the processes. The measured spectrum for the operation of the GDE with pure N_2 will be determined by HER only and should be influenced when using D_2O as solvent and is used as benchmark comparison to demonstrate how a spectrum changes when it is affected by the substitution of hydrogen with deuterium. Indeed, the characteristic frequency, or in other words the velocity of the observed charge-transfer process, is reduced from 6.6 to 1.5 Hz when using D_2O as solvent (cf. Figure 5a). The peak height which is in first proximity proportional to the resistance is increased, and the iR corrected potential also increases from −1003 to −1072 mV. Unsurprisingly, the ratio of the deuterium and hydrogen gas volume fraction (0.73:1.0) in the product gas stream agreed very well with the ratio of the corresponding thermal conductivities (0.75:1.0, λ_{D_2} = 138 mW K^{-1} cm^{-1}, λ_{D_2} = 185 mW K^{-1} cm^{-1})[46] which determine the estimated volume fractions using a thermal conductivity detector in the μ-GC. This ratio gives an approximate conversion factor between the estimated H_2 and D_2 volume fractions because the μ-GC was not calibrated for D_2 gas. The observed changes when operating the electrolysis cell with pure CO_2 and using D_2O instead of H_2O as solvent are depicted in Figure 5b. Figure S8 shows the corresponding Nyquist plots with reproduced measurements emphasizing the significance of the small differences measured. A difference can be seen for the medium-frequency process—the charge transfer—which shows a higher resistance and a slight decrease in the characteristic frequency. The fact that the ratio of the observed D_2 and H_2 volume fraction is 0.14:1.0 instead of 0.75:1.0 as expected from the ratio of the thermal conductivities strongly indicates that the FE for the parasitic deuterium evolution reaction is shifting to lower values compared to the HER which consequently results in a higher FE for CO_2RR products in D_2O-based electrolytes. Because the FEs are shifting when using D_2O as solvent, a straightforward interpretation of the obtained results during CO_2RR in terms of KIE is quite difficult. However, because the measured spectrum during the operation with pure CO_2 contains contributions of the HER and CO_2RR in superposition, we suggest that the observed slight decrease of the characteristic frequency and the increase of the medium-frequency resistance can be attributed to the D_2 formation which is slower compared to the H_2 formation in H_2O-based electrolytes (cf. Figure 5a). This hypothesis is supported by the fact that the rate-determining step during CO_2RR is often referred to be the initial electron transfer onto CO_2 to form the $CO_2^{\bullet-}$ anion radical (cf. eq 5).[42,43]

$$CO_2 + e^- \rightleftharpoons CO_2^{\bullet-} \quad (5)$$

On the other hand no clear consensus for the CO_2RR reaction mechanism exists in the literature ruling out the involvement of a hydrogen containing species in the charge transfer.[44] However, we think that a rate-determining charge transfer during CO_2RR involving a hydrogen containing species would result in more significant changes in the measured spectrum than we observed and suggest that the active species participating in the electron transfer is related to the reduction of dissolved CO_2 (aq) to form the $CO_2^{\bullet-}$ anion radical. Dunwell et al. demonstrated with a combination of in situ spectroscopic, isotopic labeling, and mass spectroscopic investigations for CO_2 conversion on gold electrodes that gaseous supplied CO_2 [followed by the dissociation to CO_2 (aq)] is not the primary carbon source during the reduction. Instead, CO_2 (aq), provided via rapid equilibrium exchange of HCO_3^- and CO_2 (aq), is postulated to be a significant but not the sole carbon source.[47]

However, the consumed CO_2 (aq), obtained via equilibrium exchange with HCO_3^-, is then replenished by the reaction of the gaseous CO_2 supply with OH^- ions at the outer boundary of the diffusional layer to form fresh bicarbonate. CO_2 (aq) can then provide very fast utilizing HCO_3^- ions to transport CO_2 (aq) analogous to a Grotthuss mechanism to the electrode surface which is subsequently reduced in the rate-limiting electron transfer. The involvement of the hydrogen containing HCO_3^- species for the mass transport of CO_2 (aq) is a second explanation why the medium-frequency process is affected by the substitution of hydrogen with deuterium without disagreeing the postulated mechanisms showing that the conversion of CO_2 to $CO_2^{\bullet-}$ is the rate-limiting electron transfer.

https://dx.doi.org/10.1021/acssuschemeng.0c04451
ACS Sustainable Chem. Eng. 2020, 8, 13759−13768

With respect to the measuring accuracy, no significant changes are observed for the high- and low-frequency process when changing the solvent from H_2O to D_2O.

CONCLUSIONS

We investigated carbon-supported tin-based GDEs employed for the electrochemical conversion of CO_2 to formate and CO in aqueous 1.0 M KOH via EIS. The goal was to elucidate the underlying physical processes to help interpreting future EIS spectra and enabling targeted optimization of CO_2 converting GDEs. We observed four features in the EIS spectrum which we tried to further specify by carrying out parameter series, namely, temperature, CO_2 partial pressure, current density, and electrolyte. Careful analysis leads us to the following interpretation of the spectrum: the 45° line in the high-frequency domain is a typical feature observed for porous electrodes representing resistances arising because of the electrical conductivity of the GDE matrix and the ionic conductivity in the pore system. The subsequent process in the high-frequency range was identified to be the conversion of CO_2 with OH^- to form bicarbonate or vice versa. Our results suggest that the medium-frequency process depicts the charge transfer from the electrode onto CO_2 (aq) to form the $CO_2^{\bullet-}$ anion radical. The small arc in the low-frequency region was assigned to the liquid phase diffusion of CO_2 to the active sites. It is important to mention that it is crucial to carefully interpret the EIS spectra because the features are in superposition with the parasitic HER and can change dramatically depending on the operating point, that is, when reducing the CO_2 volume fraction in feed gas in our specific set up to about 10 vol %, the spectrum is no longer dominated by the CO_2RR, and the observed features must be ascribed to the HER which as a consequence prevents the characterization of the GDE related to the CO_2RR. In the transport limited current density regime, this change of the dominating reaction could set-in at even higher volume fractions. Nevertheless, our assignment of physical processes to the observed loss resistances enables researchers to utilize EIS for targeted optimization of GDEs for CO_2 electrolysis and can aid in revealing degradation mechanisms.

ASSOCIATED CONTENT

Supporting Information

The Supporting Information is available free of charge at https://pubs.acs.org/doi/10.1021/acssuschemeng.0c04451.

Electrochemical cell; physical characterization of the GDE (SEM, MIP, XRD and XPS); impedance spectra and difference plots for the temperature and current series as well as spectra obtained for the operation in H_2O- and D_2O-based electrolytes; and Arrhenius plots derived from the temperature-dependent impedance spectra; comparison EIS for SnO_x / C GDE vs Sn foil (PDF)

AUTHOR INFORMATION

Corresponding Authors

Fabian Bienen − *Institute of Engineering Thermodynamics, German Aerospace Center, 70569 Stuttgart, Germany; Institute of Building Energetics, Thermal Engineering and Energy Storage, University of Stuttgart, 70569 Stuttgart, Germany;* orcid.org/0000-0002-4660-8826; Email: Fabian.Bienen@dlr.de

Kaspar Andreas Friedrich − *Institute of Engineering Thermodynamics, German Aerospace Center, 70569 Stuttgart, Germany; Institute of Building Energetics, Thermal Engineering and Energy Storage, University of Stuttgart, 70569 Stuttgart, Germany*; Email: Andreas.Friedrich@dlr.de

Authors

Dennis Kopljar − *Institute of Engineering Thermodynamics, German Aerospace Center, 70569 Stuttgart, Germany*

Armin Löwe − *Institute of Chemical Technology, University of Stuttgart, 70569 Stuttgart, Germany*

Simon Geiger − *Institute of Engineering Thermodynamics, German Aerospace Center, 70569 Stuttgart, Germany*

Norbert Wagner − *Institute of Engineering Thermodynamics, German Aerospace Center, 70569 Stuttgart, Germany*

Elias Klemm − *Institute of Chemical Technology, University of Stuttgart, 70569 Stuttgart, Germany*

Complete contact information is available at: https://pubs.acs.org/10.1021/acssuschemeng.0c04451

Author Contributions

The manuscript was written through contributions of all authors. All authors have given approval to the final version of the manuscript.

Notes

The authors declare no competing financial interest.

ACKNOWLEDGMENTS

Parts of this work were funded by the Federal Ministry for Economic Affairs and Energy (FKZ 03ET1379A/B−EnEl-Mi2.0) and by the German Federation of Industrial Research Associations (EWN03176/18).

REFERENCES

(1) Abanades, J. C.; Rubin, E. S.; Mazzotti, M.; Herzog, H. J. On the climate change mitigation potential of CO2 conversion to fuels. *Energy Environ. Sci.* **2017**, *10*, 2491−2499.

(2) Smith, P.; Davis, S. J.; Creutzig, F.; Fuss, S.; Minx, J.; Gabrielle, B.; Kato, E.; Jackson, R. B.; Cowie, A.; Kriegler, E.; van Vuuren, D. P.; Rogelj, J.; Ciais, P.; Milne, J.; Canadell, J. G.; McCollum, D.; Peters, G.; Andrew, R.; Krey, V.; Shrestha, G.; Friedlingstein, P.; Gasser, T.; Grübler, A.; Heidug, W. K.; Jonas, M.; Jones, C. D.; Kraxner, F.; Littleton, E.; Lowe, J.; Moreira, J. R.; Nakicenovic, N.; Obersteiner, M.; Patwardhan, A.; Rogner, M.; Rubin, E.; Sharifi, A.; Torvanger, A.; Yamagata, Y.; Edmonds, J.; Yongsung, C. Biophysical and economic limits to negative CO2 emissions. *Nat. Clim. Change* **2015**, *6*, 42−50.

(3) Eurostat Greenhouse Gas Emissionstatistics—Emissioninventories. https://ec.europa.eu/eurostat/statistics-explained/pdfscache/1180.pdf (accessed June 08, 2020).

(4) Jouny, M.; Luc, W.; Jiao, F. General Techno-Economic Analysis of CO2 Electrolysis Systems. *Ind. Eng. Chem. Res.* **2018**, *57*, 2165−2177.

(5) Zhang, W.; Hu, Y.; Ma, L.; Zhu, G.; Wang, Y.; Xue, X.; Chen, R.; Yang, S.; Jin, Z. Progress and Perspective of Electrocatalytic CO2 Reduction for Renewable Carbonaceous Fuels and Chemicals. *Adv. Sci.* **2017**, *5*, 1700275.

(6) Kibria, M. G.; Edwards, J. P.; Gabardo, C. M.; Dinh, C. T.; Seifitokaldani, A.; Sinton, D.; Sargent, E. H. Electrochemical CO2 Reduction into Chemical Feedstocks: From Mechanistic Electrocatalysis Models to System Design. *Adv. Mater.* **2019**, *31*, 1807166.

(7) Qiao, J.; Liu, Y.; Zhang, J. *Electrochemical Reduction of Carbon Dioxide: Fundamentals and Technologies*; CRC Press, 2016.

(8) Birdja, Y. Y.; Pérez-Gallent, E.; Figueiredo, M. C.; Göttle, A. J.; Calle-Vallejo, F.; Koper, M. T. M. Advances and challenges in

understanding the electrocatalytic conversion of carbon dioxide to fuels. *Nat. Energy* **2019**, *4*, 732−745.
(9) Hietala, J.; Vuori, A.; Johnsson, P.; Pollari, I.; Reutemann, W.; Kieczka, H. Formic Acid. *Ullmann's Encyclopedia of Industrial Chemistry*; John Wiley and Sons, 2016; pp 1−22.
(10) Bienen, F.; Kopljar, D.; Löwe, A.; Assmann, P.; Stoll, M.; Rößner, P.; Wagner, N.; Friedrich, A.; Klemm, E. Utilizing Formate as an Energy Carrier by Coupling CO 2 Electrolysis with Fuel Cell Devices. *Chem. Ing. Tech.* **2019**, *91*, 872−882.
(11) Miller, H.; Ruggeri, J.; Marchionni, A.; Bellini, M.; Pagliaro, M.; Bartoli, C.; Pucci, A.; Passaglia, E.; Vizza, F., Improving the Energy Efficiency of Direct Formate Fuel Cells with a Pd/C-CeO2 Anode Catalyst and Anion Exchange Ionomer in the Catalyst Layer. **2018**, *11*, 369, DOI DOI: 10.3390/en11020369.
(12) Hori, Y. Electrochemical CO2 Reduction on Metal Electrodes. *Modern Aspects of Electrochemistry*; Vayenas, C. G., White, R. E., Gamboa-Aldeco, M. E., Eds.; Springer New York: New York, NY, 2008; pp 89−189.
(13) Burdyny, T.; Smith, W. A. CO2 reduction on gas-diffusion electrodes and why catalytic performance must be assessed at commercially-relevant conditions. *Energy Environ. Sci.* **2019**, *12*, 1442−1453.
(14) Higgins, D.; Hahn, C.; Xiang, C.; Jaramillo, T. F.; Weber, A. Z. Gas-Diffusion Electrodes for Carbon-Dioxide Reduction: A New Paradigm. *ACS Energy Lett.* **2018**, *4*, 317−324.
(15) Rabiee, H.; Zhang, X.; Ge, L.; Hu, S.; Li, M.; Smart, S.; Zhu, Z.; Yuan, Z. Tuning the product selectivity of Cu hollow fiber gas diffusion electrode for efficient CO2 reduction to formate by controlled surface Sn electrodeposition. *ACS Appl. Mater. Interfaces* **2020**, *12*, 21670−21681.
(16) Ma, M.; Clark, E. L.; Therkildsen, K. T.; Dalsgaard, S.; Chorkendorff, I.; Seger, B. Insights into the carbon balance for CO2 electroreduction on Cu using gas diffusion electrode reactor designs. *Energy Environ. Sci.* **2020**, *13*, 977−985.
(17) Hori, Y.; Suzuki, S. Electrolytic Reduction of Bicarbonate Ion at a Mercury Electrode. *J. Electrochem. Soc.* **1983**, *130*, 2387−2390.
(18) Oloman, C.; Li, H. Electrochemical Processing of Carbon Dioxide. *ChemSusChem* **2008**, *1*, 385−391.
(19) Löwe, A.; Rieg, C.; Hierlemann, T.; Salas, N.; Kopljar, D.; Wagner, N.; Klemm, E. Influence of Temperature on the Performance of Gas Diffusion Electrodes in the CO2 Reduction Reaction. *ChemElectroChem* **2019**, *6*, 4497−4506.
(20) Zhang, J.; Luo, W.; Züttel, A. Crossover of liquid products from electrochemical CO2 reduction through gas diffusion electrode and anion exchange membrane. *J. Catal.* **2020**, *385*, 140−145.
(21) Reyes, A.; Jansonius, R. P.; Mowbray, B. A. W.; Cao, Y.; Wheeler, D. G.; Chau, J.; Dvorak, D. J.; Berlinguette, C. P. Managing Hydration at the Cathode Enables Efficient CO2 Electrolysis at Commercially Relevant Current Densities. *ACS Energy Lett.* **2020**, *5*, 1612−1618.
(22) Nwabara, U. O.; Cofell, E. R.; Verma, S.; Negro, E.; Kenis, P. J. A. Durable Cathodes and Electrolyzers for the Efficient Aqueous Electrochemical Reduction of CO2. *ChemSusChem* **2020**, *13*, 855−875.
(23) Leonard, M. E.; Clarke, L. E.; Forner-Cuenca, A.; Brown, S. M.; Brushett, F. R. Investigating Electrode Flooding in a Flowing Electrolyte, Gas-Fed Carbon Dioxide Electrolyzer. *ChemSusChem* **2020**, *13*, 400−411.
(24) Choi, S. Y.; Jeong, S. K.; Kim, H. J.; Baek, I.-H.; Park, K. T. Electrochemical Reduction of Carbon Dioxide to Formate on Tin−Lead Alloys. *ACS Sustainable Chem. Eng.* **2016**, *4*, 1311−1318.
(25) Lv, J.-J.; Jouny, M.; Luc, W.; Zhu, W.; Zhu, J.-J.; Jiao, F. A Highly Porous Copper Electrocatalyst for Carbon Dioxide Reduction. *Adv. Mater.* **2018**, *30*, 1803111.
(26) Daiyan, R.; Lu, X.; Saputera, W. H.; Ng, Y. H.; Amal, R. Highly Selective Reduction of CO2 to Formate at Low Overpotentials Achieved by a Mesoporous Tin Oxide Electrocatalyst. *ACS Sustainable Chem. Eng.* **2018**, *6*, 1670−1679.
(27) Wang, Q.; Dong, H.; Yu, H. Development of rolling tin gas diffusion electrode for carbon dioxide electrochemical reduction to produce formate in aqueous electrolyte. *J. Power Sources* **2014**, *271*, 278−284.
(28) Wang, Q.; Dong, H.; Yu, H.; Yu, H. Enhanced performance of gas diffusion electrode for electrochemical reduction of carbon dioxide to formate by adding polytetrafluoroethylene into catalyst layer. *J. Power Sources* **2015**, *279*, 1−5.
(29) Wang, Q.; Dong, H.; Yu, H.; Yu, H.; Liu, M. Enhanced electrochemical reduction of carbon dioxide to formic acid using a two-layer gas diffusion electrode in a microbial electrolysis cell. *RSC Adv.* **2015**, *5*, 10346−10351.
(30) Verma, S.; Lu, X.; Ma, S.; Masel, R. I.; Kenis, P. J. A. The effect of electrolyte composition on the electroreduction of CO2 to CO on Ag based gas diffusion electrodes. *Phys. Chem. Chem. Phys.* **2016**, *18*, 7075−7084.
(31) Bienen, F.; Kopljar, D.; Geiger, S.; Wagner, N.; Friedrich, K. A. Investigation of CO2 Electrolysis on Tin Foil by Electrochemical Impedance Spectroscopy. *ACS Sustainable Chem. Eng.* **2020**, *8*, 5192−5199.
(32) Kopljar, D.; Wagner, N.; Klemm, E. Transferring Electrochemical CO2 Reduction from Semi-Batch into Continuous Operation Mode Using Gas Diffusion Electrodes. *Chem. Eng. Technol.* **2016**, *39*, 2042−2050.
(33) Azuma, M.; Hashimoto, K.; Hiramoto, M.; Watanabe, M.; Sakata, T. Electrochemical Reduction of Carbon Dioxide on Various Metal Electrodes in Low-Temperature Aqueous KHCO3 Media. *J. Electrochem. Soc.* **1990**, *137*, 1772−1778.
(34) Raistrick, I. D.; Macdonald, J. R.; Franceschetti, D. R. *Impedance Spectroscopy: Theory, Experiment, and Applications*, 3rd ed.; John Wiley and Sons, 2018; pp 21−105.
(35) Roy, S. K.; Orazem, M. E.; Tribollet, B. Interpretation of Low-Frequency Inductive Loops in PEM Fuel Cells. *J. Electrochem. Soc.* **2007**, *154*, B1378−B1388.
(36) Svensson, A. M.; Weydahl, H.; Sunde, S. Impedance modelling of air electrodes in alkaline media. *Electrochim. Acta* **2008**, *53*, 7483−7490.
(37) Orazem, M. E.; Tribollet, B. Model-Based Graphical Methods. *Electrochemical Impedance Spectroscopy*; John Wiley and Sons, 2008; pp 353−362.
(38) Pohorecki, R.; Moniuk, W. Kinetics of reaction between carbon dioxide and hydroxyl ions in aqueous electrolyte solutions. *Chem. Eng. Sci.* **1988**, *43*, 1677−1684.
(39) Cui, C.; Han, J.; Zhu, X.; Liu, X.; Wang, H.; Mei, D.; Ge, Q. Promotional effect of surface hydroxyls on electrochemical reduction of CO2 over SnOx/Sn electrode. *J. Catal.* **2016**, *343*, 257−265.
(40) Wabner, D.; Holze, R.; Schmittinger, P. Impedance of an Oxygen Reducing Gas-Diffusion Electrode. *Z. Naturforsch., B* **1984**, *39*, 157−162.
(41) Baruch, M. F.; Pander, J. E.; White, J. L.; Bocarsly, A. B. Mechanistic Insights into the Reduction of CO2 on Tin Electrodes using in Situ ATR-IR Spectroscopy. *ACS Catal.* **2015**, *5*, 3148−3156.
(42) Wuttig, A.; Yoon, Y.; Ryu, J.; Surendranath, Y. Bicarbonate Is Not a General Acid in Au-Catalyzed CO2 Electroreduction. *J. Am. Chem. Soc.* **2017**, *139*, 17109−17113.
(43) Dunwell, M.; Luc, W.; Yan, Y.; Jiao, F.; Xu, B. Understanding Surface-Mediated Electrochemical Reactions: CO2 Reduction and Beyond. *ACS Catal.* **2018**, *8*, 8121−8129.
(44) Zhang, B. A.; Ozel, T.; Elias, J. S.; Costentin, C.; Nocera, D. G. Interplay of Homogeneous Reactions, Mass Transport, and Kinetics in Determining Selectivity of the Reduction of CO2 on Gold Electrodes. *ACS Cent. Sci.* **2019**, *5*, 1097−1105.
(45) Lee, J. H.; Tackett, B. M.; Xie, Z.; Hwang, S.; Chen, J. G. Isotopic Effect on Electrochemical CO2 Reduction Activity and Selectivity in H2O- and D2O-based Electrolytes over Palladium. *Chem. Commun.* **2019**, *56*, 106−108.
(46) Liquide, A. Gas Encyclopedia Air Liquide. https://encyclopedia.airliquide.com/ (accessed May 19, 2020).

https://dx.doi.org/10.1021/acssuschemeng.0c04451
ACS Sustainable Chem. Eng. 2020, 8, 13759−13768

(47) Dunwell, M.; Lu, Q.; Heyes, J. M.; Rosen, J.; Chen, J. G.; Yan, Y.; Jiao, F.; Xu, B. The Central Role of Bicarbonate in the Electrochemical Reduction of Carbon Dioxide on Gold. *J. Am. Chem. Soc.* **2017**, *139*, 3774−3783.

https://dx.doi.org/10.1021/acssuschemeng.0c04451
ACS Sustainable Chem. Eng. 2020, 8, 13759−13768

Supporting Information

Revealing mechanistic processes in gas-diffusion electrodes during CO2 reduction via impedance spectroscopy

Fabian Bienen[*†‡], *Dennis Kopljar*[†], *Armin Löwe*[§], *Simon Geiger*[†], *Norbert Wagner*[†], *Elias Klemm*[§] *and Kaspar Andreas Friedrich*[*†‡]

†Institute of Engineering Thermodynamics, German Aerospace Center, Pfaffenwaldring 38-40, 70569 Stuttgart, Germany

‡Institute of Building Energetics, Thermal Engineering and Energy Storage, University of Stuttgart, Pfaffenwaldring 31, 70569 Stuttgart, Germany

§ Institute of Chemical Technology, University of Stuttgart, 70569 Stuttgart, Germany

Corresponding Authors

Article II SI

*Fabian Bienen, E-mail: Fabian.Bienen@dlr.de

*Kaspar Andreas Friedrich, E-mail: Andreas.Friedrich@dlr.de

Number of pages: 14

Number of figures: 8

Number of tables: 1

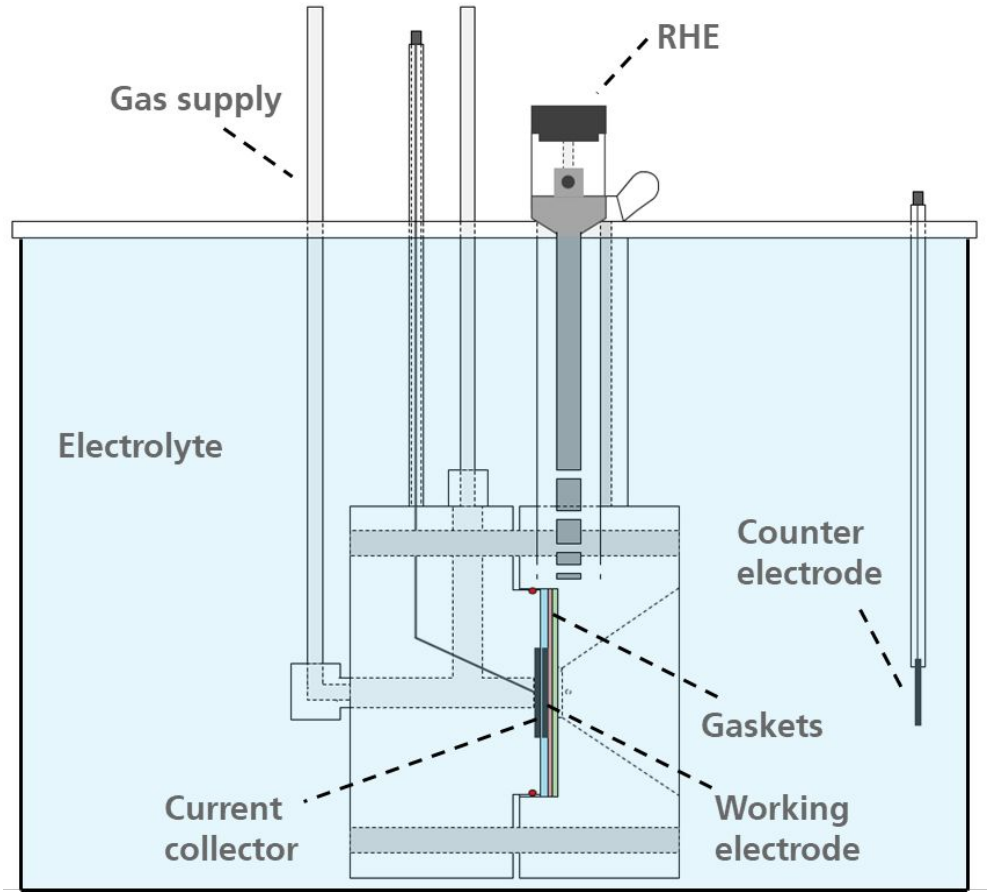

Figure S1 Schematic drawing of electrolysis cell with 3 electrode configuration. Reference electrode: Reversible hydrogen electrode (RHE); Counter electrode: Platinum; Working electrode: in-house manufactured carbon supported tin based gas-diffusion electrode (GDE). The electrolysis cell including electrolyte (1.0 M KOH*aq) vessel were put into a water bath for tempering.

Estimation CO_2 flow rate error

Since the inlet flow rate of CO_2 was used to calculate the FEs for the gas phase products a slight error occurs due to the reaction of CO_2 with OH^- present in the electrolyte and OH^- ions produced by electrochemical reactions. These phenomena reduce the real CO_2 outlet flow rate so that the FEs calculated with the species concentrations (measured via μ-GC) and the CO_2 inlet flow rate are higher than the ones calculated with the outlet flow rate. Seger et al. recently showed that under open circuit voltage (no current load) the CO_2 inlet flow rate is reduced in the outlet from 45 mL min^{-1} to approximately 43.5 mL min^{-1} when using a Cu coated GDE as cathode in 1.0 M KOH. The geometrical surface area was 2 cm^2.[1] In our system operating in 1.0 M KOH the CO_2 inlet flow was 50 mL min^{-1} and the geometrical surface area of the GDE 1 cm^2. Estimated conservatively using the data from Seger et al., the error for the CO_2 flow rate due to conversion with OH^- of the electrolyte is about 1.5 mL min^{-1}. Additionally, the error induced by the conversion of CO_2 with OH^- produced by electrochemical reactions can be estimated via Faradays law and the ideal-gas law assuming: I = 0.05 A (standard current during parameter series, except current density series), z = 2, F = 96485 A s mol^{-1}, T = 30 °C, p = 101300 Pa and R = 8.31451 J K^{-1}

mol^{-1}. After calculation the error can be estimated to be around 0.4 mL min^{-1}. Adding up both errors described above, the total error when using the CO_2 inlet instead of outlet flow rate is ~ 2.0 mL min^{-1} which is 4% referenced to the inlet flow rate of 50 mL min^{-1}. In relation to the gas phase products FEs, which are around 5% up to 15%, the absolute errors of the FEs are in the range of 0.2% and 0.6% which are insignificant.

GDE Physical characterization

The outcome of the physical characterization measurements is summarized in **Figure S2**. **Figure S2 a)** displays a SEM image of the GDE recorded with an acceleration voltage of 2.0 kV and a magnification of 20k. The heterogeneity of the microstructure becomes evident revealing a porous structure of the GDE which is essential for the functionality of the GDE. Taking the results of the mercury intrusion porosimetry (MIP) into account (cf. **Figure S2 c)**) the porosity of the electrode is about 81% and a bimodal pore size distribution is observed which is characteristic of carbon black-based GDEs. The pore diameters are ~ 3.8 µm and 90 nm. This bimodal pore system is of utmost importance for a well-performing GDE since both of the pore types fulfill a specific task during the reaction. The bigger pores with diameter above 100 µm, in literature often denoted the secondary pore system and ascribed to the voids between the carbon black agglomerates, ensure a fast transport of gaseous CO_2 inside the electrode whereas the agglomerates with pores < 100 µm are filled with the electrolyte due to capillary forces.[2] For a chemical reaction to happen, CO_2 must be transported to the active sites: CO_2 dissolves at the gas / liquid interface inside the GDE whereas this interface significantly

exceeds the geometrical surface area. Subsequently, CO_2 diffuses through the liquid phase to the active sites and is converted to carbonaceous products. The outstanding advantage of GDEs is that the diffusion length of CO_2 from the gas / liquid interface to the active sites is dramatically decreased compared to bulk diffusion in set-ups using plane cathodes. Beside the per geometrical surface area increased number of active sites, this the reason why GDEs achieve high conversion rates for CO_2RR. [2-4]

The SEM picture in **Figure S2 b)** obtained with an angle-selective back scattered electron detector shows the material contrast between the carbon network and the catalyst particles (brighter) pointing out the uniform catalyst dispersion inside the GDE. As shown previously, the particles have a diameter of around 10 nm – 40 nm while additional TEM measurements revealed that the observable catalyst particles are agglomerates consisting of crystallites with a diameter below 3 nm.[4]

The bonding condition at the surface of the GDE was investigated *via* XPS (cf. **Figure S2 d)**). The inset of the diagram shows the region of interest where the catalyst material, Sn, is specified. At about 495.4 eV and 486.9 eV one can see the peaks for the $Sn3d_{3/2}$ & $Sn3d_{5/2}$ orbital which is attributed to $Sn(+II, +IV)O_x$ ruling out the existence

of metallic Sn ($Sn3d_{3/2}$ = 492.8 eV, $Sn3d_{5/2}$ = 484.5 eV) on the catalyst surface inside the GDE. [5, 6] Unfortunately, we were not able to distinguish between SnO and SnO_2 with the XPS data at hand which can be traced back to the small differences in binding energies (SnO: $Sn3d_{3/2}$ = 494.7 eV, $Sn3d_{5/2}$ = 486.3 eV ; SnO_2: $Sn3d_{3/2}$ = 495.4 eV, $Sn3d_{5/2}$ = 486.9 eV).[5, 6]

Despite not being able to distinguish between the oxide species on the surface, it is important to generally conclude that tin oxide rather than metallic tin is present on the surface. It was shown that a meta stable tin oxide layer is present during electrochemical conversion of CO_2 under reducing potentials.[7]

Additional XRD measurements were conducted for the tin catalyst which was, in contrast to the above described procedure, directly precipitated and not on carbon support. Thermal treatment of the tin catalayst was performed as described in the experimental section. The diffractometer of the material is depicted in **Figure S3** and reveals that SnO_2 is the present species in the bulk phase.

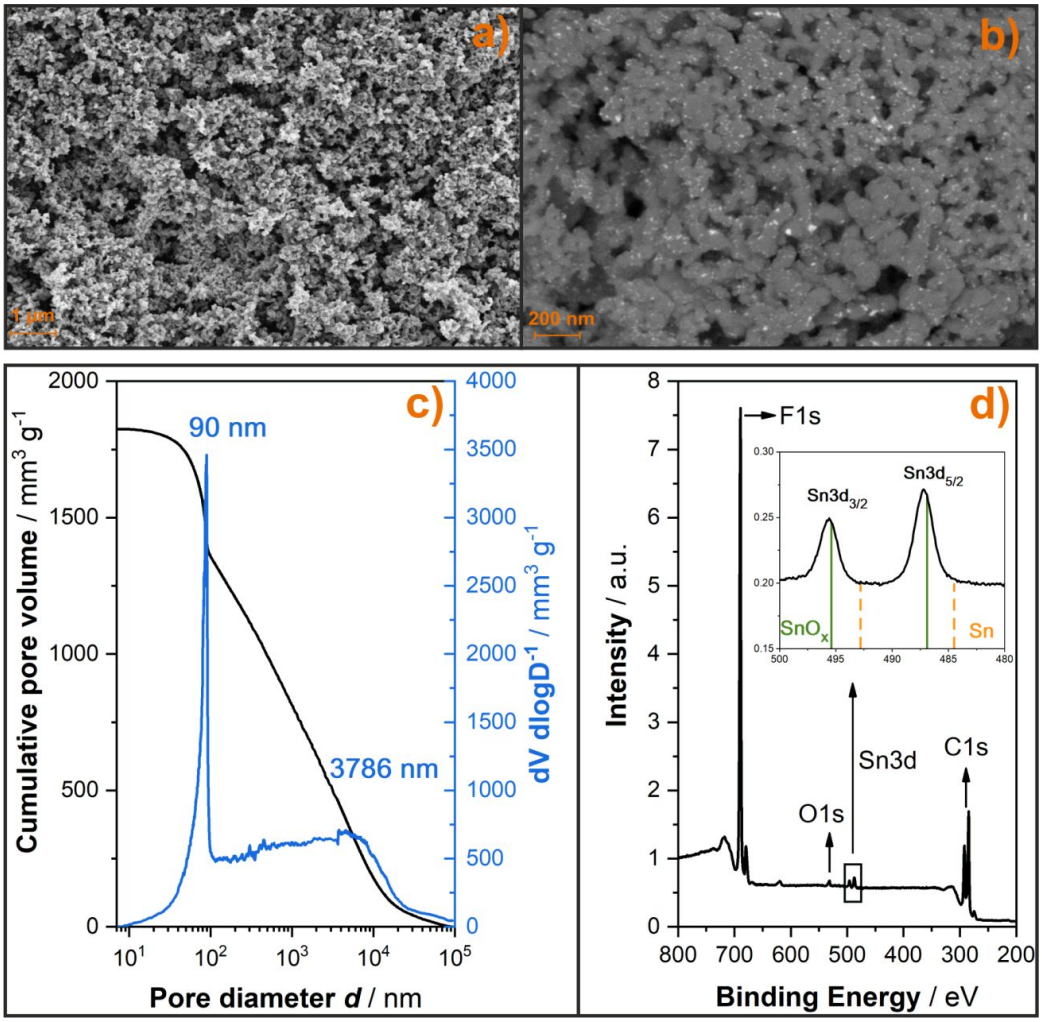

Figure S2 a) SEM image revealing porous microscopic structure of GDE **b)** material contrast image showing the homogeneous dispersion of tin catalyst on carbon support **c)** MIP measurement of the GDE showing a bimodal pore-size distribution **d)** XPS spectrum elucidating that SnO_x is the dominating species on the catalyst surface.

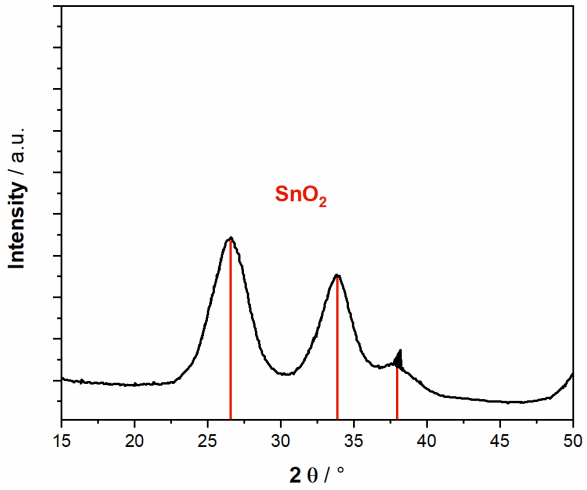

Figure S3 Diffractogram obtained for the unsupported catalyst material revealing that SnO_2 is the present species in the bulk phase.

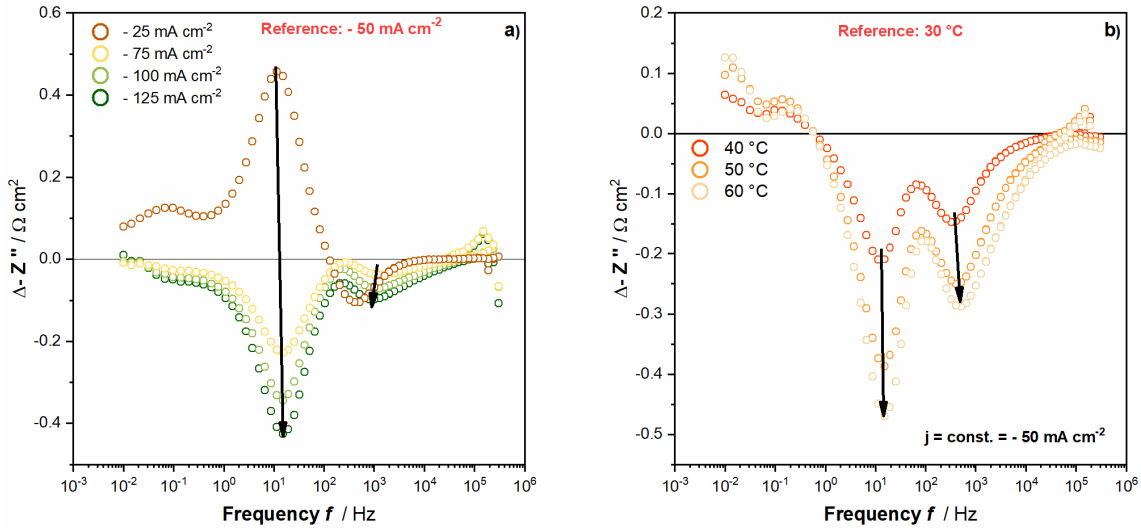

Figure S4 Difference plot of the imaginary parts for the **a)** current series whereas the data obtained for - 50 mA cm^{-2} are taken as reference **b)** temperature series whereas the data obtained for 30 °C are taken as reference.

Calculation activation energy E_a

The activation energy E_a for the high – and medium frequency process was calculated using the Arrhenius equation (Eq. S1).[8] R_F represents the corresponding faradaic resistance of the high – or medium frequency process. R_{F0} represents the pre-exponential factor. R is the universal gas constant whereas T represents the

temperature. The slope of the linearized Arrhenius equation (Eq. S2) includes the desired information about the activation energy.

$$\mathrm{R}_F = R_{F0} \bullet \exp\left(\frac{E_A}{R \bullet T}\right) \quad \text{(S1)}$$

$$\ln(R_F) = \ln(R_{F0}) + \frac{E_A}{R} \bullet \frac{1}{T} \quad \text{(S2)}$$

We did not want to perform equivalent circuit modelling (EQCM) to obtain the values for the faradaic resistances of the processes since it was not our aim to set up an equivalent circuit model. We focused on qualitative interpretation of our data since this is more convenient in the early stage of EIS analysis for CO_2RR. However, to obtain meaningful Arrhenius plots we need the values for the resistances of the high- and medium frequency process. To get these values we calculated the polarization capacitance C_p via Eq. S3 for each spectrum of the temperature series. ω describes the angular frequency. Z' and Z'' represent the real and imaginary part of the impedance.[9, 10]

$$C_p = \frac{1}{\omega} \bullet \left(\frac{-Z''}{(Z')^2 + (Z'')^2} \right) \quad \text{(S3)}$$

The Z' values of the inflection points of the plot vs C_p vs. Z' mark significant changes of the time constants and by that dividing the spectrum into sections. The width of each section is the approximate resistance of the corresponding underlying process. Figure S5 exemplarily demonstrates the procedure for the spectrum obtained at 40 °C.

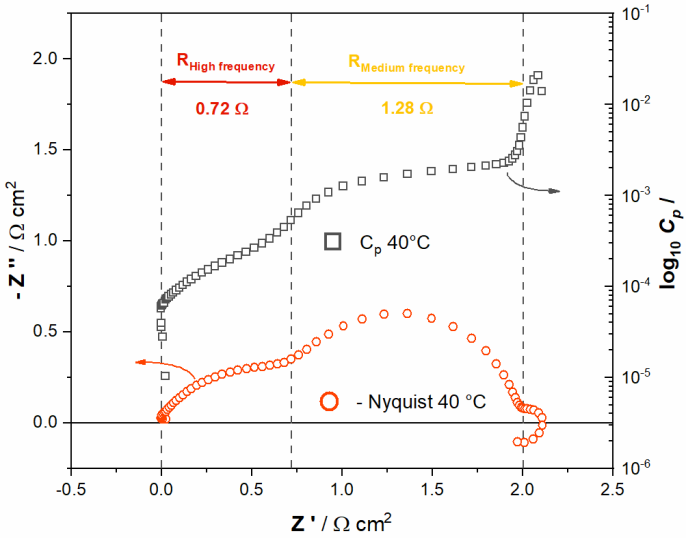

Figure S5 - Nyquist plot obtained for the operation of the GDE at 40 °C and the corresponding plot of the polarization capacitance vs. Z'. The Z' values of the inflection

points divide the spectrum into section whereas the width of a section is the approximate resistance value for the underlying process.

The resistance values for the high- and medium frequency process for the tested temperatures are displayed in Table S1. These values are inserted into Eq. S2 and plotted (cf. Figure S6). The activation energy E_a for both processes was calculated via evaluation of the slopes of the lines.

Table S1 Temperature dependent resistance values for the high- and medium frequency process.

Temperature / °C	30	30	40	40	50	50	60	60
$R_{High\ frequency}$ /	1.105	1.012	0.720	0.703	0.365	0.415	0.225	0.243

Ω								
$R_{Medium\ frequency}$ / Ω	1.646	1.624	1.284	1.408	1.108	1.014	0.982	0.884

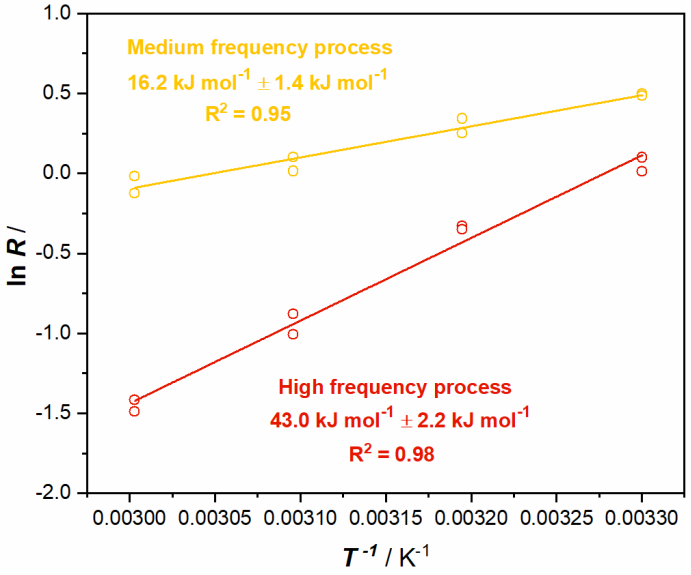

Figure S6 Arrhenius plot for the high and medium frequency resistance for the calculation of the activation energy for each process.

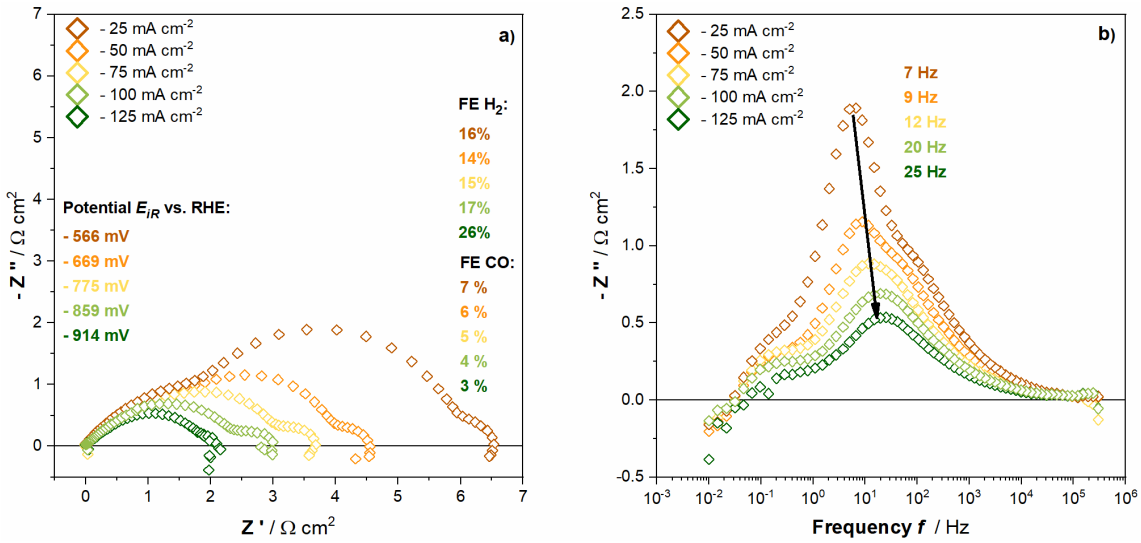

Figure S7 a) - Nyquist and **b)** imaginary part vs. frequency plot for a current series recorded during operation of the GDE with a feed gas composition of 20 vol% CO_2 and 80 vol% N_2. The diffusional arc in the low frequency domain vanishes at - 125 mA cm^{-2} and the shape resembles the spectrum obtained for the operation with pure N_2. This was interpreted as a change in the shape dominating reaction (from CO_2RR to HER) of the impedance spectrum.

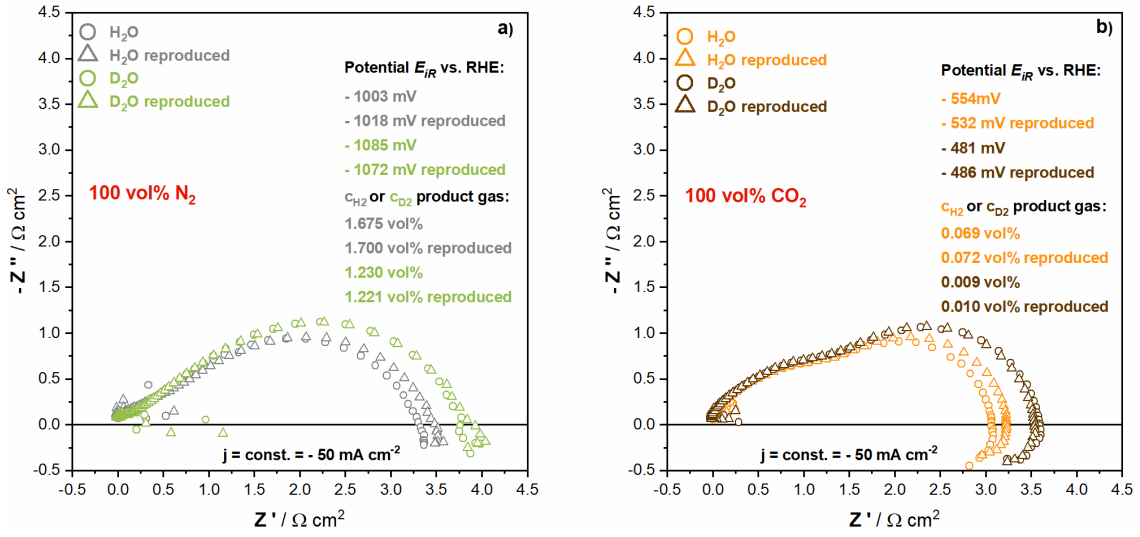

Figure S8 - Nyquist plots obtained for H_2O and D_2O based electrolytes during operation with pure **a)** N_2 and **b)** CO_2. The total polarization resistance increases using D_2O based electrolyte for both gas feeds.

Comparison of EIS spectra obtained for CO_2RR on tin foil and SnO_x / C gas-diffusion electrode

For better classification we present a brief comparison of impedance spectra recorded for the operation with pure CO_2 and N_2 on tin foil and SnO_x / C gas-diffusion electrodes (cf. **Figure S9**). The detailed information regarding the spectra for tin foil electrodes can be found in a previous work of our group. [11]

It becomes evident when looking at the change of the spectrum for the GDE when substituting N_2 with CO_2 that the shape of the spectrum significantly changes from one

semi-circle to three semi-circles. As argued in the main text we suggested that this changing shape is due to a change of the shape-determining reaction from HER to CO_2RR because the resistance of the HER is increased during operation with CO_2 while at the same time CO_2RR is favored evidenced by the faraday efficiency of 91% for the CO_2RR

In comparison, EIS measurements for tin foil electrodes in N_2 and CO_2 saturated 1.0 M $KHCO_3$ solution showed two arcs. Importantly, the shape of the spectrum remains the same when N_2 is substituted with CO_2. Merely the semi-circle diameters increase when CO_2 is used as feed gas suggesting that the shape-determining reaction is the same when operating the cell with CO_2 instead of N_2. The fact that the spectrum shape for tin foil systems is in contrast to the GDE system independent of the feed gas might be explained due to the high HER faraday efficiency (FE H_2: 87%) for CO_2 operation in the tin foil system. On the contrary, for the GDE system where the spectrum shape is dependent on the feed gas, the FE H_2 changes substantially from 100% for the operation with N_2 to 9% when operated with CO_2.

The comparison between these two different electrode systems supports our theory that depending on the reaction conditions during CO_2RR the appearance of the EIS spectrum can change according to the more dominant and, therefore, shape-determining reaction during electrolysis. A distinct observed change in the spectrum shape does not necessarily have to be attributed to the alteration of properties describing the CO_2RR but can be ascribed to a change of the investigated (spectrum

shape-determining) reaction as well. Still, simple changes for the semi-circle diameters while maintaining the same impedance spectrum shape seem to be reasonable to evaluate the degree optimization or degradation of the investigated system.

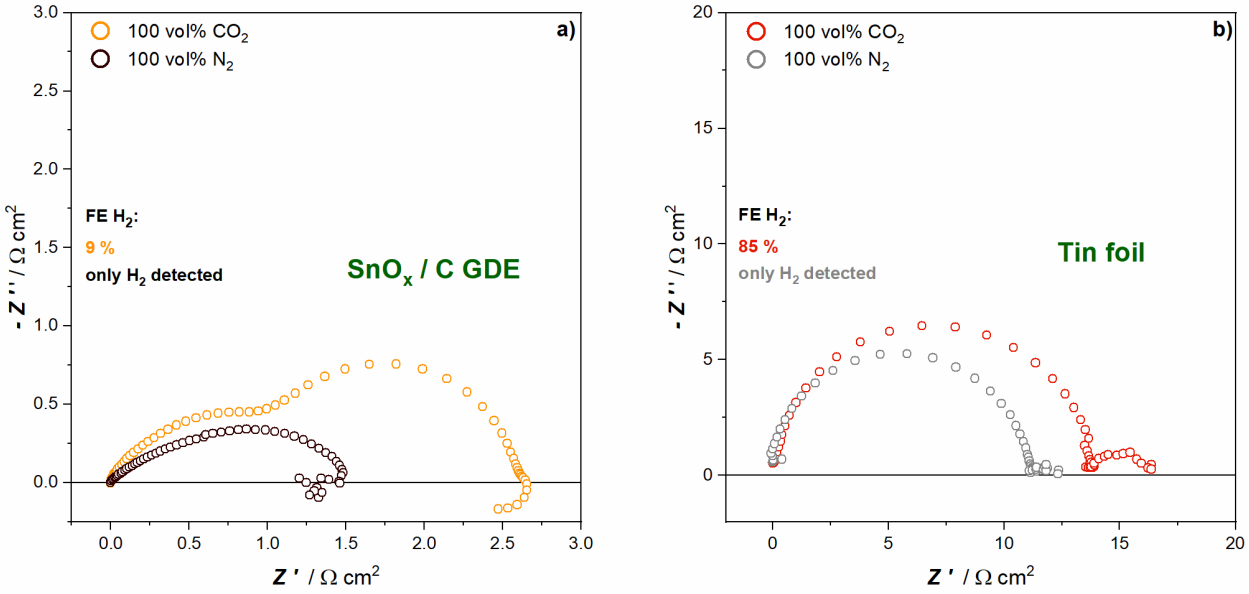

Figure S9 Comparison of impedance spectra recorded for **a)** the operation of a GDE with N_2 and CO_2 feed gas as shown in this contribution **b)** tin foil electrodes in N_2 and CO_2 saturated 1.0 M $KHCO_3$ as demonstrated in a previous work of our group.[11]

1. Ma, M.; Clark, E. L.; Therkildsen, K. T.; Dalsgaard, S.; Chorkendorff, I.; Seger, B., Insights into the carbon balance for CO2 electroreduction on Cu using gas diffusion electrode reactor designs. *Energy & Environmental Science* **2020**, 977-985, DOI 10.1039/D0EE00047G.

2. Bidault, F.; Brett, D. J. L.; Middleton, P. H.; Brandon, N. P., Review of gas diffusion cathodes for alkaline fuel cells. *Journal of Power Sources* **2009,** *187* (1), 39 - 48, DOI 10.1016/j.jpowsour.2008.10.106.

3. Higgins, D. C.; Hahn, C.; Xiang, C.; Jaramillo, T. F.; Weber, A. Z., Gas-Diffusion Electrodes for Carbon-Dioxide Reduction: A New Paradigm. *ACS Energy Letters* **2018**, 317-324, DOI 10.1021/acsenergylett.8b02035.

4. Löwe, A.; Rieg, C.; Hierlemann, T.; Salas, N.; Kopljar, D.; Wagner, N.; Klemm, E., Influence of Temperature on the Performance of Gas Diffusion Electrodes in the CO2 Reduction Reaction. *ChemElectroChem* **2019,** *6* (17), 4497-4506, DOI 10.1002/celc.201900872.

5. Ma, H.; Teng, K.; Fu, Y.; Song, Y.; Wang, Y.; Dong, X., Synthesis of visible-light responsive Sn-SnO2/C photocatalyst by simple carbothermal reduction. *Energy & Environmental Science* **2011,** *4* (8), 3067-3074, DOI 10.1039/C1EE01095F.

6. Wang, C.; Wu, Q.; Ge, H. L.; Shang, T.; Jiang, J. Z., Magnetic stability of SnO2 nanosheets. *Nanotechnology* **2012,** *23* (7), 075704, DOI 10.1088/0957-4484/23/7/075704.

7. Baruch, M. F.; Pander, J. E.; White, J. L.; Bocarsly, A. B., Mechanistic Insights into the Reduction of CO2 on Tin Electrodes using in Situ ATR-IR Spectroscopy. *ACS Catalysis* **2015,** *5* (5), 3148-3156, DOI 10.1021/acscatal.5b00402.

8. Orazem, M. E.; Tribollet, B., Model-Based Graphical Methods. In *Electrochemical Impedance Spectroscopy*, John Wiley and Sons 2008; 353-362, DOI 10.1002/9780470381588.ch18.

9. Kurzweil, P.; Ober, J.; Wabner, D. W., Method for extracting kinetic parameters from measured impedance spectra. *Electrochimica Acta* **1989,** *34* (8), 1179-1185, DOI 10.1016/0013-4686(89)87155-5.

10. Itagaki, M.; Suzuki, S.; Shitanda, I.; Watanabe, K., Electrochemical Impedance and Complex Capacitance to Interpret Electrochemical Capacitor. *Electrochemistry* **2007,** *75* (8), 649-655, DOI 10.5796/electrochemistry.75.649.

11. Bienen, F.; Kopljar, D.; Geiger, S.; Wagner, N.; Friedrich, K. A., Investigation of CO2 Electrolysis on Tin Foil by Electrochemical Impedance Spectroscopy. *ACS Sustainable Chemistry & Engineering* **2020**, 5192-5199, DOI 10.1021/acssuschemeng.9b07625.

Article III

Journal of Energy Chemistry 62 (2021) 367–376

Contents lists available at ScienceDirect

Journal of Energy Chemistry

journal homepage: www.elsevier.com/locate/jechem

http://www.journals.elsevier.com/journal-of-energy-chemistry/

Degradation study on tin- and bismuth-based gas-diffusion electrodes during electrochemical CO_2 reduction in highly alkaline media

Fabian Bienen [a,b,*], Armin Löwe [c], Joachim Hildebrand [c], Sebastian Hertle [c], Dana Schonvogel [d], Dennis Kopljar [a], Norbert Wagner [a], Elias Klemm [c], Kaspar Andreas Friedrich [a,b,*]

[a] Institute of Engineering Thermodynamics, German Aerospace Center, Pfaffenwaldring 38-40, 70569 Stuttgart, Germany
[b] Institute of Building Energetics, Thermal Engineering and Energy Storage, University of Stuttgart, Pfaffenwaldring 31, 70569 Stuttgart, Germany
[c] Institute of Technical Chemistry, University of Stuttgart, Pfaffenwaldring 55, 70569 Stuttgart, Germany
[d] Institute of Engineering Thermodynamics, German Aerospace Center, Carl-von-Ossietzky-Straße 15, 26129 Oldenburg, Germany

ARTICLE INFO

Article history:
Received 7 January 2021
Revised 13 March 2021
Accepted 14 March 2021
Available online 06 April 2021

Keywords:
Electrochemical CO_2 reduction
Heterogeneous catalysis
Gas-diffusion electrode
Electrochemical impedance spectroscopy
Catalyst leaching

ABSTRACT

This work investigated the degradation of tin – based gas-diffusion electrodes (GDE) and also a promising Bi_2O_3 GDE in electrochemical CO_2 reduction in highly alkaline media which has not been studied before. The contributions of the electrode wetting (or flooding, if excessively) and catalyst leaching on the degradation were analyzed. Therefore, electrochemical impedance spectroscopy was used to monitor the wetted surface area of the GDE in combination with post-mortem analysis of the penetration depth by visualizing the electrolyte's cation in the GDE cross-section. Furthermore, to reveal a possible degradation of the electrocatalyst, its distribution was mapped in the GDEs cross-section after operation while the catholyte was additionally analyzed via ICP-MS. The results clearly demonstrate that the SnO_2 catalyst dissolves in the reaction zone inside the GDE and might be partially redeposited near the GDEs surface. Since the redeposition process occurs only partially a steady loss of catalyst was observed impeding a clear distinction of the two degradation phenomena. Nevertheless, the deterioration of the electrode performance measured as faraday efficiency (FE) of the parasitic hydrogen evolution reaction (HER) qualitatively correlates with the differential double layer capacitance (C_{dl}). A significant difference of the rate of increase for the hydrogen FE and C_{dl} can be ascribed to the superposition of both above-mentioned degradation mechanisms. The demonstrated instability of SnO_2 contrasts with the behavior of Bi_2O_3 GDE which is stabilized during CO_2 conversion by redeposition of the diluted dissolved species as metallic Bi which is active for the CO_2 reduction reaction.

1. Introduction

Several countries have signed the Paris Agreement to commit to the joint target to keep the global warming well below 2 °C referenced to the temperature level in pre-industrial times. To achieve this target, coordinated efforts are necessary to reduce the carbon output of the international community. In the case of the EU-28 the contribution of industrial processes to the overall CO_2 emissions is around 8%. Mitigating these emissions necessitates addressing both the form of energy input as well as the source of chemical feedstock both realizable by the substitution of conventional processes by innovative routes [1–3]. In the case of carbon containing species a widely pursued strategy is to utilize CO_2 as feedstock for the electrochemical conversion to the desired carbonaceous species and by that changing the role of CO_2 from harmful waste to a valuable resource [4–6]. The composition of the obtained carbon containing products highly depends on the used catalyst and operational parameters of the electrolyzer [7,8].

One of the possible products during CO_2 conversion is formate or formic acid, depending on the prevailing pH-value. In this reaction only two electrons need to be transferred (cf. (1)) making it a relatively simple reaction from a mechanistic point of view [9,10]. It was shown by Verma et al. that formate/formic acid can indeed be produced electrochemically in a commercially competitive manner with state-of-the-art performance metrics [11]. Besides the traditional usage of formate as de-icing agent it was shown in a proof of concept study that formate solutions obtained in CO_2 electrolysis can also be used as energy carriers which opens

* Corresponding authors.
E-mail addresses: Fabian.Bienen@dlr.de (F. Bienen), Andreas.Friedrich@dlr.de (K.A. Friedrich).

https://doi.org/10.1016/j.jechem.2021.03.050

a new field of application for the produced carbonaceous species [12]. SnO_2 based electrodes are known to convert CO_2 and H_2O to formate as well as carbon monoxide in smaller quantities according to Eqs. (1) and (2). Unfortunately, the conversion of H_2O to H_2 (Eq. (3)) is a parallelly occurring parasitic reaction reducing the charge efficiency.

$$CO_2 + H_2O + 2e^- \rightleftharpoons HCOO^- + OH^- \quad (1)$$

$$CO_2 + H_2O + 2e^- \rightleftharpoons CO + 2OH^- \quad (2)$$

$$2H_2O + 2e^- \rightleftharpoons H_2 + 2OH^- \quad (3)$$

In the electrochemical CO_2 reduction reaction (CO_2RR) community it is widely known that plane electrodes converting CO_2 dissolved in the bulk electrolyte are limited to a maximum achievable current density of ≤ 35 mA cm^{-2} due to the low solubility of CO_2 in aqueous electrolyte (33 mM L^{-1} in H_2O, 25 °C, 1 atm) [7,13,14]. Enforcing a higher current density will only result in an increased hydrogen formation by water reduction as CO_2 is not transported sufficiently fast to the active sites. Therefore, so called porous gas-diffusion electrodes (GDEs) are used to improve the interplay between the liquid electrolyte, solid catalyst particle und gaseous reactant [15–18]. The porous architecture of these electrodes increases the number of active sites and significantly reduces the diffusion length of CO_2 to the catalyst surface in the liquid phase, which in consequence will lead to higher achievable current densities up to hundreds of mA cm^{-2} [19,20]. However, long-term stability of CO_2 converting SnO_2 – based GDEs has not been studied to a lager extent so far [21]. In the few instances where it has been investigated, the GDE degraded after several hours of operation which can be seen in an increase of faraday efficiency of the hydrogen evolution reaction (HER) [21,22]. Birdja et al. recently published a contribution describing a good-practice for the evaluation of the degradation of CO_2 converting electrodes. From the view point of the electrode performance (Faraday efficiency for reaction products) they suggested three key guidelines: averaging of currents for the FE calculation should be avoided (constant current operation recommended), reproduction of experiments to calculate error bars, high sampling frequency for product quantification [23].

However, taking a look into the literature usually GDE flooding and catalyst alteration are mentioned as possible degradation mechanisms during CO_2RR whereas only a few studies further investigate the underlying degradation mechanism itself. In the case of GDE wetting Leonard et al. specifically investigated the flooding mechanism of CO_2 to CO converting Ag – GDEs. They concluded that the flooding of the GDE is besides the well-known electrowetting effect promoted by the precipitation of carbonates due to the high local pH values. The hydrophobic properties of the porous architecture can be recovered after washing the electrode and diluting the carbonate salt [24]. In accordance, Jeanty et al. proposed that besides providing protons for the reaction a certain extend of wetting is beneficial to prevent the precipitation of carbonates inside the GDE and maintain carbonate removal from the reaction zone [25]. Regarding the catalyst stability of SnO_2 Lee et al. investigated the stability of SnO_2 nano-catalysts during CO_2RR to formate via post-mortem X-ray diffractometry and X-ray photoelectron spectroscopy measurements. They stated that in moderately alkaline media a metastable SnO_2 layer is present at the surface of the catalyst particle even at negative potentials which agrees with the work of Baruch et al. and Dutta et al. who used different advanced *operando* materials characterization methods like ATR-IR and Raman spectroscopy [26–28]. The latter ones also showed that besides a metastable surface SnO_2 layer the bulk material is reduced to metallic tin which is more favored at weak alkaline conditions [28]. Interestingly, to the best of our knowledge no study exists where the stability of SnO_2 during CO_2RR was characterized via elemental analysis of the catholyte to reveal a dissolved tin species which would point towards catalyst leaching. A detailed overview for possible degradation mechanisms during CO_2RR on GDEs can be found in the comprehensive review of Nwabara et al. or in the contribution of Popović et al focusing on copper-based electrodes [21,29].

In this work we investigated two possible degradation phenomena: the leaching of the catalyst out of the GDE and the flooding of the porous GDE which alters the mass transport properties of CO_2. To this end, the double layer capacitance as measure of the GDEs wetting state was monitored with time and correlated with the hydrogen FE as well as with the measured electrolyte penetration depth determined post-mortem after a variety of operation times. In addition, the catholyte was analyzed for dissolved tin species via inductively coupled plasma mass spectroscopy (ICP-MS) while post-mortem catalyst mapping in the cross-section of the GDE was used as supportive method to reveal catalyst loss or redistribution.

2. Experimental

2.1. Gas-diffusion electrode preparation

2.1.1. SnO_2 – based gas-diffusion electrodes

SnO_2 – based GDEs were prepared as described in our previous publications [20,30]. Briefly, Sn was deposited onto acetylene black (Alfa Aesar, 100% compressed, 99.9+%) as $Sn(OH)_x$ via a homogeneous precipitation procedure using $SnCl_2 \times 2\ H_2O$ (Carl Roth, >98%) as precursor. The powder was filtrated, washed and dried (100 °C) in air. The catalyst powder had a Sn loading of approximately 2.6 wt% and was mixed in a knife-mill with PTFE (Dyneon, TF 2053Z) at a weight ratio of 65 wt% (referenced to carbon) to 35 wt%. The mixture was filled in a cylindrical mask (d = 39 mm; height: 10 mm) and dry pressed for 1 min at 10.5 kN cm^{-2}. Finally, the GDE was thermally treated at 340 °C for 1 h to improve the PTFE distribution and by that increasing the mechanical stability. A detailed characterization of the material and the GDE can be found in Figs. S1 and S2 and our previous works [20,30].

2.1.2. Bi_2O_3 – based gas-diffusion electrodes

Bi_2O_3 was prepared according to Yuan et al. [31]. The method was modified for a precipitation analogous to the previous described SnO_2 – based GDEs. Therefore, conc. HCl (22.5 mL) was poured to acidify a slurry of acetylene black (13.6 g; Alfa Aesar, 100% compressed, 99.9+%), sodium dodecyl sulfate (0.865 g) and water (300 mL) while subsequently the precursor $Bi(NO_3)_3 \times 5\ H_2O$ (3.0 g; ≥98.0%, Carl Roth GmbH & Co. KG) was added. After that 1.0 M NaOH was added slowly to the slurry until a pH value of 11 was reached. Following the slurry was stirred for 2 h at room temperature and 3 h at 90 °C. The material was filtered, washed with 2 L of deionized water and dried at 100 °C overnight. The GDE preparation was the same as described for the SnO_2 – based GDEs. To archive the same molar ratio of catalyst as Sn the used amount of precursor was adjusted to the higher molar weight of Bi (approx. 4.5 wt% Bi on carbon). Transmission electron microscopy images and an X-ray diffractogram of the material are provided in the SI (Fig. S3).

2.2. Electrochemical measurements

Electrochemical measurements were conducted in a three-electrode set-up consisting of the working electrode, reversible hydrogen electrode (RHE) as reference electrode and nickel-mesh as counter electrode. Both electrodes had a geometrical surface

area of 3.14 cm^2. The gaseous backpressure of the GDE was adjusted to 3 $mbar_g$ via a water column at the CO_2 outlet while the hydrodynamic pressure was constant due to a fixed maximum column height of 41 cm. The cathode and anode chamber were separated via an anion exchange membrane (AEM, fumasep® FAB-PK-130). 1.0 M KOH (Chemsolute ≥85%) or 1.0 M NaOH (Merck ≥99%) aqueous electrolyte was circulated via a peristaltic pump at a flow rate of 5 mL min^{-1} and tempered to 30 °C. The total volume of the catholyte was 1.0 L, whereas 0.5 L of electrolyte was used as anolyte. CO_2 (4.5, Linde) was provided from the backside of the GDE at a flow rate of 50 mLn min^{-1}. The outlet gas flow was measured via a bubble-meter (Merck). Corresponding FEs for CO and H_2 were calculated via faradays law by measuring the exhaust gas-stream composition (μ-GC, Varian) and flow-rate (bubble-meter). The FE for formate was determined using the catholyte flow rate and the in- and outlet concentration of formate which was analyzed via high performance liquid chromatography (HPLC, Agilent Technologies: 1260 Infinity II LC System, Column: Hi-Plex H, 7.7 × 300 mm, 8 μm).

EIS spectra were recorded in galvanostatic operation mode with a ZAHNER-elektrik GmbH & Co. KG Zennium electrochemical workstation. The evaluation of the spectra was performed with the RelaxIS 3 software (rhd instruments GmbH & Co. KG). The spectra were recorded in a frequency range of 200 mHz–300 kHz (~5 min run time) with an excitation current of 10 mA for all experiments. Before recording EIS spectra the system was conditioned for 10 min at the desired parameter set. To monitor the time dependent wetting of the GDE the spectra were recorded consecutively with a time resolution of approx. 5 min. Each spectrum was then fitted to an equivalent circuit model (EQCM) to extract the differential double layer capacitance C_{dl} which serves herein as approximation for the electrochemical surface area (ECSA).

2.3. Post-mortem analysis

2.3.1. Scanning electron and energy dispersive X-ray microscopy

After the electrochemical characterization a selection of GDEs was prepared for post-mortem analysis to visualize the penetration depth of the electrolyte into the porous GDE. Element mapping of the electrolyte's cation was performed on the cross-section of the electrode indicating the extent to which the electrolyte has penetrated into the GDE. Therefore, the reactor was disassembled and the GDE rinsed with demineralized water. The GDE was then instantly immersed in liquid nitrogen to fix the residual electrolyte in the pore space at the location where it was present after the experiment. Consecutively, the GDE was dried at room temperature in a vacuum oven via sublimation of the frozen water until a constant pressure inside the oven was achieved indicating a completed drying process. The dried electrode was cut with a scalpel to expose the GDEs cross-section.

The scanning electron microscopy (SEM, Zeiss ULTRA PLUS) images were taken with a magnification of 60 at an acceleration voltage of 20 kV. For energy dispersive X-ray microscopy (EDX) a Bruker XFlash 5010 device was used to visualize the distribution respectively penetration depth of the electrolyte's cation. Finally, the colored images were quantitatively evaluated using ImageJ [32] to measure the penetration depth of the electrolyte's cation at several representative locations inside the GDE and averaging the results. The catalyst material was mapped as well to make qualitative statements on the degree of leaching.

2.3.2. Inductively coupled plasma mass spectrometry

Inductively coupled plasma mass spectrometry (ICP-MS) measurements were carried out for catholyte samples at t = 0 h and t = 24 h to reveal catalyst leaching. Therefore, the XSeries2 device (Thermo Fisher Scientific) equipped with an argon plasma and a quadrupole mass spectrometer was used to quantify tin or bismuth in the catholyte. Samples were prepared by pipetting a defined volume of the original electrolyte, neutralizing and acidifying with concentrated HNO_3 to a final acid concentration of 2 vol% (Rotipuran®Sup, Carl Roth), adding 1 mg L^{-1} internal standard (Sc or Lu, ICP standard solutions, 1000 mg L^{-1}, Carl Roth, Germany) and finally diluting the samples by factor 10. Calibration was carried out using Sn or Bi concentrations of 0, 0.5, 1, 10, 100, 500, 1000, 2500 μg L^{-1} (ICP standard solutions, 1000 mg L^{-1}, Carl Roth, Germany) and ensuring a correlation coefficient of at least 0.999. Detection limits were calculated as a 30 times blank concentration.

3. Results and discussion

The target of this contribution is to give insights into the degradation mechanisms of SnO_2 – based GDEs during CO_2 electrolysis. Therefore, we focused on two possible aspects: the excessive wetting/flooding of the GDE and a potential catalyst leaching. First, we tried to correlate the GDEs performance with the wetting behavior of the electrodes. The latter was characterized via EIS to obtain the double layer capacitance, C_{dl}, and post-mortem analysis of the penetration depth of the electrolyte during operation. In addition, the catalyst stability was studied via element mapping of the catalyst distribution inside the GDE as well as by ICP-MS measurements of the catholyte after the electrolysis.

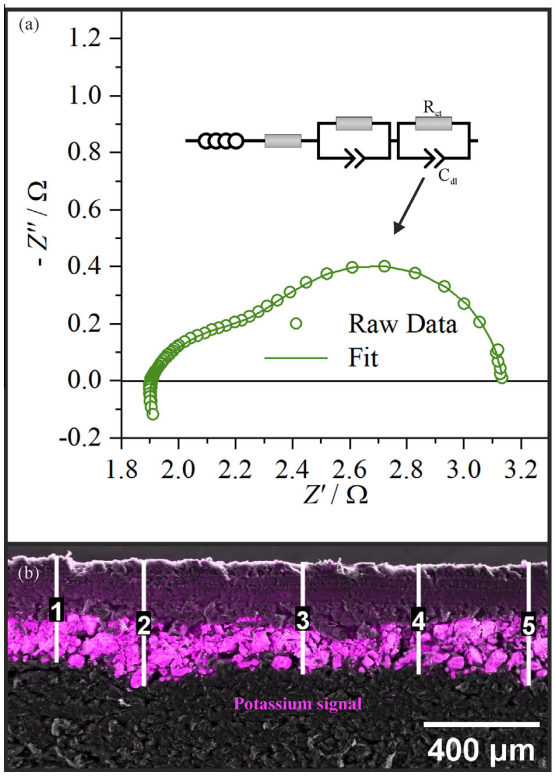

Fig. 1. (a) Exemplary – Nyquist plot (scatter) obtained for a SnO_2 – based GDE during CO_2RR at –50 mA cm^{-2} in 1.0 M aqueous KOH and fitted data (line). The used equivalent circuit model consists of: Inductance, R_Ω, 2 R – Q elements. (b) Exemplary potassium element map of the GDEs cross-section after freeze-drying procedure for the quantification of the electrolyte's penetration depth.

3.1. Evaluation approach

For a better understanding we want to elaborate the methodology for an exemplary experiment in the following. Fig. 1(a) shows an impedance spectrum of the SnO_2 – based GDE for which the spectrum shape is characteristic and typical for this type of GDE at the studied parameter sets. In a previous detailed contribution, we investigated and discussed the obtained impedance spectra for the system at hand and assigned the observed arcs to the underlying physical processes [30]. The intersection of the curve with the x-axis in the high frequency region represents the Ohmic resistance while the straight line in the high frequency region is caused by the porous architecture of the electrode. The arc in the high frequency region was suggested to correspond to the chemical reaction of CO_2 to HCO_3^-. The lower frequency region in Fig. 1 (a) is ascribed to a charge-transfer process which can be quantitatively analyzed via equivalent circuit modeling (EQCM) to extract the differential double-layer capacitance (C_{dl}) as a measure of the wetted surface area. The equivalent circuit which was fitted to the raw data consisted of the following elements: inductance, R_Ω and two R-Q Elements (cf. Fig. 1(a)). The fitted parameters of the R-Q element in the lower frequency region (R, Q, α) were used to convert the Q-value via Brugs equation into a physical meaningful capacitance value [33]. The time evolution of the C_{dl} values is generated by analyzing consecutive recorded galvanostatic impedance spectra over several hours of time.

Fig. 1(b) illustrates how the penetration depth of the electrolyte into the GDE was measured. Therefore, the GDEs cross-section was analyzed via element mapping after the GDE was dried according to the above described freeze-drying process. The electrolytes cation, potassium, was mapped via EDX and used to monitor the penetration depth of the electrolyte. The shown penetration depth (cf. Fig. 2(a)) is the average of two repetition experiments while the error bar displays the standard deviation of all measured lengths of the original sample and the reproducibility experiment. It is evident, that potassium carbonate or bicarbonate are predominantly precipitated and by that accumulated deeper inside the GDE due to the dramatically increased pH value in the reaction zone which is a result of sluggish OH^- removal into the bulk electrolyte [24,34,35].

3.2. Time dependent GDE wetting

The GDE was operated for different time spans and analyzed as described in 3.1 to visualize the time dependent wetting behavior of the GDE and to correlate the C_{dl} with the electrolyte's penetration depth (cf. Fig. S6 and Table S1) determined via cross-sectional element mapping.

The results of the galvanostatic EIS (−50 mA cm^{-2}) and penetration depth evaluation are depicted in Fig. 2(a). The C_{dl} values indicate a sharp increase of the wetted surface area at the beginning of the experiment up to ~300 min. The sharp increase is characteristic for the wetting of GDEs and can also be seen in the time dependent behavior of the electrode's potential (cf. Fig. 2(a) inset) and is caused by electrowetting which is induced by the potential dependent surface energy reduction of the liquid/solid interface [36]. As seen in Fig. 2(a) the initial potential during galvanostatic electrolysis is quite negative, resulting in a high driving force for the electrowetting. After 300 min the increase of C_{dl} becomes stationary until about ~900 min at which a more erratic increase of C_{dl} can be observed. Interestingly, this sharp increase is not pictured by the post-mortem evaluated penetration depths. The penetration depth increases with a square root like function of the time which nicely fits to the standard equation for the description of time dependent imbibition of liquids into porous material: the simplified Lucas-Washburn equation (Eq. (4)), which balances contrary acting forces induced by surface energy and viscosity effects [37]. The capillary constant includes: surface energy (liquid–solid), dynamic viscosity, contact angle, average pore radius.

$$l_{penetration} = \sqrt{k_{capillary}} * \sqrt{t} \quad (4)$$

The fact that the C_{dl} values and penetration depths do not perfectly correlate indicates that the depth of penetration is not the sole parameter influencing the double layer capacitance. Possible structural degradation as roughening, catalyst agglomeration or

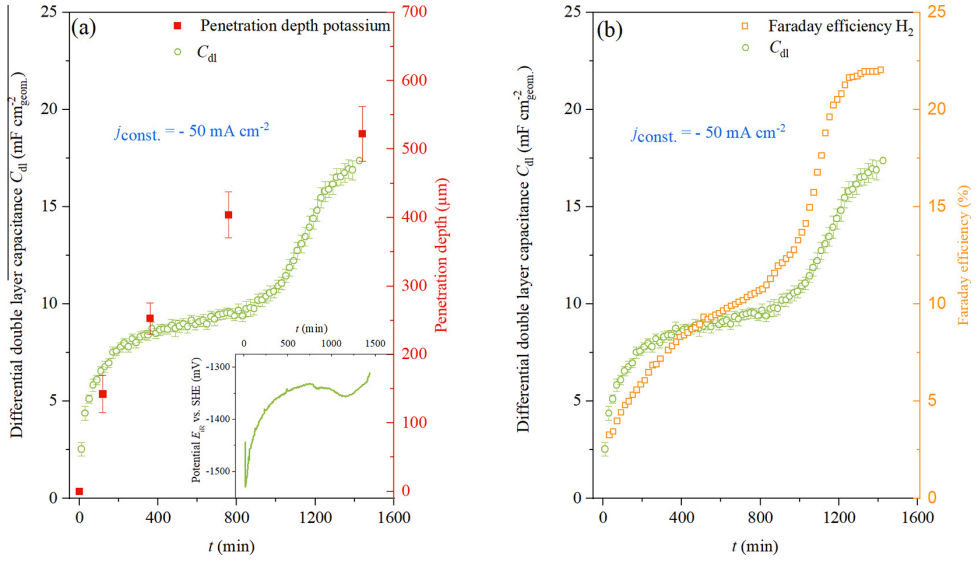

Fig. 2. (a) Monitored C_{dl} and potential for a SnO_2 – based GDE over 24 h of operation at −50 mA cm^{-2}. Post-mortem determined penetration depth of the electrolyte's cation which was fixed via rapid freezing of the GDE directly after disassembling and rinsing with de-ionized water. Inset: Corresponding time dependent electrode potential. (b) Corresponding FE of the parallelly to CO_2RR occurring parasitic HER recorded for 24 h as a measure of the performance of the GDE.

leaching, salt deposition and carbon corrosion can affect the C_{dl} values as well and cannot be excluded with certainty. However, the measured penetration depth solely indicates the macroscopic wetting of the GDE along a straight line (cf. "Evaluation approach") analogous to a continuously moving electrolyte front from electrolyte to gas side, the double-layer capacitance is ascribed to the wetted surface area inside this electrolyte front evoked by the complex porous architecture and heterogeneity (pore size distribution, tortuosity, PTFE distribution and surface functionality) of the GDE. In detail, capillary penetration is a time dependent process which highly depends on the hydrophobicity of the material and the pore radii as indicated in Eq. (4). Consequently, it can be suggested that the filling of the C_{dl} determining pores, i.e. small pores due to over proportional contribution to the surface area, occurs at a different velocity as compared to larger pores. Depending on the hydrophobicity the electrolyte penetration into the small pores can be faster or slower compared to the filling of pores with bigger radii. In contrast to the C_{dl} determination the image-based evaluation of the penetration depth does not include the time dependent progressing wetting inside an already wetted area as the resolution of the technique does not allow it. This is suggested to be the reason why the time dependent C_{dl} values and penetration depths do not perfectly correlate.

Besides the C_{dl} values Fig. 2(b) illustrates the time course of the hydrogen FE (corresponding FE for CO and $HCOO^-$ are depicted in Fig. S4). It becomes obvious that the hydrogen FE qualitatively follows the same shape of the C_{dl} curve (with a little offset) or vice versa suggesting a correlation between the wetting of the electrode and the extent to which the parasitic HER occurs.

The sharp increase of C_{dl} around 900 min is not a measurement or EQCM evaluation artifact since it is a reproducible phenomenon and at the same time the hydrogen FE indicates that something has happened to the electrode. The origin of the sharp increase of C_{dl} and hydrogen FE cannot be clarified without any doubt but might be explained with different approaches:

- There is a sudden increase (for a so far unknown reason) of the wetted surface area. A mechanical failure of the GDE was not observed and would have been visible in the element mapping.
- The change of hydrogen FE runs a head of the change of C_{dl} and not vice versa. The nature of the Helmholtz double layer which affects the specific capacitance might deviate significantly when more hydrogen is produced (increased number of adsorbed hydrogen species) which in consequence may lead to a sharply growing capacitance value. The increasing hydrogen FE can be a consequence of a possible catalyst dissolution which will be shown in the next section.

To provide further insights an exemplary potentiostatic EIS experiment was conducted to reveal a possible effect of the applied operation mode on the obtained results. The measured data of the potentiostatic experiments are depicted in Fig. S7 and show that C_{dl} follows the same trend as shown in the galvanostatic experiments.

To reveal a possible catalyst alteration, we performed galvanostatic EIS measurements and mapped the tin catalyst in the GDEs cross-section while additionally analyzing the catholyte for tin.

3.3. Catalyst leaching in SnO_2 – based GDEs

Since it was shown that the GDE degradation is not solely caused by electrode flooding we wanted to investigate the possibility of catalyst leaching. For this purpose, we performed galvanostatic electrolysis experiments at -25 mA cm^{-2}, -50 mA cm^{-2} and -75 mA cm^{-2} with simultaneous EIS measurements for 800 min and subsequent mapping of Sn in the GDEs cross-section. In addition, the catholyte was investigated via ICP-MS. The same post-mortem procedure was repeated for a GDE which was kept at OCV for 800 min. It is important to mention that for EDX mapping of Sn we had to switch the cation of the electrolyte from potassium to sodium ($K\alpha_1$ = 1.040) because the characteristic X-Ray energies of potassium ($K\alpha_1$ = 3.314 keV; $K\beta_1$ = 3.590 keV) and tin ($L\alpha_1$ = 3.444 keV; $L\beta_1$ = 3.663 keV) are too close to be separated accurately which is evident by a clearly identified broad potassium peak overlapping into the tin peak region. Higher electron beam energies to clearly identify tin ($K\alpha_1$ = 25.271 keV; $K\beta_1$ = 28.485 keV) were not accessible with the hardware at hand.

Fig. 3 shows the element maps for sodium and tin after the operation of 800 min at OCV at different current densities. It becomes evident that at OCV no significant penetration of electrolyte into the GDE can be observed which is due to the extremely hydrophobic nature of acetylene black and PTFE. The wetting starts under polarization induced by the change of the surface energy when applying a potential as illustrated by the sodium element maps for the current series. The observable penetration depths (297 μm ± 32 μm; 405 μm ± 67 μm; 541 μm ± 53 μm) correlate with the increasing current densities (respectively polarization) while the plateaus of the C_{dl} values for -25 mA cm^{-2} and -50 mA cm^{-2} also indicate an increased wetting at more negative potentials (cf. Fig. S8). Accordingly, the triple-phase region is expected to be shifted deeper inside the GDE at higher current densities which results in an elongated diffusion length for product removal. Additionally, the time course of C_{dl} points out that the wetting rate increases as well (cf. Fig. S8). These observations regarding a favored wetting at more negative potentials is expected as it follows the rules of electrocapillarity stated by Lippmann where a higher polarization leads to a decrease of the surface energy of the solid/liquid interface [36].

A loss of tin is observable when a current is applied as it is pictured by the absence of tin in the region with a significant presence of sodium. There is the possibility that the loss of tin might be overemphasized by the presence of precipitated sodium carbonate in the pore system which impedes the detection of tin as the emitted X-rays might not penetrate through the carbonate and reach the detector. To prove a possible catalyst leaching ICP-MS measurements of the catholyte were carried out to reveal a possible tin dissolution. Fig. 4(a) summarizes the results and already points out in a qualitative manner that tin can be found in the catholyte indicating a non-stable catalyst at the applied potentials in highly alkaline media.

Starting with OCV it can be seen that – contrary to the mapping results – even without polarization at a time averaged potential of $E_{iR} \sim +50$ mV vs. SHE a small amount of tin is detectable in the catholyte. The origin of the detected amount of tin must be attributed to catalyst leaching because the tin concentration in the blind sample of the electrolyte was below the detection limit (29 ng L^{-1}). At this potential and pH (≥14.0; 1.0 M NaOH) the Pourbaix diagram suggests the following dissolution reaction of the initial catalyst material SnO_2 (cf. Fig. 4(b)):

$$SnO_2 + 2OH^- \rightleftharpoons SnO_3^{2-} + H_2O \quad (5)$$

Under a load of -25 mA cm^{-2}, -50 mA cm^{-2} and -75 mA cm^{-2} the time averaged potentials (E_{iR} vs. SHE) are shifted to -1.40 V, -1.51 V and -1.58 V. According to the Pourbaix diagram metallic Sn is the thermodynamically stable phase at these potentials assuming a reasonable pH value of at least 14. This suggests that the catalyst SnO_2 might be directly reduced to metallic tin via:

$$SnO_2 + 2H_2O + 4e^- \rightleftharpoons Sn + 4OH^- \quad (6)$$

The reduction of SnO_2 to the metallic form under similar conditions was previously stated by several authors [26–28].

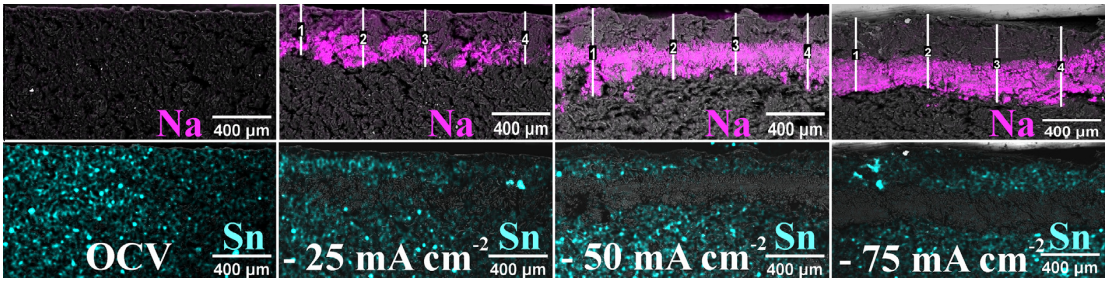

Fig. 3. Cross-sectional element maps of sodium and tin obtained for a SnO_2 – based GDE operated for 800 min at OCV and the desired current density.

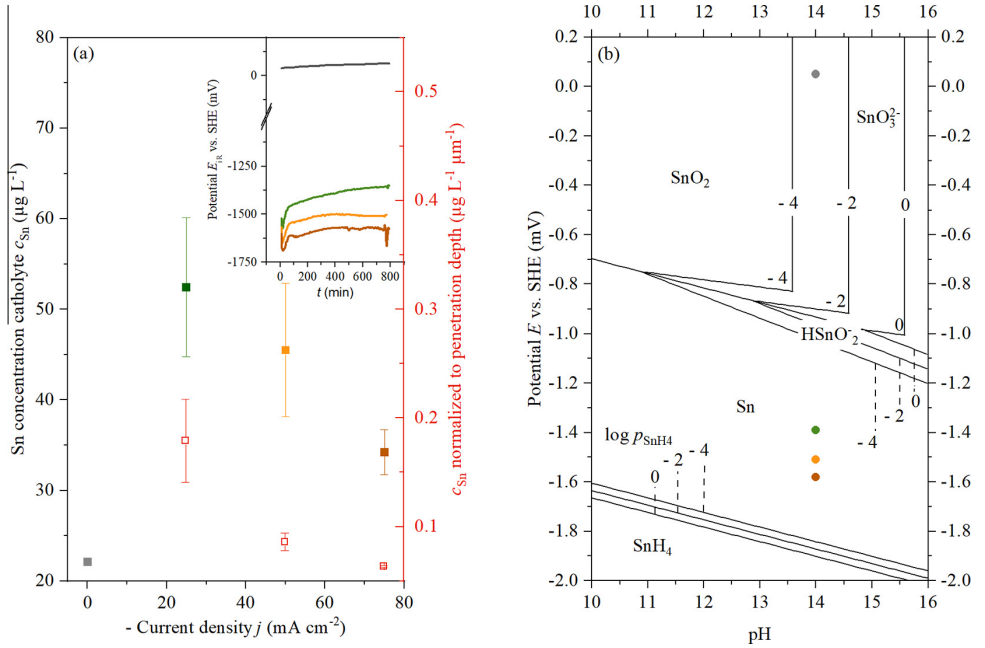

Fig. 4. (a) Concentration and normalized – with respect to penetration depth – concentration of dissolved tin species in the catholyte determined via ICP-MS measurements after CO_2 electrolysis for 800 min at the desired current density and OCV. Inset: Corresponding time dependent electrode potential. (b) Pourbaix diagram for tin calculated according to Pourbaix [38]; circles represent the iR corrected averaged potentials for the operation at the current densities shown in (a).

Additionally, the E – pH diagram emphasizes that SnO_2 can be stepwise reduced to Sn via SnO and/or dissolved SnO_3^{2-} and $HSnO_2^-$ [27,28,38]. The fact that tin can be found in the catholyte (cf. Fig. 4 (a)) shows clearly that a dissolved tin species is present and that SnO_2 reduction at least partially occurs via such mechanism. This might explain why besides a loss of catalyst material deep inside the GDE an enrichment of tin can be found near the GDEs surface. The dissolved tin species shows a tendency to move in the direction of the bulk electrolyte due to diffusion induced by the concentration gradient of dissolved tin and electromigration of the negatively charged tin ions in the direction of the anode.

Unfortunately, SnO_2 and not metallic tin is the active species in CO_2RR and might explain a degradation of the GDE in terms of catalyst alteration in addition to the observed leaching [39]. However, several authors suggested that under reduction conditions a metastable native oxide layer is present at the catalyst surface impeding the degradation of the active material. This metastable oxide layer is only stable to a certain extent, the protecting oxide layer will be reduced at extremely negative potentials [26,28,39].

As indicated in Fig. 4(a) and (b) more negative potentials seem to be beneficial for a subsequent redeposition of tin inside the GDE. It must be mentioned that due to the generated OH^- ions during CO_2RR and HER (cf. (1)–(3)) the pH value inside the porous system can be significantly higher than 14, possibly changing the thermodynamically stable tin species to $HSnO_2^-$ instead of metallic tin (cf. Fig. 4(b)). This phenomenon would be observed first for the experiment at −25 mA cm^{-2} as the corresponding averaged potential is the closest to the equilibrium line. Besides the more positive potential at this current density this might be the reason why the highest tin concentration in the catholyte can be found for the experiment at −25 mA cm^{-2}. Additionally, the potential at −75 mA cm^{-2} is significantly more negative which favors the redeposition of dissolved tin species. The reduced amount of diluted tin species at higher current densities can be seen even more pronounced when normalizing the measured tin concentration with respect to the penetration depth to decouple the effect of an increased amount of wetted surface area at higher current densities (cf. Figs. 4 and 3). Since we did not perform ICP-MS measurements for the anolyte a cross-over of dissolved SnO_3^{2-} or $HSnO_2^-$ though the AEM cannot be excluded with certainty as reason for the reduced amount of diluted tin species for −50 mA cm^{-2} and −75 mA cm^{-2} compared to −25 mA cm^{-2}.

Among the formate-producing materials, only the bismuth – based catalysts are known to be electrochemically active in the metallic state, whereas for all the others, e.g. In, Hg, the presence of a metastable oxide surface layer seems necessary for formate generation at adequate FE [40]. To overcome the unavoidable oxide reduction at the conditions at hand and to allow to investigate long-term stability of the GDE without the superimposed catalyst stability issue, we manufactured Bi_2O_3 – based GDEs and analyzed their long-term behavior in the same manner.

3.4. Degradation of Bi_2O_3 – based GDEs

To evaluate the stability of the Bi_2O_3 GDE, cross-sectional element mapping and ICP-MS measurements of the catholyte were performed after 24 h of operation at −50 mA cm^{-2} in 1.0 M KOH. According to the Pourbaix diagram metallic Bi is the stable phase (cf. Fig. 5(a)) at the observed average potential E_{iR} = −1.30 V vs. SHE (cf. Fig. 6(b) inset) and pH value ≥14. The direct electrochemical reduction of Bi_2O_3 can be described via:

$$Bi_2O_3 + 3H_2O + 6e^- \rightleftharpoons 2Bi + 6OH^- \quad (7)$$

According to Fig. 6(a) the same behavior for Bi_2O_3 can be observed as in the case of the SnO_2 – based GDE (cf. Fig. 3): compared to the non-wetted area the bismuth signal is significantly reduced in the center region of the GDE. Close to the GDEs surface which faces the electrolyte it appears that an enrichment of bismuth is observable. These observations indicate that Bi_2O_3 is leaching into the catholyte with a subsequent reduction of the diluted species in the outer region of the GDE. In fact, Vivier et al. showed in a detailed cyclic voltammetry study that the mechanism of Bi_2O_3 reduction to metallic Bi in alkaline media includes a dissolved BiO_2^- species from which the observed mobility of bismuth (cf. Fig. 6(a)) can be deduced [41]. Furthermore, the dissolution of Bi_2O_3 is favored at higher pH values which can be an explanation for the distinct loss of Bi_2O_3 in deeper layers of the GDE since the transport of produced OH^- from the active area into the bulk phase is hindered. The chemical dissolution of Bi_2O_3 and the subsequent electrochemical reduction of the diluted species to Bi probably follows these simplified reactions [41,42]:

$$Bi_2O_3 + 2OH^- \rightleftharpoons 2BiO_2^- + H_2O \quad (8)$$

$$BiO_2^- + 2H_2O + 3e^- \rightleftharpoons Bi + 4OH^- \quad (9)$$

Analogous to the characterization of the SnO_2 – based GDE, samples of the catholyte were taken at the beginning of the experiment (no polarization) and analyzed for bismuth. Interestingly, the sample taken at t = 0 min had a bismuth concentration of 22.8 μg L^{-1} (probably introduced by impurities in the KOH salt) whereas the averaged value of both samples (two identical experiments) taken after 24 h under load showed a significant lower concentration of 5.0 μg L^{-1} ± 1.2 μg L^{-1} which is close to the detection limit of 3.0 μg L^{-1} and lower than the quantification limit 9.0 μg L^{-1} (cf. Fig. 5(b)).

The ICP-MS results combined with the observations in the element mapping suggest that Bi_2O_3 partially dissolves to BiO_2^- but is quantitatively reduced again to metallic Bi so that no effective catalyst leaching can be observed with ICP-MS. Our results further indicate that bismuth impurities of the electrolyte salt are reduced to metallic bismuth as well. The different precipitation degree of the dissolved species in the tin- and bismuth – based system might be ascribed to the different potentials for the transition from dissolved to metallic species as determined by thermodynamics and illustrated in the corresponding Pourbaix diagrams. Whereas the potential for reduction of BiO_2^- to Bi is located at −0.50 V vs. SHE [38], the transition of $HSnO^-$ to Sn occurs at around −1.10 V vs. SHE, both at pH 14. The corresponding electrode potentials during electrolysis were −1.30 V and −1.51 V, respectively, indicating the difference in the driving force for the reduction.

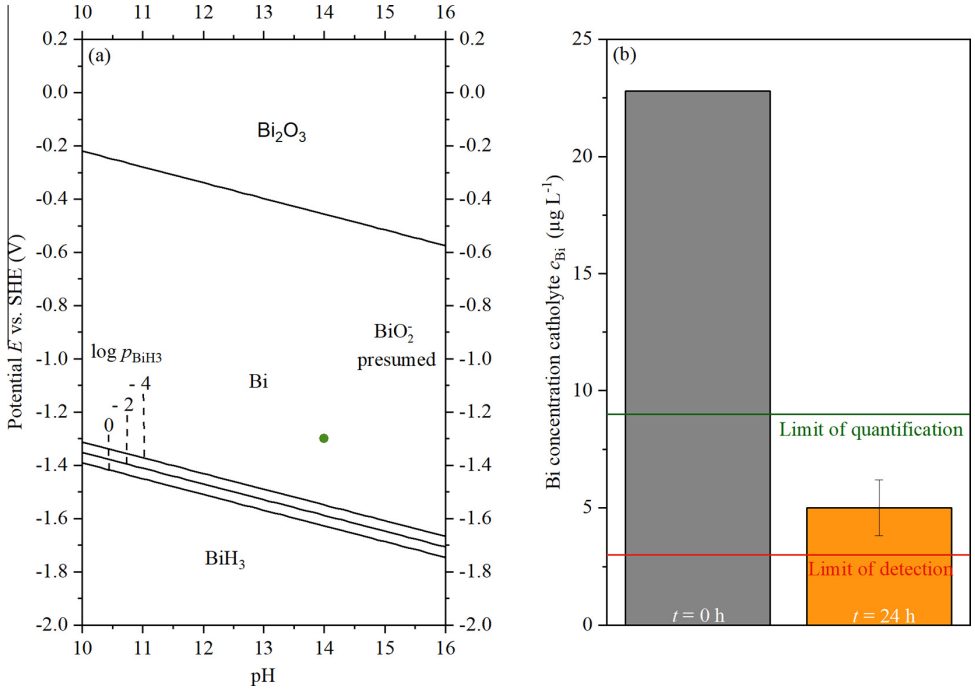

Fig. 5. (a) Pourbaix diagram for bismuth calculated according to Pourbaix [38]. (b) Bismuth concentration in catholyte determined via ICP-MS at the beginning of the experiment and after 24 h.

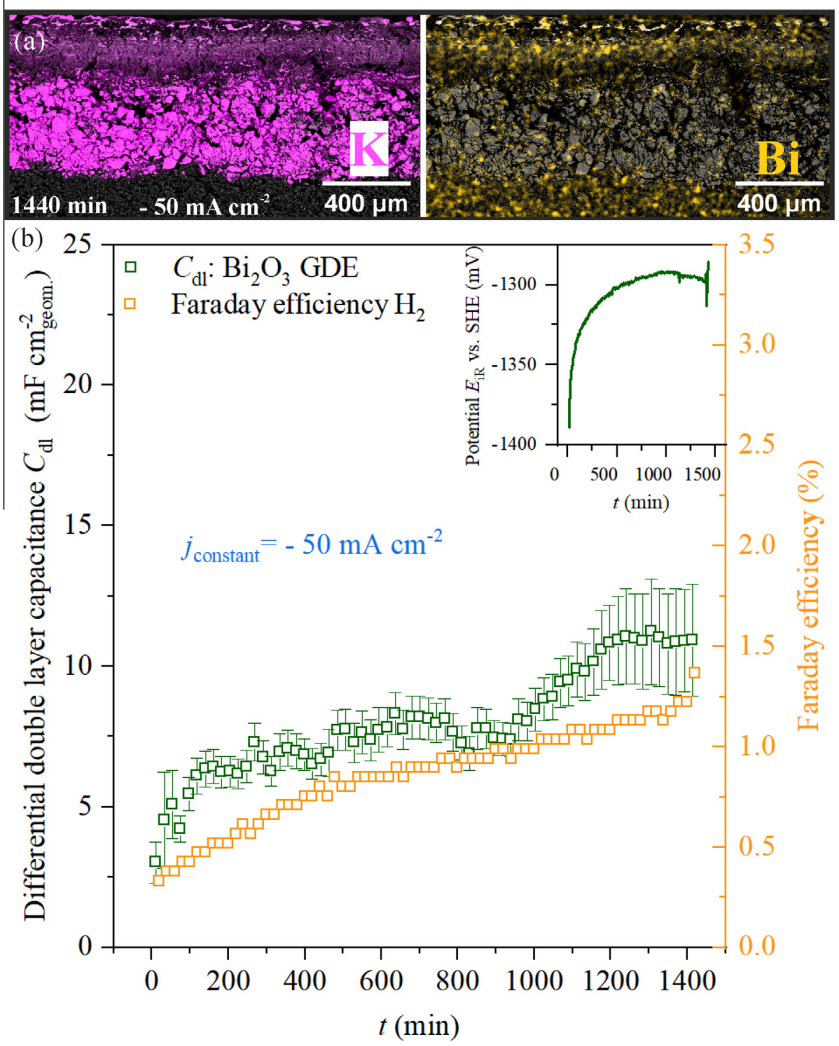

Fig. 6. (a) Cross-sectional element maps of potassium and bismuth obtained for a Bi_2O_3 – based GDE which was operated for 24 h at −50 mA cm^{-2}. (b) Corresponding time dependent behavior of C_{dl}, hydrogen FE and electrode potential.

The corresponding time course of the FE for hydrogen and the C_{dl} values for the Bi_2O_3 GDE are depicted in Fig. 6(b) (FE for CO and $HCOO^-$ are illustrated in Fig. S9). The C_{dl} curve has a similar shape as for the SnO_2 GDE indicating a comparable wetting behavior which is expected as only the catalyst material was changed. Since no effective loss of catalytically active species is observed, the increase of the hydrogen FE with time indicates a degradation process promoted by increased wetting due to:

- A mass transport problem: hindered removal of liquid phase product or blockage of gas transport pores with electrolyte or precipitated carbonate salts impeding sufficient CO_2 transport [24,25]
- A reversible change of selectivity induced by a shift of the potential to a less negative value as a result of the increased wetting which raises the number of the accessible active sites (j = const.).

In detail, two slopes of the hydrogen FE curve can be distinguished: in the region of 0–500 min a distinct increase of hydrogen FE is observable which correlates with the significant change of E_{iR} vs. SHE in this time region. Conversely, the sharp increase of C_{dl} is only observed until ~200 min instead of 500 min indicating that the on-going significant hydrogen FE increase cannot solely be attributed to the wetting. After 500 min the hydrogen FE increases with a lower rate which correlates with the time course of the potential. The substantial increase of C_{dl} at ~900 min is not reflected in FE H_2 suggesting again that an increased wetting does not necessarily result in proportionally higher hydrogen FE.

On the other hand, catalyst leaching was neglected as reason for the degradation since it was shown before, that less bismuth can be found in the catholyte at t = 24 h compared to t = 0 h. This, at first sight, reasonable assumption might not be accurate since the element mapping illustrated a diminishment of bismuth deeply inside the GDE so that a catalyst redistribution -evoked by

the reduction of Bi_2O_3 to Bi via dissolved BiO_2^- – can be concluded. Since this diminishment of catalyst is observed at the interface where the electrode is wetted and non-wetted (indicated by potassium cf. Fig. 6(a)) it might be the case that the reduced amount of catalyst in the reaction zone – which is expected to be close to the cross section of the wetted and non-wetted area – alters the electrodes performance. Additionally, even without an effective loss of catalyst material the dissolution of Bi_2O_3 and redeposition of Bi will very likely lead to bigger particles and by that reducing the catalytic surface. Unfortunately, the approach to use Bi_2O_3 GDEs was not able to completely deconvolute the impact of catalyst alteration and GDE wetting onto the degradation mechanisms to safely identify the mainly responsible phenomenon. For future work it will be helpful to directly synthesize Bi – based catalyst material instead of Bi_2O_3 so that a redistribution of the catalyst induced by dissolvable Bi_2O_3 at the applied potential and pH region (cf. Eq. (8)) can be prevented.

4. Conclusions

In this contribution we investigated the degradation of SnO_2 and Bi_2O_3 – based GDEs in the electrochemical reduction of CO_2.

Our results demonstrate that the observed GDE degradation is affected by the wetting behavior and catalyst leaching. The contribution of each degradation process cannot be quantified separately if the catalyst is not stable – as is the case for SnO_2 in highly alkaline media – which as consequence will prevent a clear assignment of the main degradation mechanism. Furthermore, under galvanostatic operation an increased wetting of the GDE will lead to a reduced potential and alter the GDEs performance due to the potentioselective nature of the CO_2RR while the reversible performance drop could falsely be assigned to an irreversible degradation phenomenon. It was not possible to conduct potentiostatic EIS measurements since the applied potential cannot be iR compensated during the EIS measurement. This would be necessary since the current in potentiostatic EIS will increase with time due to the progressing wetting induced by the applied potential.

However, besides not being able to exactly quantify the specific contribution of the electrodes wetting and catalyst leaching to the degradation of the GDE our results clearly show that SnO_2 is not a suitable catalyst for the long-term operation of a CO_2 electrolyzer in highly alkaline media: without controlling the local pH value (i.e. incorporation of an ionomer) SnO_2 will be leached out of the GDE and might be redeposited as tin metal which is not active for CO_2RR but instead favors HER. ICP-MS measurements of the catholyte indicate that this redeposition is not quantitative and that the catalyst will be lost over time. To overcome the catalyst leaching and to deconvolute the possible degradation processes, Bi_2O_3 GDEs were manufactured as it was hypothesized that reduction to metallic bismuth will not deteriorate performance as in contrast to most formate-producing catalysts bismuth is active for CO_2RR in metallic form. Unfortunately, similar as in the case of SnO_2, dissolution of Bi_2O_3 was observed as evidenced from cross-sectional bismuth maps of the GDE. In contrast to the SnO_2 – based GDE the diluted dissolved species was redeposited quantitatively as demonstrated by ICP-MS measurements which pointed out that there was no bismuth accumulation in the catholyte. This and the fact that redeposited metallic bismuth is active for CO_2RR itself is strongly suggested to be the reason why the degradation of the Bi_2O_3 GDE is less distinct compared to the SnO_2 GDE.

However, to clearly solve the problem of two superimposed degradation mechanisms, we suggest for future investigation the direct preparation of Bi GDEs since the metallic species is the active species for CO_2RR and according to the Pourbaix diagram stable in highly alkaline media and the negative potentials at hand. Consequently, the alteration of the GDE due to a redistribution of the active material via dissolving and redepositing – even if quantitatively – can be prevented and the contribution of the GDEs wetting onto the electrodes degradation clearly determined.

Declaration of Competing Interest

The authors declare that they have no known competing financial interests or personal relationships that could have appeared to influence the work reported in this paper.

Acknowledgments

Parts of this work were funded by the German Federation of Industrial Research Associations (EWN03176/18). The authors wanted to thank Ina Plock who conducted the SEM/EDX measurements, Christina Schmitt who performed XRD measurements and Nina Bengen for support in ICP-MS.

Appendix A. Supplementary data

Supplementary data to this article can be found online at https://doi.org/10.1016/j.jechem.2021.03.050.

References

[1] J.C. Abanades, E.S. Rubin, M. Mazzotti, H.J. Herzog, Energy Environ. Sci. 10 (2017) 2491–2499.
[2] P. Smith, S.J. Davis, F. Creutzig, S. Fuss, J. Minx, B. Gabrielle, E. Kato, R.B. Jackson, A. Cowie, E. Kriegler, D.P. van Vuuren, J. Rogelj, P. Ciais, J. Milne, J.G. Canadell, D. McCollum, G. Peters, R. Andrew, V. Krey, G. Shrestha, P. Friedlingstein, T. Gasser, A. Grübler, W.K. Heidug, M. Jonas, C.D. Jones, F. Kraxner, E. Littleton, J. Lowe, J.R. Moreira, N. Nakicenovic, M. Obersteiner, A. Patwardhan, M. Rogner, E. Rubin, A. Sharifi, A. Torvanger, Y. Yamagata, J. Edmonds, C. Yongsung, Nat. Clim. Change 6 (2015) 42–50.
[3] Eurostat, 2019.
[4] M. Jouny, W. Luc, F. Jiao, Ind. Eng. Chem. Res. 57 (2018) 2165–2177.
[5] W. Zhang, Y. Hu, L. Ma, G. Zhu, Y. Wang, X. Xue, R. Chen, S. Yang, Z. Jin, Adv. Sci. 5 (2017) 1700275.
[6] M.G. Kibria, J.P. Edwards, C.M. Gabardo, C.-T. Dinh, A. Seifitokaldani, D. Sinton, E.H. Sargent, Adv. Mater. 31 (2019) 1807166.
[7] J. Qiao, Y. Liu, J. Zhang, Electrochemical Reduction of Carbon Dioxide: Fundamentals and Technologies, CRC Press, 2016.
[8] Y.Y. Birdja, E. Pérez-Gallent, M.C. Figueiredo, A.J. Göttle, F. Calle-Vallejo, M.T.M. Koper, Nat. Energy 4 (2019) 732–745.
[9] X. Zhang, S.-X. Guo, K.A. Gandionco, A.M. Bond, J. Zhang, Mater. Today. Adv. 7 (2020) 100074.
[10] S. Zhao, S. Li, T. Guo, S. Zhang, J. Wang, Y. Wu, Y. Chen, Nano-Micro Lett. 11 (2019) 62.
[11] S. Verma, B. Kim, H.-R.-M. Jhong, S. Ma, P.J.A. Kenis, ChemSusChem 9 (2016) 1972–1979.
[12] F. Bienen, D. Kopljar, A. Löwe, P. Assmann, M. Stoll, P. Rössner, N. Wagner, A. Friedrich, E. Klemm, Chem. Ing. Tech. 91 (2019) 872–882.
[13] Y. Hori, Electrochemical CO2 reduction on metal electrodes, in: C.G. Vayenas, R.E. White, M.E. Gamboa-Aldeco (Eds.), Mod. Asp. Electrochem., Springer, New York, 2008, pp. 89–189.
[14] T. Burdyny, W.A. Smith, Energy Environ. Sci. 12 (2019) 1442–1453.
[15] D.C. Higgins, C. Hahn, C. Xiang, T.F. Jaramillo, A.Z. Weber, ACS Energy Lett. 4 (2018) 317–324.
[16] H. Rabiee, X. Zhang, L. Ge, S. Hu, M. Li, S. Smart, Z. Zhu, Z. Yuan, ACS Appl. Mater. Interfaces 12 (2020) 21670–21681.
[17] T.N. Nguyen, C.T. Dinh, Chem. Soc. Rev. 49 (2020) 7488–7504.
[18] D.M. Weekes, D.A. Salvatore, A. Reyes, A. Huang, C.P. Berlinguette, Acc. Chem. Res. 51 (2018) 910–918.
[19] C. Oloman, H. Li, ChemSusChem 1 (2008) 385–391.
[20] A. Löwe, C. Rieg, T. Hierlemann, N. Salas, D. Kopljar, N. Wagner, E. Klemm, ChemElectroChem 6 (2019) 4497–4506.
[21] U.O. Nwabara, E.R. Cofell, S. Verma, E. Negro, P.J.A. Kenis, ChemSusChem 13 (2020) 855–875.
[22] Y.J. Sa, C.W. Lee, S.Y. Lee, J. Na, U. Lee, Y.J. Hwang, Chem. Soc. Rev. 49 (2020) 6632–6665.
[23] Y.Y. Birdja, J. Vaes, ChemElectroChem 7 (2020) 4713–4717.
[24] M.E. Leonard, L.E. Clarke, A. Forner-Cuenca, S.M. Brown, F.R. Brushett, ChemSusChem 13 (2020) 400–411.
[25] P. Jeanty, C. Scherer, E. Magori, K. Wiesner-Fleischer, O. Hinrichsen, M. Fleischer, J. CO2 Util. 24 (2018) 454–462.
[26] S. Lee, J.D. Ocon, Y.-I. Son, J. Lee, J. Phys. Chem. C 119 (2015) 4884–4890.

Article III

[27] M.F. Baruch, J.E. Pander, J.L. White, A.B. Bocarsly, ACS Catal. 5 (2015) 3148–3156.
[28] A. Dutta, A. Kuzume, M. Rahaman, S. Vesztergom, P. Broekmann, ACS Catal. 5 (2015) 7498–7502.
[29] S. Popovic, M. Smiljanic, P. Jovanovic, J. Vavra, R. Buonsanti, N. Hodnik, Angew. Chem. Int. Ed. 59 (2020) 14736–14746.
[30] F. Bienen, D. Kopljar, A. Löwe, S. Geiger, N. Wagner, E. Klemm, K.A. Friedrich, ACS Sustainable Chem. Eng. 8 (2020) 13759–13768.
[31] C.-C. Miao, G.-Q. Yuan, ChemElectroChem 5 (2018) 3741–3747.
[32] C.A. Schneider, W.S. Rasband, K.W. Eliceiri, Nat. Methods 9 (2012) 671–675.
[33] G.J. Brug, A.L.G. van den Eeden, M. Sluyters-Rehbach, J.H. Sluyters, J. Electroanal. Chem. 176 (1984) 275–295.
[34] N. Gupta, M. Gattrell, B. MacDougall, J. Appl. Electrochem. 36 (2006) 161–172.
[35] X. Lu, C. Zhu, Z. Wu, J. Xuan, J.S. Francisco, H. Wang, J. Am. Chem. Soc. 142 (2020) 15438–15444.
[36] A.J. Bard, L.R. Faulkner, Electrochemical Methods: Fundamentals and Applications, second ed., John Wiley & Sons, Incorporated, 2000.
[37] E.W. Washburn, Phys. Rev. 17 (1921) 273–283.
[38] M. Pourbaix, Atlas of Electrochemical Equilibria in Aqueous Solutions, Pergamon Press, 1966.
[39] Y. Chen, M.W. Kanan, J. Am. Chem. Soc. 134 (2012) 1986–1989.
[40] J.E. Pander, M.F. Baruch, A.B. Bocarsly, ACS Catal. 6 (2016) 7824–7833.
[41] V. Vivier, C. Cachet-Vivier, S. Mezaille, B.L. Wu, C.S. Cha, J.Y. Nedelec, M. Fedoroff, D. Michel, L.T. Yu, J. Electrochem. Soc. 147 (2000) 4252.
[42] R.E.F. Einerhand, W.H.M. Visscher, E. Barendrecht, Electrochim. Acta 34 (1989) 345–353.

Supporting Information

Degradation study on tin- and bismuth-based gas-diffusion electrodes during electrochemical CO_2 reduction in highly alkaline media

Fabian Bienen[*a,b], *Armin Löwe*[c], *Joachim Hildebrand*[c], *Sebastian Hertle*[c], *Dana Schonvogel*[d], *Dennis Kopljar*[a], *Norbert Wagner*[a], *Elias Klemm*[c], *Kaspar Andreas Friedrich*[*a,b]

[a]Institute of Engineering Thermodynamics, German Aerospace Center, Pfaffenwaldring 38-40, 70569 Stuttgart, Germany

[b]Institute of Building Energetics, Thermal Engineering and Energy Storage, University of Stuttgart, Pfaffenwaldring 31, 70569 Stuttgart, Germany

[c] Institute of Technical Chemistry, University of Stuttgart, Pfaffenwaldring 55, 70569 Stuttgart, Germany

[d]Institute of Engineering Thermodynamics, German Aerospace Center, Carl-von-Ossietzky-Straße 15, 26129 Oldenburg, Germany

***Corresponding Authors**

E-mail addresses: Fabian.Bienen@dlr.de (Fabian Bienen); Andreas.Friedrich@dlr.de (Kaspar Andreas Friedrich)

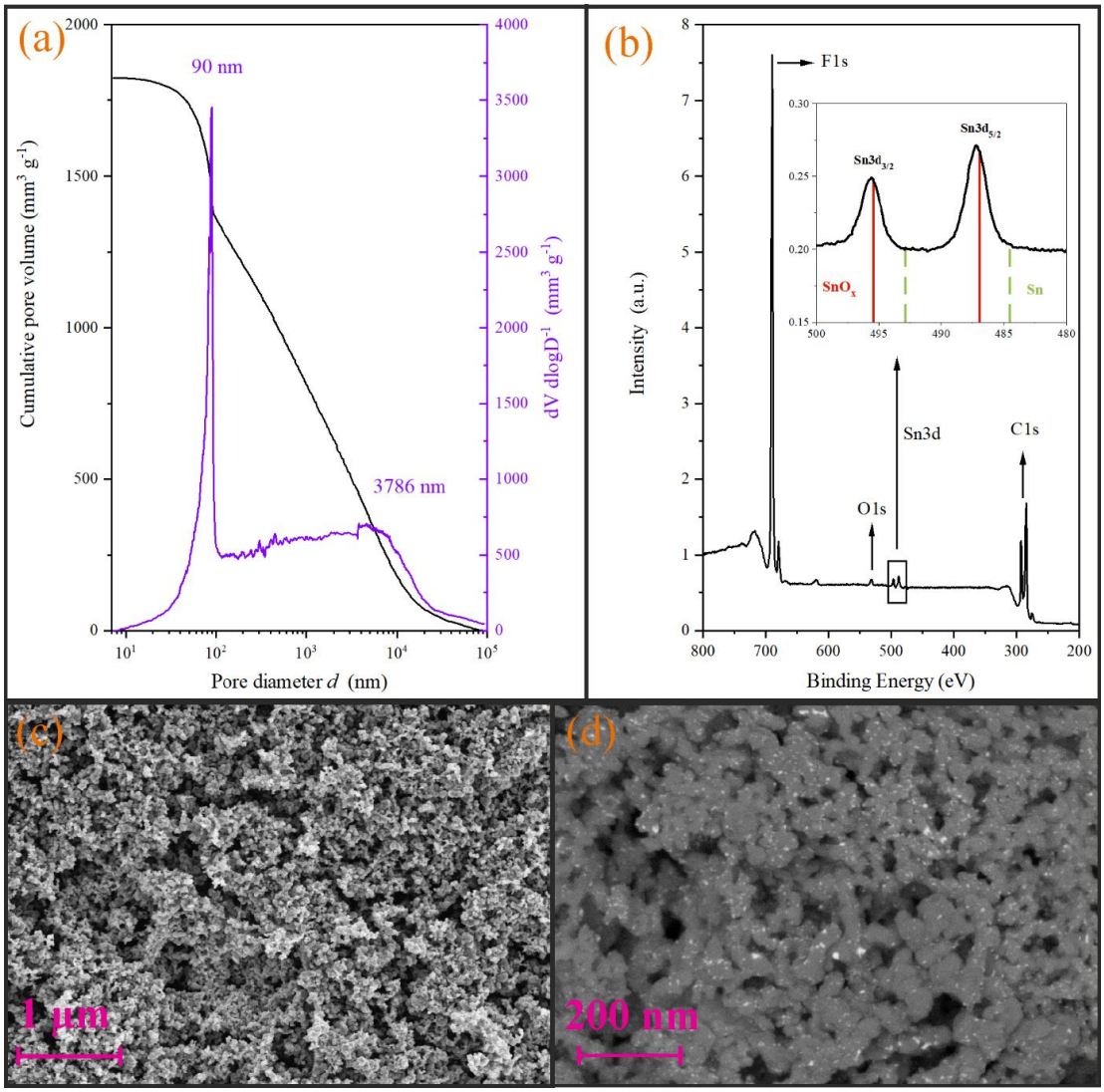

Fig. S1 (a) Hg-Porosimetry revealing a bimodal pore system (b) XPS spectrum showing that SnO_x is dominating the catalyst surface; peak deconvolution to distinguish between SnO_2 and SnO was not possible with hardware at hand) (c) SEM image emphasizing the porous structure of the GDE (d) material contrast elucidating the homogeneous dispersion of tin catalyst on carbon support [1].

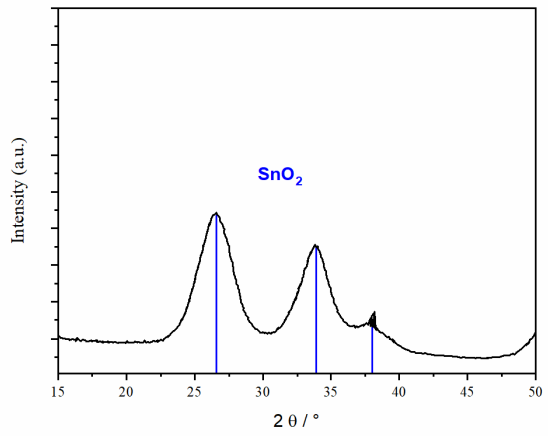

Fig. S2 Diffractogram obtained for the unsupported catalyst material showing that SnO_2 is the dominating species in the bulk phase of the catalyst [1].

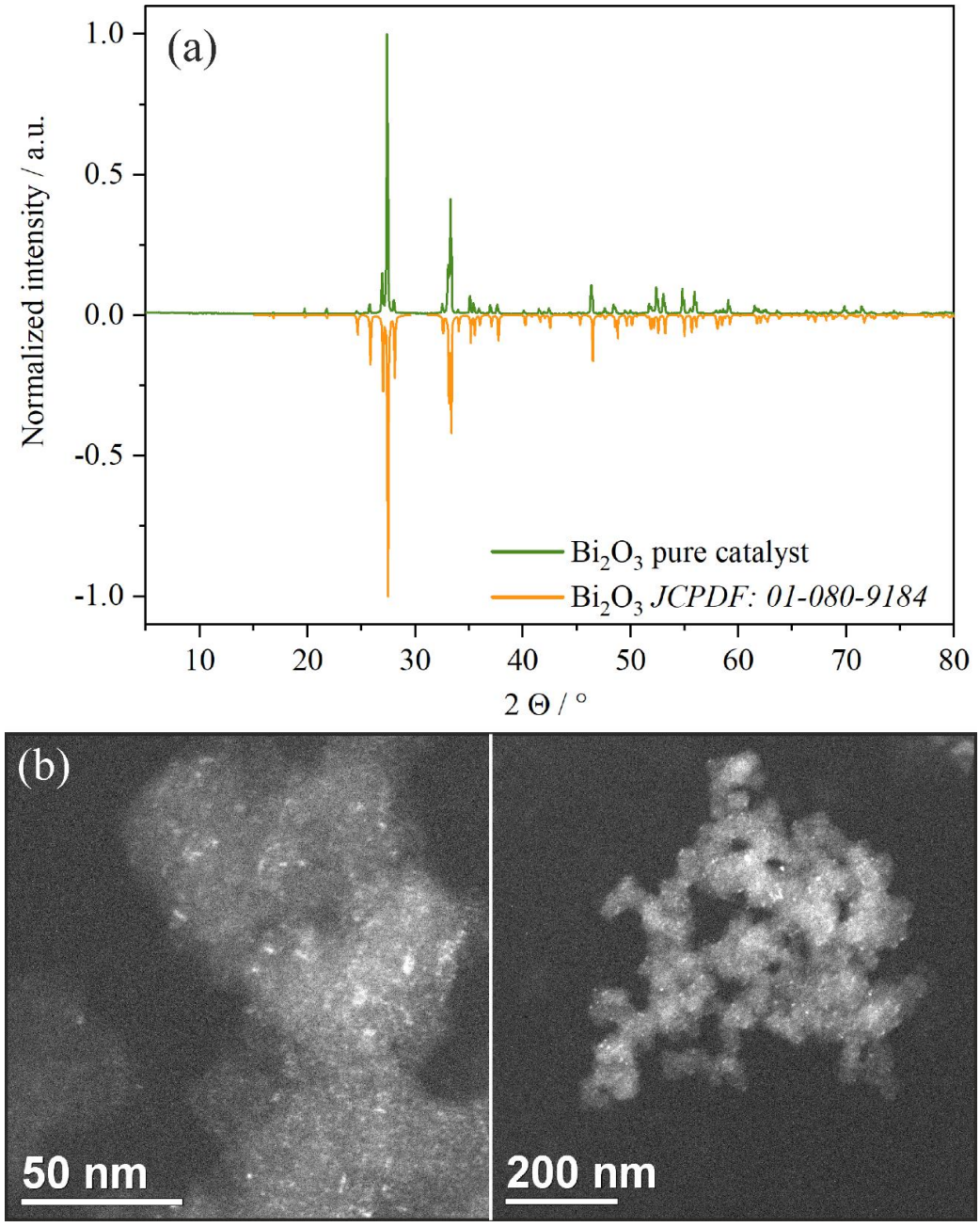

Fig. S3 (a) Diffractogram obtained for the unsupported catalyst material revealing that Bi_2O_3 is the present species in the bulk phase. (b) Dark field TEM images of the supported Bi_2O_3 catalyst emphasizing a homogeneous distribution of Bi_2O_3.

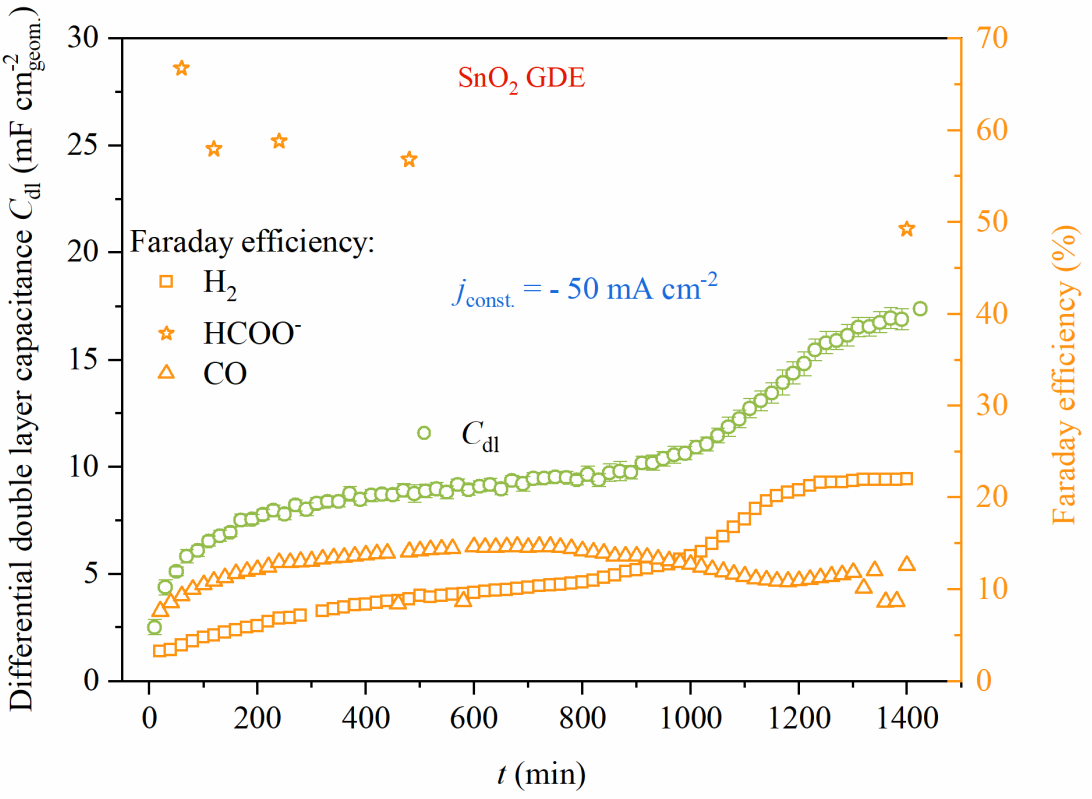

Fig. S4 Exemplary overview of time resolved FE for H_2, CO and $HCOO^-$. Galvanostatic operation of an SnO_2 based GDE at - 50 mA cm^{-2} in 1.0 M KOH. Total FE is smaller than 100% due to cross-over of $HCOO^-$ through the anion exchange membrane (AEM) with subsequent oxidation at the anode [2].

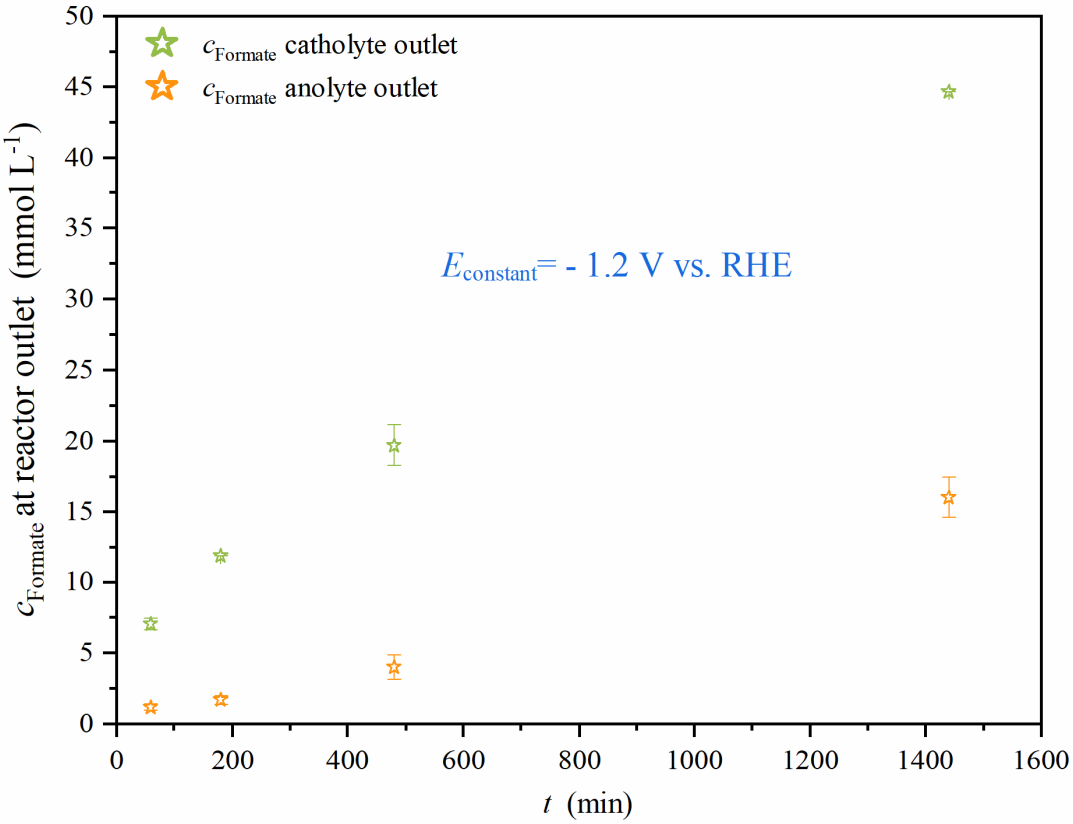

Fig. S5 Formate concentration at the reactor outlet of the anolyte and catholyte cycle revealing formate cross-over through the AEM. Potentiostatic operation of an SnO_2-based GDE in 1.0 M KOH at - 1.2 V vs. RHE.

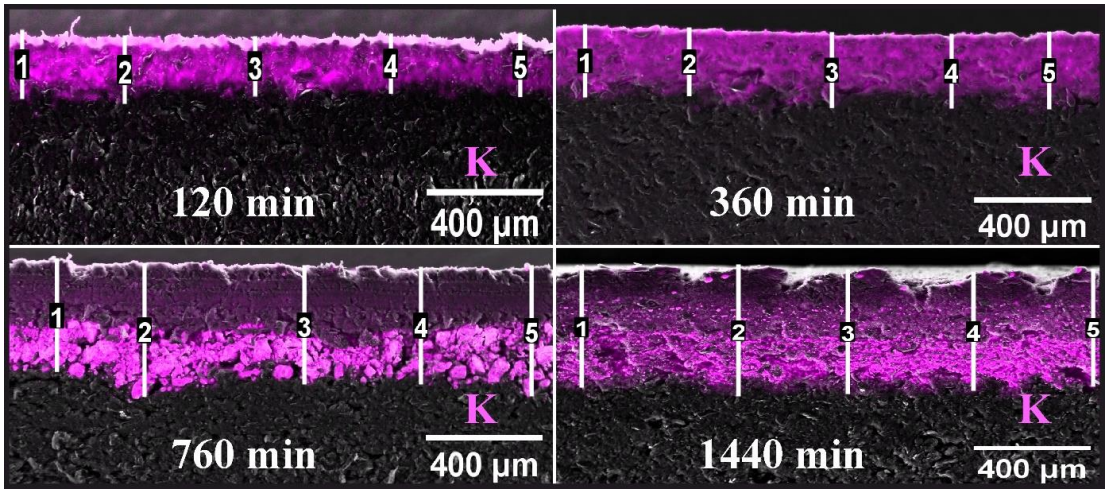

Fig. S6 Exemplary maps of potassium in the GDEs cross-section after operation at - 50 mA cm^{-2} for the desired time interval.

Table S1 Evaluated penetration depths at 5 different spots obtained for two independent similar experiments for each operation time.

Time / min	**Length 1** / µm	**Length 2** / µm	**Length 3** / µm	**Length 4** / µm	**Length 5** / µm	**Average** / µm	**Standard deviation** / µm
120	181	180	156	156	167	142	27
120	106	110	126	132	112		
360	235	220	244	240	249	253	23
360	299	271	271	231	267		
744	355	421	373	368	412	404	34
780	405	468	437	376	426		
1440	492	520	563	598	569	522	40
1440	489	533	504	480	475		

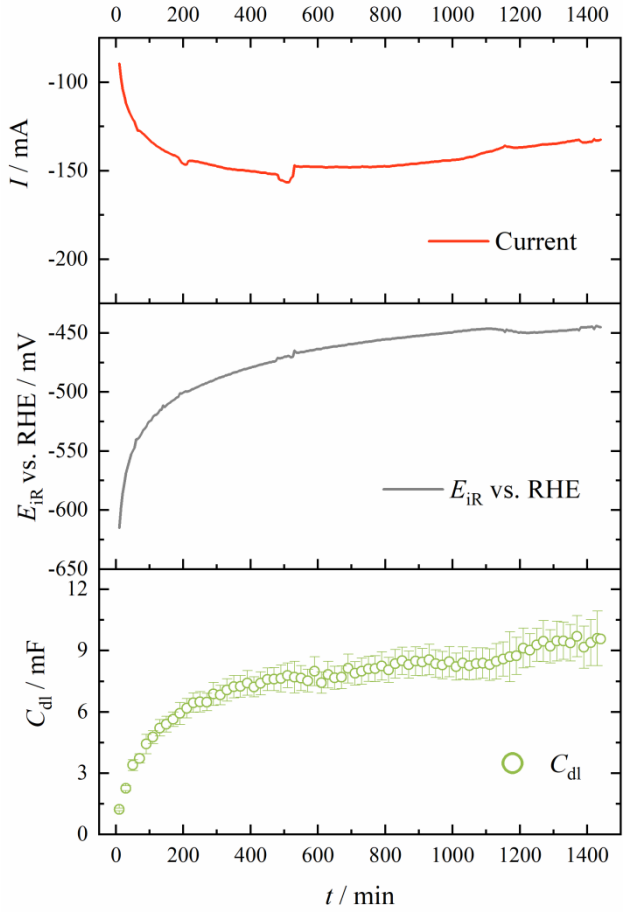

Fig. S7 Calculated C_{dl} values for an exemplary potentiostatic EIS measurement when operating a SnO_2-based GDE in 1.0 M KOH at - 1.2 V vs. RHE. Additionally, the measured current and iR-corrected potential are plotted.

Firstly, Fig. S7 shows that potentiostatic EIS is not potentiostatic in the very meaning of the word (see E_{iR} curve). This is due to the progressing wetting which is induced by the applied potential. The electrolyte will cover more and more active sites so that the resulting current will increase. The potential during potentiostatic EIS cannot be iR corrected “on the fly” so that the real potential of the electrode (affected by the increasing current) is not constant. The time course of the real applied potential and C_{dl} show the same shape as for the galvanostatic EIS experiments indicating that the obtained results should not depend on the applied operation mode.

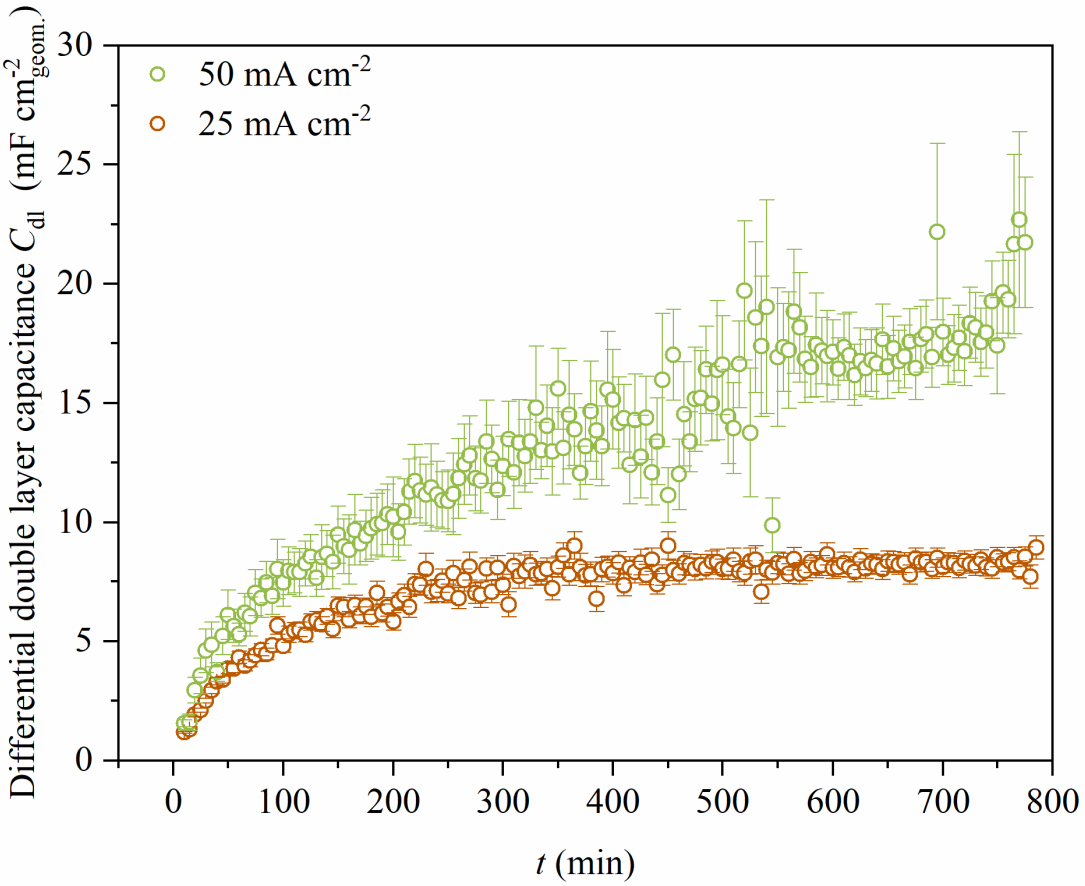

Fig. S8 Time dependent double layer capacitance values extracted from galvanostatic EIS measurements of an SnO_2 based GDE in 1.0 M NaOH at - 25 mA cm^{-2} and - 50 mA cm^{-2}.

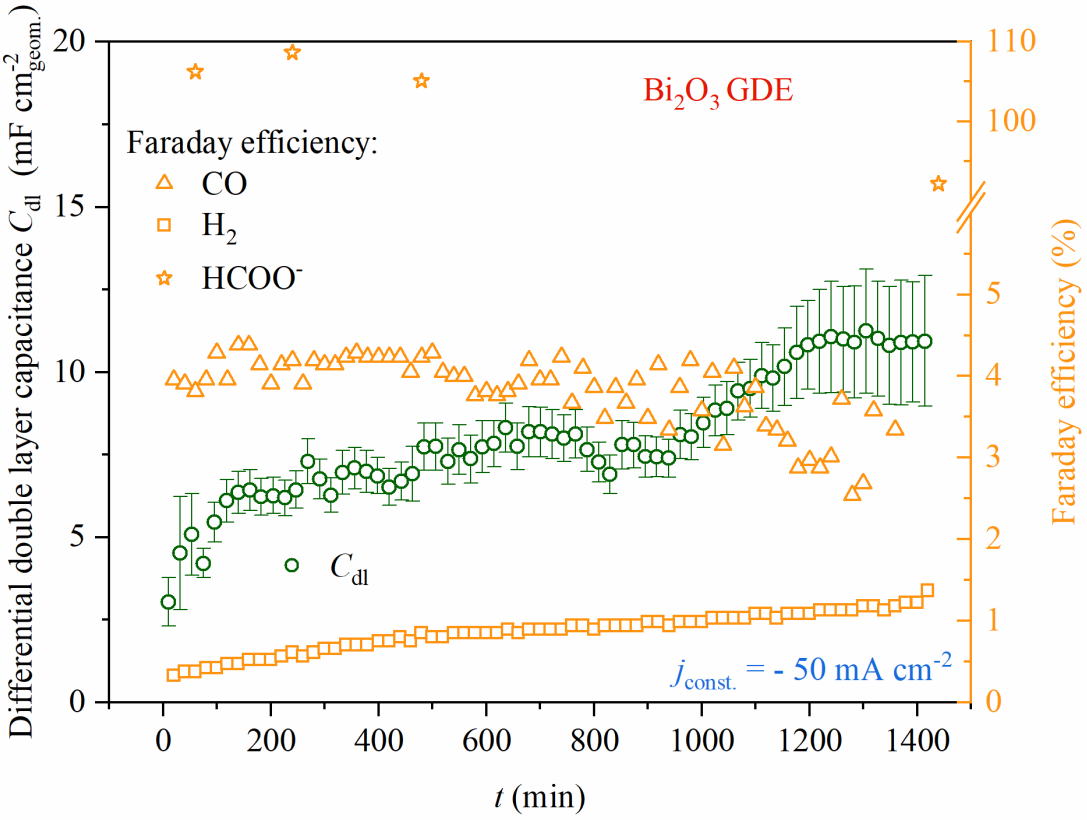

Fig. S9 Exemplary overview of time resolved FE for H_2, CO and $HCOO^-$. Galvanostatic operation of a Bi_2O_3 based GDE at - 50 mA cm^{-2} in 1.0 M KOH.

References

[1] F. Bienen, D. Kopljar, A. Löwe, S. Geiger, N. Wagner, E. Klemm, K.A. Friedrich, ACS Sustainable Chem. Eng., 8 (2020) 13759–13768.
[2] J. Zhang, W. Luo, A. Züttel, J. Catal., 385 (2020) 140–145.

Utilizing Formate as an Energy Carrier by Coupling CO_2 Electrolysis with Fuel Cell Devices

Fabian Bienen[1,‡], Dennis Kopljar[1,‡,*], Armin Löwe[2,‡], Pia Aßmann[1], Marvin Stoll[2], Paul Rößner[2], Norbert Wagner[1], Andreas Friedrich[1], and Elias Klemm[2]

DOI: 10.1002/cite.201800212

Electrochemical reduction of CO_2 to useful chemicals can change the role of CO_2 from harmful waste to a valuable feedstock. Despite a lot of progress in the alkaline electrochemical conversion of CO_2 to formate, there is still a lack of potential applications for the generated aqueous formate solution. Here, the general ability of formate to be used as an energy or hydrogen carrier is discussed and compared to well-known energy storage chemicals. Concepts to employ formate solution as an energy carrier by combining CO_2 electrolysis with the reconversion of formate into electricity via a direct formate fuel cell or catalytic decomposition to H_2 combined with a proton exchange membrane fuel cell are demonstrated.

Keywords: CO_2 reduction, Direct formate fuel cells, Energy carriers, Gas diffusion electrodes, Power-to-X technologies

Received: November 19, 2018; *revised:* April 15, 2019; *accepted:* April 16, 2019

1 Introduction

Some of the most important challenges society and industry are facing in the next decades are related to facilitating a shift of energy and chemical production away from fossil towards renewable resources and feedstocks, and to establish a circular, sustainable, and carbon-neutral economy [1]. Increasing the share of renewable energy in the global energy mix inevitably requires concepts of energy storage due to the fluctuating nature of most of the renewable energy sources such as wind and solar energy [2]. In this respect, the low-temperature electrochemical reduction of CO_2 (CO_2RR) on the cathode of an electrochemical cell is a promising approach to employ excess electricity from renewables and store it as chemical energy [3 – 10].

In principle, depending on the electrocatalyst [11 – 13] and the reaction conditions [14 – 16], a vast variety of products are accessible, from which, however, only few have been demonstrated so far to yield promising key figures regarding selectivity and reaction rates. From the accessible products, only CO and formic acid/formate (pKa = 3.77) have been shown to be produced with sufficient performance values, namely, at Faradaic efficiency (FE) above 80 % and current densities in the order of 100 mA cm^{-2} for hundreds of hours [17]. This is not surprising, as production of these two-electron transfer products is kinetically favorable on state-of-the-art catalysts (Sn- and Ag-based for formate and CO, respectively) without yielding an array of different products as on copper-based systems [18]. In recent years, also techno-economic analyses have been published which confirm that formic acid (not formate, see later) and CO are closest to reach economically competitive conditions [19 – 22]. This is facilitated by their relatively high market price. For CO or syngas, i.e., a mixture of CO and H_2, the application possibilities are manifold and its production via electrolysis is highly promising regarding the much-quoted and desired sector coupling, i.e., the integration of electricity from renewable resources into other fields of application, here, the chemical sector or the production of fuels.

On the contrary, although many studies are focused on the production of formate, its application and prospect as product remains quite elusive. It is often overlooked that it is not formic acid (FA) but formate that is produced in CO_2RR as in almost all instances neutral to alkaline conditions are employed, requiring an additional acidification step if the FA market is targeted. Furthermore, for both formate and FA, an energy-intensive separation from the electrolyte would be mandatory, questioning if this route is economically reasonable at all. While market potential for potassium formate, which is nowadays mainly used as deicing agent, is small, it is often referred to its potential as energy vector in energy storage applications. This applies

[1]Fabian Bienen, Dennis Kopljar, Pia Aßmann, Dr. Norbert Wagner, Prof. Dr. Andreas Friedrich
dennis.kopljar@dlr.de
German Aerospace Center (DLR), Institute of Engineering Thermodynamics, Pfaffenwaldring 38 – 40, 70569 Stuttgart, Germany.
[2]Armin Löwe, Marvin Stoll, Paul Rößner,
Prof. Dr.-Ing. Elias Klemm
University of Stuttgart, Institute of Chemical Technology, Pfaffenwaldring 55, 70569 Stuttgart, Germany.
[‡]*These authors contributed equally.*

for its use in H_2 storage, i.e., dehydrogenation and subsequent use in proton exchange membrane fuel cells (PEMFCs) or as fuel in direct liquid fuel cells (DLFCs), Fig. 1 [23, 24]. However, to the best of the authors' knowledge, studies proving the coupling of CO_2 electrolysis (CO_2EL) with these approaches of reconversion into electricity and critically assessing the system potential have not been published so far. Here, it is argued that in order to justify the considerable work on the electrochemical generation of formate in a process which lends itself to be transferred into large-scale applications, it is crucial to consider the valorization of the product. This is the starting point of the present contribution discussing these possible valorization pathways in a proof-of-concept study. The aim of this work is to experimentally demonstrate the feasibility of coupling the formate-rich product stream from CO_2EL with subsequent use in the above-mentioned applications. To the best of the authors' knowledge, this is the first time this has been published. To introduce the motivation, the experimental study is embedded into an elaborate discussion on the meaningfulness and suitability of formate as energy carrier as well as an introduction into the corresponding technologies. In that respect, relevant results from literature are included to describe the importance of optimizing the interface between the respective processes rather than optimizing each technology individually.

2 Concept of Electricity Storage Using Formate as Hydrogen Carrier

2.1 Evaluation of Formate as Energy or Hydrogen Carrier

The unique advantage of utilizing power-to-gas/liquid/chemicals or more generally power-to-X technology for energy storage application is the combination of the unprecedented energy content that can be stored in chemical bonds, simple scalability of the processes, and the ability to transport and store significant amounts of energy over a long period of time [2]. At the moment, various compounds are discussed as being attractive for chemical energy storage, ranging from methanol, ethanol, FA, or other liquid organic hydrogen carriers (LOHCs) to H_2, methane, or ammonia, with each technology exhibiting certain advantages and drawbacks [2, 25, 26]. As none of the chemical storage alternatives is superior in every aspect, it depends on the specific application and the rather subjective weighting of different properties to favor one over the other. Also, for the subsequent release of electricity in times of demand, different routes exist depending on the carrier, from which two approaches will be discussed herein: (1) the reforming or dehydrogenation of the compound with the subsequent use of the produced H_2 in hydrogen-fed fuel cells and (2) the direct utilization in liquid-fed fuel cells. While the first approach benefits from the already mature H_2/O_2-fuel cell technology, the latter is characterized by the compactness of the system but exhibits much lower technology readiness level (TRL). However, for certain niche applications, similar technologies, e.g., methanol, ethanol, and also FA fuel cells, have already been brought to demonstration scale proving their potential in certain off-grid applications, such as portable devices, supply logistics, or military equipment in which practicability outweighs price, energy density (see below), or scalability [27].

Naturally, being a liquid energy carrier when dissolved in aqueous solution, formate can be considered advantageous over gaseous compounds regarding safety, ease of transport, and storage. Although volumetric energy density of FA is in the same order of magnitude as compressed H_2 at 700 bar (~1.3 kWh L^{-1}), with 2.1 kWh L^{-1} (1.72 kWh kg^{-1}) it is rather moderate compared to methanol and ethanol with 4.82 kWh L^{-1} (6.09 kWh kg^{-1}) and 6.32 kWh L^{-1} (8.0 kWh kg^{-1}), respectively. For formate, exclusively taking into account energy density is even more problematic than for formic acid, as the formate salt is usually dissolved and diluted in water, further decreasing energy content to 756, 151, and 76 Wh L^{-1} for 10, 2, and 1 M, respectively. This sets strict limitations to its use in energy storage applications, in particular, when high energy density is indispensable, such as in electromobility. Thus, it is evident that neither aqueous potassium formate nor diluted FA solution can be considered promising in this application.

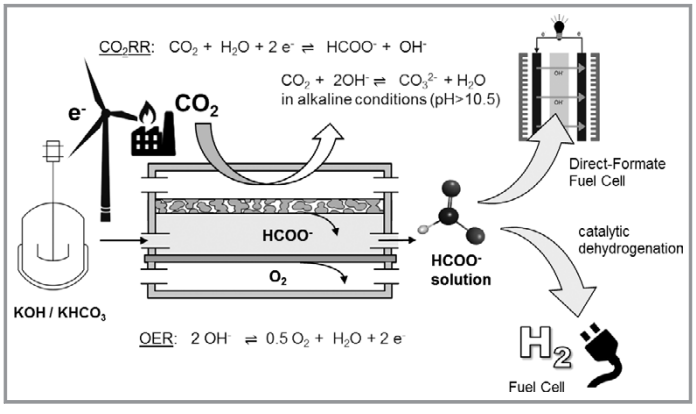

Figure 1. Coupling of CO_2 electrolysis to formate with the subsequent reconversion into electricity using fuel cell technologies.

However, instead of discussing theoretical energy densities, it can be reasonable to compare the realizable energy densities. In certain DLFCs, e.g., only diluted feed streams can be used and/or only partial oxidation realized, which reduces the available energy density considerably. The first holds true for direct-methanol fuel cells and, to lower extent, to direct-formic acid fuel

cells for which fuel crossover through the membrane limits the concentration at which the fuel cell works properly to 2 – 4 M [27]. Partial oxidation is, e.g., encountered in direct-ethanol fuel cells, where mostly just the 4-electron reaction towards acetic acid takes place instead of complete 12-electron oxidation to CO_2, thus, drastically decreasing the available energy density down to 252 Wh L^{-1} for partial oxidation of a 2 M solution. On the contrary, as it will be described later, direct formate fuel cells (DFFCs) running on concentrations as high as 15 M have been reported [28], corresponding to an energy density of 1.13 kWh L^{-1}. Yet, in the end, more important is the applicability of the technology and the advances that can be made in the performance of the energy-recovering system in comparison to competing electricity storage technologies, i.e., how much electrical energy can realistically be recovered and how efficiently. In this regard, performance reported with DFFC and dehydrogenation of formate are so far highly overlooked but indeed very promising, as will be discussed in the respective chapters.

Another important aspect, when the discussion is set in the context of green chemistry and the implementation of electricity from renewable resources, is the generation of the energy carrier. Formate can be regarded as being particularly promising as it is directly produced from CO_2 and electricity. But also the generation of methanol produced from CO_2 and renewable hydrogen (or directly from CO_2EL), ethanol and furfural from fermentation of biomass residues, or glycerol as waste product from biodiesel can be considered sustainable. Furthermore, formate salts are environmentally benign and less harmful than methanol and FA, the latter being also highly corrosive. On the contrary, other suggested storage chemicals such as hydrazine, ammonia, and borohydride might have high hydrogen content and show promising results when used in a DLFC, but are highly toxic or dangerous and, thus, rather unsuitable for decentralized or portable applications.

In summary, formate shows certain intriguing aspects which make its use attractive, particularly, when considering the coupling of its generation by electrolysis with electricity recovering by fuel cell technologies. A definite and critical assessment, however, must comprise a complete and quantitative analysis of the whole process chain starting from its production, transportation, and use [29]. Importantly, it has to take into account the specific field of application to find the niche where its use is competitive and reasonable. A decisive factor will be a successful further development of the technologies to improve performance, efficiency, and price.

2.2 Routes of Reconversion of Formate into Electricity

In the following, two routes to reconvert formate into electricity are described and important aspects for the coupling with CO_2EL are addressed.

2.2.1 Direct Formate Fuel Cell

In a DFFC, formate and O_2 are used to generate electricity. A sketch of the working principle is shown in Fig. 2. The corresponding electrochemical reactions are the oxygen reduction reaction (ORR) and the formate oxidation reaction (FOR), according to:

Cathode (ORR):

$$O_2 + 2H_2O + 4e^- \rightleftharpoons 4OH^- \quad E^0 = 0.40 \text{ V vs SHE} \tag{1}$$

Anode (FOR):

$$2HCOO^- + 6OH^- \rightleftharpoons 2CO_3^{2-} + 4H_2O + 4e^- \quad E^0 = -1.05 \text{ V vs SHE} \tag{2}$$

Overall:

$$2HCOO^- + 2OH^- + O_2 \rightleftharpoons 2CO_3^{2-} + 2H_2O \quad U^0 = 1.45 \text{ V} \tag{3}$$

The reaction at the cathode is already known from the H_2/O_2 alkaline fuel cell, which is the conversion of oxygen and water to hydroxide. At the anode, potassium formate (HCOOK) reacts with KOH to potassium carbonate and water. These two half-cell reactions are separated by an anion-exchange membrane (AEM). The transport of OH^-

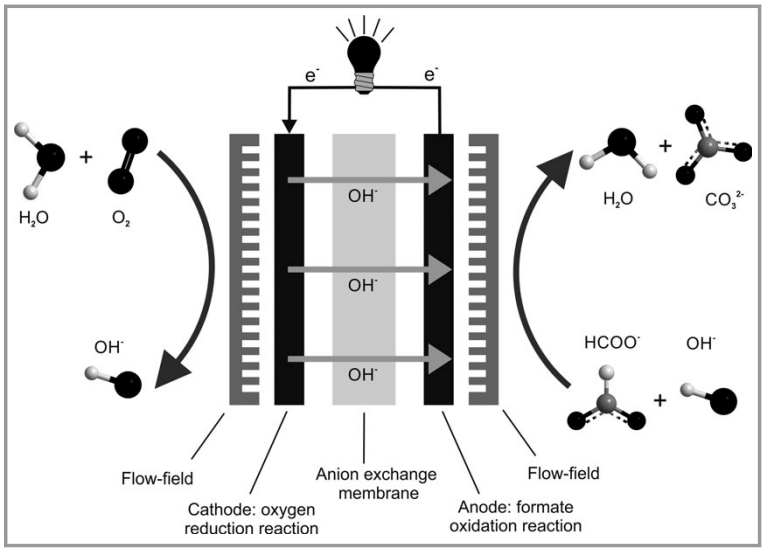

Figure 2. DFFC scheme showing the components of the cell, reactants, and products.

from the cathode to the anode compartment maintains the charge neutrality during operation. The theoretical cell voltage is 1.45 V (pH 14) [30], the highest among all common fuel cell systems.

The DFFC system provides certain beneficial properties. In comparison to FA, potassium formate shows low toxicity and is not corrosive which makes it easy to handle, store, and transport. Compared to acidic environment, alkaline medium accelerates the kinetics of both ORR and FOR (on Pd) while it also enables the use of non-noble metal catalysts [31]. Another advantage is that fuel crossover is significantly lower since OH^- is transported through the AEM from the cathode to the anode which is in the counter direction of a possible HCOOK crossover [32].

For these reasons, the use of DFFCs has gained a lot of interest in the last years and prompted considerable output of literature (see overview in [33]). Several authors demonstrated that operating DFFCs with pure O_2 at elevated temperatures (up to 60 °C) is beneficial [31, 34, 35] and that their performance exhibits a strong dependence on the composition of the feed. Studying the literature, it appears that the interaction between formate concentration, fuel cell performance, and oxidation kinetics is highly dependent on the system and not fully understood yet. Wang et al. report that the energetic efficiency reaches a maximum of 32 % at 4 M HCOOK [36]. According to Bartrom et al., the DFFC performance exhibits an optimum at a concentration of 1 M [28]. The latter also showed that oxidation kinetics is positively influenced by high formate concentrations up to 15 M which is advantageous regarding energy density of the fuel. Unfortunately, this does not translate into better performance in the full cell which is argued to be a matter of efficiency of fuel delivery to the active site, anode utilization, and ohmic losses. To the best of the authors' knowledge, the best DFFC performance with a model fuel stream was demonstrated by Tran et al. [32] who reported an energy density of 302 mW cm^{-2} for a fuel cell operating with pure oxygen at 60 °C, 1 M HCOOK, and 2 M KOH. Indeed, the published results already indicate reasonable applicability of the system to power certain portable devices. Based on their system performance, Wang et al. calculated that already 100 mL of 4 M HCOOK solution would facilitate the charging of a representative mobile phone field charger of 12 Wh when their device is scaled to a membrane electrode assembly (MEA) size of 200 cm^2 [36].

2.2.2 Formate Decomposition to H_2 and Use in Hydrogen-Fed Fuel Cells

Catalytic decomposition of formate can proceed via two different pathways. First, via the preferred dehydrogenation (Eq. (4)) forming H_2 and carbonate, or second, via decarbonylation (Eq. (5)), resulting in CO and OH^-. In both cases, water serves as source of protons. When the generated H_2 is used in a fuel cell, a CO content of less than 20 ppm is necessary to prevent poisoning of the electrocatalyst [23].

$$HCOO^- + OH^- \rightleftharpoons H_2 + CO_3^{2-} \quad (4)$$

$$HCOO^- \rightleftharpoons CO + OH^- \quad (5)$$

While a lot of research is done on the decomposition of FA – a concept particularly promoted by the group of Beller et al. [37] and Grasemann and Laurenczy [38] for H_2 storage – only a handful of publications deal with the decomposition of formate solutions. In this regard, particularly the studies of Su et al. [39] and Bi et al. [40] showed highly promising results, successfully introducing heterogeneously catalyzed hydrogen storage based on ammonium and potassium bicarbonate/formate, respectively. Besides demonstrating reversibility of de-/hydrogenation using a carbon-supported Pd catalyst, in both cases formate salts were decomposed to H_2 with yields > 90 % at optimized conditions and, importantly, without detection of CO. The latter can be explained by the mechanistic observation that the decomposition of FA follows a formate pathway which yields 100 % selectivity towards CO_2 and H_2 [41]. Furthermore, as dehydrogenation of formate results in the formation of (bi)carbonate (pKa = 10.5) instead of gaseous CO_2, as shown in Fig. 3, a mostly undiluted H_2 stream is produced which is of great advantage when coupling the process to a hydrogen-fed fuel cell [42].

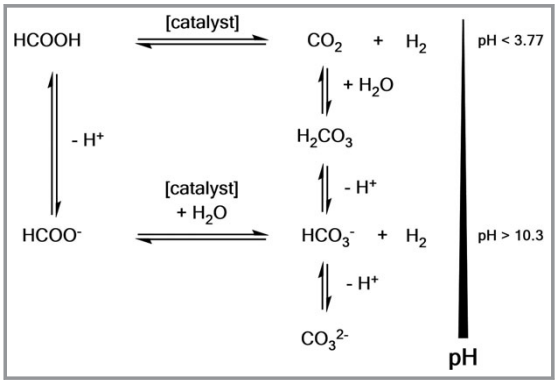

Figure 3. FA/formate decomposition and the connection to the carbonate cycle in aqueous solution.

2.3 Coupling of CO_2 Electrolysis with Subsequent Formate Utilization

To establish formate obtained from CO_2EL as a reasonable energy carrier, its electrochemical production has to be of high energetic efficiency at relevant production rates and yield a product stream of high concentration. Unfortunately, so far, CO_2EL often lacks in all of the above aspects. In terms of energetics, the sluggish reaction kinetics of both cathode and anode (oxygen evolution) reaction (OER) as well as ohmic losses throughout the cell contribute to a low efficiency. Accordingly, reported values barely exceed 30 – 40 % at

relevant current densities which increases specific energy input and, thereby, the cost of the electrolysis [43]. Besides the development of more efficient catalysts to decrease overpotentials, the limited conductivities of electrodes, membranes, and electrolytes cause ohmic losses that are reflected in the overall cell voltage as well and must be kept at a minimum. While a highly conductive electrolyte is favorable in all electrochemical applications, its choice also strongly affects the activity and product distribution [44, 45] by determining the composition in the electrochemical double layer, and thus, the kinetics and diffusion characteristics. The choice is further complicated by the required compatibility in the subsequent energy-recovering process, e.g., regarding the coupling product potassium (bi)carbonate, which forms both during alkaline CO_2EL as well as during both utilization steps. Precipitation by (locally) exceeding the solubility limit of the solvent causing a blocking of the pores of the catalyst support and reducing lifetime of the electrode might be a result.

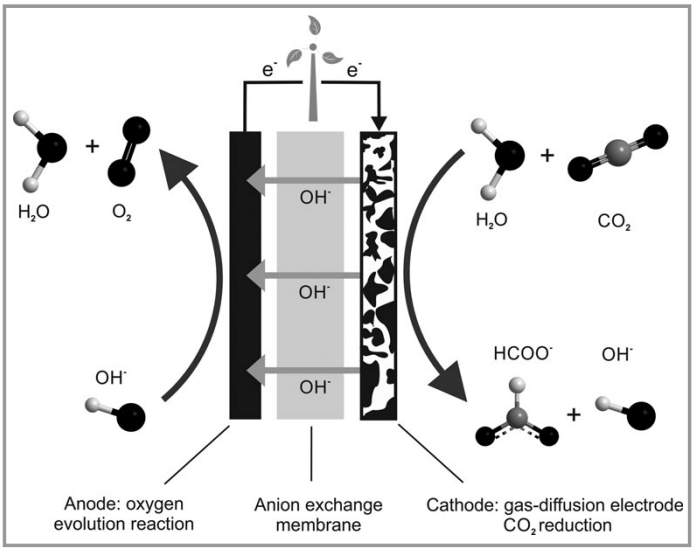

Figure 4. Filter-press type flow-through electrolysis cell for alkaline CO_2EL.

Of utmost importance, when the formate-rich product stream is to be used in energy-related applications, is to obtain a high concentration. Current density and residence time are obvious parameters to maximize concentration. However, so far, achieved concentrations at single-pass are well below 0.5 M, if reported at all [6], which is too low to obtain a reasonable energy density. This suggests that recirculation of the product stream to enhance total residence time and to accumulate formate is mandatory. To the best of the authors' knowledge, this has only been done by Kaczur et al. who introduced a unique three-compartment setup in which, despite working under alkaline conditions, the end product is FA at extremely high concentration up to 4 M [46]. When operating at high concentrations, it becomes reasonable to switch from cation-exchange membranes (CEMs), e.g., Nafion, which are employed in a majority of literature studies, to AEMs as shown in Fig. 4. This is important, as in neutral to alkaline conditions, the CEM transports K^+ instead of protons to maintain charge neutrality, which leads to an increasing accumulation and depletion of OH^- and K^+ in the cathode and anode chambers, respectively. In turn, this yields a corresponding opposite shift in pH on either side of the membrane and an increase of reactor voltage. This is negligible at small residence time and single-pass but becomes a problem at high recirculation rates. Using an AEM would allow for the compensation of this effect [47, 48]. Important aspects that arise are AEM availability, price, stability at high pH, and selectivity for OH^- over $HCOO^-$. Both the change in composition by accumulation of (bi)carbonate and formate, but also inevitable product crossover and oxidation would necessitate finding an optimum point of operation regarding product yield, efficiency, and concentration.

To deal with the low solubility of CO_2 in aqueous media, which limits the maximum current density on planar electrodes to a few mA cm^{-2} [49] and, therefore, again, the product concentration, gas diffusion electrodes (GDEs) are commonly used. These highly porous electrodes provide a high internal surface area at which the three-phase boundary forms and where the reaction takes place. Thereby, gaseous CO_2 can be fed and diffusion paths of dissolved CO_2 to the active sites can be minimized to a thin electrolyte film enabling current densities of several hundred mA cm^{-2}. Recently, the high performance of a hydrophobic GDE, comprised of polytetrafluorethylene (PTFE)-bound carbon black and loaded with a nanosized SnO_x catalyst, was demonstrated, by which up to 400 mA cm^{-2} at FE > 80 % could be achieved [3]. Fig. 5 shows the significant increase in activity with such electrodes compared to a plain tin foil.

3 Experimental Section

3.1 Electrochemical Reduction of CO_2

3.1.1 Catalyst and Electrode Preparation

SnO_x nanoparticles supported on carbon black were prepared as recently described in [3], based on the homogenous precipitation method via urea decomposition by Song and Kang [50]. Acetylene Black was suspended in double-distilled water by strong magnetic stirring (16 h) and ultrasonication (1 h). The targeted percentage of tin on carbon black was 2.5 wt %. $SnCl_2{\cdot}2H_2O$ and urea were added in concentrations of 0.01 and 0.5 M, respectively, and hydrolysis was performed at 90 °C for 4 h. The black solid was fil-

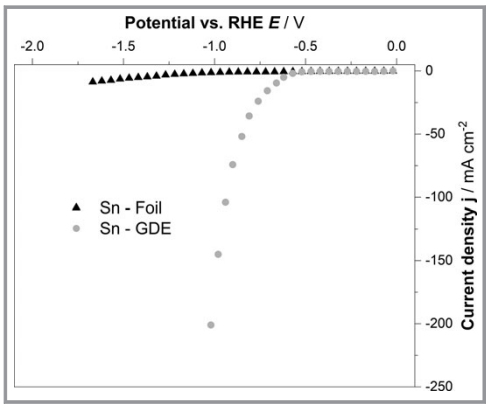

Figure 5. Linear sweep voltammetry displaying an elevated activity for Sn-GDE compared to Sn foil.

tered, carefully washed with water and dried at 100 °C overnight. The preparation of GDEs was performed by a dry pressing method described in [3]. In short, the SnO_2-loaded carbon is mixed with PTFE powder in the desired ratio in a knife mill and a portion of the mixture is transferred to a cylindrical mask (7.07 cm^2). Electrodes were pressed, extracted from the mask and undertaken thermal treatment at 340 °C for 10 min under nitrogen atmosphere.

3.1.2 Electrolysis Setup

Electrolysis was performed in a custom-made three-compartment cell operated in semi-batch mode under galvanostatic conditions at 1000 mA cm^{-2}. The cathode chamber consists of two parts, a gas side and a liquid side, separated by the GDE. The anode compartment is separated by a Nafion® 117 membrane. The GDE (sealed against the frame by an acrylonitrile butadiene styrene (ABS) plate leaving 1 cm^2 of geometrical surface area), a fine Ni mesh and an Hg/HgO (1 M KOH) electrode serve as working, counter, and reference electrode, respectively. CO_2 was constantly fed at 28 mL min^{-1}, while the electrolyte was added batchwise. Aqueous solutions of 2 M $KHCO_3$ (27 mL, adjusted to pH = 10 by $KOH_{(s)}$) and 5 M KOH (30 mL) were used as catholyte and anolyte, respectively. Electrolyte temperature was set to 50 °C by circulating the electrolyte trough heat exchangers in a thermostat. The final formate concentration was determined via high-performance liquid chromatography (HPLC).

3.2 Direct Formate Fuel Cell

3.2.1 Electrode Preparation

At the cathode side, a silver-based GDE supplied by Covestro Germany AG, was used. The anodes were prepared in-house via drop casting onto a gas diffusion layer (Sigracet 29 BC, SGL Carbon). The ink consists of 9.6 vol % ultra-pure water (Alfa Aesar, HPLC grade), 86.5 vol % 2-propanol (Chemsolute®, LC-MS quality), 3.8 vol % alkaline ionomer fumion (Fumatech) and a mass concentration of 13.5 mg mL_{Ink}^{-1} of carbon-supported palladium (Alfa Aesar, 10 wt % Pd, Type 487). The ink was sonicated for 2 h. The ink was drop-casted onto the gas diffusion layer (GDL) mounted onto a heating plate until an approximate metal loading of 0.31 mg cm^{-2} catalyst was attained.

3.2.2 Experimental Procedure

The experiments were carried out in a gold-plated 25 cm^2 (5 cm × 5 cm) in-house designed fuel cell at 25 °C. The DFFC was operated with three different formate-rich fuels at the anode side, introduced through a flow field on the back side of the electrodes: a solution obtained from CO_2 electrolysis (pH 11.3, 2.0 M $KHCO_3$ before CO_2RR electrolysis, 0.26 M $HCOO^-$) and a model formate solution with 2.0 M $KHCO_3$ (Roth, > 99.5 %), 0.25 or 1 M HCOOK (Sigma Aldrich, 99 %), and KOH pellets (AppliChem, 85 %) to obtain a pH of 11.3. The cathode fuel was pure oxygen (Linde, quality 4.5). The flow rate for the circulating anode fuel was 5 mL min^{-1}. Before recording the *U-j* curve (potentiostat: Zahner, Zennium), the formate solution was circulated for at least 1 h to ensure comparable wetting grades. Before entering the fuel cell, O_2 was routed through a washing flask with water at 25 °C. The pressure at the oxygen side was 4 mbar. The anode and cathode were separated by an anion exchange membrane of the type AHA from ASTOM Corporation (placed for at least 12 h in 1 M KOH solution before use). The *U-j* curve was then recorded in 25-mV steps until a cell voltage of 200 mV was attained.

3.3 Formate Decomposition to H_2 and Use in H_2/O_2 PEMFCs

3.3.1 Formate Decomposition

Formate decomposition was performed in closed-batch mode for characterization of process parameters and open-batch mode (hydrogen releasing) for the PEMFC supply. For characterization measurements, 34 mg of the used Pd/C powder (5 wt % Pd, Sigma-Aldrich) were placed in a stirred autoclave and 8 mL of a 1 M FA, FA/HCOOK mixture (50:50), or HCOOK solution, adjusted for its pH with KOH, were added. The autoclave was heated to a temperature of 80 °C and the pressure was monitored for 90 min. The recorded pressure was compensated for the temperature-related increase. Gas phase analysis was done with an offline Agilent 7890A gas chromatograph (GC), equipped with a Poropak Q and Molsieve 5A column, connected to a thermal conductivity detector (TCD).

3.3.2 Energy Recovery in PEMFCs

As proof of concept, the gas obtained by formate decomposition was transferred to a F107 PEMFC (h-tec, Hydrogen Energy Systems) with an electrode area of 16 cm^2 and a maximum power output of 200 mW (pure H_2/air). The cathode side was operated with atmospheric air in diffusion mode, while the anode was directly connected to the decomposition reactor without any further flow regulation. Simultaneous to starting the decomposition reaction, the monitoring of the fuel cells open circuit voltage (OCV) was enabled.

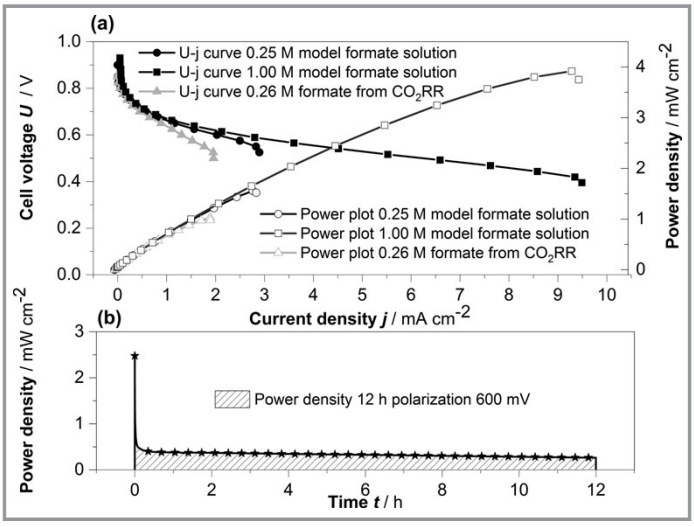

Figure 6. a) *U-j* curves and power plots for model formate fuels and formate fuel obtained from CO_2RR, b) potentiostatic operation of DFFC operating with formate obtained from CO_2RR.

4 Proof of Concept

4.1 Electrochemical Reduction of CO_2 to Formate

The formate-rich electrolyte employed as fuel in the following chapters was prepared by CO_2RR in the experimental setup described in [8]. A formate concentration of 0.26 M HCOOK is achieved within 30 min at a set current density of 1000 mA cm^{-2} with average FE to formate of 75 %. The respective cathode potential (vs standard hydrogen electrode (SHE)) dropped from −1.66 to about −1.52 V within the first 5 min and then steadily increased to about −1.62 V until the end of the experiments. The final solution showed a pH of 11.3 and was directly used as feed in the subsequent steps. As mentioned above, the obtained concentration is too low to obtain a reasonable energy density of the product stream. Although it is not in the scope of this study, in further work, higher concentrations > 1 M have to be targeted. This is important, independent of the specific product utilization but for its use in energy storage applications this holds particularly true.

4.2 Direct Formate Fuel Cell

Following electrolysis, the obtained product stream is used as feed in the DFFC device described in the Sect. 3. The results are summarized in Fig. 6. In Fig. 6a, the performances of the DFFC setup for the operation with a model formate fuel and a formate fuel obtained from CO_2RR are demonstrated. The OCV for the DFFC operating with the model formate fuel is 900 mV while the OCV for the DFFC supplied with the fuel from CO_2RR is 855 mV. These deviations from the theoretical value of 1.45 V (see Sect. 2.3) can be attributed to the mixed potential phenomenon which can be traced back to the oxidation of the anode catalyst and inevitable fuel crossover resulting in internal currents [51]. Nevertheless, the *U-j* curves show the characteristic shape, whereby at small overvoltage, the shapes are dominated by kinetic resistance followed by an interval where ohmic losses are decisive. Mass transport limitation can be observed at a current density of ∼9.50 mA cm^{-2} (1 M $HCOO^-$), 2.90 mA cm^{-2} (0.25 M $HCOO^-$), and 1.96 mA cm^{-2} operating with fuel from CO_2RR. The corresponding maximum power densities are 3.75, 1.52, and 1.03 mW cm^{-2}. Obviously, the discrepancy between the curves must be attributed to the varying composition of the fuel solutions.

Comparing the runs with model formate solutions, the importance of a high formate concentration can clearly be seen. This aforementioned relationship was also observed by several authors [28, 34, 35]. Additionally, the mass transport limitation shifts to higher current densities and the maximum power density increases. The formate concentration and the pH value are nearly identical for the model solution and the one from CO_2RR. Accordingly, the deviation of the *U-j* curves must be attributed to the remaining environment which could have an impact on the $HCOO^-$ diffusion coefficient. The explanation of this behavior requires further work and is not in the focus of this publication.

Comparing the maximum power density of 3.75 mW cm^{-2} of the DFFC operating with 1 M $HCOO^-$ model solution with the, to the authors' knowledge, best DFFC performance of 302 mW cm^{-2} [32], a discrepancy of two orders of magnitude can be observed. This difference is mainly attributed to the higher operating temperature (60 °C vs 25 °C) boosting the kinetic of the FOR and the additional potassium hydroxide (2 M KOH instead of $KHCO_3$) in the fuel stream increasing the cell voltage. Nevertheless, the successful demonstration of this concept can also clearly be seen in Fig. 6b where the DFFC runs in constant voltage mode at 600 mV with formate-rich feed generated by CO_2RR. Over a time of 12 h,

energy is generated. The comparatively poor numerical results of our system should not be overemphasized because the used DFFC system was not optimized at all since the objective of this part of our work was to demonstrate a proof-of-concept for the re-electrification of a formate solution generated by CO_2 electrolysis.

4.3 Formate Decomposition and Use in PEMFCs

Decomposition of a 1 M HCOOK solution was evaluated in terms of hydrogen yield and CO concentration using a Pd/C catalyst in a batch autoclave at various temperatures. CO is a typical poison for Pd-based catalysts and must be avoided at all costs but also because concentrations as low as 20 ppm [23] can be detrimental for the subsequent PEMFC. Fig. 7 shows the pH dependency of the decomposition. It is evident that alkaline conditions are beneficial regarding both yield and selectivity towards the dehydrogenation pathway. As described in Sect. 2.3, literature suggests that dehydrogenation is favored when starting with formate instead of formic acid as the mechanism towards H_2 production proceeds via a formate intermediate on metal catalysts [41]. Accordingly, CO evolution is suppressed to such an extent that it falls below the limit of detection, i.e., [CO] < 15 ppm. The increase in the H_2 yield with increasing pH value, in turn, can be explained by a combination of the falling rate of CO-induced catalyst deactivation and the removal of bicarbonate from the equilibrium which is converted into carbonate in highly alkaline solution (pH > 10.5).

To demonstrate a proof-of-concept, a 0.26 M HCOOK solution (pH = 11.3 with $KHCO_3$ concentration slightly increased from 2.0 to 2.25 M by conversion of CO_2 with KOH during electrolysis) obtained from CO_2RR was decomposed in semi-batch mode and the produced gas phase was directly transferred to a PEMFC. The maximum power density of the applied educational fuel cell system was measured to be 11 mW cm^{-2} achieved with H_2/air feed. Fig. 8 shows the obtained cell power over time. To compare a formate solution of higher concentration and pH (1 M, pH 14), the cell power of such a model solution was also recorded. In both cases the maximum power output could be reached temporarily, however, as the formate fuel is not continuously fed but provided once in the beginning, the power output decreases according to the decomposition kinetics of formate. A quantitative evaluation shows that the model 1 M formate solution provides a total energy output, which is significantly larger than expected from the ratio of the initial concentrations of the formate solutions, i.e., approximately factor 15 compared to factor 4. This can be explained with

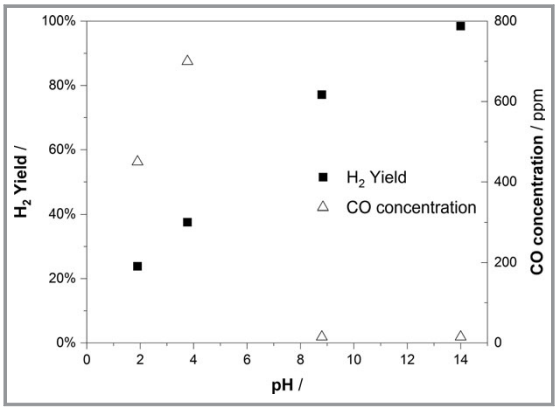

Figure 7. H_2 yield and CO concentration as function of the pH of the formate containing solution. Catalyst: 34 mg Pd/C, T = 80 °C, 1 M HCOOK/HCOOH. CO concentration below the limit of quantification for pH between 8.8 and 14.

the results discussed for the formate decomposition, where a higher pH value results in a higher H_2 yield. In addition, the formate solution from CO_2RR contained a high concentration of potassium carbonate which could limit the H_2 yield by impeding the equilibrium shift towards the product side (see Fig. 5). This may easily be avoided by choosing other conducting salts in CO_2RR, like KCl, which are not involved in the reaction equilibrium. Last, the resulting H_2 flow was not controlled, thus, making an exact quantitative evaluation difficult.

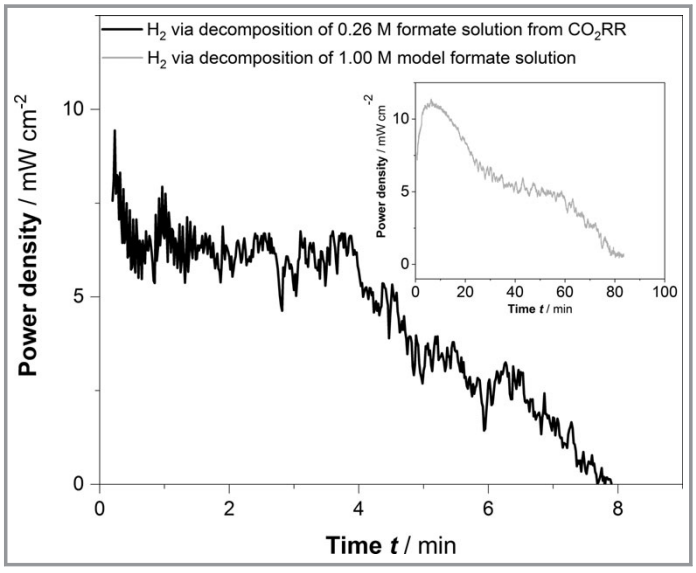

Figure 8. PEMFC output power over time obtained with H_2 supplied through the decomposition at 80 °C of a model 1 M HCOOK solution at pH = 14 and the 0.26 M solution from CO_2RR at pH = 11.3.

It was proven that, in principal, the stored chemical energy can successfully be recovered. Further investigations need to focus on the decomposition kinetics and, in particular, the reactor concept including a constant power release and a robust on-/off-functionality with regard to H_2 supply. In continuous mode, the reactor concept has to be adapted for accurate and robust release of the gas avoiding pulsation and entrainment. The latter is under development by the group of Wasserscheid for the release of H_2 from LOHCs [52, 53]. The advantage of formate decomposition is that it is less endothermic ($\Delta H_R^0 = 4\,kJ\,mol^{-1}$) [54], compared to the one of LOHC dehydrogenation ($\Delta H_R^0 = 36\,kJ\,mol^{-1}$ to $136\,kJ\,mol^{-1}$) [55] and that it takes place at lower temperatures.

5 Conclusion

Electrochemical CO_2 reduction to formate at alkaline conditions has been shown to proceed with promising selectivities and current densities using inexpensive and earth-abundant electrode materials. While literature on CO_2RR to formate often refers to the high potential for energy storage applications, we want to stress that although tremendous efforts are being made to optimize this reaction. So far, there is no clear and reasonable exploitation strategy in sight, as long as the reconversion of formate to electricity in subsequent processes has not been established properly and until the coupling of CO_2RR with these processes is not accounted for. Furthermore, owing to the rather low volumetric energy density and costly electrolysis, potential applications are limited to cases where applicability and public acceptance are more important than just price or energy density. This is mainly the case in decentralized, portable, and off-grid applications but not in electro-mobility or stationary energy storage. To this end, the proof-of-concept study herein successfully demonstrates for the first time that utilizing the product stream from CO_2EL directly as feed in a DFFC or indirectly in a PEMFC after H_2 release via catalytic decomposition facilitates storage and recovery of electricity. It is further shown how the specification of the CO_2EL product stream significantly influences the achievable electricity recovery, namely, how decisive product concentration obtained by CO_2EL and the compatibility of composition and pH value of the electrolyte are. Although performance indicators of the non-optimized devices given herein are far from being optimal, literature data give rise to the assumption that utilizing the feed in more optimized systems bears high promise.

Finally, summarizing the message from this contribution, three critical issues are identified which must be tackled and resolved before CO_2EL to formate and subsequent energy recovery can become a reasonable technology for energy storage.

- All involved technologies must be further optimized to facilitate adequate round-trip efficiency. So far, an efficiency of ~20 % estimated from state-of-the-art studies is too low to be reasonable.
- Efficient coupling of the technologies, as described in this contribution, is necessary. In that respect, optimization of possible formate concentration and compatibility/optimization of the electrolyte for both electricity storage and electricity recovery steps is essential, as shown herein.
- Finally, a complete and detailed life cycle, techno-economic and socio-economic and policy assessment starting with the capture of CO_2 from different sources and ending with the recovery of electricity has to be performed for different application scenarios. Importantly, this might reveal potential niche applications in which formate from CO_2EL indeed shows superior characteristics compared to competing technologies, either performance-wise, from environmental viewpoint, or even in terms of economic considerations.

Especially the last point has to be tackled to guide further development in this field and realize the potential of this promising technology towards a meaningful future for energy storage applications.

Parts of this work were funded by the Federal Ministry for Economic Affairs and Energy (FKZ 03ET1379A/B – EnElMi2.0). We would like to thank Covestro Deutschland AG for providing GDEs for the DFFC measurements.

Abbreviations

ABS	acrylonitrile butadiene styrene
AEM	anion-exchange membrane
CEM	cation-exchange membrane
CO_2EL	CO_2 electrolysis
CO_2RR	CO_2 reduction reaction
DFFC	direct formate fuel cell
DLFC	direct liquid fuel cell
FA	formic acid
FE	Faradaic efficiency
FOR	formate oxidation reaction
GC	gas chromatograph
GDE	gas diffusion electrode
GDL	gas diffusion layer
HPLC	high-performance liquid chromatography
LOHC	liquid organic hydrogen carrier
MEA	membrane electrode assembly
OCV	open circuit voltage
OER	oxygen evolution reaction
ORR	oxygen reduction reaction
PEMFC	proton exchange membrane fuel cell
PTFE	polytetrafluorethylene
SHE	standard hydrogen electrode
TCD	thermal conductivity detector
TRL	technology readiness level

References

[1] J. Leclaire, D. J. Heldebrant, *Green Chem.* **2018**, *20 (22)*, 5058 – 5081. DOI: https://doi.org/10.1039/C8GC01962B
[2] F. Ausfelder et al., *Chem. Ing. Tech.* **2015**, *87 (1 – 2)*, 17 – 89. DOI: https://doi.org/10.1002/cite.201400183
[3] D. Kopljar, N. Wagner, E. Klemm, *Chem. Eng. Technol.* **2016**, *39 (11)*, 2042 – 2050. DOI: https://doi.org/10.1002/ceat.201600198
[4] B. Endrődi, G. Bencsik, F. Darvas, R. Jones, K. Rajeshwar, C. Janáky, *Prog. Energy Combust. Sci.* **2017**, *62*, 133 – 154. DOI: https://doi.org/10.1016/j.pecs.2017.05.005
[5] L. C. Weng, A. T. Bell, A. Z. Weber, *Phys. Chem. Chem. Phys.* **2018**, *20 (25)*, 16973 – 16984. DOI: https://doi.org/10.1039/c8cp01319e
[6] A. Del Castillo, M. Alvarez-Guerra, J. Solla-Gullón, A. Sáez, V. Montiel, A. Irabien, *J. CO_2 Util.* **2017**, *18*, 222 – 228. DOI: https://doi.org/10.1016/j.jcou.2017.01.021
[7] H. R. Q. Jhong, F. R. Brushett, P. J. A. Kenis, *Adv. Energy Mater.* **2013**, *3 (5)*, 589 – 599. DOI: https://doi.org/10.1002/aenm.201200759
[8] D. Kopljar, A. Inan, P. Vindayer, N. Wagner, E. Klemm, *J. Appl. Electrochem.* **2014**, *44 (10)*, 1107 – 1116. DOI: https://doi.org/10.1007/s10800-014-0731-x
[9] P. Jeanty, C. Scherer, E. Magori, K. Wiesner-Fleischer, O. Hinrichsen, M. Fleischer, *J. CO_2 Util.* **2018**, *24*, 454 – 462. DOI: https://doi.org/10.1016/J.JCOU.2018.01.011
[10] D. Kopljar, A. Inan, P. Vindayer, R. Scholz, N. Frangos, N. Wagner, E. Klemm, *Chem. Ing. Tech.* **2015**, *87 (6)*, 855 – 859. DOI: https://doi.org/10.1002/cite.201400135
[11] Q. Lu, J. Rosen, F. Jiao, *ChemCatChem* **2015**, *7 (1)*, 38 – 47. DOI: https://doi.org/10.1002/cctc.201402669
[12] A. J. Martín, G. O. Larrazábal, J. Pérez-Ramírez, *Green Chem.* **2015**, *17 (12)*, 5114 – 5130. DOI: https://doi.org/10.1039/C5GC01893E
[13] A. S. Varela, W. Ju, P. Strasser, *Adv. Energy Mater.* **2018**, *8 (30)*, 1703614. DOI: https://doi.org/10.1002/aenm.201703614
[14] J. T. Feaster, C. Shi, E. R. Cave, T. Hatsukade, D. N. Abram, K. P. Kuhl, C. Hahn, J. K. Nørskov, T. F. Jaramillo, *ACS Catal.* **2017**, *7 (7)*, 4822 – 4827. DOI: https://doi.org/10.1021/acscatal.7b00687
[15] C. W. Lee, N. H. Cho, K. D. Yang, K. T. Nam, *ChemElectroChem* **2017**, *4 (9)*, 2130 – 2136. DOI: https://doi.org/10.1002/celc.201700335
[16] R. M. Arán-Ais, D. Gao, B. Roldan Cuenya, *Acc. Chem. Res.* **2018**, *51 (11)*, 2906 – 2917. DOI: https://doi.org/10.1021/acs.accounts.8b00360
[17] A. J. Martín, G. O. Larrazábal, J. Pérez-Ramírez, *Green Chem.* **2015**, *17 (12)*, 5114 – 5130. DOI: https://doi.org/10.1039/C5GC01893E
[18] K. P. Kuhl, E. R. Cave, D. N. Abram, T. F. Jaramillo, *Energy Environ. Sci.* **2012**, *5 (5)*, 7050 – 7059. DOI: https://doi.org/10.1039/c2ee21234j
[19] M. Jouny, W. Luc, F. Jiao, *Ind. Eng. Chem. Res.* **2018**, *57 (6)*, 2165 – 2177. DOI: https://doi.org/10.1021/acs.iecr.7b03514
[20] S. Verma, B. Kim, H. R. M. Jhong, S. Ma, P. J. A. Kenis, *ChemSusChem* **2016**, *9 (15)*, 1972 – 1979. DOI: https://doi.org/10.1002/cssc.201600394
[21] R. Masel, R. Ni, Z. Liu, Q. Chen, R. Kutz, L. Nereng, D. Lutz, K. Lewinski, *Energy Procedia* **2014**, *63*, 7959 – 7962. DOI: https://doi.org/10.1016/j.egypro.2014.11.832
[22] J. M. Spurgeon, B. Kumar, *Energy Environ. Sci.* **2018**, *11 (6)*, 1536 – 1551. DOI: https://doi.org/10.1039/c8ee00097b
[23] A. K. Singh, S. Singh, A. Kumar, *Catal. Sci. Technol.* **2016**, *6 (1)*, 12 – 40. DOI: https://doi.org/10.1039/C5CY01276G
[24] M. Pérez-Fortes, J. C. Schöneberger, A. Boulamanti, G. Harrison, E. Tzimas, *Int. J. Hydrogen Energy* **2016**, *41 (37)*, 16444 – 16462. DOI: https://doi.org/10.1016/j.ijhydene.2016.05.199
[25] P. Preuster, A. Alekseev, P. Wasserscheid, *Annu. Rev. Chem. Biomol. Eng.* **2017**, *8*, 445 – 471 DOI: https://doi.org/10.1146/annurev-chembioeng-060816-101334
[26] M. Bevilacqua, J. Filippi, H. A. Miller, F. Vizza, *Energy Technol.* **2015**, *3 (3)*, 197 – 210. DOI: https://doi.org/10.1002/ente.201402166
[27] B. C. Ong, S. K. Kamarudin, S. Basri, *Int. J. Hydrogen Energy* **2017**, *42 (15)*, 10142 – 10157. DOI: https://doi.org/10.1016/j.ijhydene.2017.01.117
[28] A. M. Bartrom, J. Ta, T. Q. Nguyen, J. Her, A. Donovan, J. L. Haan, *J. Power Sources* **2013**, *229*, 234 – 238. DOI: https://doi.org/10.1016/j.jpowsour.2012.12.007
[29] D. H. Setiadjid, *Chem. Eng. Trans.* **2018**, *70*, 409 – 414. DOI: https://doi.org/10.3303/CET1870069
[30] H. Miller, J. Ruggeri, A. Marchionni, M. Bellini, M. Pagliaro, C. Bartoli, A. Pucci, E. Passaglia, F. Vizza, *Energies* **2018**, *11 (2)*, 369. DOI: https://doi.org/10.3390/en11020369
[31] A. M. Bartrom, J. L. Haan, *J. Power Sources* **2012**, *214*, 68 – 74. DOI: https://doi.org/10.1016/j.jpowsour.2012.04.032
[32] K. Tran, T. Q. Nguyen, A. M. Bartrom, A. Sadiki, J. L. Haan, *Fuel Cells* **2014**, *14 (6)*, 834 – 841. DOI: https://doi.org/10.1002/fuce.201300291
[33] L. An, R. Chen, *J. Power Sources* **2016**, *320*, 127 – 139. DOI: https://doi.org/10.1016/j.jpowsour.2016.04.082
[34] J. Jiang, A. Wieckowski, *Electrochem. Commun.* **2012**, *18 (1)*, 41 – 43. DOI: https://doi.org/10.1016/j.elecom.2012.02.017
[35] X. Yu, A. Manthiram, *Appl. Catal., B* **2015**, *165*, 63 – 67. DOI: https://doi.org/10.1016/j.apcatb.2014.09.069
[36] L. Q. Wang, M. Bellini, J. Filippi, M. Folliero, A. Lavacchi, M. Innocenti, A. Marchionni, H. A. Miller, F. Vizza, *Appl. Energy* **2016**, *175*, 479 – 487. DOI: https://doi.org/10.1016/J.APENERGY.2016.02.129
[37] D. Mellmann, P. Sponholz, H. Junge, M. Beller, *Chem. Soc. Rev.* **2016**, *45 (14)*, 3954 – 3988. DOI: https://doi.org/10.1039/C5CS00618J
[38] M. Grasemann, G. Laurenczy, *Energy Environ. Sci.* **2012**, *5 (8)*, 8171 – 8181. DOI: https://doi.org/10.1039/c2ee21928j
[39] J. Su, L. Yang, M. Lu, H. Lin, J. Su, L. Yang, M. Lu, H. Lin, *ChemSusChem* **2015**, *8 (5)*, 813 – 816. DOI: https://doi.org/10.1002/cssc.201403251
[40] Q. Y. Bi, J. D. Lin, Y. M. Liu, X. L. Du, J. Q. Wang, H. Y. He, Y. Cao, *Angew. Chem., Int. Ed.* **2014**, *53 (49)*, 13583 – 13587. DOI: https://doi.org/10.1002/anie.201409500
[41] S. Singh, S. Li, R. Carrasquillo-Flores, A. C. Alba-Rubio, J. A. Dumesic, M. Mavrikakis, *AIChE J.* **2014**, *60 (4)*, 1303 – 1319. DOI: https://doi.org/10.1002/aic.14401
[42] H. Wiener, Y. Sasson, J. Blum, *J. Mol. Catal.* **1986**, *35 (3)*, 277 – 284. DOI: https://doi.org/10.1016/0304-5102(86)87075-4
[43] H. R. M. Jhong, S. Ma, P. J. Kenis, *Curr. Opin. Chem. Eng.* **2013**, *2 (2)*, 191 – 199. DOI: https://doi.org/10.1016/j.coche.2013.03.005
[44] H. Y. Kim, I. Choi, S. H. Ahn, S. J. Hwang, S. J. Yoo, J. Han, J. Kim, H. Park, J. H. Jang, S. K. Kim, *Int. J. Hydrogen Energy* **2014**, *39 (29)*, 16506 – 16512. DOI: https://doi.org/10.1016/j.ijhydene.2014.03.145
[45] J. Wu, F. G. Risalvato, F.-S. Ke, P. J. Pellechia, X.-D. Zhou, *J. Electrochem. Soc.* **2012**, *159 (7)*, F353 – F359. DOI: https://doi.org/10.1149/2.049207jes
[46] H. Yang, J. J. Kaczur, S. D. Sajjad, R. I. Masel, *J. CO_2 Util.* **2017**, *20*, 208 – 217. DOI: https://doi.org/10.1016/j.jcou.2017.04.011

[47] E. J. Dufek, T. E. Lister, M. E. McIlwain, *Electrochem. Solid-State Lett.* **2012**, *15 (4)*, B48 – B50. DOI: https://doi.org/10.1149/2.010204esl
[48] Y. Hori, H. Ito, K. Okano, K. Nagasu, S. Sato, *Electrochim. Acta* **2003**, *48 (18)*, 2651 – 2657. DOI: https://doi.org/10.1016/S0013-4686(03)00311-6
[49] C. Oloman, H. Li, *ChemSusChem* **2008**, *1 (5)*, 385 – 391. DOI: https://doi.org/10.1002/cssc.200800015
[50] K. C. Song, Y. Kang, *Mater. Lett.* **2000**, *42 (5)*, 283 – 289. DOI: https://doi.org/10.1016/S0167-577X(99)00199-8
[51] D. A. J. Rand, A. L. Dicks, *Fuel Cell Systems Explained*, 3rd ed., John Wiley & Sons, Chichester **2018**.
[52] P. Preuster, A. Alekseev, P. Wasserscheid, *Annu. Rev. Chem. Biomol. Eng.* **2017**, *8 (1)*, 445 – 471. DOI: https://doi.org/10.1146/annurev-chembioeng-060816-101334
[53] P. Preuster, C. Papp, P. Wasserscheid, *Acc. Chem. Res.* **2017**, *50 (1)*, 74 – 85. DOI: https://doi.org/10.1021/acs.accounts.6b00474
[54] P. Atkins, J. de Paula, *Atkins' Physical Chemistry*, Oxford University Press, Oxford **2006**.
[55] K. Müller, J. Völkl, W. Arlt, *Energy Technol.* **2013**, *1 (1)*, 20 – 24. DOI: https://doi.org/10.1002/ente.201200045

